Experimental Study on Geocell-Reinforced Bases under Static and Dynamic Loading

By
Sanat Kumar Pokharel
B.E., University of Roorkee (Indian Institute of Technology, Roorkee), India, 1988
M.Sc., Norwegian University of Science and Technology, Trondheim, Norway, 1997

Submitted to the Department of Civil, Environmental, and Architectural Engineering and the Graduate Faculty of the University of Kansas in partial fulfillment of the requirements for the degree of Doctor of Philosophy

_____
Chairperson Dr. Jie Han

Committee members

_____
Dr. David J. Ekerdt

_____
Dr. Anil Misra

_____
Dr. Robert L. Parsons

_____
Dr. C. Bryan Young

Date Defended: October 13, 2010

The Dissertation Committee for Sanat Kumar Pokharel certifies that this is the approved version of the following dissertation:

Experimental Study on Geocell-Reinforced Bases under Static and Dynamic Loading

_____

Dr. Jie Han, Chairperson

Date approved: October 13, 2010

ABSTRACT

Geocells are a three-dimensional honeycomb type of geosynthetics used to reinforce weak soils and base courses of roads since the 1970s. However, this technology has been hindered by the lack of a reliable design method. The development of a reliable design method requires in-depth understanding of the geocell reinforcement mechanisms. In this study, laboratory model and full-scale moving wheel tests were conducted on geocell-reinforced granular bases over weak subgrade.

Plate loading tests were conducted in the medium-scale and large-scale geotechnical boxes at the University of Kansas and full-scale moving wheel tests were conducted in the accelerated pavement testing facility at Kansas State University. Four types of geocells including one high-density polyethylene (HDPE) and three novel polymeric alloy (NPA) geocells were tested in the medium-scale plate loading tests. The effects of geocell confinement and other influence factors on the behavior of granular bases were studied. One selected type of NPA geocell was used in the large-scale cyclic plate loading tests and the moving wheel tests. The subgrade used in the large-scale plate loading tests was an artificial mix of Kansas River sand and kaolin while A-7-6 clay was used in the moving wheel tests. Four types of infill materials including crushed limestone aggregate (AB-3), quarry waste (QW), Kansas River (KR) sand, and Recycled Asphalt Pavement (RAP) were used as the base courses in this study.

More than 50 medium-scale plate loading tests, 12 large-scale cyclic plate loading tests, and 4 moving wheel tests on unpaved road sections were conducted. The road sections were exhumed and examined after all the large-scale cyclic plate loading tests and the

moving wheel tests. The benefits of NPA geocell reinforcement were evaluated in terms of the number of wheel passes at 75 mm of rut depth and the vertical stress distribution.

The test results were analyzed separately in terms of different test methods. It is shown that geocells placed in a circular shape performed better than those in an elliptical shape. NPA geocells increased the stiffness and ultimate bearing capacity of granular bases by 1.5 to 2.0 times. NPA geocell-reinforced bases had higher stiffness and bearing capacity than HDPE geocell-reinforced bases. NPA geocells significantly reduced permanent deformations of granular bases with the number of cycles or wheel passes and increased stress distribution angles. The existence of geocells made compaction more difficult and it was found that the relative compaction of infill materials in geocells is important for the performance of geocell-reinforced bases.

The established design method for the planar geosynthetic reinforcement was modified for the NPA geocell-reinforced bases over weak subgrade and calibrated based on the test results from the large-scale cyclic plate loading tests and the moving wheel tests. The California Bearing Ratios (CBR) of the subgrade and base course, the number loading cycles or wheel passes required for 50 to 75 mm rut, the height of geocell, and the thickness of the base course were the variables used to calibrate this design formula. The design method was used to verify the test results and yielded a good comparison.

Dedicated to my parents,

Mr. Hari Prasad Pokharel and Mrs. Sarala Pokharel

ACKNOWLEDGEMENT

First of all, I would like to express my deepest gratitude to Professor Jie Han for giving me the opportunity to work on such an interesting project. It would not have been possible to complete this work without his excellent guidance, unswerving encouragement, and support that I received throughout my Ph.D. study.

I would like to thank Professors Robert Parsons, Anil Misra, Bryan Young, and David Ekerdt for their kind consent to be the members of my Ph.D. committee and their valuable suggestions. I am grateful to Professor Dov Leshchinsky from the University of Delaware for his valuable suggestions on my work, Professor Adolfo Matamoros from KU for his time when I was learning to operate the MTS loading system, and Professor Mustaque Hossain from Kansas State University for his great support and help during the moving wheel tests.

I am grateful to KU Transportation Research Institute (Grant #DT0S59-06-G-00047, provided by the US Department of Transportation – Research and Innovative Technology Administration) and PRS Mediterranean, Inc. in Israel for funding this research project. I greatly appreciate the support I received from Dr. Robert Honea, the director of the KU Transportation Research Institute and Mr. Oded Erez, president, Mr. Izhar Halahmi, chief scientist, and Dr. Ofer Kief, pavement and soil consultant, of PRS Mediterranean in Israel.

This acknowledgement will remain incomplete without thanking my friends, Mr. Milad Jowkar, Dr. Xiaoming Yang, and Mr. Yu Qian for their tireless help in my experimental work. I would like to sincerely thank Mr. Jim Weaver, Lab Manager at KU, for his help in the laboratory and Mr. Matthew Maksimowiczat for his technical support. I am also thankful to Dr. Sari Abusharar, Ms. Yanli Dong, Mr. Cheng Lin, Dr. Fei Wang, Dr.

Yong Li, Mr. Subhash Thakur, Dr. Anil Bhandari, Mr. Jitendra Thakur, Mr. Fatih Alemdar, Mr. Josh Barton, Mr. Kahle Loveless, and Mr. AJ Rahman for their help at different stages of the experimental work and Mr. Randy Testa, Dr. Chandra Manandhar, and Mr. Luke McIntosh for their help in moving wheel tests at Kansas State University.

I am particularly indebted to my wife, Pratima, source of my strength and motivation, more so at difficult times and my daughters Pranjali and Prashanna for putting up with my crazy schedule as a Ph.D. student. I would like to thank my sisters, relatives, and friends for their moral support and taking pride in my success.

.

TABLE OF CONTENTS

LIST OF TABLES

LIST OF FIGURES

CHAPTER ONE

INTRODUCTION

1.1 Background

An estimated 80% of all roads in the world are unpaved and a majority of them are low-volume (Tingle and Jersey, 2007). According to the AASTHO (American Association of State Highway and Transportation Officials) report, approximately 20% of pavements fail due to insufficient structural strength (Mengelt et al., 2000). While limited resources are available for repair, maintenance, and rehabilitation of low-volume roads (Tingle and Jersey, 2007), a sustainable option to overcome this problem is to develop an innovative pavement stabilization technique with a suitable reinforcement alternative that improves the overall structural strength, reduces operational costs, and minimizes maintenance requirements. Geosynthetic reinforcement is one of the established techniques of subgrade improvement and base reinforcement for over 40 years (Giroud and Han, 2004a, b). Geosynthetics have been used in different civil engineering works such as foundation support, reinforced slopes, erosion control, retaining walls, and subgrade improvement and reinforcement to base courses of road sections. Since the 1970s, geosynthetics, mostly planar reinforcement (such as geogrid and woven geotextile), have been used to improve the performance of both paved and unpaved roads. For these applications, geosynthetic sheets are placed at the subgrade-base interface or within the base course to increase bearing capacity of subgrade or provide confinement to base courses. Geocells, in a form of three-dimensional interconnected honeycomb polymeric cells, are ideal for soil confinement. Based on a comprehensive literature review by Yuu et al. (2008), theories and design methods are far behind the

applications of geocells in the field, especially for roadway applications, due to a lack understanding of mechanisms and influencing factors for geocell reinforcement.

Most of the published research thus far has focused on planar reinforcement and has resulted in several design methods for geotextile or geogrid-reinforced unpaved roads (for example, Steward et al., 1977; Giroud and Noiray, 1981; Giroud and Han, 2004a, b). More research is needed to develop such a design method for three-dimensional interconnected geocells. Three experimental test methods were used in this study, which include medium-scale box tests on geocell-reinforced bases, large-scale box tests on geocell-reinforced bases over weak subgrade, and accelerated moving wheel tests on geocell-reinforced bases over weak subgrade. Three different infill materials were used, which include well-graded AB-3 aggregate, poorly-graded Kansas River sand, quarry waste, and recycled asphalt pavement. With help of these extensive experimental tests and test data, this research proposes a design method for geocell-reinforced unpaved roads.

1.2 Geocell

The concept of lateral confinement by cellular structures dates back to 1970s. The United States Army Corps of Engineers developed this idea for providing lateral confinement to improve the bearing capacity of poorly graded sand (Webster, 1979a). The predecessors of present geocells were sand grids made up of paper soaked in phenolic water resistant resin. Later, metallic geocells, especially those made of aluminum, were chosen because of strength requirements, but they proved unfeasible because of handling difficulty and high cost. Geocells have also been made using geogrid sheets jointed by bodkin bars (for example, Carter and Dixon, 1995). At the present time high-density polyethylene (HDPE) is the

common polymer used to make geocells by welding extruded HDPE strips together to form honeycombs. Recently, a new type of polymer, NEOLOY^{TM} polymeric alloy, is used to make geocells. Geocells come in different shapes and sizes. **Figure 1.2.1** shows the pictures of geocells in different stages.

(a) Bundled geocell for easy transportation

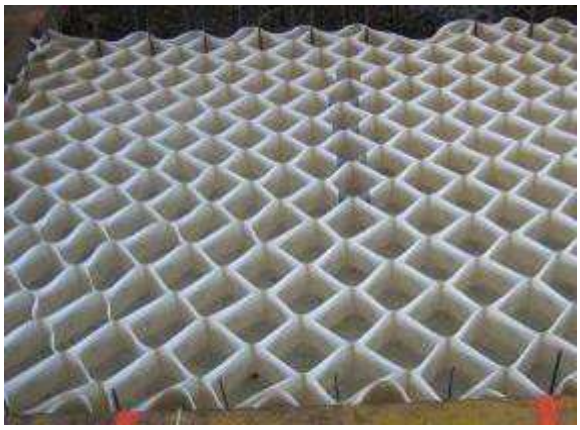

(b) Expanded geocell ready for filling

(c) Filling up the geocells with base material

(d) Compaction after filling

Figure 1.2.1 Neoloy Polymeric Geocells at different stages

In the present study, majority of the experiments were carried out with geocells made of NEOLOY polymeric alloy (referred as NPA geocells in this dissertation), which is a nano-composite alloy of polyester/polyamide nano-fibers, dispersed in polyethylene matrix.

1.3 Geocell-reinforced Granular Bases

Most of the time unpaved roads are subjected to repeated loads; they can be either permanent areas and roads such as parking lots and county roads or temporary roads such as access roads and haul roads in a construction area. A typical geocell-reinforced section is shown in **Figure 1.3.1**. The typical section consists of a weak subgrade, a nonwoven geotextile as a separator, a geocell-reinforced granular base, and a cover layer. The traffic load from the axles is transmitted to the subgrade through the reinforced base course. Principally, the reinforced base course is assumed to be stiff enough to resist the deformation and transmit the stress to the subgrade causing it to deform. This phenomenon is however, more complicated in case of a three dimensional reinforcement such as geocell. Properties of reinforcing geocell, base and subgrade materials, and the interaction of geocell with the soil contributing to the vertical and horizontal confinement characterize the overall behavior of the reinforced composite section.

The inclusion of three dimensional geocell structure as soil reinforcement has been found to be effective in soil confinement. Past research showed that geocell reinforcement at the base course of an unpaved road improves the engineering behavior of the reinforced composite section, such as stiffness and bearing capacity.

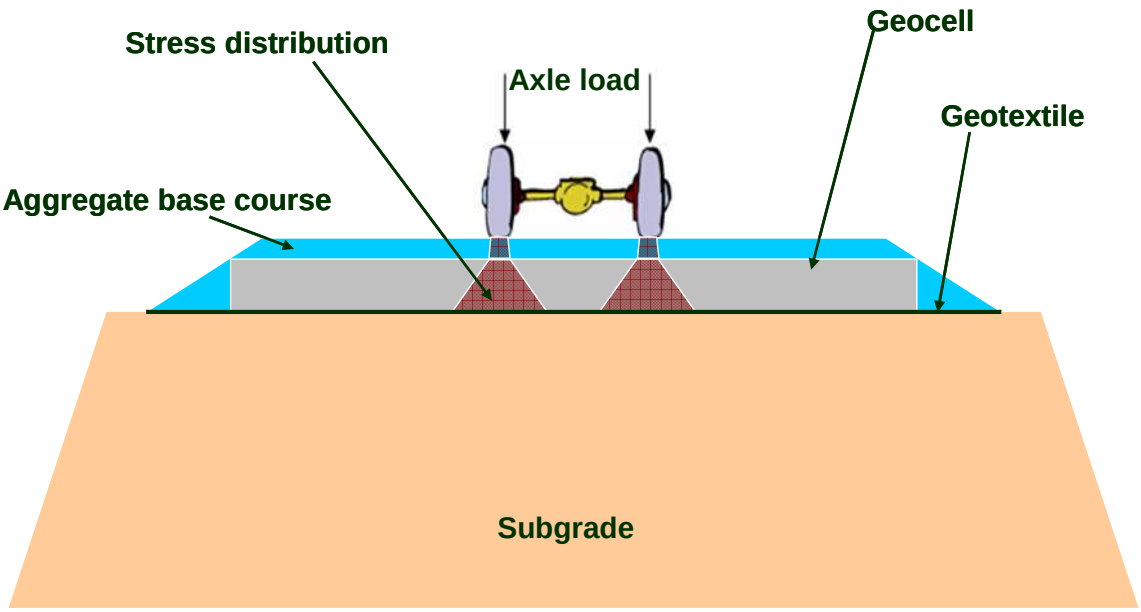

Figure 1.3.1 Typical section of geocell-reinforced unpaved road

1.4 Problem Statements

Despite the effectiveness of the geocell system, the acceptance of geocells for base reinforcement of unpaved roads is limited due to the lack of design method. However, the lack of design method results from limited understanding of the load transfer mechanisms, limited methods for quantifying the benefits, and limited full-scale performance data. The factors influencing the behavior of geocell-reinforced bases under static and dynamic loading are not well understood.

1.5 Research Objectives

The objectives of the research are to understand the load transfer mechanism of geocell-reinforced bases in unpaved roads, and identify and evaluate the influence factors as a

function of load-deformation level under static and dynamic loads based on medium-scale plate load tests, large-scale plate load tests, and accelerated moving wheel load tests representing real-time traffic in the laboratory, and develop a design method for geocell-reinforced unpaved roads based on test data from the large-scale plate load test and the accelerated moving wheel tests.

1.6 Research Methodology

This research was conducted by adopting the following methodologies: (1) an extensive literature review on geosynthetic reinforced bases in unpaved roads with an emphasis on geocell reinforcement including load transfer mechanisms and influence factors; (2) medium-scale box tests on geocell-reinforced bases under static and cycle loads to evaluate the effect of geocell reinforcement and its influence factors; (3) large-scale box tests on geocell-reinforced bases over weak subgrade under cyclic loads to evaluate the load transfer mechanisms through the geocell-reinforced bases; (4) accelerated moving wheel tests to verify the performance of geocell-reinforced bases over weak subgrade under real-world traffic; and (5) development of a design method for geocell-reinforced bases over weak subgrade based on the test data from the large-scale box tests and accelerated moving wheel tests. The medium-scale and large-scale box tests were performed at the University of Kansas (KU) while the accelerated moving wheel tests were performed in the accelerated pavement testing (APT) facility at Kansas State University (KSU).

1.7 Organization of this Dissertation

This dissertation is organized in eight chapters. Chapters 3 through 6 describe the experimental study that forms the backbone of this dissertation.

Chapter 1 - Introduction: This chapter gives highlights on the background, problem statement, research objectives, and research methodology.

Chapter 2 - Literature review: This chapter contains the reviews of past studies pertinent to present research. The major focus of this chapter is to compile existing knowledge and findings in the area of geocell-reinforced soils and identify the gaps that need to be bridged to achieve the objective of the present study.

Chapter 3 - Materials used in the experimental study: This chapter describes the properties of all the materials used in three tests discussed in chapters 4 through 6.

Chapter 4 - Medium-size plate load tests: This chapter describes the test equipment and procedures, and analyzes the results obtained from medium-size plate load tests under static and cyclic loading.

Chapter 5 - Large-scale plate load tests: This chapter describes the test equipment and procedures, and analyzes the results obtained from large-scale plate load tests under cyclic loading.

Chapter 6 - Accelerated moving wheel tests: This is the final chapter on experimental study that describes the test equipment and procedures, and analyzes the results obtained from the accelerated moving wheel tests.

Chapter 7 – Development of design method: Based on the test results from the large-scale plate load tests and the accelerated moving wheel tests discussed in Chapters 5 and 6, a design method was developed and presented in this chapter.

Chapter 8 - Conclusions and recommendations: This chapter provides the final conclusions from this study and recommendations for future work.

CHAPTER TWO

LITERATURE REVIEW

2.1 Introduction

As mentioned in **Chapter 1**, the pioneering studies on three-dimensional soil confinement cells in the 1970s, later named as "Geocell", were focused on the feasibility of the confinement structure (Webster and Watkins, 1977; Webster and Alford, 1978; and Webster, 1979 a, b). The research then considered the confinement of poorly-graded beach sand and the properties and geometry of the geocell. The later studies from 1980s to 1990s broadened the scopes of the research and investigated a number of influence factors. The major concerns of these studies were on the effects of geocell height to width ratio (i.e., aspect ratio), tensile stiffness of geocell material, strength and density of infill material, subgrade condition, loading type and location, and conjunctive use with other planar geosynthetic reinforcement. Recent studies have been more focused on geocell-reinforced bases for unpaved roads including the current study. Yuu et al. (2008) summarized the past studies on geocells from triaxial compression tests, laboratory model tests, and field tests. An overview of the previous studies is summarized in **Table 2.1.1** and the individual studies are explained in the sections to follow.

Table 2.1.1 Overview of previous studies on geocell reinforcement

Study on	Carried out by
Geometric ratio of geocell	Rea and Mitchell (1978); Shimizu and Inui (1990); Mhaiskar and Mandal (1992a, 1992b, 1994, 1996); Mandal and Gupta (1994)
Failure mechanism	Mitchell et al.(1979)
Properties of geocell	Shimizu and Inui (1990); Dash et al. (2001a, 2001b)
Effectiveness of geocell	Bathurst and Jarrett (1988); Dash et al. (2003); Dash et al. (2004)
Loading area, position and type	Rea and Mitchell (1978); Shimizu and Inui (1990); Mhaiskar and Mandal (1992a, 1992b, 1994, 1996); Chang et al. (2007)
Infill density	Mhaiskar and Mandal (1992a, 1992b, 1994, 1996); Dash et al. (2001a, 2001b)
Type and size of geocell	Dash et al. (2001a, 2001b)

2.2 Experimental Studies

2.2.1 Triaxial compression tests

Bathurst and Karpurapu (1993) conducted large-scale triaxial compression tests on isolated composite specimens of geocell-reinforced aggregate soil. The 200 mm high specimen had height to diameter ratio as unity. The tests confirmed the stiffening effect of geocell confinement and showed that the increase in the soil strength was imparted by the confinement effect of the geocell. A simple elastic membrane model (**Figure 2.2.1**) was

proposed to estimate the additional apparent cohesion (c_r) present in the composite using **Equation 2.2.1**.

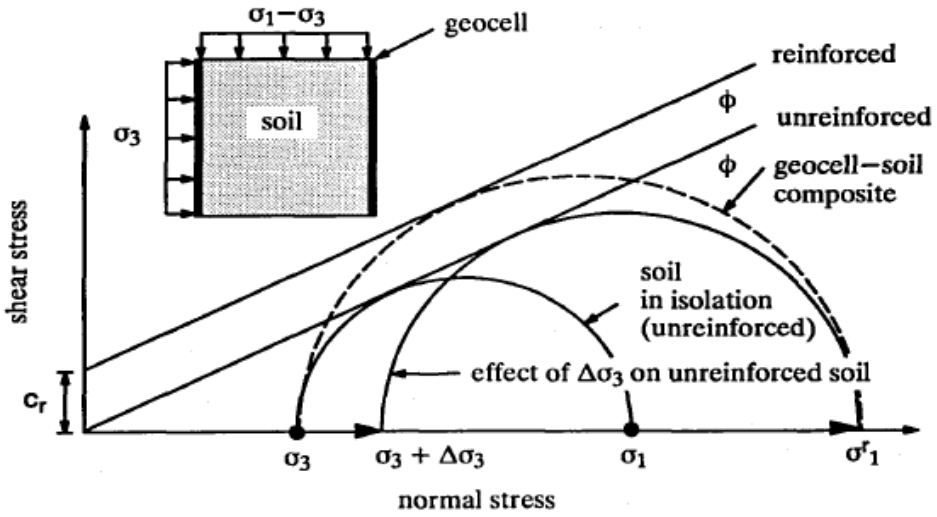

Figure 2.2.1 Mohr circles and failure envelopes for unreinforced and geocell-reinforced soil (reproduced from Bathurst and Karpurapu, 1993).

$$c_r = \frac{\Delta\sigma_3}{2}\tan\left[\frac{\pi}{4}+\frac{\phi}{2}\right] \qquad \textbf{Equation 2.2.1}$$

where

$\Delta\sigma_3$ = additional confining stress induced by geocell confinement;

ϕ = peak friction angle of the infill soil.

Rajagopal et al. (1999) studied the influence of geocell confinement on the strength and stiffness behavior of granular soil encased in single and multiple geocells. This study

found that the granular soil developed a large amount of apparent cohesive strength due to geocell confinement. The induced apparent cohesive strength was found to depend on the tensile modulus of geocell, but the frictional strength of the granular soil was not affected by the geocell confinement. This study further suggested that the use of a single geocell in triaxial tests was not adequate to represent the real behavior of geocell-reinforced soils.

Madhavi Latha and Murthy (2007) conducted triaxial tests to study the effect of reinforcement form on strength improvement of geosynthetic-reinforced sand through regular triaxial compression tests. All reinforced samples were found to exhibit improved stress-strain responses. Cellular reinforcement was found to be more effective in improving the strength. The results from the tests were consistent with the theoretical calculations using **Equation 2.2.1** suggested by Bathurst and Karpurapu (1993).

2.2.2 Laboratory plate load tests

Rea and Mitchell (1978) conducted plate load tests on sand-filled square shaped paper grid cells to identify different modes of failure and arrive at optimum dimensions of the cell. As one of the pioneering works in the research of geocell reinforcement, this study used paper grid cells formed in a regular square pattern of 51 mm width, and a 915 mm square box with flexible rubber bottom was placed on a spring base. This study reported a sudden and well-defined failure in the reinforced section under static loading.

de Garidel and Morel (1986) experimented with cellular structures made up of geotextile to develop new soil strengthening techniques for low-volume roads. The test was carried out in a rigid metallic pit of 2 m height x 2 m width x 1.4 m depth. Punching tests carried out by a rigid circular plate on cellular geotextile structures infilled with fine sand

found a remarkable increase in the rigidity for fine sand at a large displacement while it was not appreciable in a small displacement. Load-settlement curves showed a regular honeycomb structure of elementary polypropylene meshes at 10 cm x 10 cm size had the highest increase in the rigidity as compared with a 3-dimensional fiber-soil composite and a regular and continuous honeycomb structure made up of bonded geotextile strips.

Jamnejad et al. (1986) conducted both monotonic and repeated plate loading tests to demonstrate the advantages gained from the use of geocell (it was mentioned as honeycomb type grid system in their paper) reinforcement in pavement construction. The tests were carried out on a 200 mm thick geocell-reinforced base underlain by a 600 mm thick firm subgrade. The tests showed increased stiffness and failure load with the increase in infill density; improved elastic properties of the base layer; and improved cyclic response and retarded cyclic degradation by the inclusion of geocell reinforcement. The cells without any filled adjacent cells failed at the ultrasonic welds due to bursting while the cells with filled adjacent cells failed by buckling. Jamnejad et al. (1986) also compared the measured stresses at the geocell-reinforced base-subgrade interface and the measured permanent deformations against theoretical solutions (i.e., Boussinesq, Westergaard, Burmister, and Ahlvin and Ulery) for uniform or two-layer systems without geocell. The comparisons showed that these theoretical solutions could not properly predict the performance of the composite system. On a similar setup Kazerani and Jamnejad (1987) found geocell reinforcement could significantly improve the load-deformation and stress distributing characteristics of poorly graded materials and reduce the thickness requirement of the bases by 20-30%. They concluded that a design procedure for geocell reinforced structures could be developed based on a limited allowable vertical compressive strain at the base-subgrade interface. Similar results were reported by Bathurst and Jarrett (1988) on the improved bearing capacity of geocomposite mattress, for example, a stiffer geocell material improved the bearing capacity

to double. The effect of the properties of infill material on the performance of unpaved and paved road sections subjected to cyclic loading (Kazerani and Jamnejad, 1987) is shown in **Figure 2.2.2**. The figure shows that both the strength of the subgrade and the quality of infill material play important roles in improving the performance of the geocell-reinforced road section.

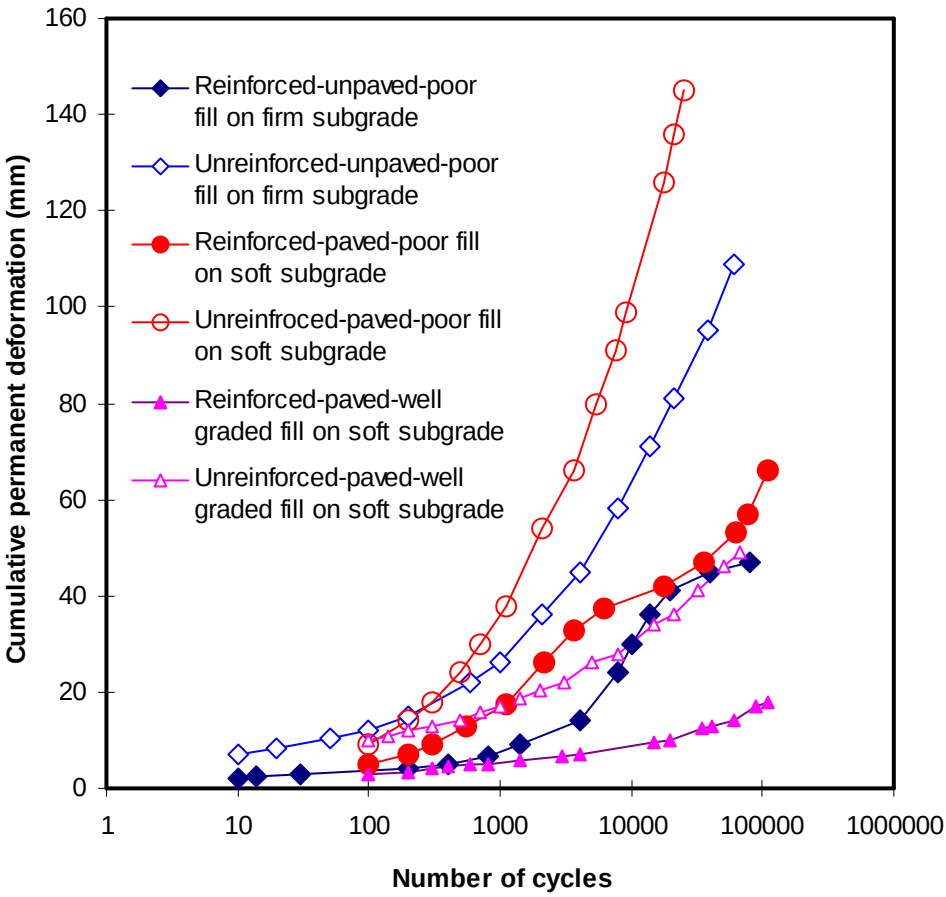

Figure 2.2.2 Effect of quality of infill material and subgrade strength on geocell-reinforced road sections under cyclic loading (reproduced from Kazerani and Jamnejad, 1987)

Shimizu and Inui (1990) examined the possibility of reinforcing soft ground by geotextile cell and found that the installation of a cell wall increased the bearing capacity of the ground. The bearing capacity was found to increase with increased height and reduced area of the individual cell, and the extent of increase in the bearing capacity was correlated to the horizontal stiffness of the cell material. The load-settlement relation in **Figure 2.2.3** shows that the increase in the bearing capacity of the reinforced soft ground is dependent on the material property of the cell wall. Geocell A had about four times and geocell B had three times greater tensile stiffness than the stiffness of geocells C and D.

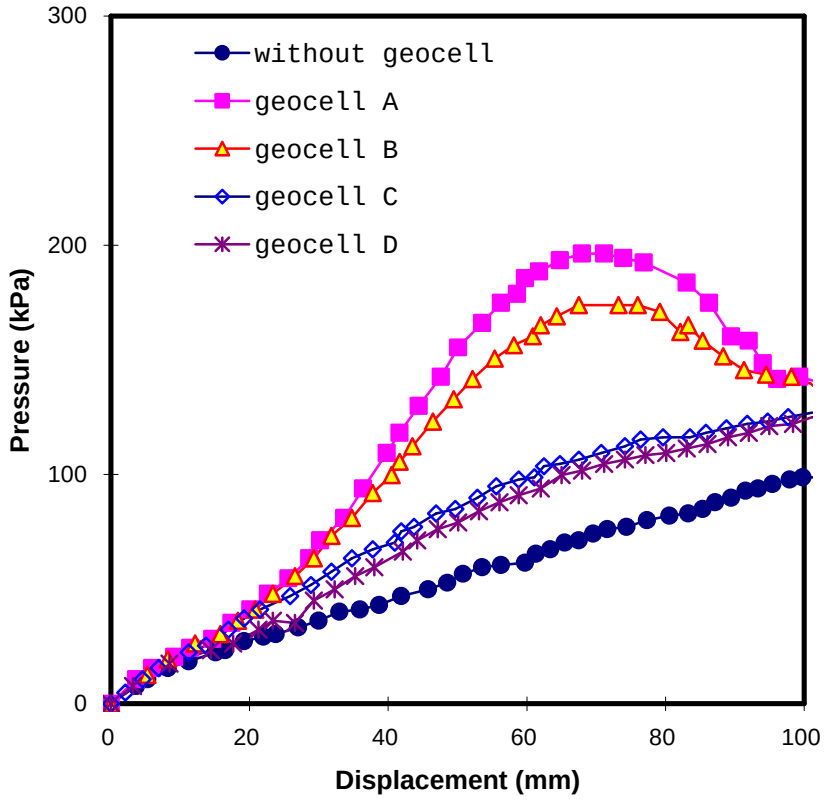

Figure 2.2.3 Load- settlement relations of geocell-reinforced soft ground (reproduced from Shimizu and Inui, 1990)

Mhaiskar (1992) investigated the effectiveness of geocell structure on soft clay for different geocell material, width and height, and relative density of the infill material. Dash et al. (2001a) conducted comprehensive laboratory-model tests to evaluate bearing capacity of a strip footing supported by a sand bed confined with geocell reinforcement. The static plate loading tests were performed in a steel tank of 1.2 m length by 0.332 m wide by 0.7 m deep filled with sand. These tests investigated the influence of factors on the bearing capacity of the reinforced section such as the pattern of geocell formation, the pocket size, the height and width of geocell mattress, the depth to the top of geocell mattress, the tensile stiffness of geocell material, and the relative density of the infill material. The test results showed the improvement in the ultimate bearing capacity of the geocell-reinforced section by up to 8 times that of the unreinforced section. This study found that the geocell mattress could improve the performance at its width equal to the footing width; however, to substantially reduce the surface heave the geocell mattress should not be placed at a depth more than half the width of the footing. This study recommended that to intercept all the potential rupture planes formed in the foundation soil the optimum ratio of the width of the geocell mattress to the footing width should be 4.0. The tests did not show any significant improvement in bearing capacity when the ratio of the height of geocell to width of footing was beyond 2.0. Better results were obtained when the geocell mattress was placed at a depth of 10% of the footing width. In addition to the tensile strength, this study identified that the aperture size and orientation of ribs of the geogrid used to construct the geocell affected the load carrying mechanism of the composite structure. Because of dilation-induced load transfer from soil to geocell, better performance with denser infill soil was also reported. **Figure 2.2.4** shows the improvement factors of geocell-reinforced soils at different relative density. The improvement factor is defined as the ratio of the footing pressure on the

geocell-reinforced soil at a given settlement to that on the unreinforced soil at the same settlement. Better performance was observed with higher infill density at a larger settlement.

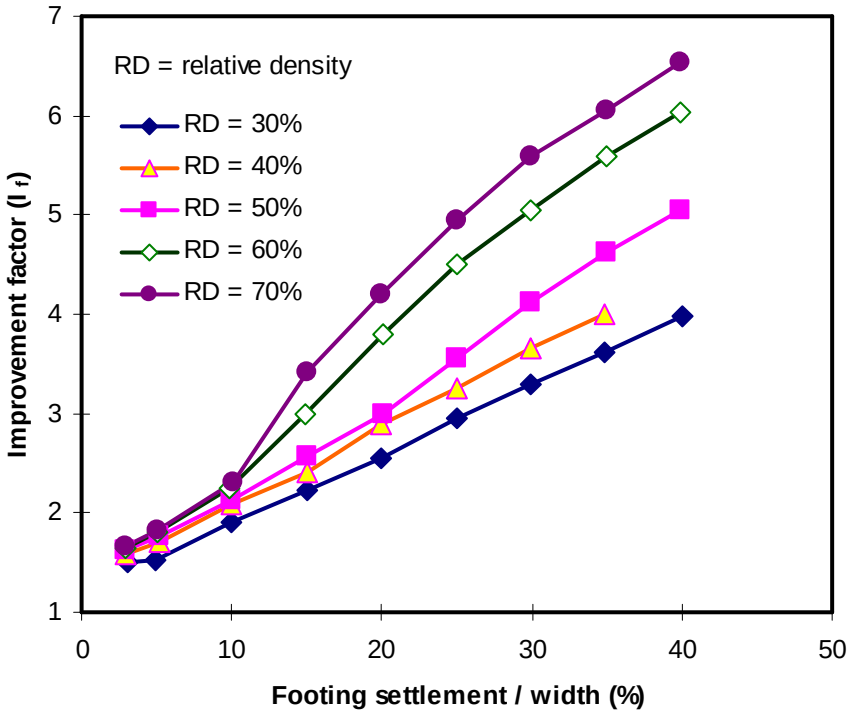

Figure 2.2.4 Effect of density of infill material (reproduced from Dash et al., 2001a)

Similar tests carried out by Dash et al. (2001b) with additional planar geosynthetic reinforcement found that a layer of planar reinforcement placed at the base of the geocell mattress enhanced the load carrying capacity and stability against a rotational failure, but the effect was negligible at a large height of geocell mattress. A cumulative beneficial effect of the planar reinforcement and the geocell mattress was found when the height of the geocell mattress was half of the width of the footing. There was no benefit observed when the planar reinforcement was placed on top of the geocell. Dash et al. (2003) conducted laboratory model tests using a circular footing on geocell-reinforced sand underlain by soft clay to study

the influence of the width and height of a geocell mattress and a planar geogrid layer at the base of the geocell. They reported substantial benefits from the geocell reinforcement in improving the bearing capacity and reducing surface heaving. Dash et al. (2004) carried out laboratory model tests to study the relative performance of different forms of geosynthetic reinforcement in sand. These model tests demonstrated that geocell was the most advantageous soil reinforcement technique compared to other planar and randomly distributed mesh elements. This study represented the performance with a non-dimensional improvement factor defined as the ratio of footing pressure to a given settlement between the reinforced and unreinforced soil. The comparison showed that the values of improvement factor for geocell, planar reinforcement, and randomly distributed reinforcement were 8.0, 4.0, and 1.8, respectively. Therefore, geocell reinforcement made the most improvement in the performance. This study also noted that the confinement by geocell created a better composite material, redistributed the footing load over a wider area, and reduced settlement.

Madhavi Latha et al. (2006) developed a theoretical model to calculate the cohesive strength (c_g) of a geocell-reinforced composite by assuming all round confinement to the soil provided by the membrane stresses in the wall of geocell. It was also assumed that the angle of internal friction of the geocell layer is same as that of the infilled soil. **Equation 2.2.1** was used to develop the theoretical solution in **Equation 2.2.2**.

$$\Delta\sigma_3 = \frac{2M}{D_0}\left[\frac{1-\sqrt{1-\varepsilon_a}}{1-\varepsilon_a}\right]$$

$$c_r = \frac{\Delta\sigma_3}{2}\sqrt{k_p}$$

Equation 2.2.2

where

c_r = additional cohesive strength of geocell

$\Delta\sigma_3$ = additional confining stress provided by geocell membrane

M = modulus of geocell material

D_o = initial diameter of geocell

ε_a = axial strain

k_p = coefficient of passive earth pressure

Chang et al. (2007) investigated the bearing capacity and dynamic elastic performance of geocell-reinforced sandy soil (classified as SP in USCS classification) under static and dynamic plate loading test. The static tests were conducted in a 150 cm long by 90 cm wide box with 60 cm deep sandy soil to understand the reinforcing mechanism of geocells and evaluate the bearing capacities under static loading. The performance of the geocell-reinforced sandy soil under dynamic loading was studied in a 45.7 cm long by 45.7 cm wide by 70 cm deep box. The plate used for static test had a diameter of 20 cm while for the dynamic test a 5.08 cm diameter plate was used. The reinforced section had a marked improvement in bearing capacity over the unreinforced section, and the increase in the bearing capacity was more for geocells with a higher height. The tests also showed that geocell-reinforced section had 50% less settlement compared with the unreinforced section. Chang et al. (2008) conducted similar tests in the same test boxes with the same geocells and sandy infill material but with different sizes of the loading plate. Two different geocell heights (7.5 cm and 15 cm) and two circular plate sizes (20 cm and 30 cm in diameter) were used in the static loading tests while a 10 cm diameter plate was used in the dynamic loading tests. The results showed that the bearing capacity of sandy soil was improved by 1.4 times and the settlement was also reduced. Under the repeated loading, 15 cm high geocell-reinforced sand exhibited the larger initial settlement than the 7.5 cm high geocell-reinforced

one. The dynamic modulus of subgrade reaction was found to increase after 100 cycles of loading for the 15 cm high geocell-reinforced section and it was higher than that for the 7.5 cm high geocell-reinforced section. The tests showed that the friction resistance between soil particles and geocells and the tensile strength of the geocell material at seams were the two factors affecting the performance of the reinforced section.

Laboratory and numerical studies have demonstrated that geocells can significantly increase bearing capacity and reduce settlements as shown in **Figure 2.2.5**. Based on the back-calculated results, Han et al. (2008a) showed a two fold increase in the elastic modulus of the geocell-reinforced base over the unreinforced one and cited the complexity of the problem and the lack of full-scale performance as two reasons hampering the establishment of a good design method for geocell-reinforced bases.

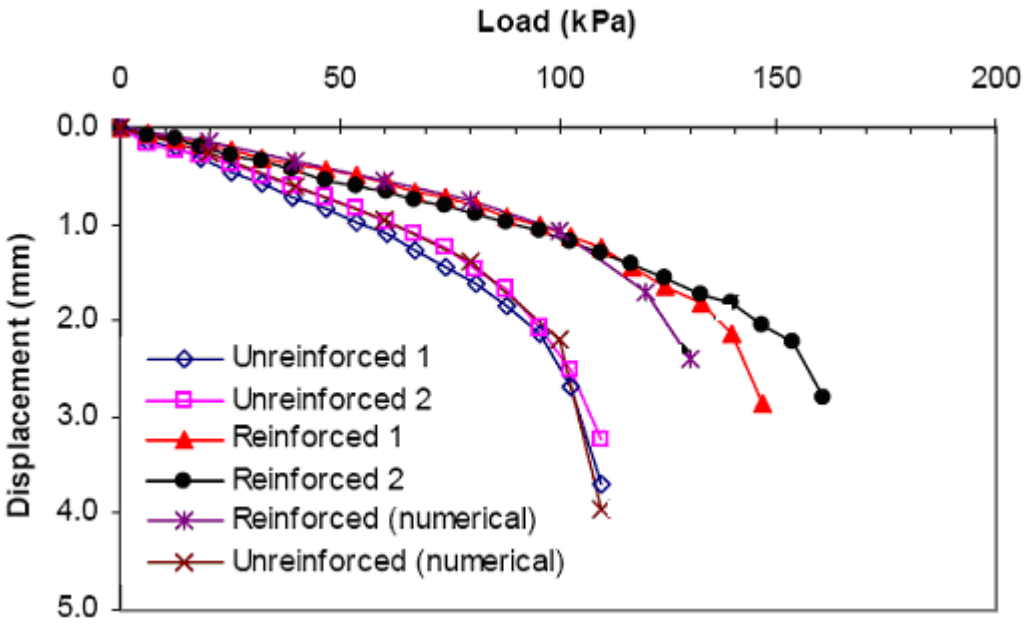

Figure 2.2.5 Load-displacement results from laboratory model test and numerical results (reproduced from Han et. al., 2008a)

2.2.3 Field tests

The earliest reported field testing of geocell-reinforced bases made up of plastic tube assembly and soil was on access roads over soft subgrade (Webster and Watkins, 1977). Webster and Alford (1978) conducted a follow-up field test with geocells made of aluminum and concluded that the geocell-reinforced layer system is suitable as a wet weather base course construction technique. Webster (1979a, b) conducted field tests on geocell-reinforced bases over beach sand and showed that square and hexagonal shaped geocells performed better than rectangular ones and their benefit decreased as the geocell unit width increased.

Cowland and Wong (1993) studied the performance of road embankments on soft clay supported by geocell-reinforced foundations. A 5 km stretch of road embankment on the soft clay deposits overlain by alluvium was supported by the geocell-reinforced foundation. Field monitoring of the performance of the geocell-reinforced foundation proved that the geocell-reinforced foundation was satisfactory for supporting the embankment constructed on the very soft clays, and the geocell-reinforced foundation performed as a plastic-reinforced rock fill raft.

Edil et al. (2002) carried out field tests with industrial by-products as the infill material in the geocell. The geocell acted as a reinforcing layer and the geotextile as a separator for the geocell infill and subgrade. All the monitored sections provided adequate support to the construction equipment and allowed the completion of the pavement structure. During 12-month monitoring, all the sections essentially achieved the performance requirements.

2.3 Reinforcement Mechanisms

Mitchell et al. (1979) identified several possible failure modes of sand-filled square-shaped paper grid cells including i) cell penetration into the soft subgrade below; ii) bursting of the cell when the infill material exert stresses exceeding the bursting strength; iii) buckling of the cell wall when there is insufficient lateral restraint for the cell wall and the cell walls are directly loaded; iv) bearing capacity failure by shear failure of the underlying soft subgrade; v) Bending failure, of the soil-geocell composite behaving like a slab, caused by excessive wheel load; vi) durability failure caused by prolonged exposure to the environment; and vii) excessive rutting caused by large number of load repetitions. As compared with the unreinforced base, the geocell-reinforced base can provide lateral and vertical confinement, tensioned membrane effect, and wider stress distribution. Lateral confinement, increased bearing capacity, and tensioned membrane effect were identified as the major reinforcement mechanisms (Giroud and Noiray, 1981) for geotextile reinforcement. Understanding of these mechanisms originated from static plate load tests, but later research have been focused on these mechanisms under cyclic loading. Giroud and Han (2004a and b) modified the Giroud and Noiray (1981) design method and devised a design method for geogrid-reinforced unpaved roads considering these mechanisms. The parameters used in the Giroud and Han (2004a and b) method include geometry of road structures, traffic axles and loads, rut depth, properties of base course and subgrade materials, and geogrid properties. The geocell-reinforced bases exhibit bending resistance, tensile strength, and shear strength, and intercept the failure planes from the subgrade (Zhou and Wen, 2008). **Figure 2.3.1** shows the details of the geocell reinforcement mechanism.

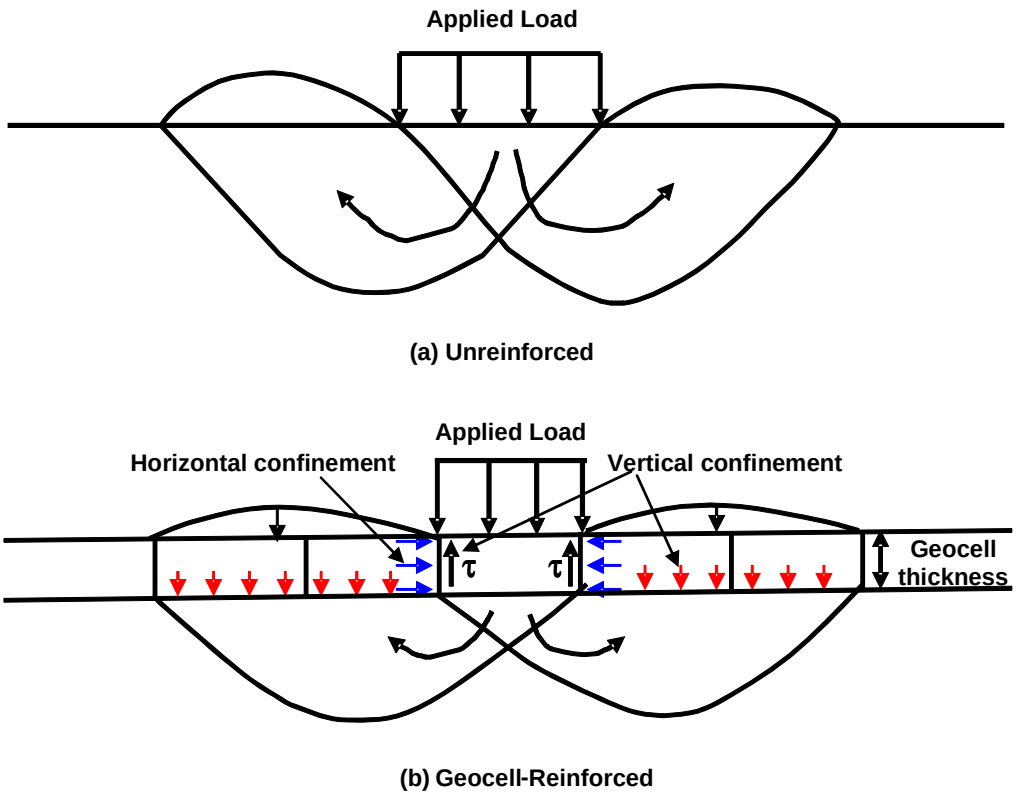

Figure 2.3.1 Unreinforced and geocell-reinforced soil behavior (reproduced from Pokharel et al., 2010)

2.3.1 Confinement effect

Due to the three-dimensional structure, the geocell can provide lateral confinement to soil particles within cells as shown in **Figure 2.3.1**. The geocell provides the vertical confinement in two ways: (1) the friction between the infill material and the geocell wall and (2) the geocell-reinforced base acts as a mattress to restrain the soil from moving upward outside the loading area. Gourves et al. (1996) carried out compression tests to explain the confinement effect and used finite element analysis to verify the results. Han et al. (2008a, b) investigated the load transfer mechanism between infill and geocell by carrying out both experimental and numerical study on the behavior of geocell-reinforced sand under a vertical

load. The studies showed that geocells could increase the bearing capacity and elastic modulus of the reinforced sand by providing confinement to the infill material. Mhaiskar (1992) identified the hoop stress in the geocell wall as the most significant contributing factor towards resisting loads and suggested a geocell with higher modulus and less extensibility be desired.

2.3.2 Tensioned membrane (beam) effect

The tensioned membrane or beam effect is referred to as the tension developed in the curved geocell-reinforced mattress to resist the vertical load (Rajagopal et. al., 1999; Dash et. al., 2004; and Zhou and Wen, 2008). However, to mobilize the tensioned membrane effect, the pavement structure must deform significantly (Giroud and Han, 2004a). As the geocell-reinforced section is stiffer than the surrounding soil, the curved surface exerts upward reaction and reduces the net stress applied to the subgrade. Douglas (1997) suggested that the concept of coefficient of subgrade reaction, originally intended for monotonic loading, can be successfully extended to linear, repeated-load behavior also.

2.3.3 Stress distribution

Mhaiskar (1992) indicated that a dense infill provides a higher load carrying capacity and geocell reinforcement distributes the load over a wider area. Wayne et al. (1998) also pointed out that the planar geosynthetic-reinforced bases can distribute the applied load to a wider area compared to the unreinforced base. A higher bearing capacity can be achieved with smaller thickness of geocell-reinforced bases (Bathurst and Jarrett, 1988). The inclusion

of the geocell and the confinement effect thereof would increase the stiffness of the reinforced base. The wider stress distribution contributed by geocell reinforcement reduces the stress at interface between the base and the subgrade and increases the bearing capacity of the foundation.

2.3.4 Increase in bearing capacity and stiffness of geocell-reinforced soil

Rea and Mitchell (1978) showed a very significant increase in the bearing capacity of the paper grid cell-reinforced dry sand under both static and repeated loads. They suggested the optimum values of the loaded area diameter to cell width as 1.5 and the cell depth to width ratio as 2.25. Based on the studies conducted by Webster (1979a and b), analytical formulae were proposed by Mitchell et al. (1979) to predict the capacity of the geocell-reinforced sand base against various failure modes. Mhaiskar and Mandal (1992a) conducted plate loading tests in a mild steel box (85 cm length by 75 cm width). The subgrade was 48cm thick marine clay and the base course was 10 cm thick sand. The test showed that geocell-reinforced sand had better performance than geotextile reinforcement to increase the bearing capacity. The bearing capacity ratio which is defined as the ratio of bearing capacity in the reinforced section to that in the unreinforced section was reported to be as high as 2.6. Under the similar test set up Mhaiskar and Mandal (1992b) suggested a geocell width to height ratio of 0.5 as a practical limit and Mhaiskar and Mandal (1994) showed that the horizontal sidewalls of geocells carried most of the stresses when the loads were applied on a geocell system and the bearing capacity was improved by 200%.

Mandal and Gupta (1994) conducted static plate loading tests in a rectangular tank (61 cm by 31 cm) on 40 cm thick marine clay overlain by a sand layer with and without geocell

to study load-settlement characteristics and evaluate the increase in bearing capacity. The results from the tests showed the significant improvement of bearing capacity only at large settlement and a smaller geocell opening size needed in order to get the maximum benefit from geocell reinforcement. Meyer (2007) carried out static and dynamic plate load tests on geocell-reinforced dry sand and gravel base material in a large-scale test box (2 m x 2 m x 2 m) to determine the bearing capacity of geocell-reinforced soil over soft subgrade. The tests showed that the bearing capacity of the reinforced section increased with the increase in cell height the layer thickness of the base course. The increase was observed in both the material and was in the order of 30 to 40 percent. With the increase of the cell height, the measured stresses on the top of the subgrade were reduced by about 30 percent. Zhou and Wen (2008) conducted model studies on reinforced sand cushion over soft soil and they found that the geocell-reinforced sand cushion provided substantial reduction in settlement of the underlying soft soil and improved of the bearing capacity.

Mengelt et al. (2006) found that in the resilient modulus tests, plastic deformation decreased significantly for both coarse and fine-grained soils when reinforced with geocells and the geocell-reinforced granular soils exhibited increased resistance to rutting.

2.4 Influence Factors

2.4.1 Effect of geocell dimension

Rea and Mitchell (1978) showed that the optimum values of the diameter to width ratio of the geocell equal to 1.5 and the cell height to width ratio equal to 2.25 to achieve a significant increase in bearing capacity of dry sand under both static and repeated loads. Mitchell et al. (1979) conducted plate load tests on geocell-reinforced sand laid on a hard

surface and found that both the bearing capacity and stiffness of the geocell-reinforced sand increased with the increase in the number of cell joints under a given area of the footing. Dash et al. (2001a) demonstrated that the improvement in the bearing capacity by geocell was not significant when the ratio of the geocell height to the footing width exceeded 2.0.

2.4.2 Effect of stiffness of geocell material

Bathurst and Jarrett (1988) reported that stiffer geocell provided better improvement to the reinforced soil, which was supported by the recent study conducted by Pokharel et al. (2010).

For a given geocell height and a geocell width to height ratio, the elastic modulus of the geocell played more important role than the seam strength in improving the performance of geocell-reinforced soil (Mhaiskar and Mandal, 1996).

2.4.3 Effect of infill material and cover thickness

Mitchell et al. (1979) found that an aggregate cover on top of the geocell-reinforced section did not contribute towards the increase of the bearing capacity; however, it provided the protection to the geocell.

As previously discussed in **Section 2.2.2**, better quality of infill material results in better performance of the geocell-reinforced section (Kazerani and Jamnejad, 1987). Mhaiskar and Mandal (1996) also found a denser infill advantageous. Similar observation by Dash et al (2001a) is shown in **Figure 2.2.4** and discussed in **Section 2.2.2**.

2.4.4 Effect of strength and stiffness of subgrade

Rea and Mitchell (1978) studied the effect of subgrade stiffness on the ultimate bearing capacity of the geocell-reinforced sand. They observed that higher subgrade stiffness resulted in greater ultimate bearing capacity of reinforced sand and the improvement was valid in case of resistance to repeated loads also. The curve in **Figure 2.4.1** shows an increase of 1 kPa/mm in the modulus of subgrade reaction resulted in 5% increase in the ultimate bearing capacity of the geocell-reinforced sand. This finding was supported by the study conducted by Shimizu and Inui (1990) as shown in **Figure 2.2.3** and discussed in **Chapter 2.2.2**.

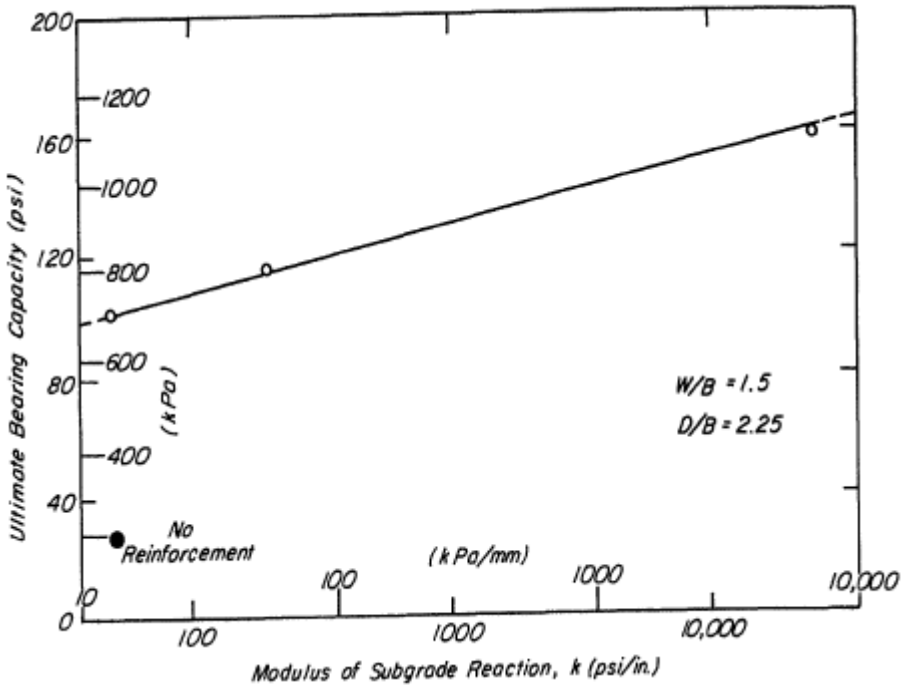

Figure 2.4.1 Effects of subgrade stiffness on the ultimate bearing capacity of grid-reinforced sand (reproduced from Rea and Mitchell, 1978)

2.5 Design Methods for Unpaved Roads

There are several design methods proposed by different researchers on planar geosynthetic reinforcement (specially the geotextile and geogrid) since the late 1970s. The design method discussed here is the recent one developed and verified by Giroud and Han (2004a and b) for geogrid-reinforced unpaved roads since this method will be modified for geocell-reinforced unpaved roads. The theoretical equation developed by Giroud and Han (2004a) for required base course thickness (h) is given in **Equation 2.5.1**.

$$h = \frac{1 + k \log N}{\tan \alpha_0 \left[1 + 0.204\left(R_E - 1\right)\right]} \times \left(\sqrt{\frac{P}{\pi r^2 \left(\frac{s}{f_s}\right)\left\{1 - \xi \exp\left[-\omega\left(\frac{r}{h}\right)^n\right]\right\} N_c c_u}} - 1 \right) r$$

Equation 2.5.1

where

r= radius of tire contact area (m)

N= number passes

P = wheel load (kN)

c_u = undrained cohesion of the subgrade soil (kPa)

N_c = bearing capacity factor

R_E = modulus ratio of base course to subgrade soil

α_0 = reference stress distribution angle (degrees)

k = constant depending on base course thickness and reinforcement

s = allowable rut depth (mm)

f_s = factor equal to 75 mm

ξ, ω, n are constants

Equation 2.5.1 can be simplified as;

$$h = \frac{1.26 + (0.96 - 1.46J^2)\left(\frac{r}{h}\right)\log N}{f_E} \times \left(\sqrt{\frac{P}{\pi r^2 m N_c c_u}} - 1\right) r \qquad \textbf{Equation 2.5.2}$$

where

J = aperture stability modulus of geogrid (N-m/^{0})

f_E = modulus ratio factor

m = bearing capacity mobilization factor

The other terms in **Equation 2.5.2** are explained below:

The slope of the line plotted as logN against 1/tanα is a function of aperture stability modulus of geogrid and expressed in Equation **2.5.3**.

$$\frac{1}{\tan\alpha} = \frac{1 + k\log N}{\tan\alpha_1} \qquad \textbf{Equation 2.5.3}$$

where α = stress distribution angle for the case where the number of passes is N; α_1 = stress distribution angle for the case where the number of passes is 1; and k is a constant depending on reinforcement and thickness of base course.

The wheel load P (kN) is half of the axle load in case of dual-wheel axles and equal to pA, in which A (m^2) is the tire contact area and p is the tire contact pressure (kPa). In the theoretical study, the tire contact area is replaced by a circular area.

Giroud and Han (2004a) used the value of N_c = 3.14 for a unreinforced base, N_c = 5.14 for a geotextile-reinforced base, and N_c = 5.71 for a geogrid-reinforced base.

Modulus ratio factor is

$$f_E = 1 + 0.204(R_E - 1) \qquad \textbf{Equation 2.5.4}$$

The limited modulus ratio of base course to subgrade is

$$R_E = \frac{E_{bc}}{E_{sg}} = \min\left(\frac{3.48 CBR_{bc}^{0.3}}{CBR_{sg}}, 5.0\right) \qquad \textbf{Equation 2.5.5}$$

where E_{bc} = resilient modulus of base course (MPa);

E_{sg} = resilient modulus of subgrade soil (MPa);

CBR_{bc} = California Bearing Ratio (CBR) of base course; and

CBR_{sg} = CBR of subgrade.

The bearing capacity mobilization coefficient is

$$m = 1 - \xi \exp\left[-\omega \left(\frac{r}{h} \right)^n \right]$$ **Equation 2.5.6**

where ξ, ω, and n are unknown parameters that should be determined by experimental data. When a serviceability criterion expressed by an allowable rut depth different from 75 mm is considered, the mobilization factor can be expressed as;

$$m = \left(\frac{s}{f_s} \right) \left\{ 1 - \xi \exp\left[-\omega \left(\frac{r}{h} \right)^n \right] \right\}$$ **Equation 2.5.7**

where s = allowable rut depth (mm) and f_s = factor equal to 75 mm.

This equation is suggested only for 50 mm < rut depth < 100 mm. The rut depth is defined as the maximum vertical deformation from the highest point on the wheel track to the adjacent lowest point. Although a 75 mm maximum allowable rut depth is widely used, AASHTO design guidelines (AASHTO, 1993) consider allowable rut depths from 13 to 75 mm.

The undrained shear strength of subgrade soil can be estimated by

$$c_u = f_c CBR_{sg}$$ **(Equation 2.5.8)**

where f_c= factor equal to 30 kPa (Giroud and Noiray, 1981).

2.6 General Observation from Past Studies

The literature review clearly shows a gap between the theory and practice; therefore, there is an urgent need for the development of a design method for geocell-reinforced bases in unpaved roads. The following findings have been obtained from the past studies:

i. Geocell-reinforced bases perform better than unreinforced bases and reduce maintenance requirements for unpaved roads.
ii. Geocells perform better than other planar geosynthetic reinforcements.
iii. Geocells provide confinement, tensioned membrane effect, and wider distribution of the applied stress, which result in increased bearing capacity and stiffness of the base course.
iv. Properties of geocell and infill material play important roles in improving the behavior of reinforced bases.
v. Factors such as aspect ratio of geocell, type and location of loading, and strength of subgrade also play important roles in the effectiveness of the geocell-reinforced bases.

CHAPTER THREE

MATERIALS USED IN THE EXPERIMENTAL STUDY

Three experimental studies were carried out in this research: (1) static and repeated plate loading tests were conducted on geocell-reinforced bases over a firm bottom in a medium-scale loading system at the KU geotechnical laboratory; (2) cyclic plate loading tests were conducted on geocell-reinforced bases over soft subgrades in a large geotechnical box equipped with a servo hydraulic MTS loading system available at KU; and (3) full-scale moving wheel tests were carried out in the Accelerated Pavement Testing (APT) facility at the KSU. This chapter discusses the characteristics of different materials used in these three experimental studies.

3.1 Geocell Type and Characteristics

Four types of geocell were used for the tests in the experimental studies. The properties of these geocells are given in **Table 3.1.1** and their stress-strain relationships are shown in **Figure 3.1.1**. Type I geocell was made of regular HDPE having tensile strength of 12.5 MPa. The other three types of geocell used in this research were NEOLOY^{TM} polymeric alloy which is a nano-composite alloy of polyester/polyamide nano-fibers, dispersed in polyethylene matrix. It has the same polymeric composition but different extrusion subroutines. The novel polymeric alloy (NPA) is characterized by flexibility at low temperatures similar to HDPE with elastic behavior similar to engineering thermoplastic. The novel polymeric alloy geocell products, referred as NPA geocells, have a lower thermal expansion coefficient and larger creep resistance, and higher tensile stiffness and strength than HDPE geocells. Type II NPA geocell (shown in **Figure 3.1.2**) had a tensile strength of

19.1 MPa and had two perforations of 100 mm^2 area each on each pallet. NPA geocells Type III and Type IV geocells had tensile strengths of 20.9 and 21.3 MPa, respectively. Except for Type II, all other types of geocell used in this research did not have any perforation. Field studies have shown that the measured strains in the field for geosynthetics are typically within 2%. The elastic moduli of the four types of geocell at 2% strain are provided in **Table 3.1.1**. The creep resistance properties of HDPE and NPA geocell material (Type II) are given in **Table 3.1.2** and other properties NPA material are given in **Table 3.1.3**. The stress-strain curves were measured at a strain rate of 10%/minute at 23^o Celsius. The modulus of Type IV was 1.4 times that of Type I. The heights of the geocells used in this research were 75 mm, 100 mm, and 150 mm. They were used for reinforcing both single and double layered sections depending on the thickness of the base curse. All geocells had wall thickness of 1.1 mm except Type I that was 1.5 mm thick.

Table 3.1.1 Properties of geocells

Type	Material	Wall thickness (mm)	Height (mm)	Tensile strength (MPa)	Elastic modulus at 2% strain (MPa)
I	HDPE	1.5	100	12.5	310
II	NPA	1.1	100	19.1	355
III	NPA	1.1	100	20.9	350
IV	NPA	1.1	100	21.3	440

Table 3.1.2 Creep resistance properties of the HDPE and the NPA materials (from PRS Mediterranean, Inc., Israel)

Stress to create 10% strain at 23°C for (Years)	HDPE (N/mm)	NPA (N/mm)
25	3.41	5.82
50	3.33	5.65
75	3.27	5.56

Table 3.1.3 Other properties of the NPA material (from PRS Mediterranean, Inc., Israel)

Properties		Description	Unit	Test method
Tensile strength		>20	N/mm	PRS method
Allowed strength for design of 50 yrs		>5.7	N/mm	ASTM D6992
Creep reduction factor		<3.5		ASTM D6992
Coefficient of thermal expansion		≤80	ppm/°C	ISO 11359-2
(CTE)				ASTM E831
Flexural Storage Modulus at	30°C	>750	MPa	ISO 6721-1
	45°C	>650		ASTM E2254
	60°C	>550		
	80°C	>300		
Oxidative Induction Time (OIT)		≥100	minutes	ISO 11375-6, ASTM D3895
				(OIT @ 200°C, 35kPa)
Durability to UV Degradation		>400	minutes	ASTM D5885
				(HPOIT @ 150°C, 3500kPa)

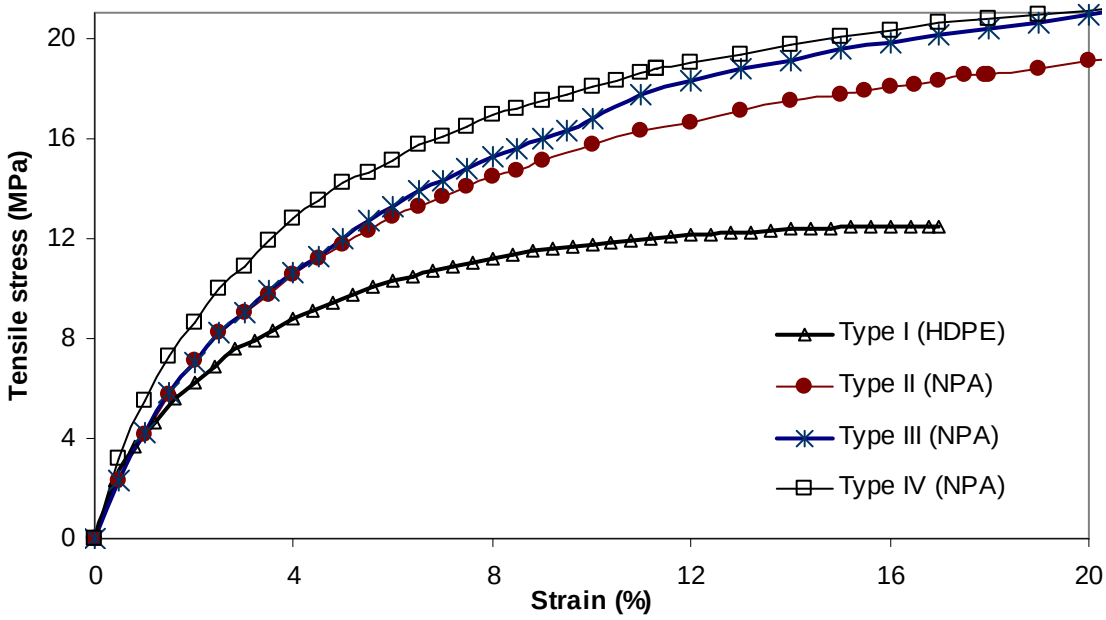

Figure 3.1.1 Tensile stress-strain curves of geocells

Figure 3.1.2 Picture of Type II NPA geocell in the medium-size box

3.2 Geotextile Material

A 3.5 oz (99.65 g) non-woven geotextile was used between subgrade and base course as a separator in case of all the geocell-reinforced sections over weak subgrade in the large geotechnical box at KU and the APT at KSU. The picture of the geotextile used in these tests is shown in **Figure 3.2.1**.

Figure 3.2.1 Picture of the geotextile used in the experiments

3.3 Subgrade Materials and Characteristics

In case of the medium-size plate loading test the base of the hard wooden box was served as the subgrade; however, weak subgrade was prepared for large-scale plate loading tests and moving wheel tests. A mixture of 25% Kaolin and 75% Kansas River sand (hereinafter referred to as KR-I sand) was prepared as the subgrade for the large-scale plate

loading test while a locally available clay in Kansas, was used as the subgrade in the moving wheel tests.

3.3.1 Subgrade mixture of kaolin and Kansas River (KR-I) sand used in large box tests

The subgrade used for the large-scale plate loading test was a weak soil artificially made by mixing kaolin and KR-I sand with water. The properties of KR-I sand will be discussed in details in **Chapter 3.4.1**. Initially a subgrade of 15% kaolin and 85% KR-I sand was prepared. California Bearing ratio (CBR) tests were conducted following ASTM D 1883 to estimate the strength of the subgrade in Loadtrac II instrument as shown in **Figure 3.3.1**. The CBR versus moisture content curve for this mixture was very steep (i.e., CBR was sensitive to moisture content) at about 2% CBR value; therefore, it was difficult to maintain the required CBR of about 2% for the box tests. Later a different mix ratio of 25% kaolin and 75% KR-I sand by weight was tested and chosen for the subgrade. The grain-size distribution of KR-I sand is presented in **Figure 3.3.2**. Standard Proctor compaction tests (ASTM D698 – 00a) were performed to obtain the compaction curve for this subgrade as shown in **Figure 3.3.3**. The maximum dry density of the mix was 2.01 Mg/m^3, which corresponds to the optimum moisture content of 10.8%. A series of laboratory unsoaked CBR tests were performed for the subgrade at different water contents. The CBR vs. moisture content curve is presented in **Figure 3.3.4**. The subgrade soil was compacted at a water content of 11.4% for the large-scale plate loading tests to achieve a CBR of approximately 2%, which was verified by vane shear and DCP tests during the subgrade preparation. Unconfined compression tests and vane shear tests were also carried out and a correlation between the CBR value and the undrained shear strength (c_u) was established (c_u in kPa = 20.5 CBR in %). The calculation for this correlation is shown in **Table 3.3.1**.

Table 3.3.1 Unconfined compression tests on subgrade of large box test

Description	Measured Values
Height of the specimen	14.4 cm
Diameter of the specimen	7.2 cm
Moisture content (average of 3 samples)	11.06 %
Unconfined compression strength (q_u)	
Sample 1	74.3 kPa
Sample 2	81.6 kPa
Sample 3	114.7 kPa
Average q_u value	90.2 kPa
Average undrained shear strength (c_u) = q_u /2	45.1 kPa
CBR value at 11.06% water content on the specimen obtained from vane shear test	2.2 %
Therefore, the unconfined compressive strength	$c_u \text{ in kPa} = \frac{45.1}{2.2} = 20.5 \times CBR \text{ in \%}$

Figure 3.3.1 CBR test in Loadtrac II

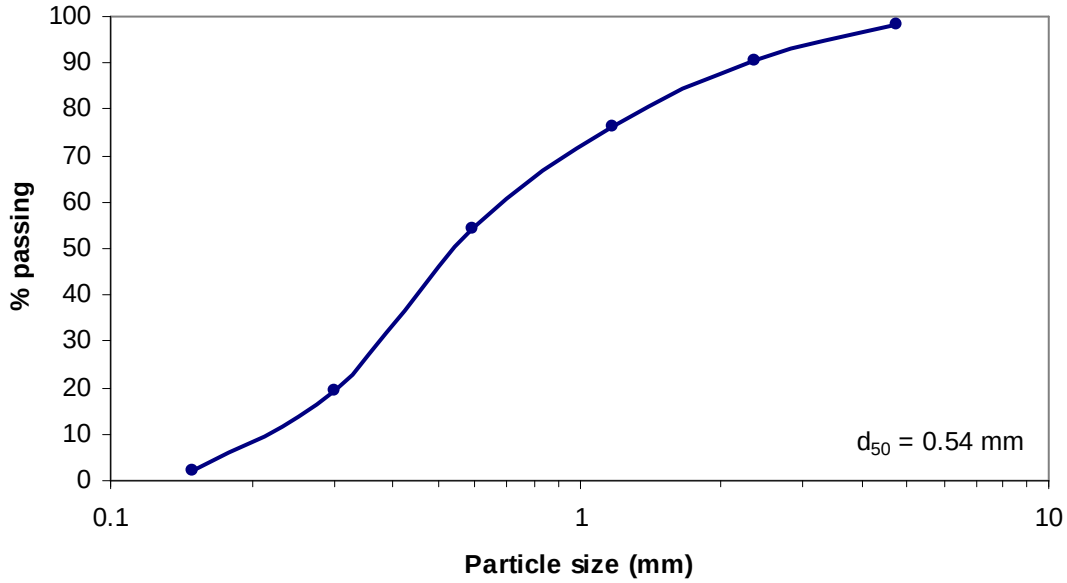

Figure 3.3.2 Grain size distribution curve of KR-I sand

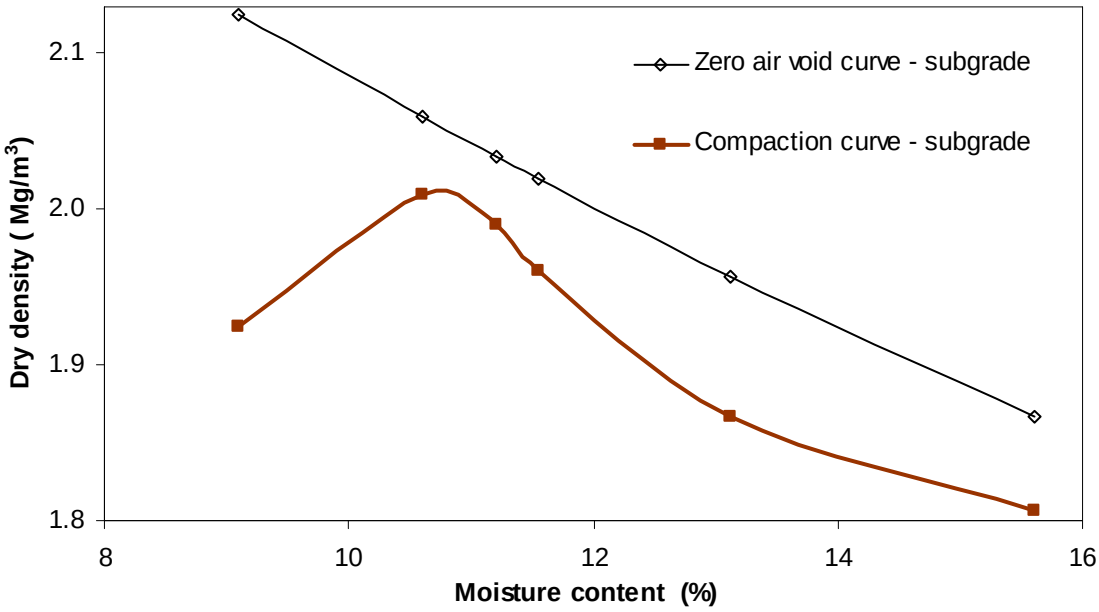

Figure 3.3.3 Standard Proctor compaction curve of the subgrade used for large-scale plate loading tests

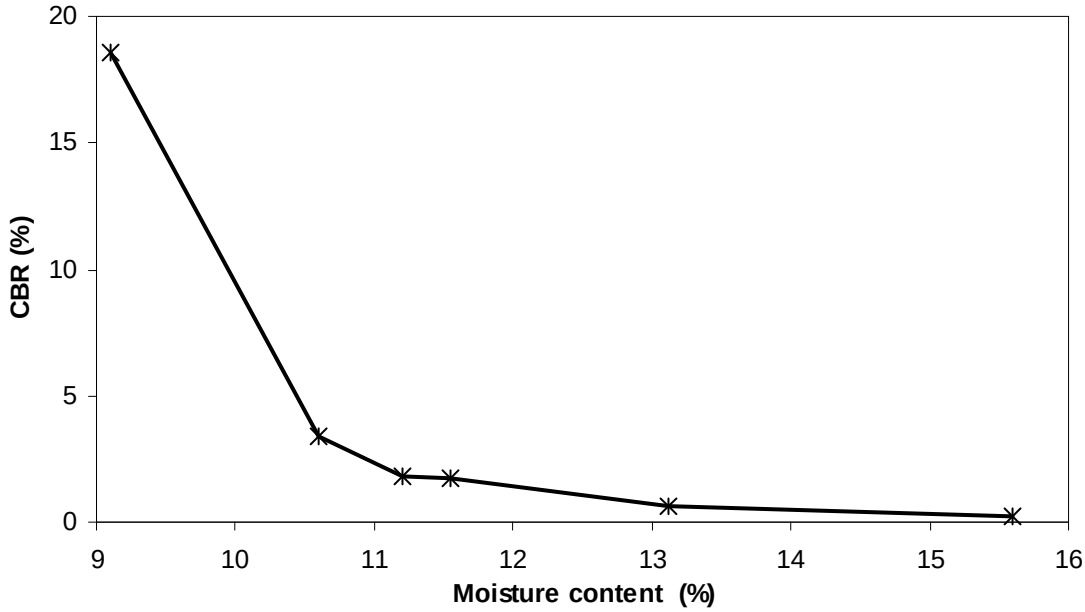

Figure 3.3.4 CBR vs. moisture content curve of the subgrade used for large-scale plate loading tests

3.3.2 Subgrade used in the moving wheel tests

A type of clay, locally known as Keats pit in the Manhattan area of Kansas, was used as the subgrade in the moving wheel tests. This clay is classified as A-7-6 based on the AASHTO Soil Classification System. Standard Proctor compaction and CBR tests on this soil were carried out in the laboratory. The optimum moisture content and the maximum dry density were 21% and 1.61 Mg/m^3, respectively. The standard Proctor compaction curve and the CBR values at different moisture contents are shown in **Figures 3.3.5** and **3.3.6**, respectively. A CBR of 3% was achieved at approximately 26% moisture content in the laboratory; however, it was achieved at approximately 21% in the test pit.

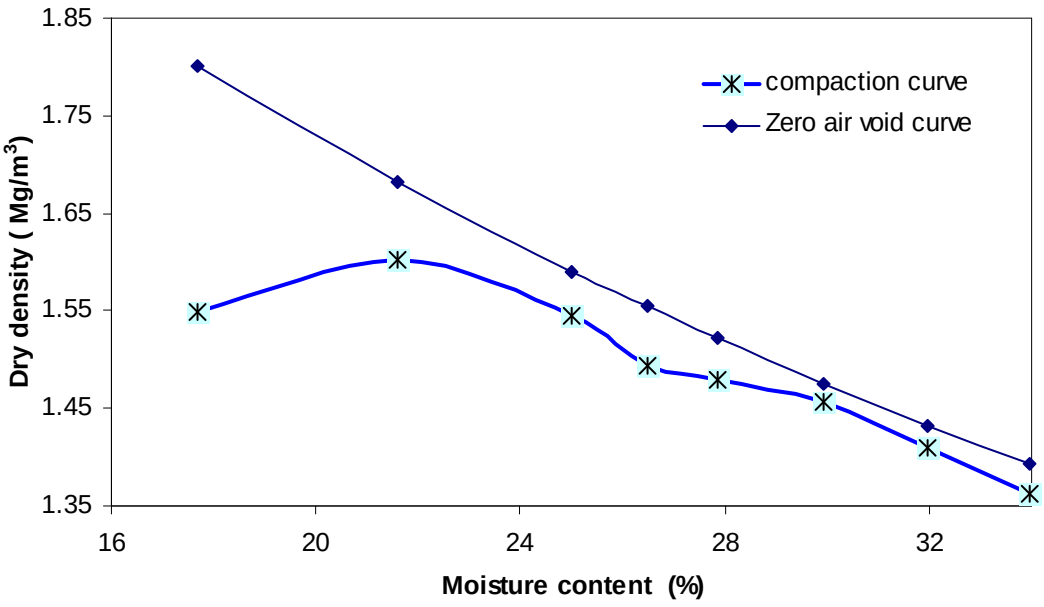

Figure 3.3.5 Standard Proctor compaction curve of the subgrade (A-7-6)

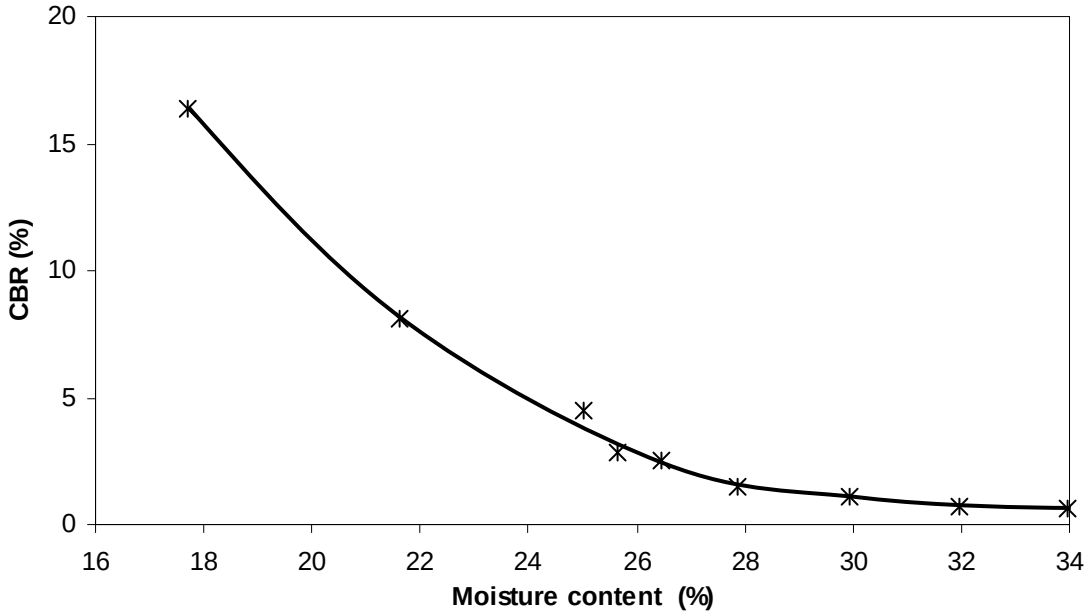

Figure 3.3.6 Moisture content-CBR curve of the subgrade (A-7-6)

This subgrade had Young's modulus of 10.3 MPa and unconfined compressive strength of 104.6 kPa at 22.7% moisture content. The details of these tests can be found in Yang (2010). Unconfined compression tests and vane shear tests were carried out and a correlation between the CBR value and the undrained shear strength (c_u) was established (c_u in kPa = 19.7 CBR in %). The calculation for this correlation is shown in **Table 3.3.2**.

Table 3.3.2 Unconfined compression tests on subgrade of moving wheel test

Description	Measured Values
Height of the specimen	15.7 cm
Diameter of the specimen	7.12 cm
Moisture content (average of 2 samples)	22.0 %
Unconfined compression strength (q_u)	
Sample 1	109.72 kPa
Sample 2	104.56 kPa
Average q_u value	107.14 kPa
Average undrained shear strength (c_u) = q_u /2	53.57 kPa
CBR value at 22% obtained from vane shear test at the test pit	2.72 %
Therefore, the unconfined compressive strength	$c_u \text{ in kPa} = \frac{53.57}{2.72} = 19.7 \times CBR \text{ in \%}$

3.4 Base Course Materials and Characteristics

Three different materials, Kansas River sand also known as pea gravel (hereinafter referred to as KR-II sand), quarry waste (hereinafter referred to as QW-I), and AB-3 aggregate base material (hereinafter referred to as AB-3-I) were used as base courses in medium-size plate loading tests. In large-scale plate loading tests, KR-I sand and AB-3-I were used as the base course materials. In the moving wheel tests, AB-3 aggregate (hereinafter referred to as AB-3-II), quarry waste (hereinafter referred to as QW-II), KR-I sand, and two types of Recycled Asphalt Pavement from the same source (hereinafter referred to as RAP-I and RAP-II) were used as base courses. Kansas River sand is locally

available sand from Kansas River in Kansas. Quarry waste (QW) is the waste material produced during aggregate production in quarries. The QW and AB-3 used in the tests were brought from local limestone quarry sites in Kansas.

Sieve analyses for grain size distribution were done for Kansas River sands, QW, and AB-3. Relative density tests were carried out for Kansas River sands. Standard Proctor compaction tests and CBR tests were carried on QW, AB-3, and RAP materials. The plastic and liquid limit tests (ASTM D4318 – 10) were carried out for QW-I and AB-3-I. Specific gravity tests (ASTM D854 – 06) were done for KR-I sand, QW-I, and AB-3-I.

3.4.1 Kansas River (KR-I) sand

Kansas River (KR-I) sand used in this study was a poorly-graded sub-rounded river sand having a mean particle size (d_{50}) = 0.54 mm, coefficient of curvature = 0.95, coefficient of uniformity = 3.1, and specific gravity = 2.62. The grain size distribution curve of KR-I sand was shown in **Figure 3.3.2**. **Figure 3.4.1** shows the standard compaction curve for KR-I sand. The optimum moisture content of 6.3% and the maximum dry density of 1.77 Mg/m^3 were obtained from the standard Proctor tests.

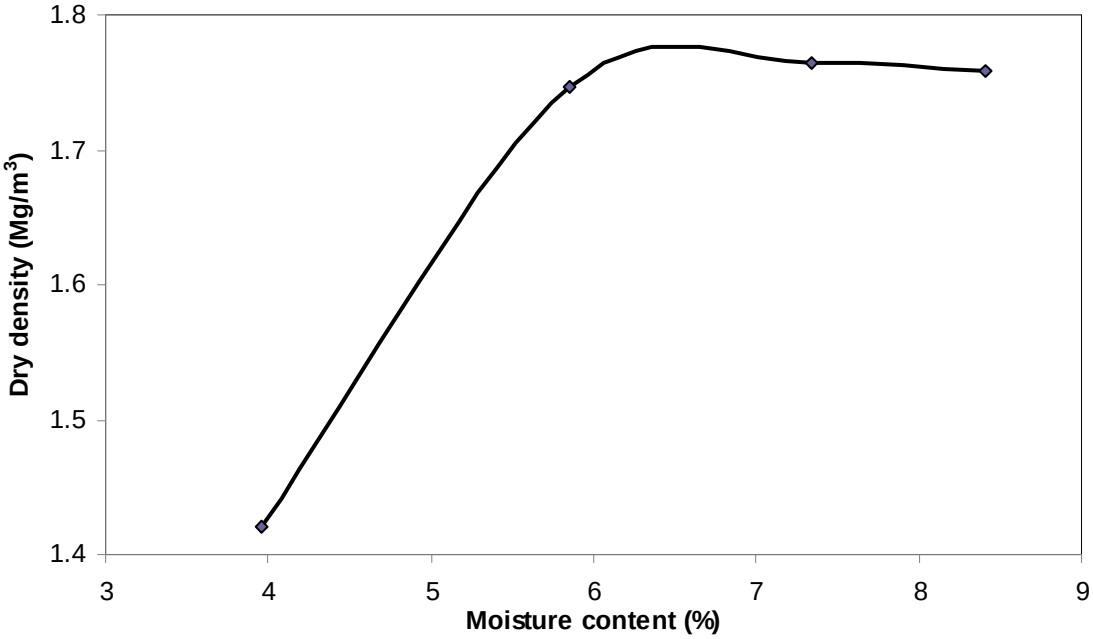

Figure 3.4.1 Standard Proctor compaction curve of KR-I sand

3.4.2 Kansas River (KR-II) sand

KR-II sand used in this study was a poorly-graded sub-rounded river sand having a mean particle size (d_{50}) = 2.6 mm, minimum void ratio = 0.354, maximum void ratio = 0.583, specific gravity = 2.65 at 20^{o}C, coefficient of curvature = 0.98, and coefficient of uniformity = 2.73. The grain-size distribution curve of KR-II sand is shown in **Figure 3.4.2**. The peak angle of internal friction of the sand at 70% relative density was 37.3^{o}, which was obtained from three consolidated drained (CD) triaxial tests. The details of these triaxial tests on the KR-II sand can be found in the paper by Bhandari and Han (2009).

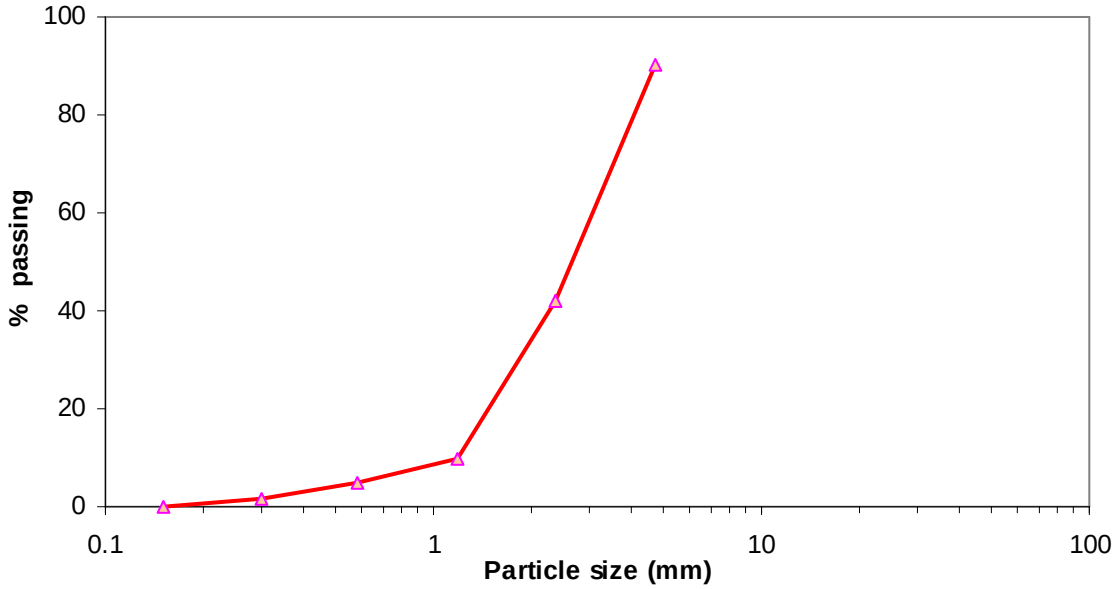

Figure 3.4.2 Grain-size distribution curve of KR-II sand

3.4.3 Quarry waste (QW-I)

QW-I material used for the large-scale plate loading tests was obtained from Hamm Quarry Inc. located in North Lawrence, Kansas. It had a mean particle size (d_{50}) = 1.2 mm, liquid limit = 20, plastic limit = 12, specific gravity = 2.76 at 20^{o}C, coefficient of curvature = 0.77, and coefficient of uniformity = 12. The grain-size distribution of QW-I is shown in **Figure 3.4.3**. Standard Proctor tests were conducted on the QW-I to obtain the optimum moisture content of 9% and the maximum dry density of 2.1 Mg/m^3, respectively. The results of standard Proctor compaction tests and the CBR tests for the QW-I are shown in **Figures 3.4.4 and 3.4.5**, respectively. California Bearing Ratio (CBR) tests showed that the QW-I had the CBR value of 57% at 7% moisture content and 38% at the optimum moisture content, respectively.

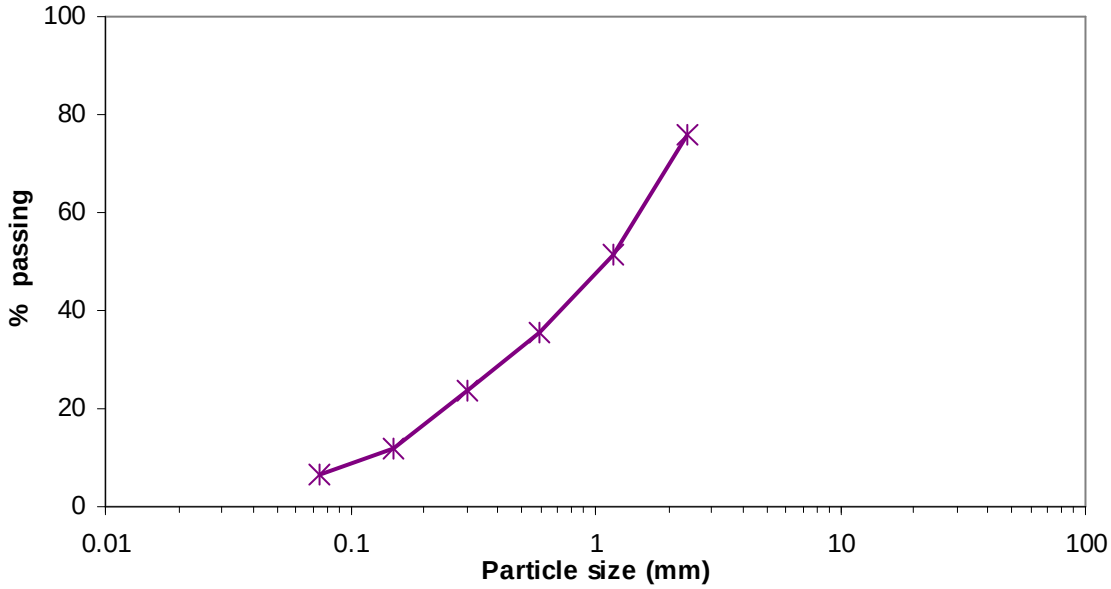

Figure 3.4.3 Grain-size distribution curve of QW-I

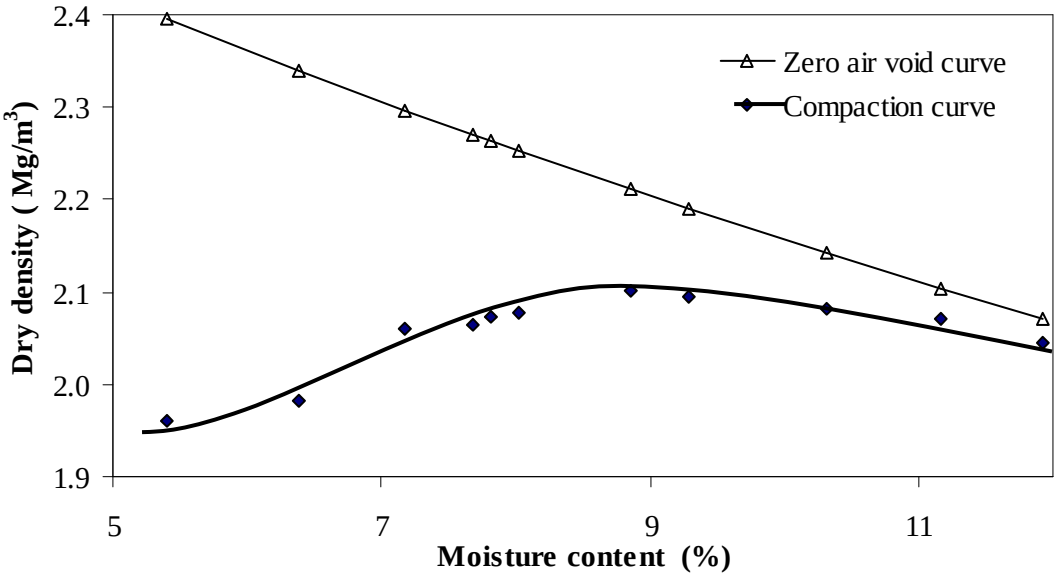

Figure 3.4.4 Standard Proctor compaction curve of QW-I

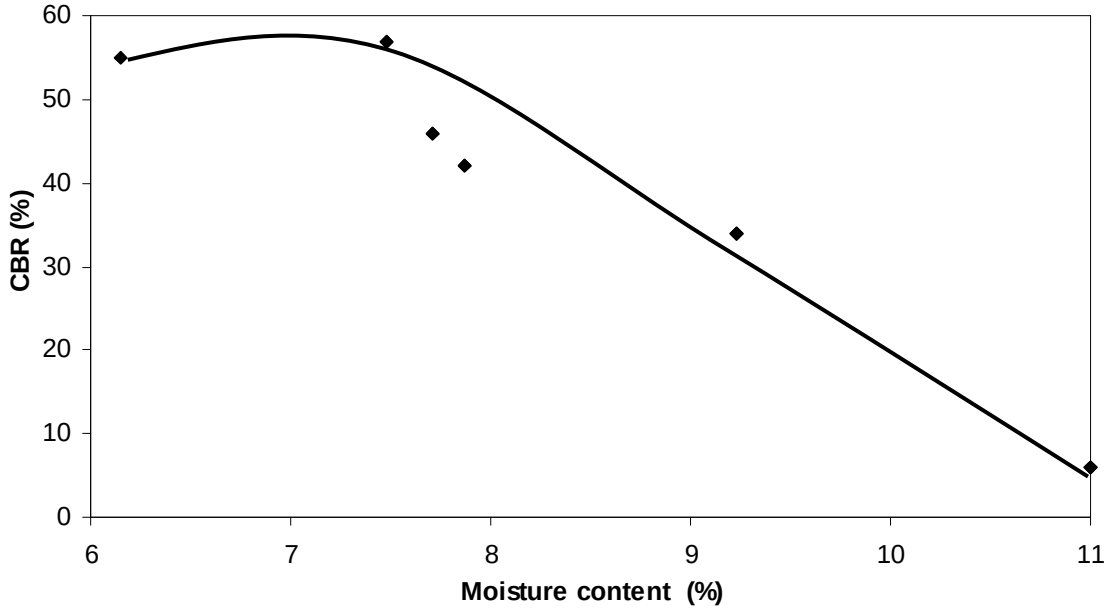

Figure 3.4.5 CBR curve of QW-I

3.4.4 Quarry waste (QW-II)

The QW-II used in the study was brought from a local quarry site near Manhattan in Kansas. QW-II had a mean particle size (d_{50}) = 1.3 mm, a coefficient of curvature = 2.3, a coefficient of uniformity = 24, an optimum moisture content = 11%, and a maximum dry density = 2.06 Mg/m^3. The grain-size distribution of QW-II is shown in **Figure 3.4.6**. **Figures 3.4.7 and 3.4.8** show the standard Proctor compaction and CBR curves for QW-II, respectively. The CBR values of QW-II were 48% at 8.8% moisture content and 19% at the optimum moisture content, respectively.

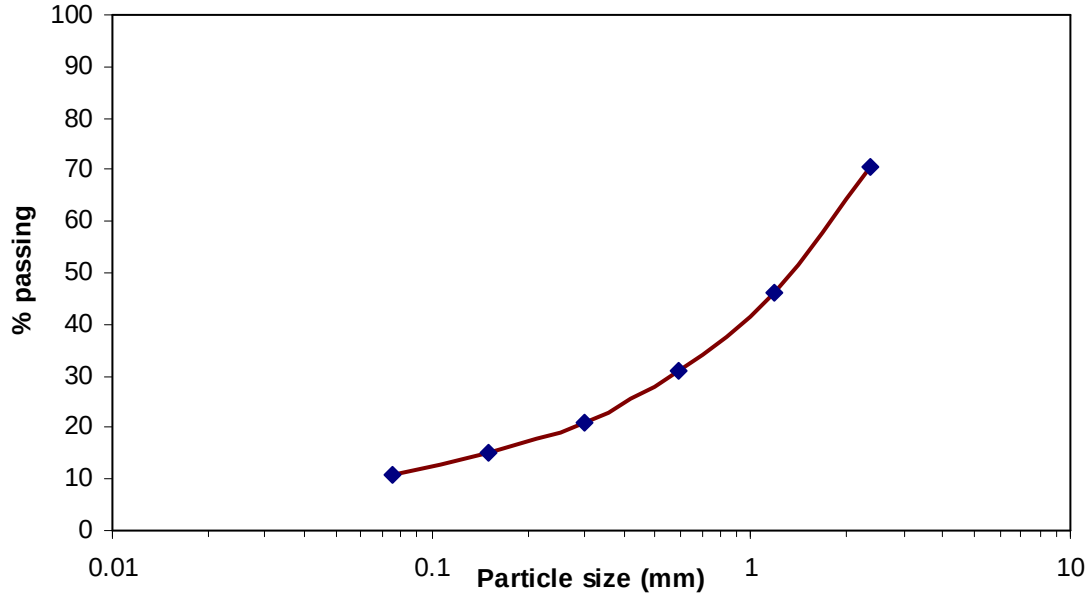

Figure 3.4.6 Grain-size distribution curve of QW-II

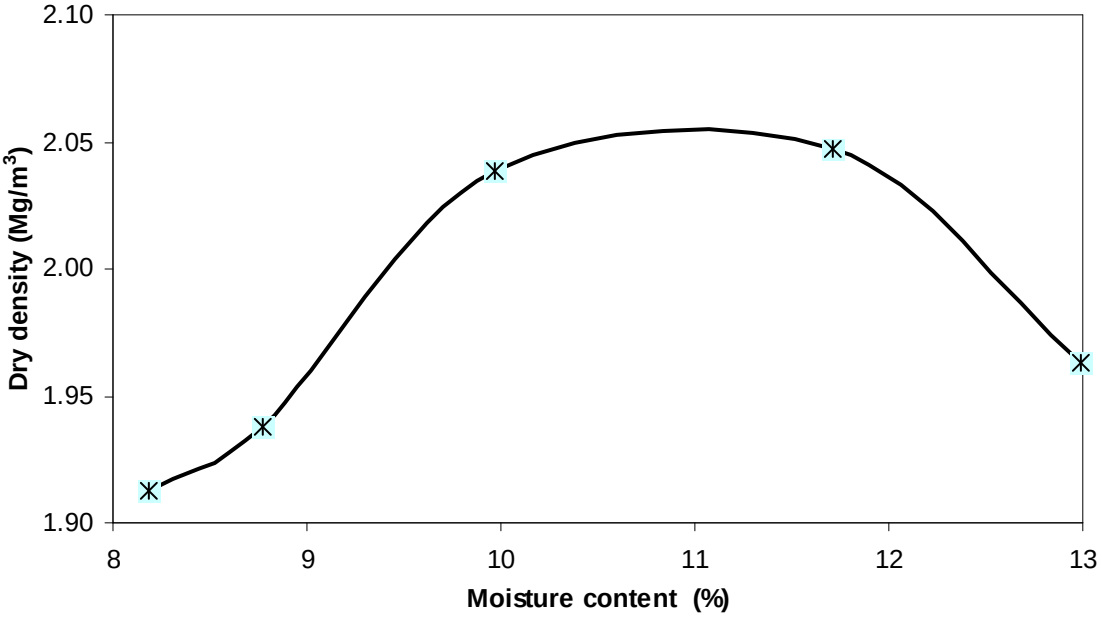

Figure 3.4.7 Standard Proctor compaction curve of QW-II

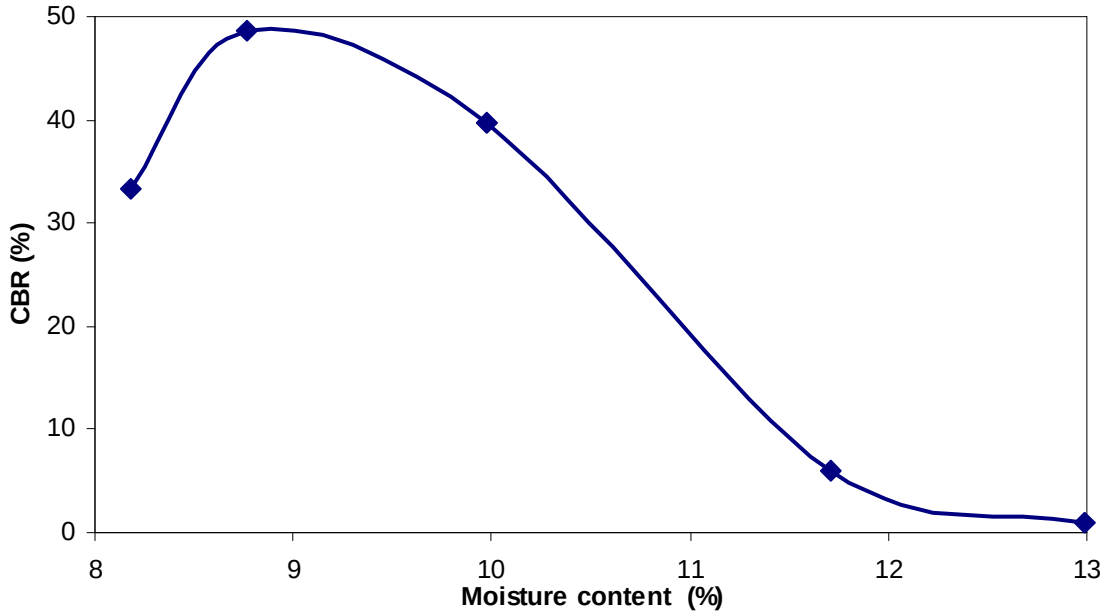

Figure 3.4.8 CBR curve of QW-II

3.4.5 AB-3-I aggregate

AB-3-I aggregate used for the tests was a well-graded base course material widely used in pavement applications in Kansas. This AB-3 material was obtained from Hamm Quarry Inc. located in North Lawrence, Kansas. The grain-size distribution of AB-3-I is shown in **Figure 3.4.9**. It had a mean particle size (d_{50}) = 7.0 mm, liquid limit = 20, plastic limit = 13, specific gravity = 2.69 at 20^{o}C, optimum moisture content = 10%, and maximum dry density = 2.08 Mg/m^{3}. The results of the standard Proctor compaction tests and the CBR tests for the AB-3-I are shown in **Figures 3.4.10** and **3.4.11**, respectively. The CBR values were 75% at 7.1% moisture content and 46% at the optimum moisture content, respectively.

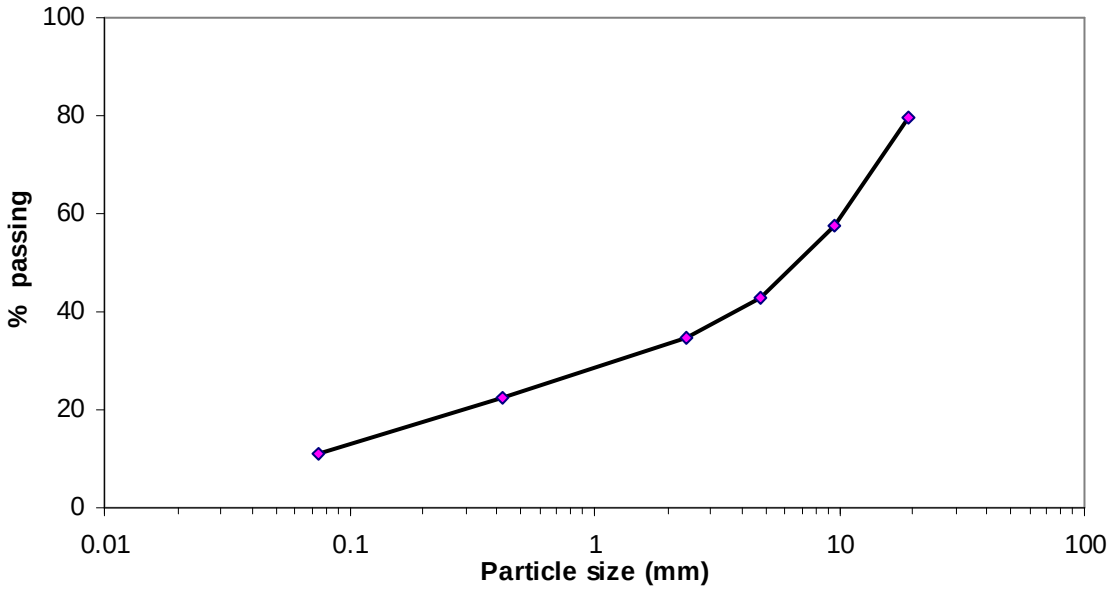

Figure 3.4.9 Grain-size distribution curve of AB-3-I aggregate

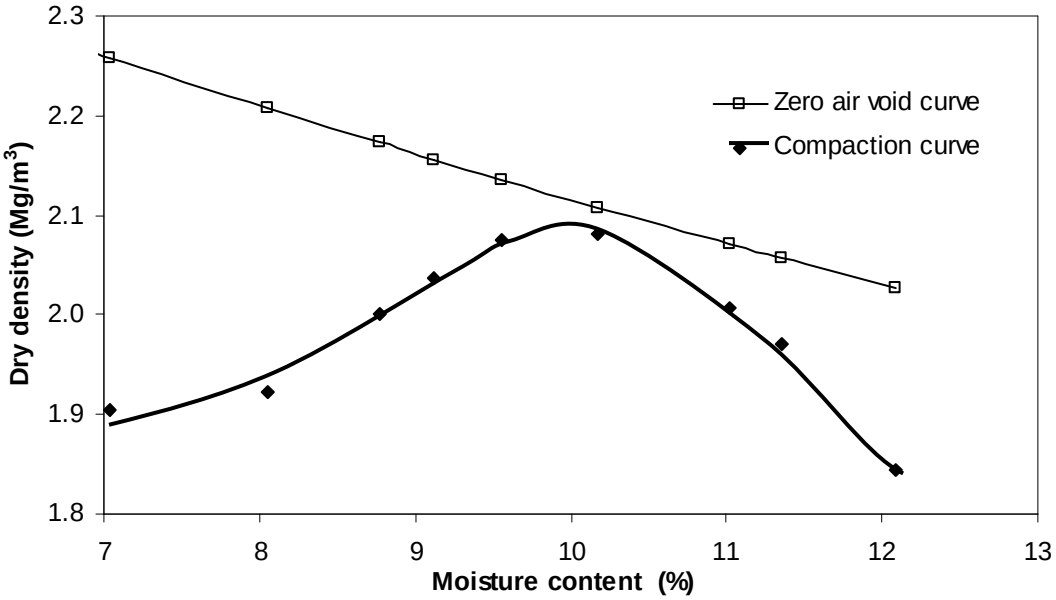

Figure 3.4.10 Standard Proctor compaction curve of AB-3-I aggregate

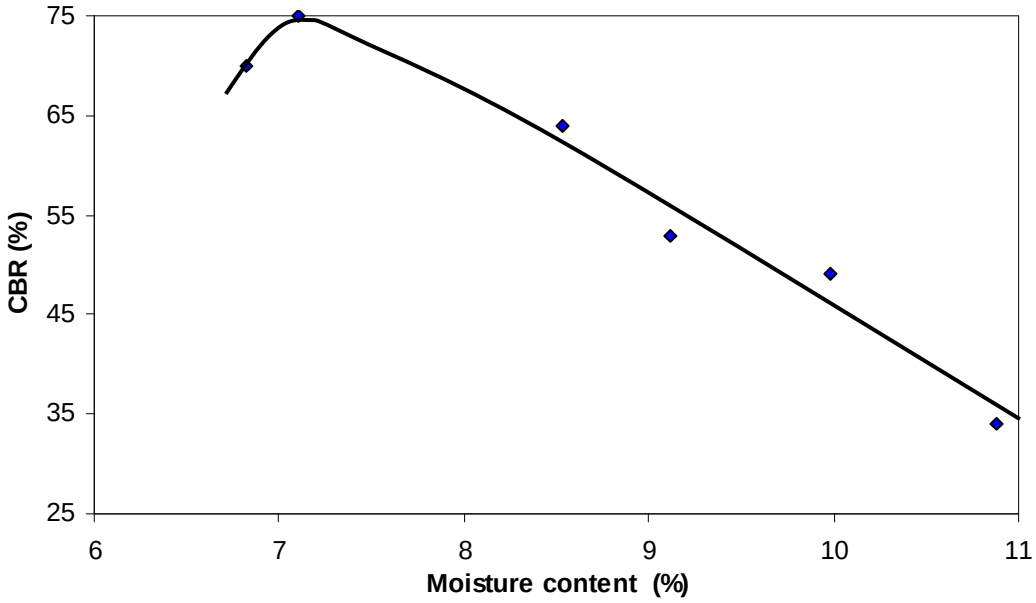

Figure 3.4.11 CBR curve of AB-3-I aggregate

3.4.6 AB-3-II aggregate

AB-3-II aggregate used in the moving wheel tests was a well-graded base course material, which is commonly used in pavement applications in Kansas. The major difference of this material from AB-3-I was the source quarry site that is located near Manhattan, Kansas. The grain-size distribution of AB-3-II is shown in **Figure 3.4.12**. It had a mean particle size (d_{50}) = 4.4 mm, a coefficient of curvature = 1.55, and a coefficient of uniformity = 21. **Figures 3.4.13** and **3.4.14** show the standard Proctor compaction and CBR curves for AB-3-II. Standard Proctor tests indicated that AB-3-II had the optimum moisture content of 10.2% and the maximum dry density of 2.13 Mg/m^3, respectively. AB-3-II had CBR values of 56% at 9.6% moisture content and 45% at the optimum moisture content, respectively. Direct shear tests showed that this aggregate had the friction angle = 52.4^0 and cohesion = 9.7 kPa at the peak strength and friction angle = 47.2^0 and cohesion = 4.7 kPa at the residual strength, respectively. The details of these direct shear tests can be found in Yang (2010).

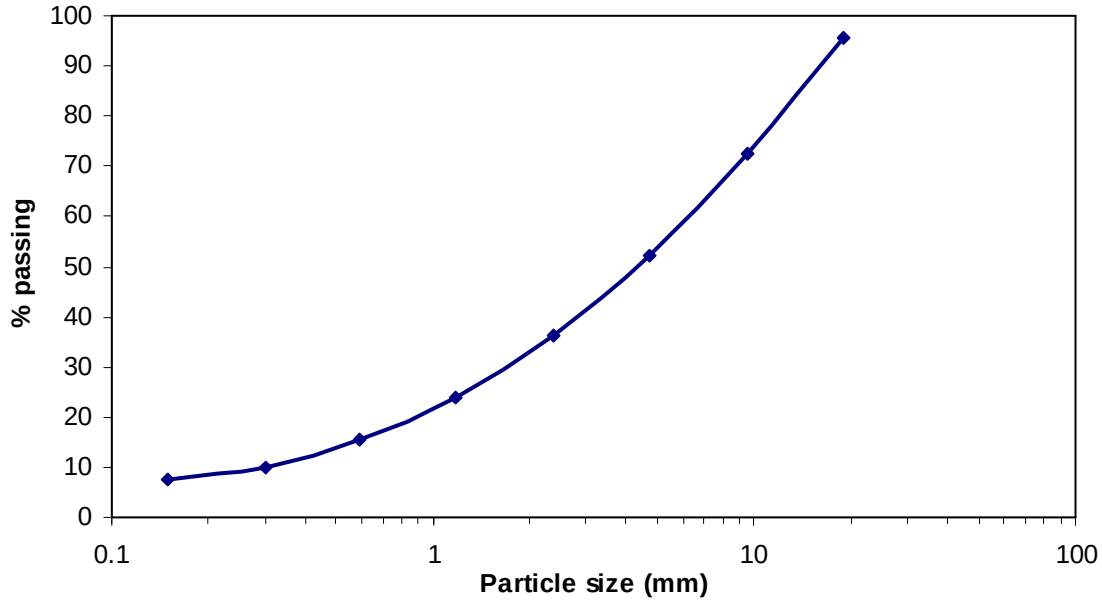

Figure 3.4.12 Grain-size distribution of AB-3-II aggregate

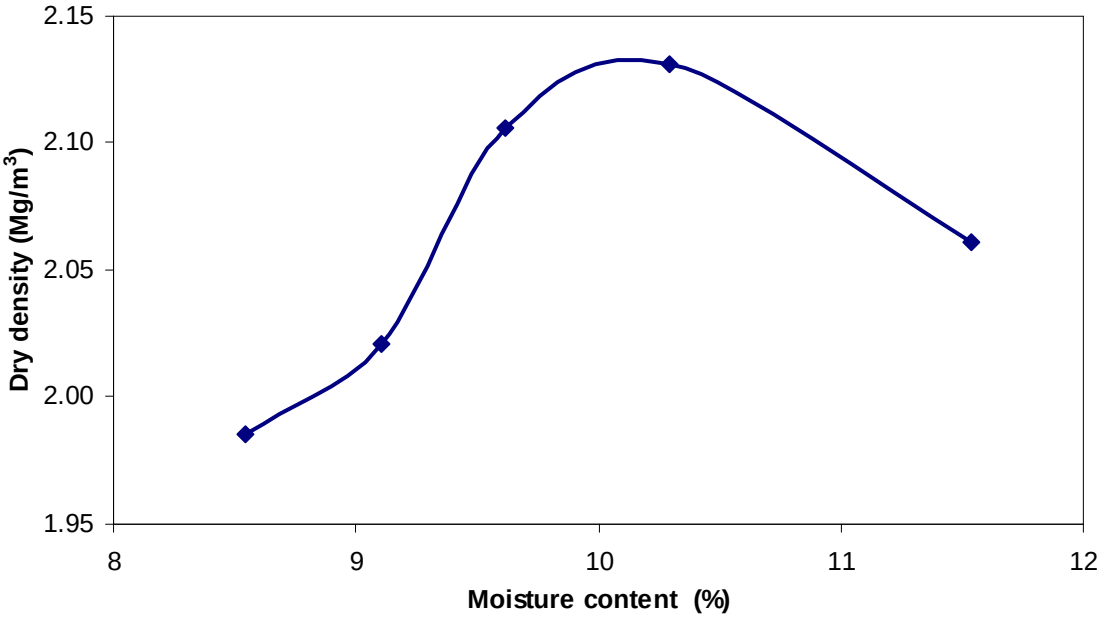

Figure 3.4.13 Standard Proctor compaction curve of AB-3-II aggregate

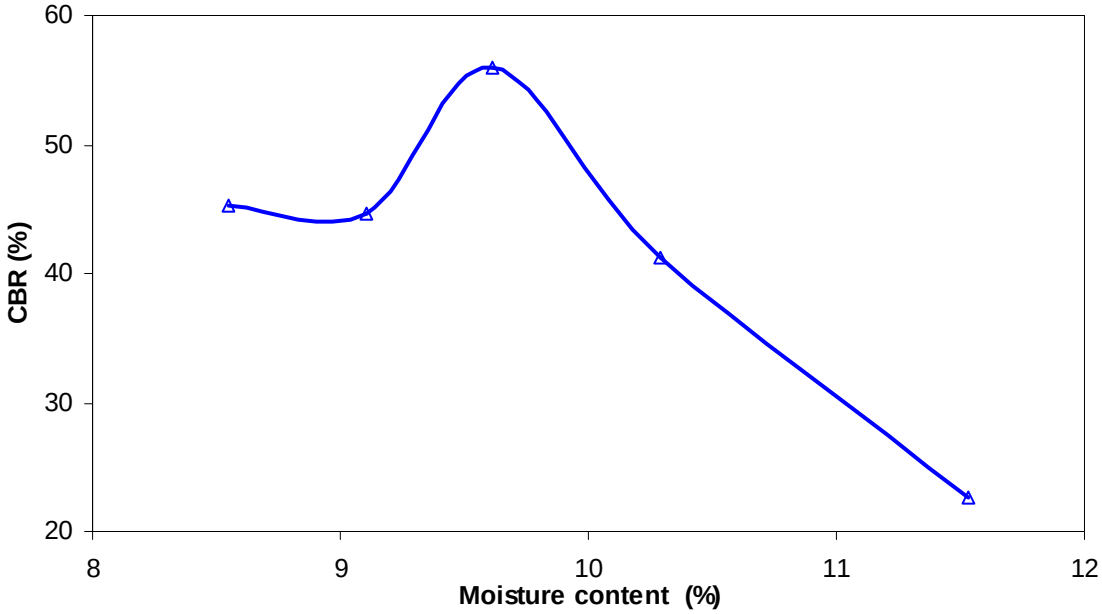

Figure 3.4.14 CBR curve of AB-3-II aggregate

3.4.7 Recycled asphalt pavement (RAP)

Two types of RAP, named in the dissertation as RAP-I and RAP-II, from the same asphalt plant were used in the moving wheel tests. Both the RAP materials were brought from a local asphalt contractor in Manhattan, Kansas. RAP-II was a fractioned RAP, i.e., fractionated, crushed, and sieved through a smaller sieve from RAP-I. Therefore, RAP-II had a finer gradation. All the RAP was sieved through a screen of 5 cm opening size before being placed as the base course. The ignition method determined the binder contents in RAP-I and RAP-II at 6.52% and 6.39%, respectively. The standard Proctor compaction and CBR curves for RAP-I are shown in **Figures 3.4.15** and **3.4.16** and those for RAP-II in **Figures 3.4.17** and **3.4.18**, respectively. Test results showed that RAP-I had an optimum moisture content of 6%, a maximum dry density of 1.81 Mg/m^3, and a CBR value of 10% at 5% moisture content and 8% at the optimum moisture content. RAP-II had an optimum moisture

content of 7.6%, a maximum dry density of 1.99 Mg/m^3, and a CBR value of 10.5% at 7.5% moisture content and 10.3% at the optimum moisture content.

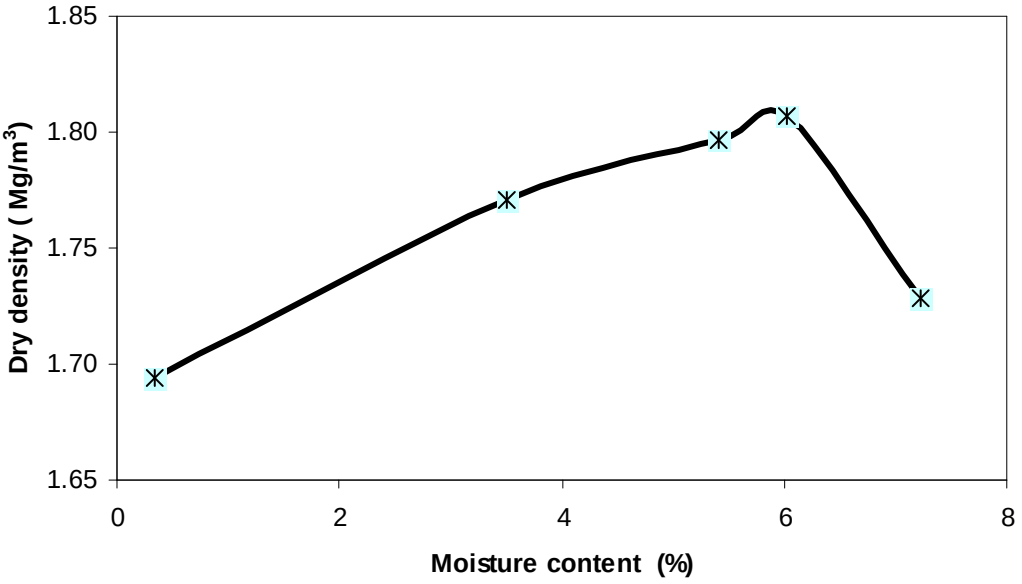

Figure 3.4.15 Standard Proctor compaction curve of RAP-I

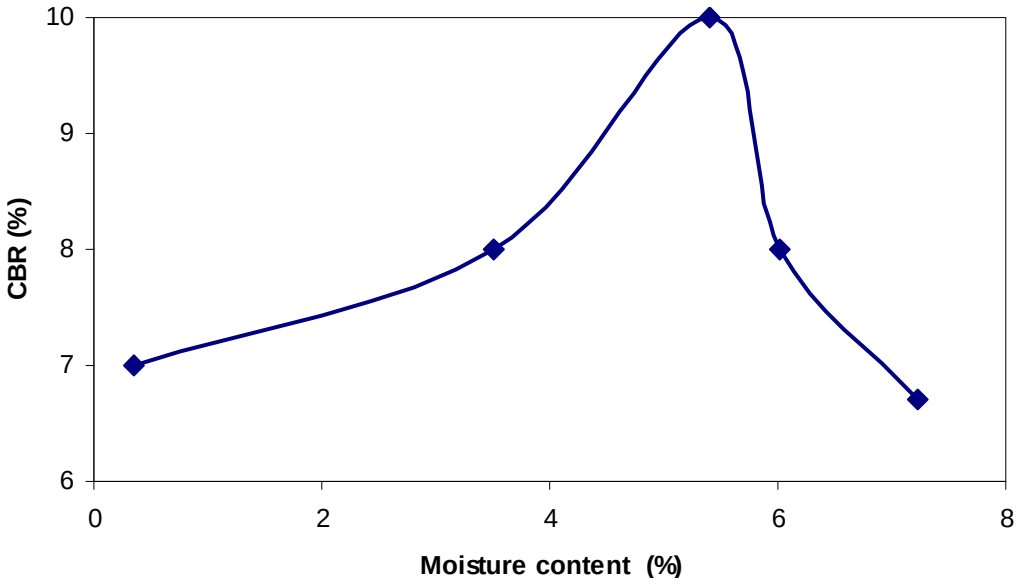

Figure 3.4.16 CBR curve of RAP-I

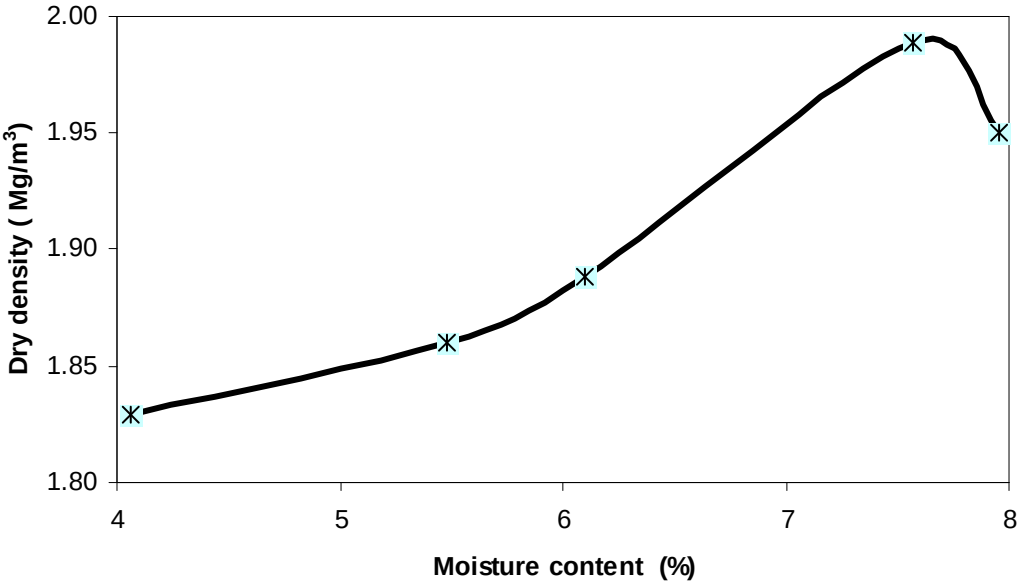

Figure 3.4.17 Standard Proctor compaction curve of RAP-II

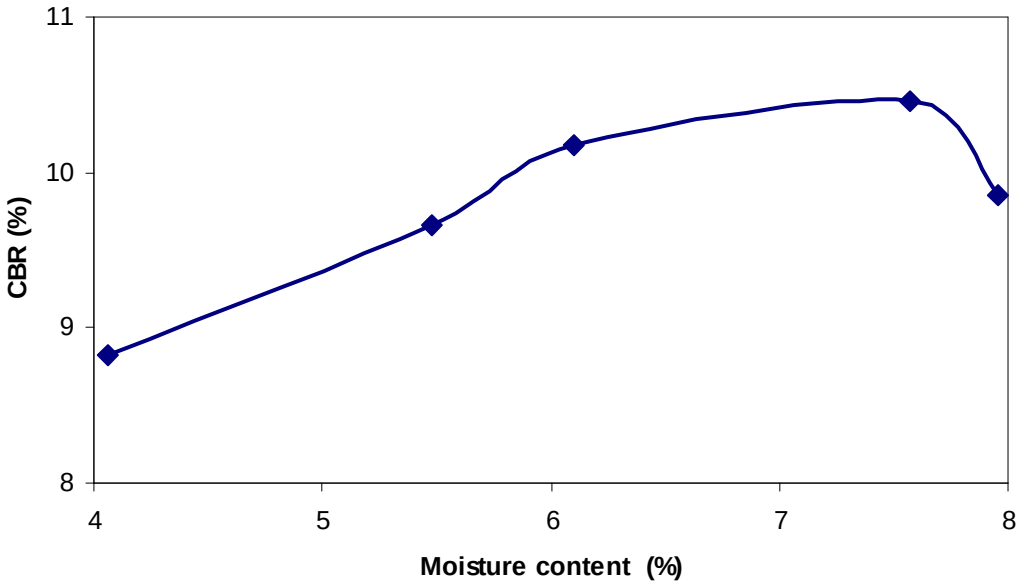

Figure 3.4.18 CBR of RAP-II

CHAPTER FOUR

MEDIUM-SCALE PLATE LOADING TESTS

Plate loading tests in a medium-size loading apparatus were conducted to investigate the effects of geocell confinement and other influence factors on the behavior of granular bases before large-scale plate loading tests and full-scale moving wheel tests. A series of static and repeated loading tests on both unreinforced and geocell-reinforced bases courses with different infill material and different arrangements of geocells were conducted with this loading apparatus. HDPE geocells were used only in the static load tests. Novel polymeric alloy (NPA) geocells were used in all the tests including single and multi geocell-reinforced sections. This chapter describes the details of these tests and discusses their results.

4.1 Static Plate Loading Tests

This study experimentally investigated the factors influencing the behavior (stiffness and bearing capacity) of single geocell-reinforced bases including the shape, type, embedment, height of geocells, and quality of infill materials. Three of four types of geocells investigated in this study were NPA geocells. Two boxes with different sizes were used: Box A (60.5 cm x 60.5 cm x 12 cm high) and Box B (80 cm x 80 cm x 12 cm high). The first few tests were carried out in Box A and later Box B was used. Potential scale effects on test results were checked. Stiffness and ultimate bearing capacity of geocell-reinforced base courses with different type geocells, their arrangement, and infill materials were examined. The stiffness is defined as the slope of the initial portion of the load-displacement curve while the ultimate bearing capacity is the last load before the failure of the base. The influence of geocell reinforcement with different thickness of the base course and height of geocell was

also evaluated. Some of the influence factors discussed herein have not been well investigated in the past, such as the shape of the geocell, the embedment of the geocell, and the difference between the single and multiple geocells. In addition, the geocells used in this study were made of novel polymeric alloy (NPA) using a new manufacturing technology, which has not been evaluated before.

4.1.1 Test equipment and setup

This medium-size loading apparatus was designed and fabricated at the geotechnical laboratory at the KU Department of Civil, Environmental, and Architectural Engineering. The loading system had a 150 mm diameter air cylinder with a maximum air pressure of 900 kPa. The steel loading plate was 150 mm in diameter and 10 mm thick. **Figures 4.1.1, 4.1.2, 4.1.3, and 4.1.4** show the details of the test boxes (Boxes A and B). Box A was square, had a plan area of 366,000 mm^2, and was used for single geocell tests under static loading. For multi-cell tests and all the repeated loading tests (discussed in the later sections), a bigger square box (Box B) with a plan area of 640,000 mm^2 was used. Boxes A and B were also used to investigate a possible boundary effect. Geocell was placed at the center of the box and its shape and size depended on the designed layout of a circular or elliptical shape. All the geocells in this study were 100 mm high, except for double layer reinforcement where 75 mm high NPA geocells were used. For single geocell tests, unconfined and confined tests were conducted. For an unconfined test, the geocell was filled with granular material inside the cell only without surrounding soil outside the geocell. The infill material was placed and compacted to the desired density inside the cell in two layers, each being 50 mm thick. For a confined test, the geocell was filled and embedded in the granular material. For a 120 mm thick base, the infill material was placed into the box including the geocell and compacted to

the desired density in three layers, 50 mm each for the first two layers and 20 mm for the top cover. For a 170 mm thick base (i.e., two layers of 75 mm high geocells plus 20 mm cover), compaction was carried out in three 50 mm lifts and one 20 mm top cover. The KR-II sand was compacted to 70% relative density and the QW-I was compacted to 95% maximum density on the drier side (approximately 7% moisture) of the compaction curve. The bottom wooden plate of the test box was served as a firm subgrade for the tests because the primary purpose of this study was to evaluate the behavior of geocell-reinforced bases. A loading plate of 152 mm diameter was placed at the center of the geocell for the reinforced case or at the center of the box for the unreinforced case. Loads were applied in increments by adjusting air pressure in the air cylinder. After each load increment was applied, settlements of the plate were monitored by digital dial gauges until they became stable. Settlements were mostly complete within 5 minutes of loading for each load increment. The test was terminated when the base could not continue to hold the load (i.e., failure occurred).

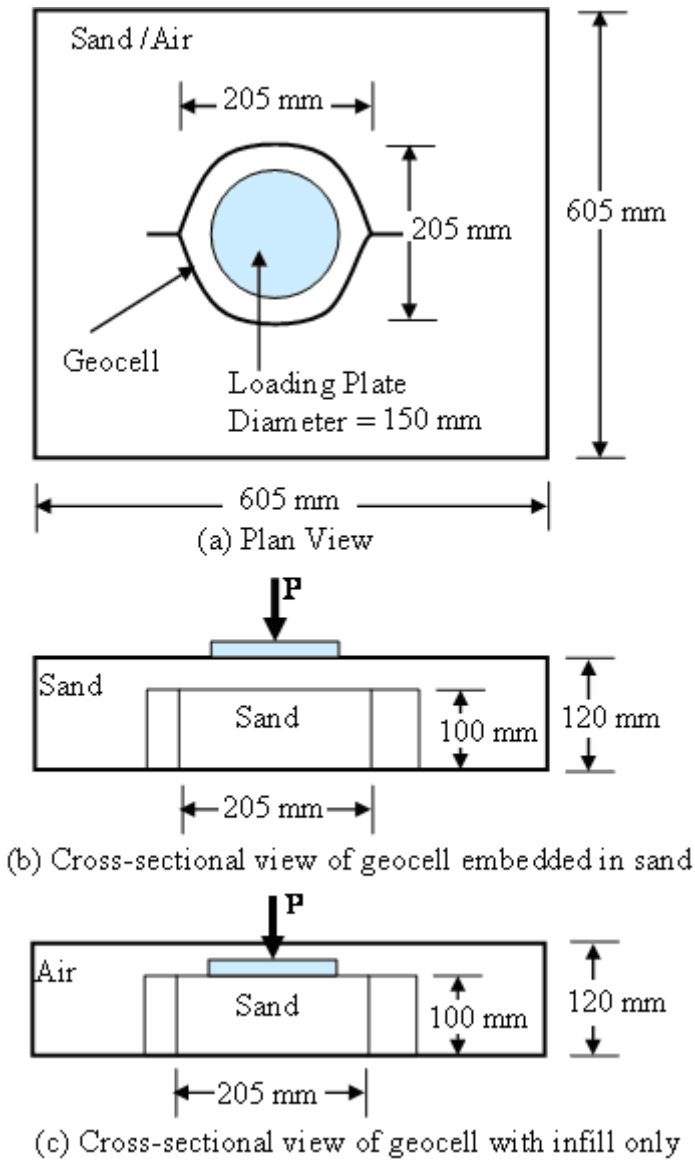

Figure 4.1.1 Test box (Box A) for a single geocell layout

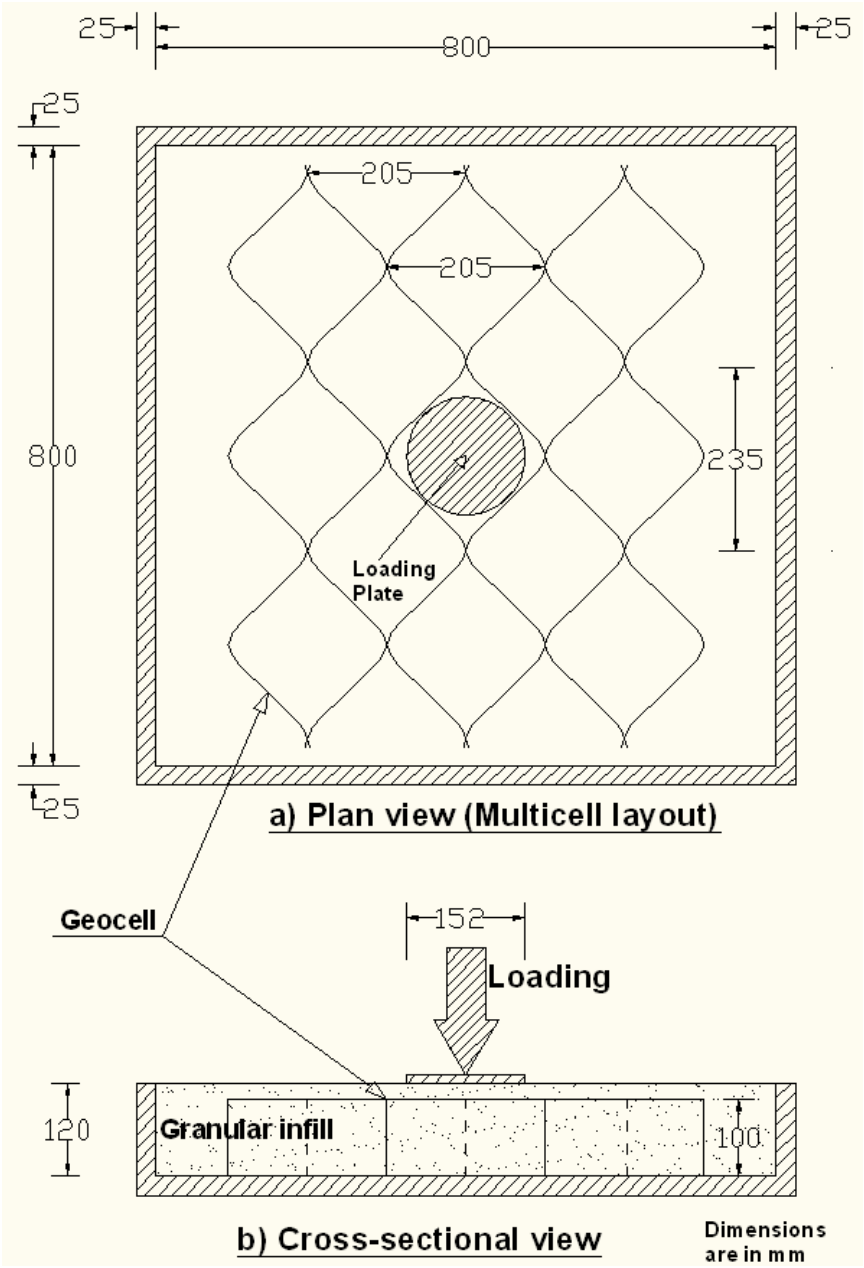

Figure 4.1.2 Test box (Box B) with a multiple geocell layout

(**a**) A single geocell in Box A

(**b**) Multiple geocells in Box B

Figure 4.1.3 Layout of single and multiple geocells embedded in KR-II sand

Figure 4.1.4 Loading frame and test in process in Box B

4.1.2 Boundary effect of box size

To examine if there was any boundary effect because of the size of the test box, four static plate loading tests were carried out for unreinforced and single Type II geocell-reinforced KR-II sand in both Boxes A and B. The height of the geocell used in these cases was 100 mm. The pressure-displacement curves of these tests are shown in **Figure 4.1.5**. For both unreinforced and reinforced sections, there was no appreciable difference in the test results; therefore, Box A was used for single geocell tests under static loading.

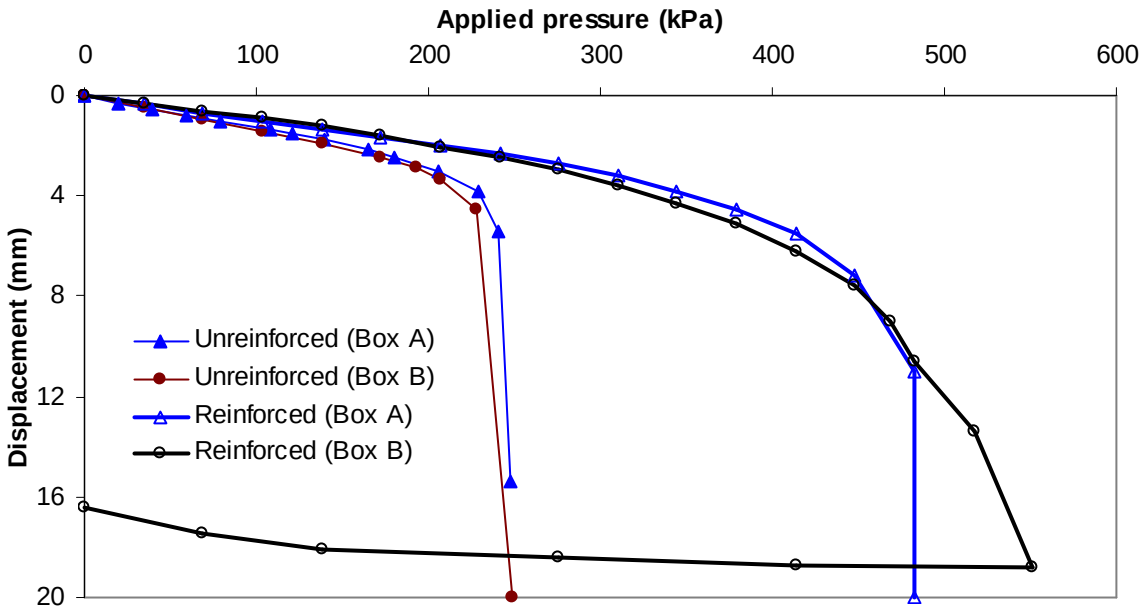

Figure 4.1.5 Effect of box sizes on test results

4.1.3 Repeatability of test method

The credibility of a test method is often established if its test results are repeatable. To examine the repeatability of the test method used in this study, Type II geocell was tested

under both confined and unconfined conditions in Box A with the KR-II sand infill. Three tests were carried out under a confined condition and two tests were carried out under an unconfined condition. **Figure 4.1.6** shows that the test method used in this study is generally repeatable.

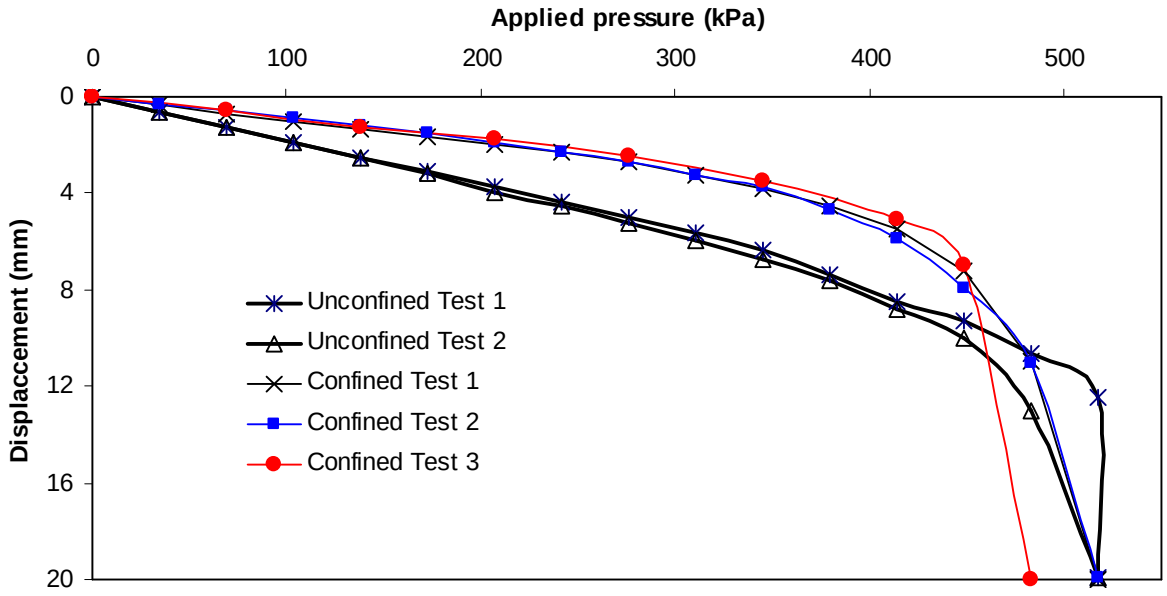

Figure 4.1.6 Repeatability of the test method

4.1.4 Effect of geocell shape

Different shapes of geocell have been investigated by other researchers in the past. Most of their studies were focused on either circular or box-shaped geocells, for example, Rea and Mitchell (1978) and Simizu and Inui (1990). In practice nowadays, however, geocells are placed in an elliptical or near circular shape.

This study investigated Types I, III, and IV geocells with elliptical and circular shapes. All these tests had single geocells embedded in the KR-II sand. In the first set of tests, the

geocell was laid out in an elliptical shape with the major axis length along the weld side equal to 260 mm and the minor axis length equal to 185 mm. After the test, the exhumation showed that the cell with an initially elliptical shape changed to a near circular shape, which had the major axis length along the weld side of 235 mm and the minor axis length of 200 mm (Pokharel et al., 2009a). The shapes of the geocell before and after the test are illustrated in **Figure 4.1.7**. In the second set of tests, geocells with a circular shape and a diameter of 205 mm were used. No obvious change in the geocell shape was observed after the test.

The results of the above tests are summarized in **Figure 4.1.8**. In all cases the reinforced sections were found to perform better than the unreinforced section. The geocells starting with a circular shape showed stiffer and stronger responses than those starting with an elliptical shape for all three types of geocell-reinforced sand. **Figure 4.1.8** also shows that the reinforced base with a higher stiffness geocell (for example, Type IV) had higher stiffness and ultimate bearing capacity than those with a lower stiffness geocell (for example, Types I and III). The stiffness of the base is defined as the slope of the initial linear portion (i.e., applied pressure/displacement). The ultimate bearing capacity is defined as the last applied pressure at which the test could be maintained stable before failure.

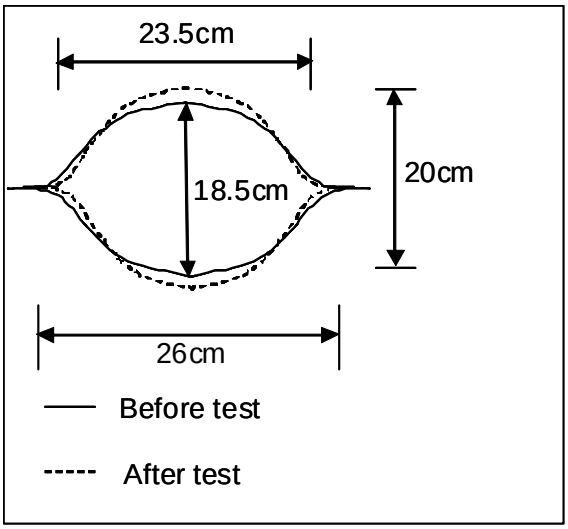

(a) Shape change after test

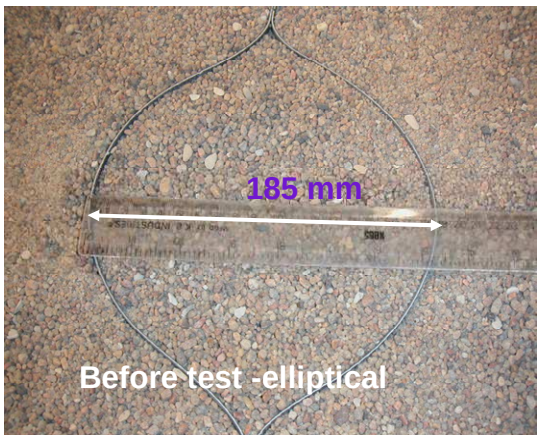

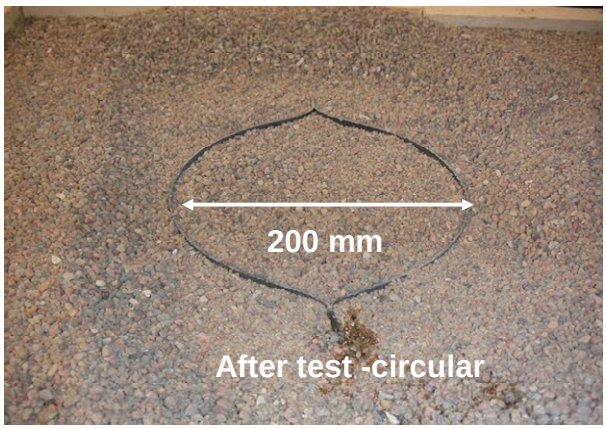

(b) Elliptically laid before test

(c) Near circular shape at failure

Figure 4.1.7 Change of geocell shape after test

It was observed that the geocell was lifted up appropriately by 8 mm from the firm base after each test when the geocell was placed in an elliptical shape and by 5 mm when placed in a circular shape. These data indicate that the infill material escaped from the bottom of the cell under the load. The improvement of the interface properties between the

geocell and the infill can minimize the chance for the geocell being uplifted and is expected to further increase the bearing capacity of the reinforced base. The geocells with an initially elliptical shape failed abruptly while the geocells with an initially circular shape failed gradually. Due to the change of the geocell shape from an initially elliptical to circular shape, the sand particles inside the geocell had more movement, uplifted the geocell, and then resulted in a sudden failure. In addition, no breakage of geocell was observed after these tests.

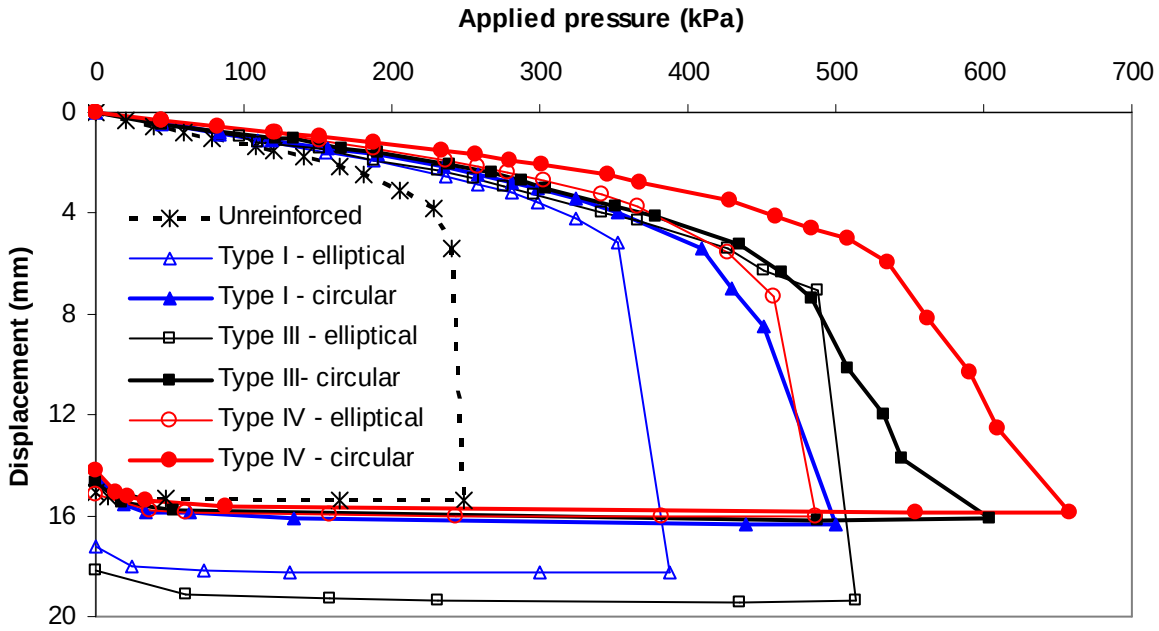

Figure 4.1.8 Effect of geocell initial shape on pressure-displacement curves of single geocell-reinforced KR-II sand (reproduced from Pokharel et al. 2009a)

As the geocell with a near circular shape was found to be more efficient, further plate loading tests to study the geocell-reinforced bases were carried out with geocells laid out in a near circular shape.

4.1.5 Effect of geocell properties

The properties of geocell material (especially modulus) are reported to have an influence on the stiffness and ultimate bearing capacity of geocell-reinforced bases. To verify the influence of geocell properties on the stiffness and ultimate bearing capacity of geocell-reinforced bases, plate loading tests were carried out on all four types of single geocell embedded in the KR-II sand. The unreinforced KR-II sand base was tested as the baseline case for comparison. The increase in the stiffness and ultimate bearing capacity for both geocell shapes (elliptical and circular) in the case of the geocell embedded in sand is clearly evident from the test results in **Figures 4.1.8** and **4.1.9**. For all tests, the geocell-reinforced base failed or yielded at approximately 5 mm displacement, which is equivalent to 3.3% of the diameter of the loading plate.

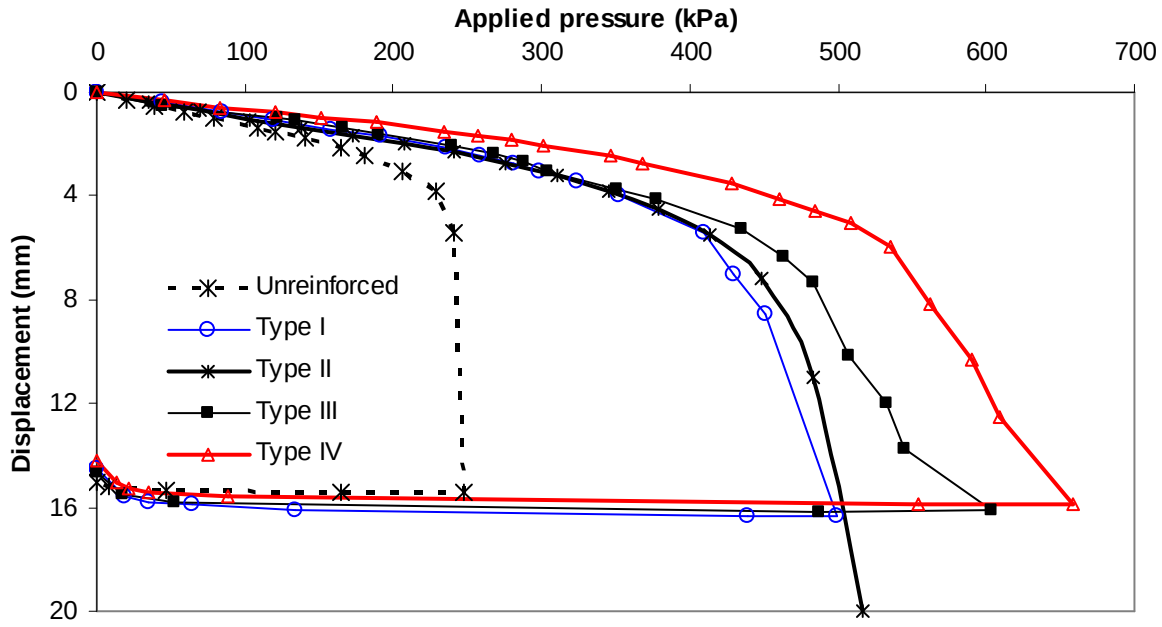

Figure 4.1.9 Effect of geocell type on pressure-displacement curves of single geocell-reinforced KR-II sand in a circular layout

The above results can be expressed in terms of an improvement factor, which is defined as the ratio of the stiffness or ultimate bearing capacity of the reinforced base to that of the unreinforced base. The stiffness improvement factor is the ratio of the slope of the initial portion of the load-displacement curve for the reinforced base to that of the unreinforced base. As summarized in **Table 4.1.1**, geocell reinforcement increased the stiffness by a factor of 1.3 to 2.0 and the ultimate bearing capacity of sand by a factor of 1.5 to 2.5 depending upon the type and the initial shape of geocell. These results are in good agreement with those obtained experimentally and numerically by Han et al. (2008a) earlier. The NPA geocells showed more improvement than the regular HDPE geocell. The degree of improvement in the performance of the reinforced base by the geocell depends on the elastic modulus of the geocell sheet. As discussed earlier, the geocell placed in a circular shape had higher stiffness and ultimate bearing capacity than that placed in an elliptical shape. Overall, Type IV geocell placed in a circular shape was the most effective in increasing the ultimate bearing capacity and reducing the settlement.

Table 4.1.1 Improvement factors for stiffness and bearing capacity of geocell-reinforced KR-II sand

Reinforcement type	Elastic modulus at 2% strain (MPa)	Improvement factor for shape of geocell			
		Elliptical layout		Circular layout	
		Bearing capacity	Stiffness	Bearing capacity	Stiffness
Type I	310	1.5	1.3	1.8	1.5
Type II	355	NA	NA	1.9	1.6
Type III	350	1.9	1.3	2.0	1.7
Type IV	440	2.0	1.8	2.5	2.0

When the improvement factor of the stiffness is plotted against the elastic modulus of the geocell at 2% strain in **Figure 4.1.10**, an excellent correlation was achieved with the R^2 value of 0.99 provided other factors remain unchanged. A similar result is obtained for the improvement factor of ultimate bearing capacity (R^2 = 0.99) plotted against the elastic modulus at 2% strain. Type II geocell with a circular layout improved the stiffness by 1.6 and the ultimate bearing capacity by a factor of 1.9, which were less than those by Type III and Type IV geocells. The perforations on the sides of the Type II geocells could be the reason for this difference in addition to the elastic modulus. Even though the walls of Type II, Type III, and Type IV geocells made of the novel polymeric alloy were 30% thinner than those of Type I geocell (i.e., the regular HDPE geocell), Type I, II and III geocells performed better than the regular HDPE geocell. This result implies that the improvement factors on stiffness and bearing capacity depended on the elastic modulus of the geocell sheet.

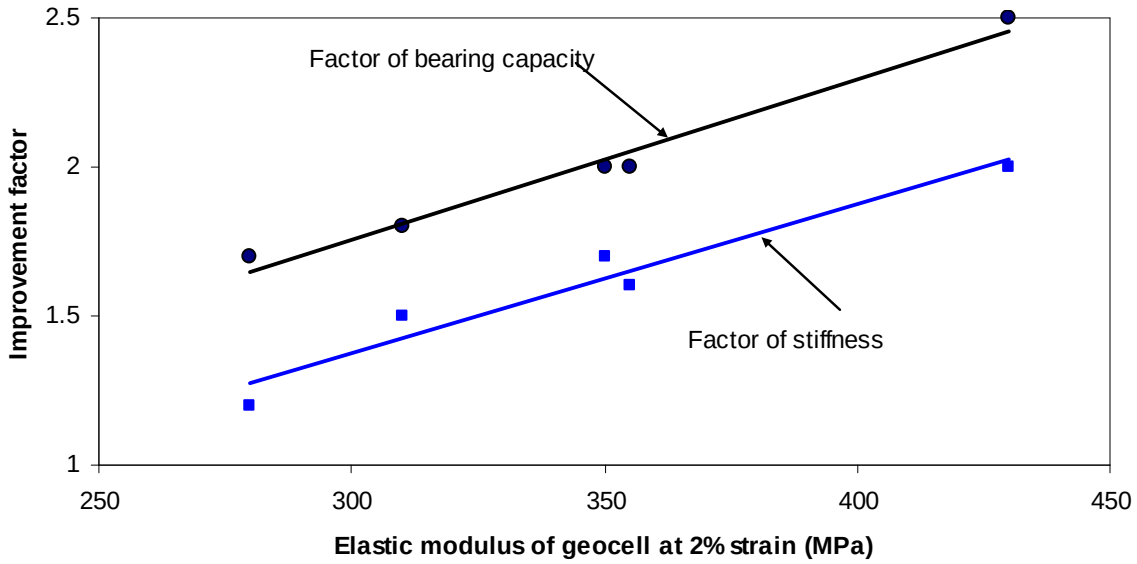

Figure 4.1.10 Relationship between the elastic modulus of geocell sheet and the improvement factor for stiffness and ultimate bearing capacity

4.1.6 Effect of embedment

Six plate loading tests were conducted to study the embedment effect of geocell by its surrounding soil based on both unconfined and confined single cell tests. The test in which the geocell was embedded in sand is referred to as the confined test while the test in which the geocell was not embedded in sand (i.e., in air) is referred to as the unconfined test. The pressure-displacement curves for a total of six unconfined and confined single geocell tests with three types of geocells laid out in a circular shape are shown in **Figure 4.1.11**. As expected, the stiffness of the unconfined geocell infilled with the sand was lower than that of the confined one. All the unconfined geocells failed along the welds while the confined cells remained intact throughout the tests. As mentioned earlier, the infill sand uplifted the geocell and escaped from the bottom of the geocell in the confined tests.

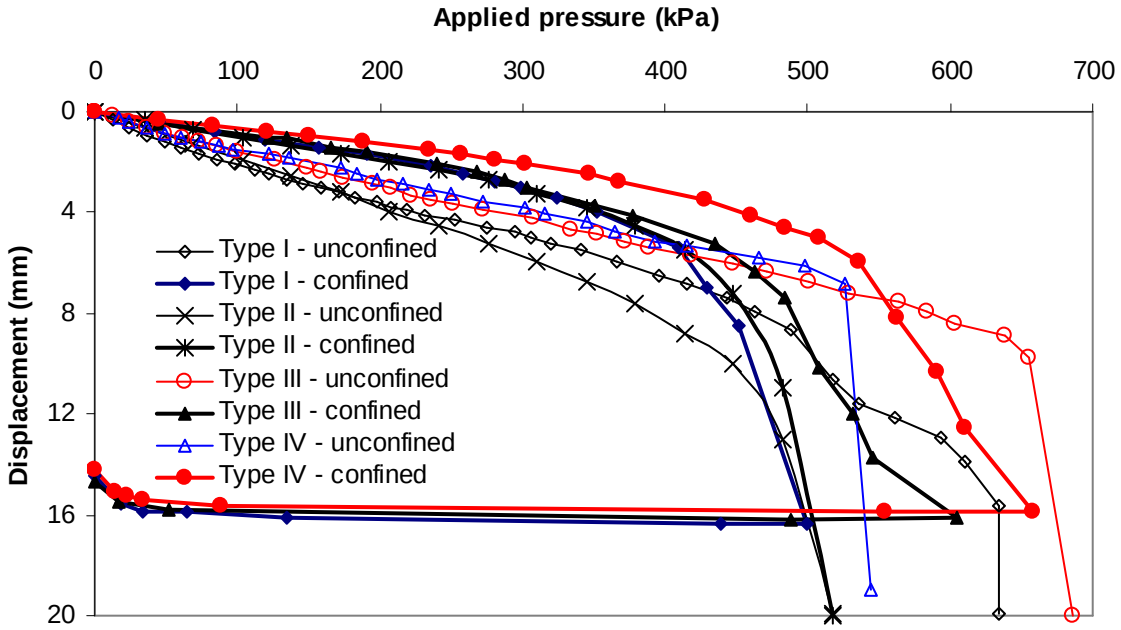

Figure 4.1.11 Effect of confinement on pressure-displacement curves of single geocell-reinforced KR-II sand (reproduced from Pokharel et. al., 2009a)

Surprisingly, the unconfined geocells had higher ultimate load capacities than those embedded in the sand except for Type II and Type IV geocells. During the test it was observed that the unconfined geocell first expanded laterally and then failed due to the breakage of the weld under the load. The lateral expansion increased the cross section of the geocell, therefore, the average stress at the bottom of the cell was reduced and the load capacity was increased. For Type II and Type IV geocells, the weld of the unconfined geocell failed suddenly and early, possibly because of the weak weld strength for this specific geocell. For the confined geocell, however, the easier failure mode was the uplifting of the geocell and escaping of the sand from the bottom of the geocell, possibly because the lateral expansion was minimized due to the confinement from the surrounding soil. This phenomenon happened when the base course was underlain by a firm subgrade. If a soft subgrade exists, however, the failure mode may be different and should be further

investigated. All unconfined geocells infilled with sand ruptured along the weld line of the two geocell pallets while all those embedded in the soil did not rupture. These tests show that more weld resistance is needed to prevent rupture under an unconfined condition. In multiple geocell tests, such weld breakage was not observed since the surrounding soil (especially that contained in adjacent cells of the interconnected honeycomb structure) minimizes the deformations of the loaded cell and immobilizes the rupture of the weld line.

4.1.7 Effect of geocell height

Shimizu and Inui (1990) found that an increase of height and area of geocell increased the bearing capacity of the reinforced foundation and the extent of the increase was correlated with the horizontal stiffness of the cell material. The geocell-reinforced section showed an improvement in the bearing capacity and such an improvement became more significant for a higher cell height (Dash et al., 2004). There exist an optimum geocell height/width ratio and an optimum loading area width/geocell width ratio. To study the effect of geocell height on the stiffness and bearing capacity of single geocell-reinforced bases, tests were carried out on the KR-II sand sections with and without a single geocell. The 120 mm thick section included a 100 mm high geocell infilled with sand plus a 20 mm sand cover while the 170 mm thick section contained two 75 mm high geocells placed one on top of the other without any offset and infilled with sand plus a 20 mm sand cover. A cover of 20 mm was used as it is commonly used in practice. These tests were done under a confined condition with a circular geocell layout. **Figure 4.1.12** shows the pressure-displacement curves for unreinforced and reinforced sections with two different base thicknesses. It is shown that both the unreinforced and reinforced sections with a smaller thickness had higher ultimate bearing capacities than those with a larger thickness. This difference can be explained as the

firm bottom in the thinner section forced the failure surface to occur in a shallower depth and increased the bearing capacity. This phenomenon has been well explained by Mandel and Salençon (1972) in their theoretical solution. As mentioned in **Table 4.1.1** and also reported by Pokharel et al. (2009b) for the 120 mm thick test section, Type II NPA geocell improved the stiffness and ultimate bearing capacity by factors of 1.6 and 1.9, respectively. For the 170 mm thick test section, however, Type II NPA geocell improved the stiffness and ultimate bearing capacity by factors of 1.3 and 1.6, respectively. It is worth pointing out that a thicker base should have higher stiffness and ultimate bearing capacity if a weak subgrade existed and controlled the failure mode, as demonstrated by Han et al. (2008b).

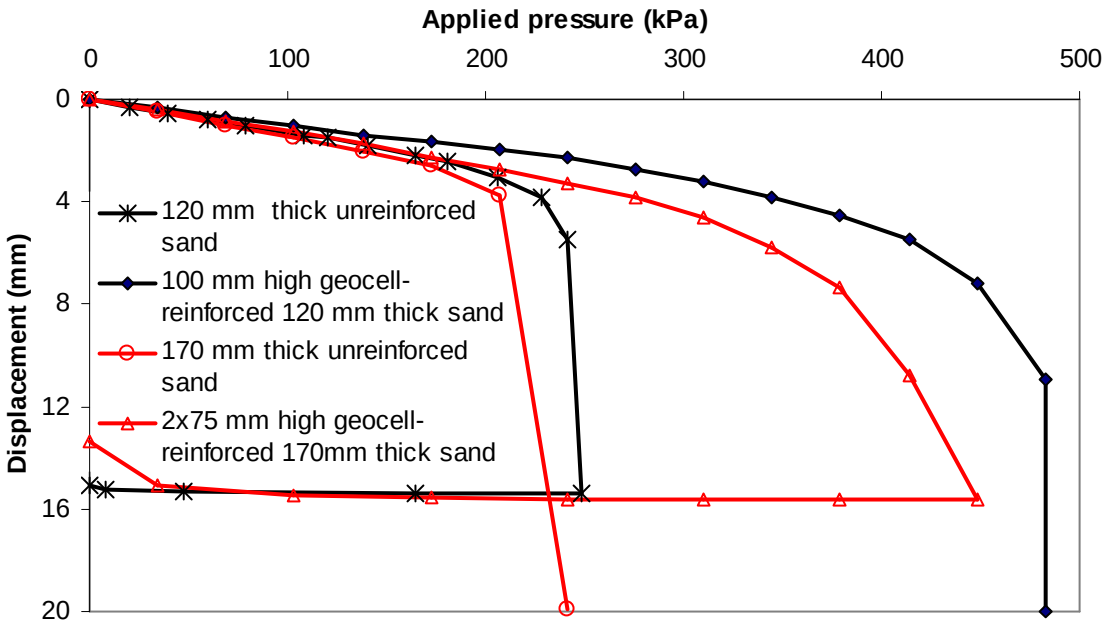

Figure 4.1.12 Effect of base thickness on pressure-displacement curves of single geocell-reinforced KR-II sand

Compaction has been an issue for discussion while using geocell as soil reinforcement. To examine the compaction effect, different compaction procedures were adopted for preparing single geocell-reinforced bases. NPA Type II geocell was used in this study. In the first test section, the infill material QW-I was placed at the first lift of 100 mm followed by compaction and then the 20 mm QW-I cover as the second lift followed by compaction. This compaction resulted in the degree of compaction at 88%. The second test section was prepared with three lifts as explained in the preceding section, which resulted in 95% compaction. **Figure 4.1.13** shows that under the static loading of 900 kPa, the 95% compacted section experienced only about one-half of the deformation experienced by the 88% compacted section (i.e., the 95% compaction produced a two-fold stiffness value compared to the 88% compaction). This comparison shows that the degree of compaction had a significant effect on the performance of geocell-reinforced bases. Therefore, all the later tests with QW-I and AB-3-I were carried out at 95% compaction.

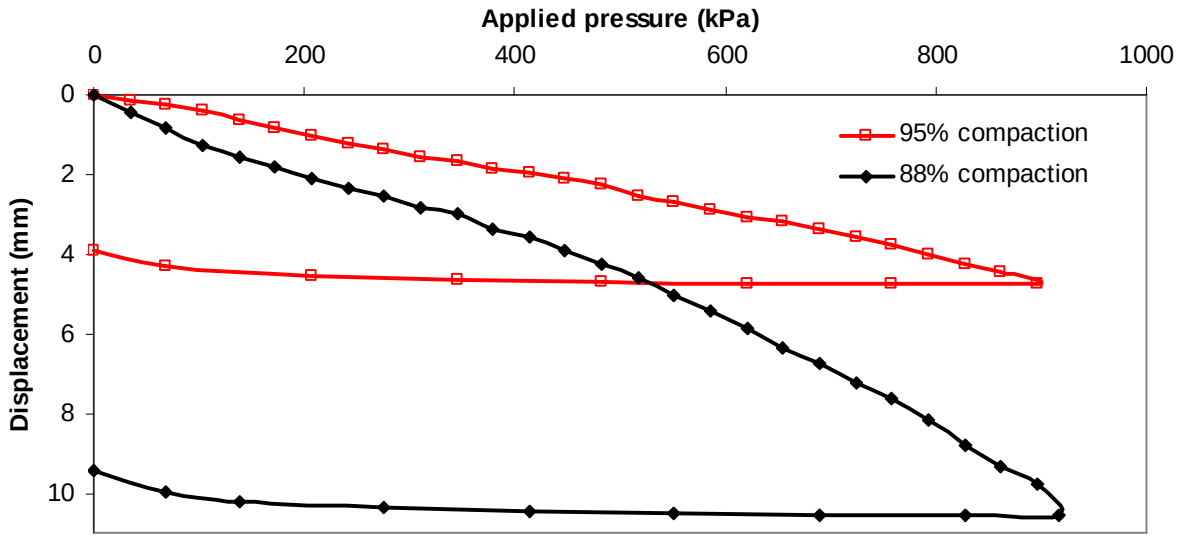

Figure 4.1.13 Effect of compaction on pressure-displacement curves of single geocell-reinforced QW-I bases

4.1.9 Effect of infill material

Since stiffness and bearing capacity of a base depend on the quality of its material, a study was conducted to examine the effect of single geocell reinforcement for two base materials: the KR-II sand and the QW-I. NPA Type II geocell was used in this study. Since the KR-II sand does not contain any fines, it is not sensitive to moisture. In addition, the KR-II sand is a river sand with sub-rounded particles so that it is relatively weak without any confinement. However, the QW-I had approximately 7% fines; therefore, it is sensitive to moisture and has apparent cohesion under an unsaturated condition. The KR-II sand was compacted to approximately 70% relative density. The QW-I was compacted to approximately 97% maximum dry density at the moisture content of 7% and had 58% CBR. As shown in **Figure 4.1.14**, the QW-I was much stiffer and stronger than the KR-II sand. Due to the limited capacity of the load system, the tests for the QWa were carried out to the maximum static pressure of 900 kPa only. The test results show that the geocell significantly improved the performance of the KR-II sand. However, limited improvement was observed for the geocell-reinforced QW-I. It is known that one of the contributions of geocell is to provide apparent cohesion to granular material resulting from lateral confinement; therefore, the cohesion existing in the base material minimizes the benefit of the geocell by providing lateral confinement under static loading. However, if the QW-I becomes completely dry or saturated, the apparent cohesion would be lost. Under such a condition, the benefit of the geocell is expected to be greater, which should be verified through future research.

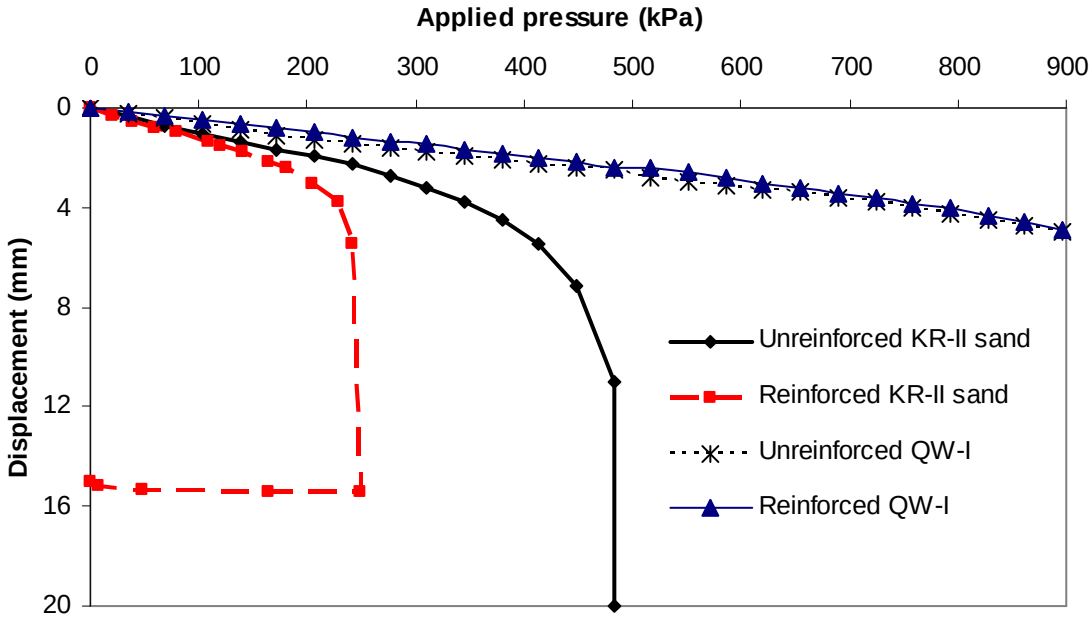

Figure 4.1.14 Effect of base materials on pressure-displacement curves of single geocell-reinforced bases

4.1.10 Effect of multi-cell reinforcement

To compare the behavior of geocell-reinforced bases with single geocell reinforcement and multi-cell reinforcement, a 9 geocell (3 x 3) reinforced section was also tested in Box B. The KR-II sand was used as the infill material. The test section had 10 cm high NPA Type II geocell with the KR-II sand infill covered by 20 mm KR-II sand. **Figure 4.1.15** shows the comparison of the pressure-displacement curves of single and multi geocell-reinforced sections. It is clearly shown that the multi-cell reinforcement further improved the performance of the KR-II sand as compared with the single geocell reinforcement. The improvement factors for the stiffness and ultimate bearing capacity by the multi-cell reinforcement were 2.0 and 3.1, respectively.

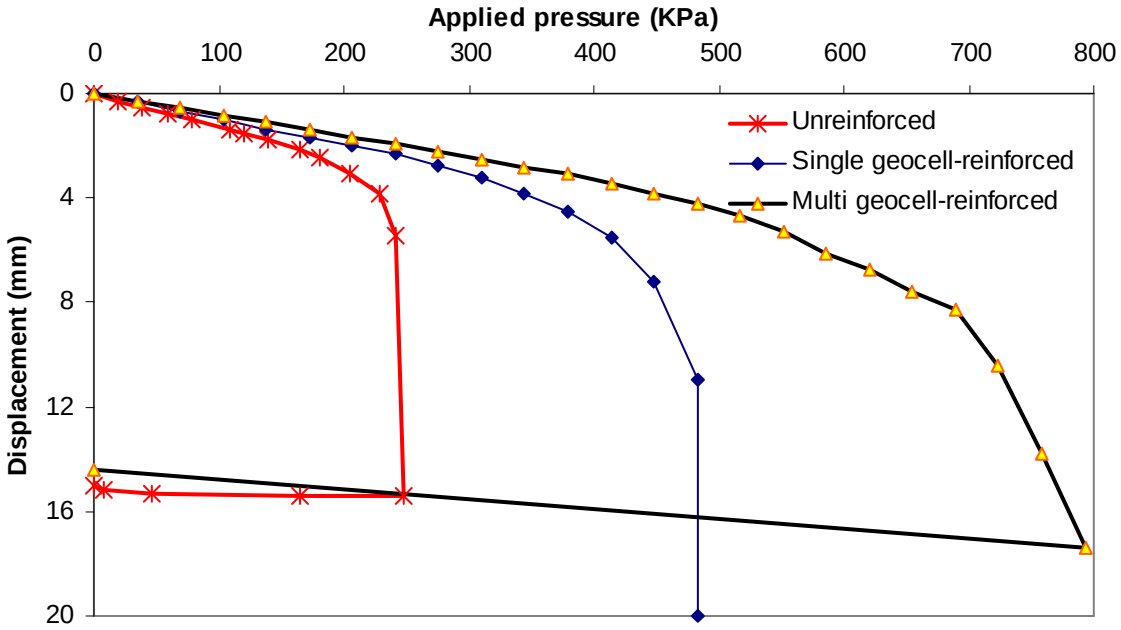

Figure 4.1.15 Effect of multi-geocell reinforcement on pressure-displacement curves of geocell reinforced KR-II sand

4.1.11 Summary

This section presented an experimental study to investigate six key influence factors on the behavior of single geocell-reinforced bases under static loading: the placement shape of the geocell, the type of the geocell, the embedment of the geocell, the thickness of the reinforced section, the quality of the infill material, and the multi-cell reinforcement. To ensure the validity of the test method, its boundary effect and repeatability were first examined. The following findings are summarized from this study:

(1) The geocell placed in a circular shape had higher stiffness and bearing capacity of the reinforced base than that placed in an elliptical shape.

(2) The performance of geocell-reinforced bases depended on the elastic modulus of the geocell sheet. The NPA geocell with a higher elastic modulus had higher stiffness

and bearing capacity of the reinforced base. Type III and Type IV geocells made of the novel polymeric alloy were found to have significantly higher stiffness and ultimate bearing capacity than Type I geocell made of HDPE.

(3) The improvement factors for the geocell-reinforced bases over the unreinforced bases ranged from 1.3 to 2.0 in terms of stiffness and 1.5 to 2.5 in terms of bearing capacity. The geocell with a higher elastic modulus, specially the NPA geocells, had a higher improvement factor.

(4) The unconfined geocell had a lower stiffness but a higher ultimate load capacity as compared with the confined geocell due to its lateral expansion, except for NPA Type IV geocell which had the relatively weak weld strength but the highest modulus.

(5) All the unconfined geocells failed at the welds while the confined geocells failed by the uplifting of the geocell and then the escaping of the sand particles from the bottom.

(6) A thinner unreinforced or geocell-reinforced base on a firm subgrade had a higher bearing capacity than the thicker unreinforced or geocell-reinforced base, respectively.

(7) Under static loading, geocell reinforcement had more significant improvement in the cohesionless Kansas River (KR-II) sand than the quarry waste (QW-I) with an apparent cohesion.

(8) The multiple geocell-reinforced base courses had higher stiffness and bearing capacity than single geocell-reinforced base courses. Therefore, multi-cell reinforcement could further improve the performance of the sand as compared with single geocell reinforcement.

4.2 Repeated Plate Loading Tests

This section presents the results of the experimental study conducted to investigate the influence of geocell reinforcement on the performance of granular bases under repeated loading. The influences of both single and multiple geocell reinforcements with different infill materials are compared and evaluated in terms of permanent deformation, percentage elastic deformation, and traffic benefit ratio (TBR).

4.2.1 Test setup

Figure 4.1.2 shows the details of the NPA geocell layout and the test box (Box B) for the repeated tests. The picture of the layout in Box B was shown in **Figure 4.1.3(b)**. For repeated loading tests on single and multiple geocell-reinforced bases, the NPA Type II geocell was placed at the center of the box and laid out in a near circular shape as suggested by Pokharel et al (2009a). All NPA geocells used in this test were 100 mm high with a 2 cm thick fill cover. For all the tests, the geocells were filled and embedded in the infill material. KR-II sand was placed and compacted to 70% relative density inside and/or outside the cell in three layers: two 5 cm thick layers and one 2 cm cover layer. The QW-I was compacted to a dry density equal to 95% of the maximum dry density on the drier side (approximately 7% moisture content) of the compaction curve. The AB-3-I was also compacted to a dry density equal to 95% of the maximum dry density on the drier side (approximately 9% moisture content) of the compaction curve. For comparison purposes, unreinforced bases were prepared in a similar way and tested under repeated plate loading for 150 cycles of repeated loading. Like the static plate loading test, no subgrade existed for all the repeated loading tests because the primary purpose of this study was to evaluate the influence of the geocell

reinforcement on the behavior of base courses. The wooden bottom plate of the box B was served as the subgrade for all the tests.

A loading plate was placed at the center of the geocell for the reinforced case or at the center of the box for the unreinforced case. Loads were applied in increments by adjusting air pressure in the air cylinder. The repeated load was applied at 1min/cycle. The test was terminated after 150 cycles except the unreinforced sand that could not hold the applied load (i.e., failure occurred). As Pokharel et al. (2009a and b and 2010) and Han et al. (2010) showed, the ultimate bearing capacities of the unreinforced and geocell-reinforced AB-3-I and QW-I bases were higher than the tire pressure of a typical highway truck (i.e., 552 kPa). Therefore, a repeated load of 552 kPa was applied for all the tests with AB-3-I and QW-I bases. Pokharel et al. (2010) showed that the ultimate bearing capacities of multiple geocell-reinforced, single geocell-reinforced, and unreinforced KR-II sand were approximately 715, 500, and 230 kPa, respectively. Since the ultimate bearing capacity of the multiple geocell-reinforced KR-II sand was higher than 552 kPa, a repeated load of 552 kPa was applied on the multiple geocell-reinforced KR-II sand. Since the ultimate bearing capacity of the single geocell-reinforced KR-II sand was lower than 552 kPa, the repeated load test on the single geocell-reinforced KR-II sand was done at an applied pressure of 345 kPa (corresponding to approximately 70% of its ultimate bearing capacity, which is also close to the tire pressure of typical construction equipment). Due to the low ultimate bearing capacity of the unreinforced KR-II sand (230 kPa), a repeated load test at either 552 kPa or 345 kPa pressure was impossible. For a comparison purpose, a repeated load test was also performed on the multiple geocell-reinforced KR-II sand at an applied pressure of 345 kPa.

4.2.2 Pressure-displacement cycles

The pressure-displacement cycles of the single geocell-reinforced KR-II sand under repeated loading of 345 kPa were presented in Pokharel et al. (2009a) and are also shown here in **Figure 4.2.1**. The pressure-displacement cycles of the multiple geocell-reinforced KR-II sand are given in **Figure 4.2.2**. The pressure-displacement cycles of the unreinforced and multiple geocell-reinforced sections for all three infill materials under repeated loading of 552 kPa are shown in **Figure 4.2.3** through **Figure 4.2.8**. It is shown that in each cycle, there are elastic and plastic (also called permanent deformation). The permanent deformation accumulated with the increasing number of cycles during the test.

The stiffness values of the unreinforced and reinforced bases at the first loading cycle can be determined based on the slopes of the linear portions of the pressure-displacement curves. As discussed in **Section 4.1,** the stiffness of the single geocell-reinforced KR-II sand section was approximately 1.5 times that of the unreinforced section. The improvement factors for the stiffness values over the unreinforced cases found from the present tests are shown in **Table 4.2.1.**

Table 4.2.1 Improvement factors for stiffness of NPA geocell-reinforced base materials

Base material	**Improvement factor for stiffness of NPA type II geocell-reinforced section over the unreinforced section**	
	Single geocell-reinforced	**Multiple geocell-reinforced**
KR-II sand	1.5	2.0
QW-I	1.3	1.5
AB-3-I	1.3	1.7

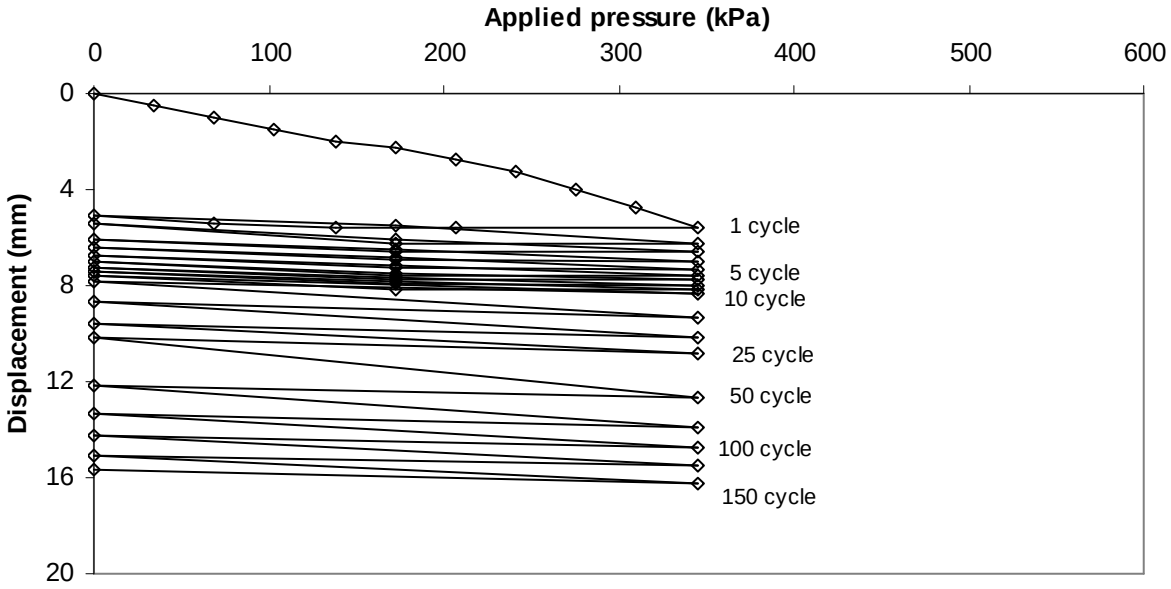

Figure 4.2.1 Pressure-displacement cycles of single geocell-reinforced KR-II sand under reapeated loading of 345 kPa

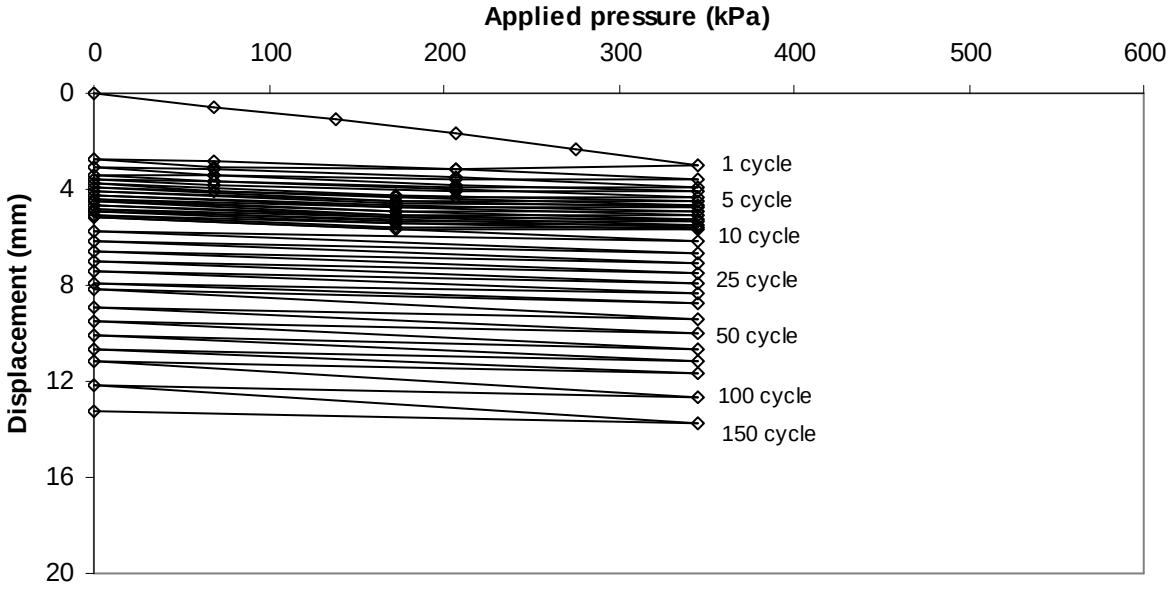

Figure 4.2.2 Pressure-displacement cycles of multiple geocell-reinforced KR-II sand under reapeated loading of 345 kPa

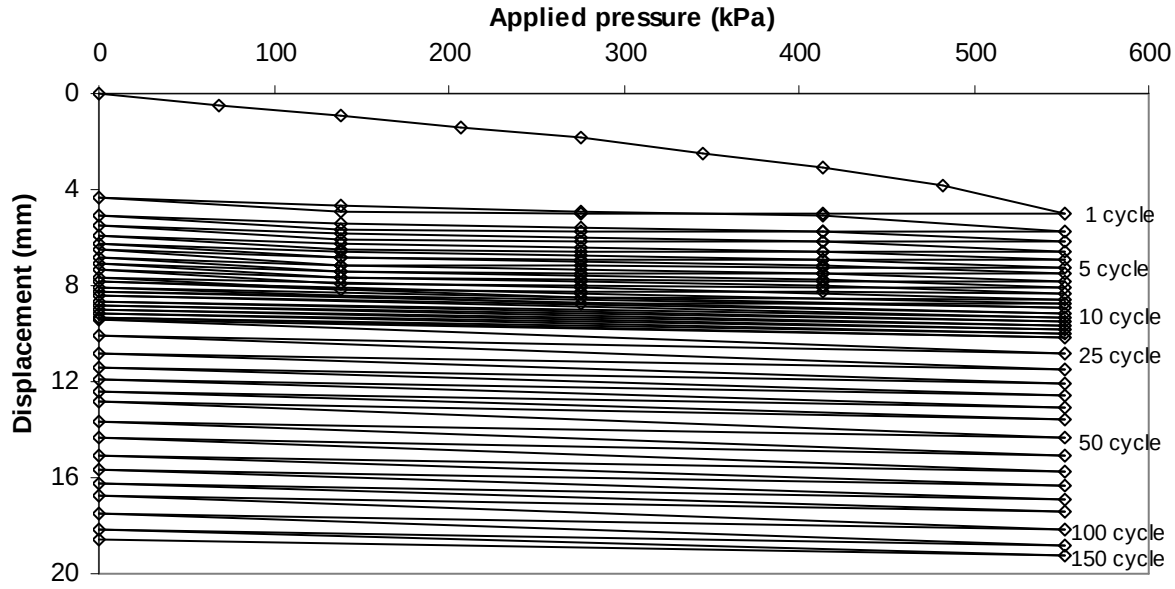

Figure 4.2.3 Pressure-displacement cycles of multiple geocell-reinforced KR-II sand under reapeated loading of 552 kPa

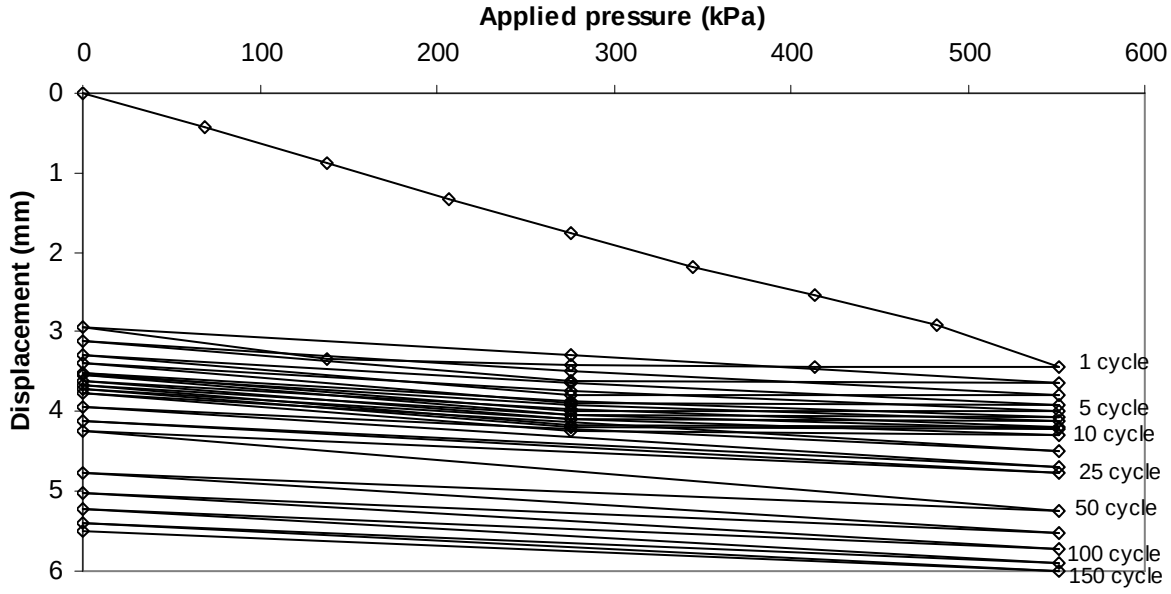

Figure 4.2.4 Pressure-displacement cycles of unreinforced WQ-I under reapeated loading of 552 kPa

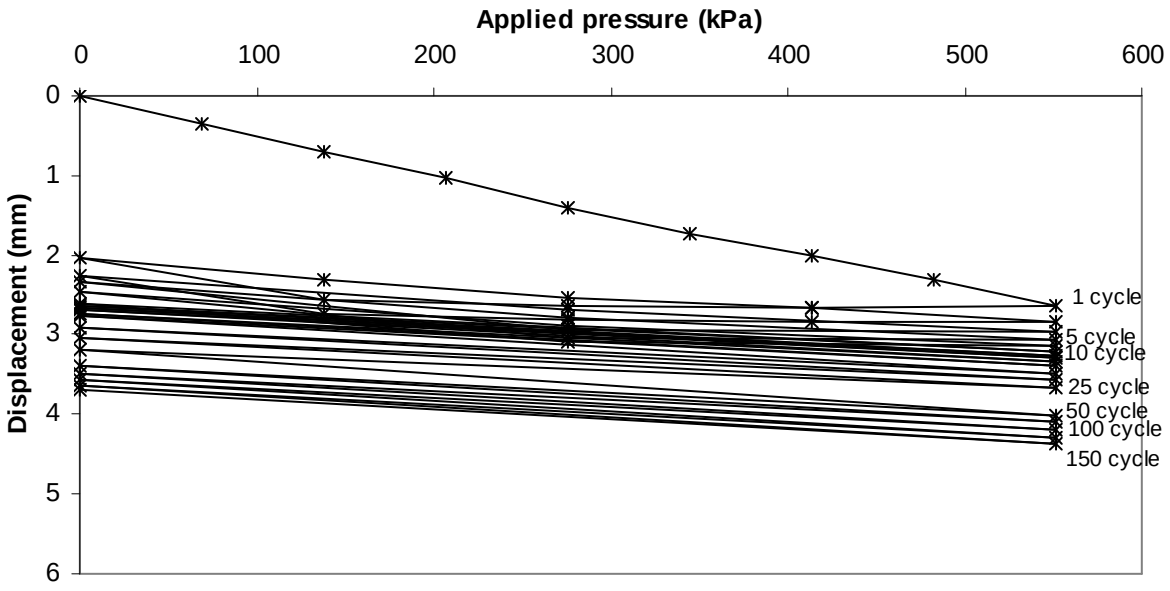

Figure 4.2.5 Pressure-displacement cycles of single geocell-reinforced QW-I under reapeated loading of 552 kPa

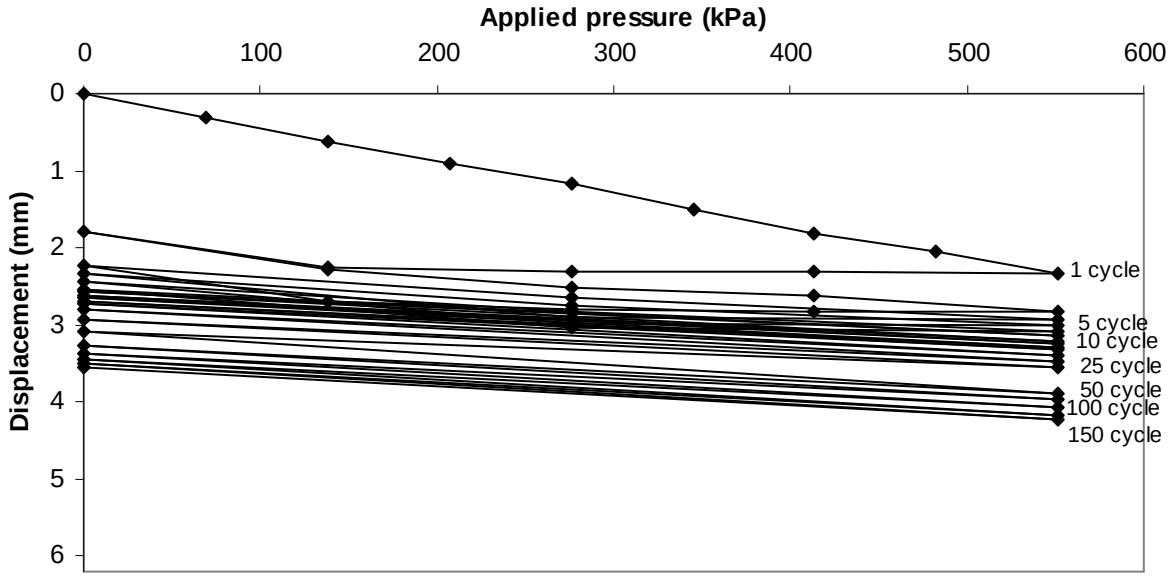

Figure 4.2.5 Pressure-displacement cycles of multiple geocell-reinforced QW-I under reapeated loading of 552 kPa

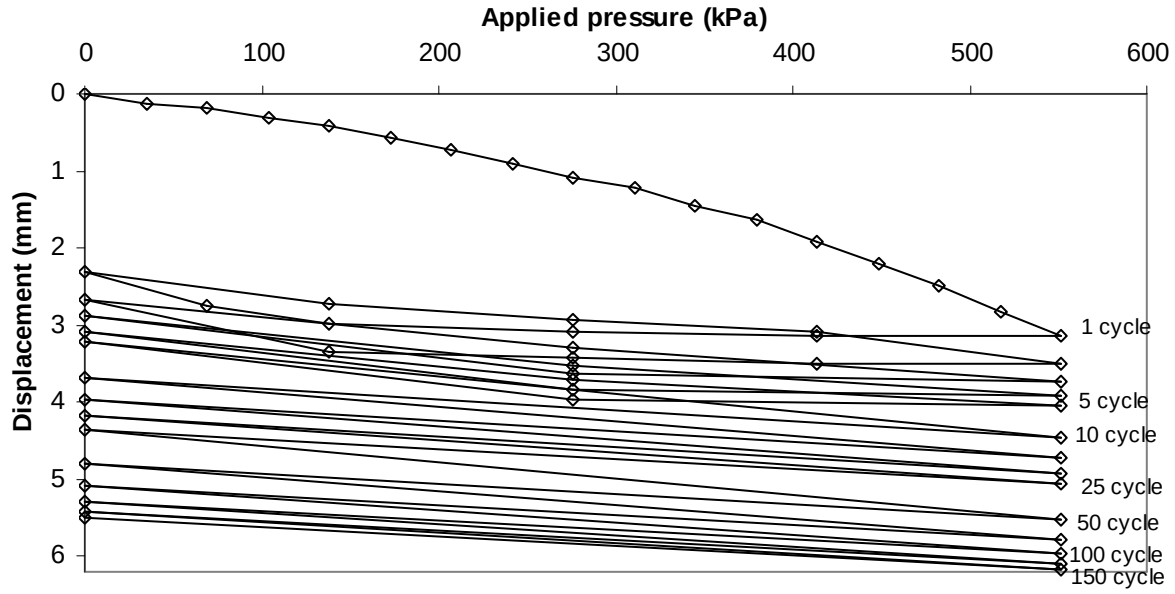

Figure 4.2.6 Pressure-displacement cycles of unreinforced AB-3-I aggregate under reapeated loading of 552 kPa

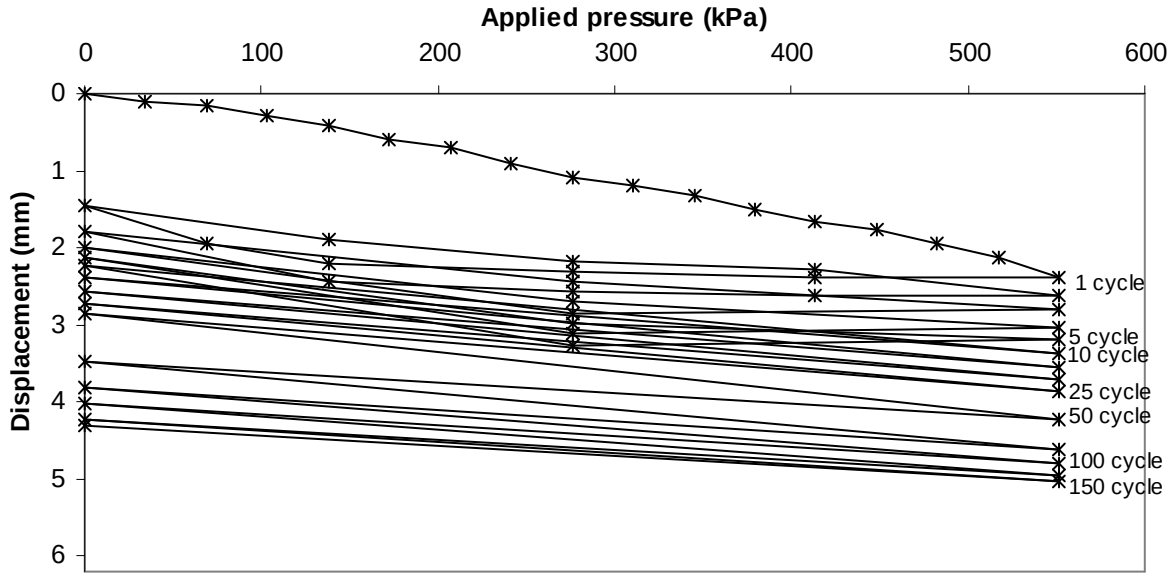

Figure 4.2.7 Pressure-displacement cycles of single geocell-reinforced AB-3-I aggregate under reapeated loading of 552 kPa

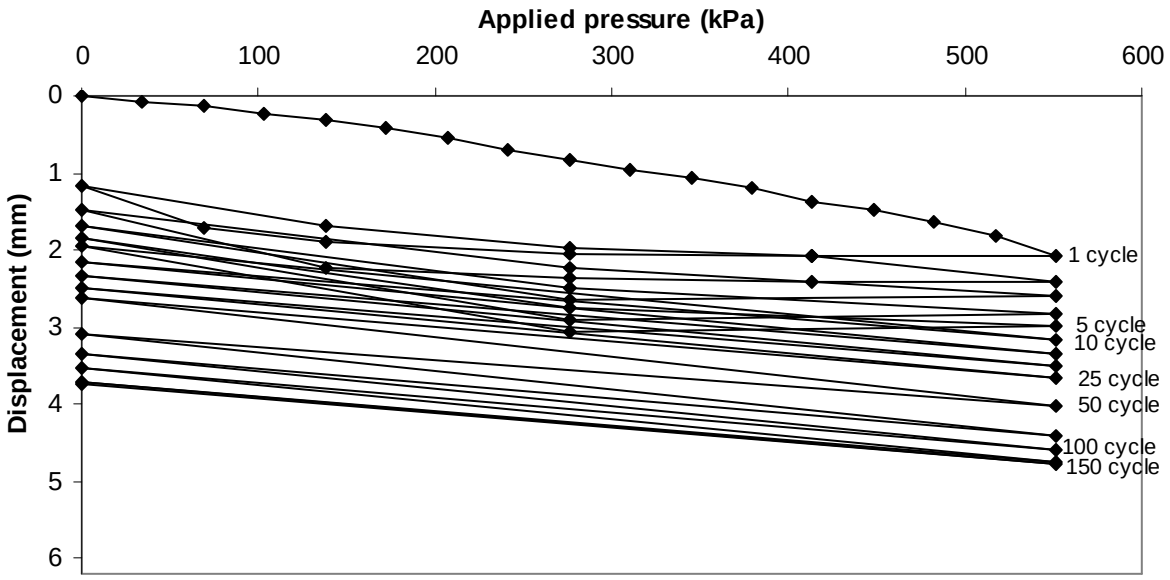

Figure 4.2.8 Pressure-displacement cycles of multiple geocell-reinforced AB-3-I aggregate under reapeated loading of 552 kPa

4.2.3 Permanent deformation vs. number of cycles

Figure 4.2.9 presents the cumulative deformation vs. the number of cycles of the KR-II sand under three different conditions: the single geocell reinforcement at a maximum pressure of 345 kPa and the multiple geocell reinforcement at 345 kPa and 552 kPa under repeated loading. The difference between the two curves at 0 and the maximum pressure is the elastic deformation for the corresponding test. Since the unreinforced KR-II sand section failed at 230 kPa (Pokharel et al., 2009c), a repeated load test under a pressure of 345 kPa was not possible. However, the single NPA Type II geocell-reinforced KR-II sand section under the repeated loading of 345 kPa survived 150 cycles of loading. The same pressure in the case of multiple NPA Type II geocell-reinforced KR sand section produced only 84% of that deformation after 150 loading cycles. This comparison demonstrates that the multiple geocell reinforcement further improved the performance of reinforced bases. Under a higher

applied pressure of 552 kPa, the multiple geocell-reinforced section deformed more than that under a lower pressure of 345 kPa. It is interesting to note that the deformation vs. number of cycle curves for the multiple geocell-reinforced sections under these two different pressures are nearly parallel after 50 cycles.

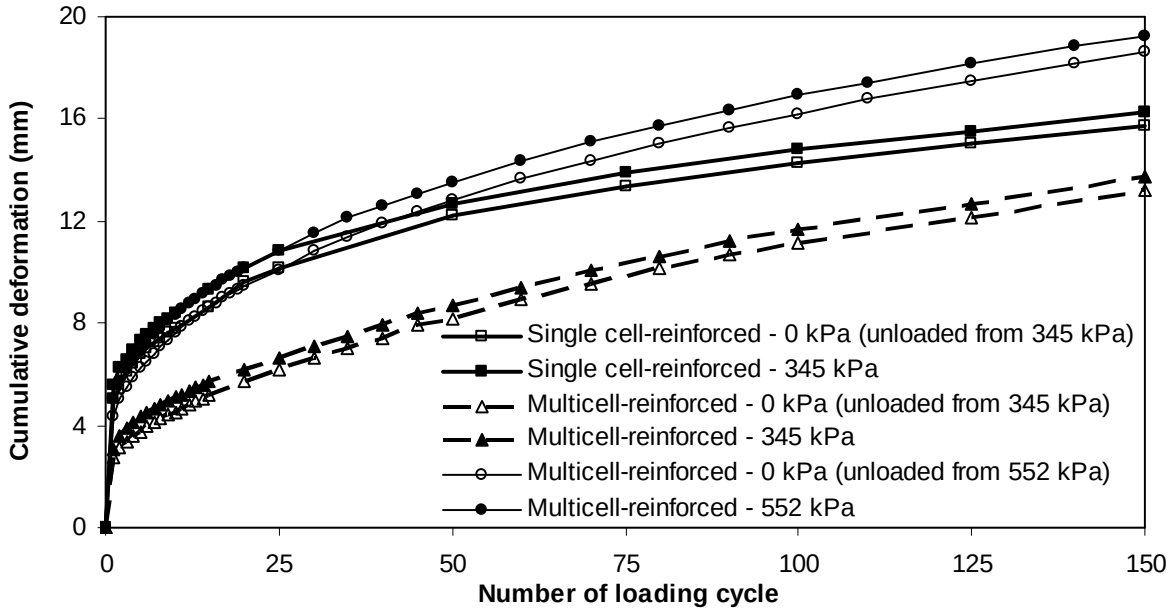

Figure 4.2.9 Cumulative deformations of KR-II sand bases under repeated loading

Figures 4.2.10 and **4.2.11** present the cumulative deformations of unreinforced, single geocell-reinforced, and multiple geocell-reinforced QW-I and AB-3-I bases, respectively under repeated loading of 552 kPa. The curves show the cumulative deformations at each cycle for the maximum pressure (552 kPa) and the minimum pressure (0 kPa). It is clearly shown that both single and multiple geocell reinforcement reduced the cumulative deformations as compared with the unreinforced base. The reduction in the cumulative deformation started from the first loading cycle and continued with the number of cycles.

The cumulative deformations for the QW-I and AB-3-I bases with a single geocell reinforcement measured at 150 cycles at the maximum pressure or zero pressure were reduced by 50% and 33% as compared with the unreinforced QW-I and AB-3-I bases, respectively, at the same number of cycles. The inclusion of multiple geocell reduced the cumulative deformation by 55% for the QW-I base and 40% for the AB-3-I base, respectively. These comparisons demonstrate that multiple geocell reinforcement further improved the performance of reinforced bases slightly. Pokharel et al. (2010) showed that the geocell reinforcement did not show any benefit in the performance of QW-I bases under static loading because QW-I had apparent cohesion. The repeated loading test clearly showed that geocell reinforcement improved the performance of QW-I and AB-3-I bases under repeated loading even though these materials have apparent cohesion.

Figure 4.2.12 presents a special case where the cumulative deformation of the confined, single geocell-reinforced QW-I under repeated loading is compared with an unconfined case. It is clearly shown that the confinement of the geocell by the surrounding soil reduced the cumulative deformation. It is understandable that soil confinement and geocell confinement have the same effect.

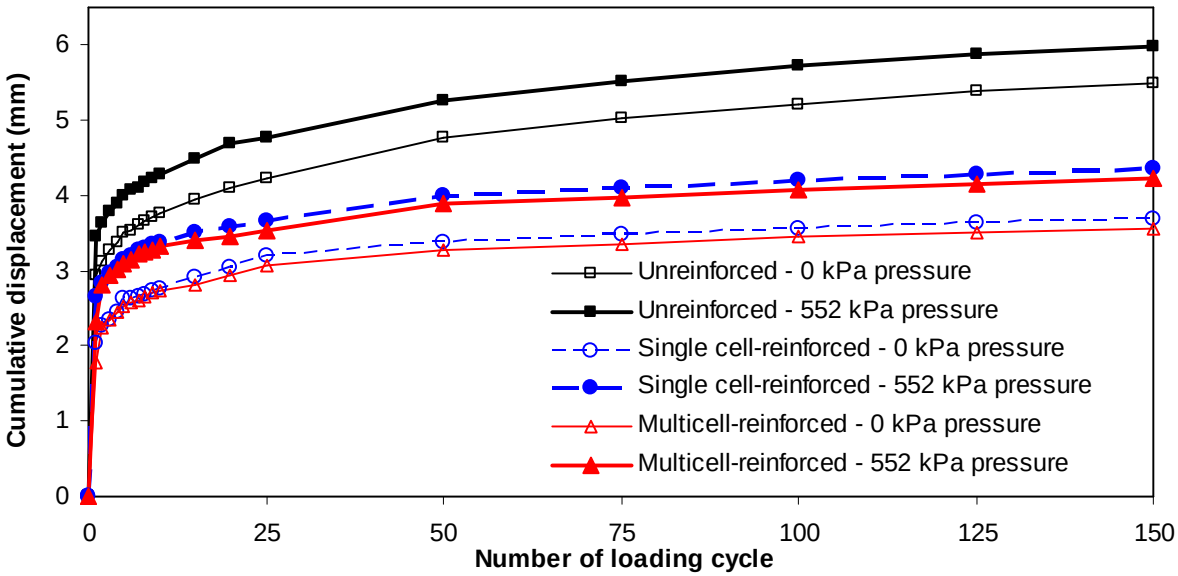

Figure 4.2.10 Cumulative deformations of QW-I bases under repeated loading

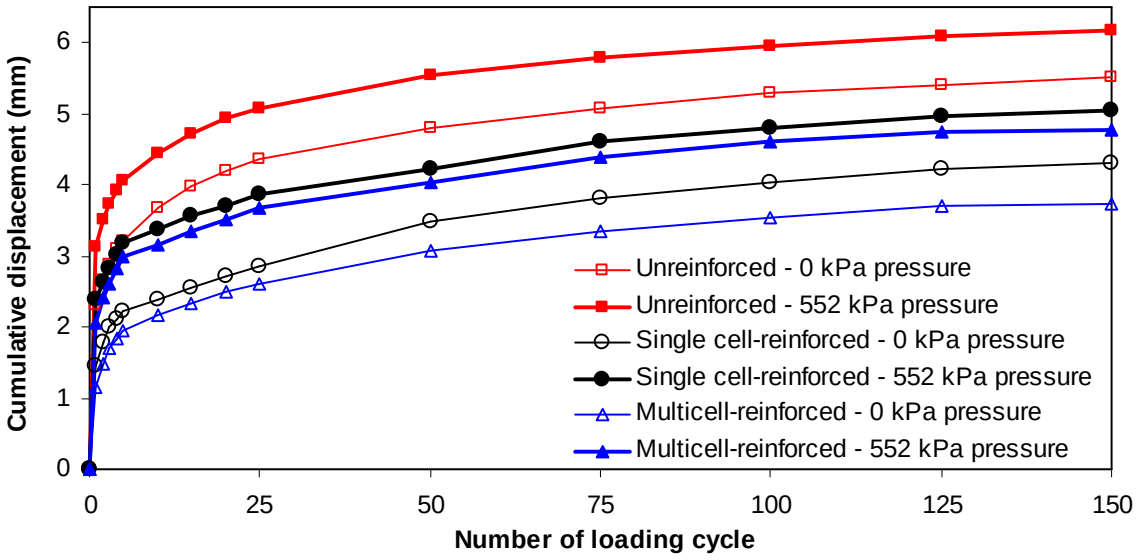

Figure 4.2.11 Cumulative deformations of AB-3-I bases under repeated loading

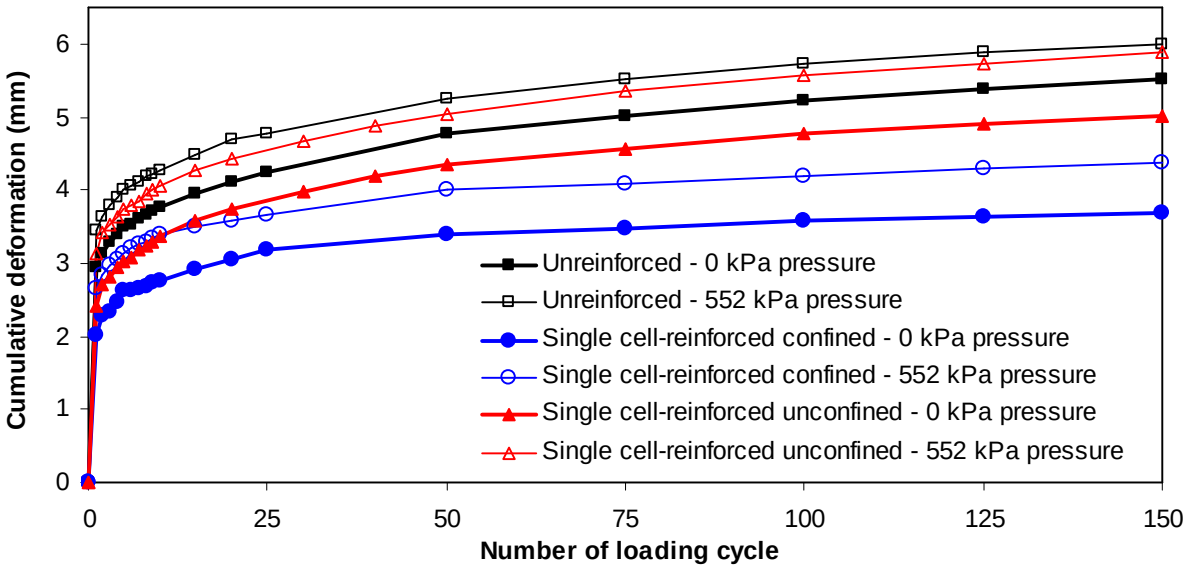

Figure 4.2.12 Cumulative deformations of confined and unconfined single geocell-reinforced QW-I bases

Figure 4.2.13 shows a comparison of the permanent deformations of unreinforced and NPA Type II geocell-reinforced bases with three different infill materials under repeated loading of 552 kPa. Permanent deformations are the deformations after unloading (i.e., zero pressure). Since the unreinforced KR sand could not sustain the applied pressure of 552 kPa, no test data is shown in this figure. However, the test data of the multiple NPA Type II geocell-reinforced KR-II sand in **Figure 4.2.13** clearly show the significant benefit of geocell reinforcement in stabilizing the KR-II sand. **Figure 4.2.13** also shows that the AB-3-I and QW-I bases had the similar performance under the repeated loading, which was much better than the reinforced KR-II sand. It is worth pointing out that since QW-I is more sensitive to moisture than AB-3-I, it may behave differently from AB-3-I when they are saturated. Further research is needed to evaluate their behavior under a saturated condition.

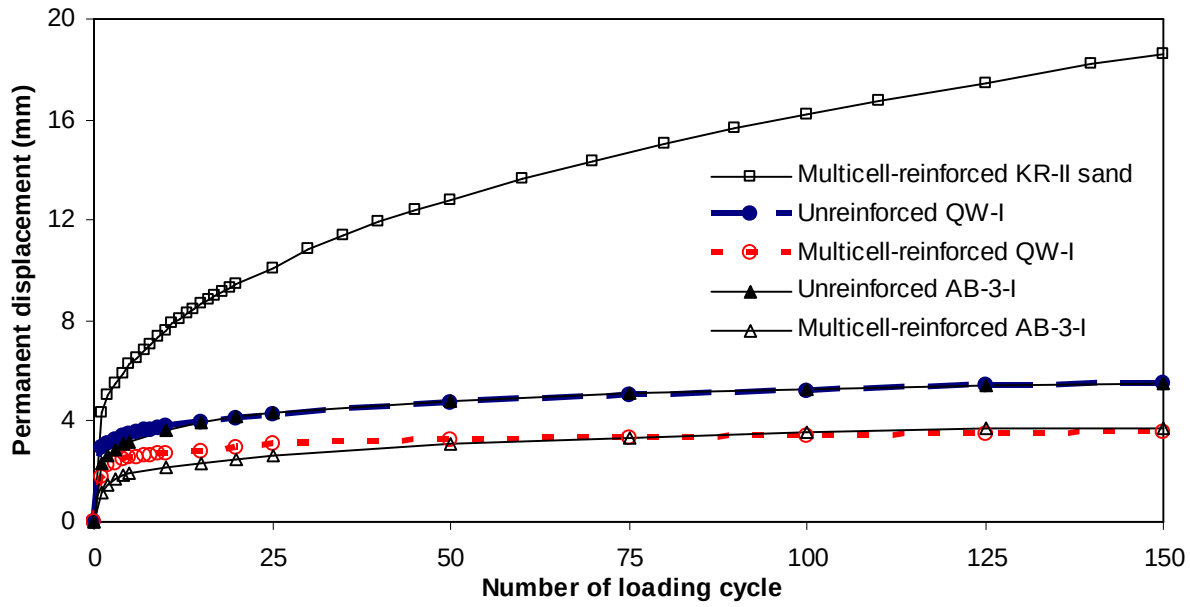

Figure 4.2.13 Comparison of permanent deformations under 552 kPa repeated loading

4.2.4 Elastic deformation

The elastic deformations of unreinforced and single NPA Type II geocell-reinforced sections with the number of loading cycles are plotted in **Figure 4.2.14** for QW-I and AB-3-I sections. The elastic deformation is the rebound of the base when unloaded from the maximum pressure to the zero pressure. The elastic deformations of multiple geocell-reinforced KR-II sand and unreinforced and multiple geocell-reinforced QW-I and AB-3-II sections are plotted in **Figure 4.2.15**. **Figure 4.2.14** shows that the single NPA Type II geocell-reinforced sections had higher elastic deformation than the respective unreinforced sections of QW-I and AB-3-I. The amount of elastic deformation was slightly high at the beginning but later stabilized to a constant value. In case of the multiple NPA Type II geocell-reinforced sections, it was almost constant after initial 10 cycles in the KR-II sand section; however, in case of QW-I and AB-3-I aggregate section it became fairly constant after 75 cycles.

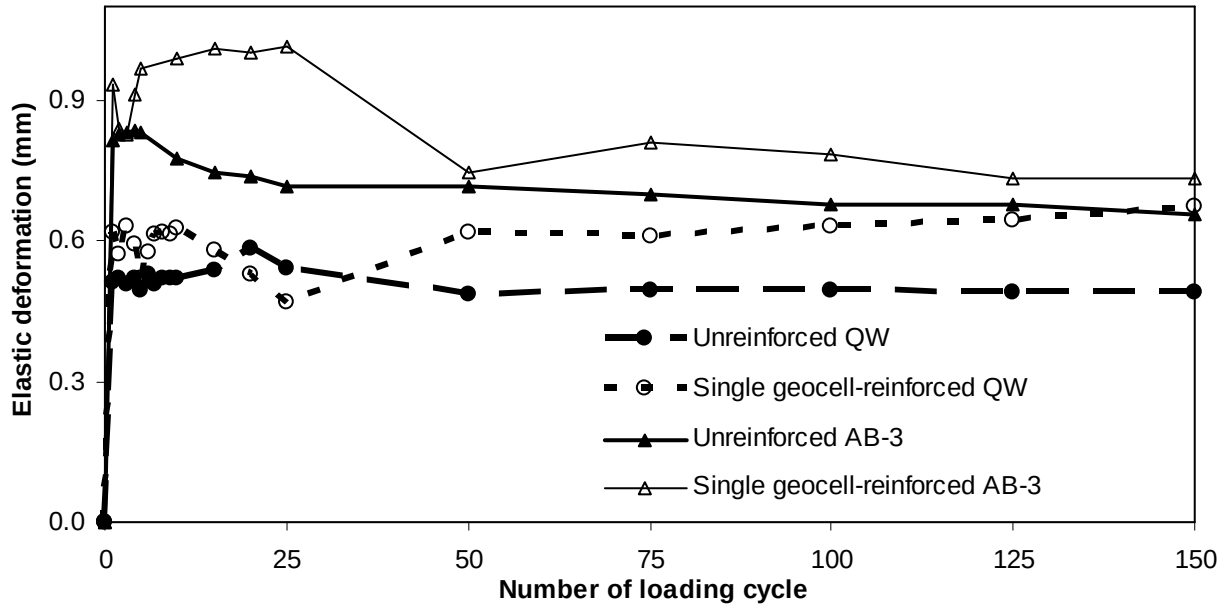

Figure 4.2.14 Comparison of elastic deformations of unreinforced and single geocell-reinforced QW-I and AB-3-I under 552 kPa repeated loading

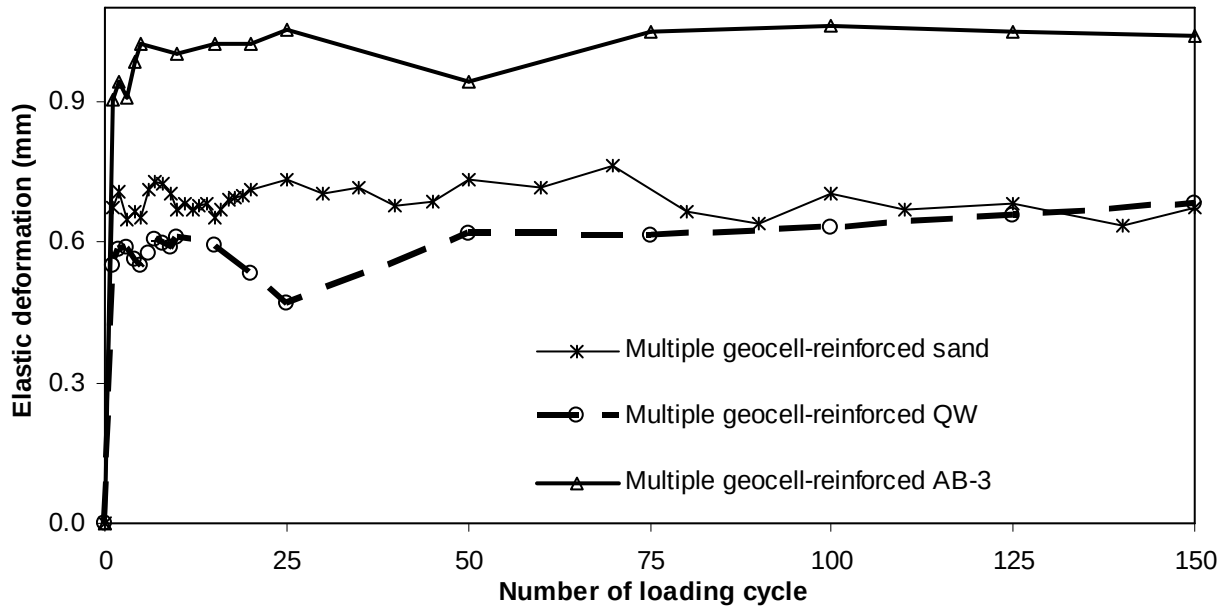

Figure 4.2.15 Comparison of elastic deformations of multiple geocell-reinforced K-II sand, QW-I, and AB-3-I bases under 552 kPa repeated loading

4.2.5 Percentage of elastic deformation

Figures 4.2.16 to **4.2.20** present the elastic deformation as a percentage of total deformation for all three materials: reinforced KR-II sand and both reinforced and unreinforced QW-I and AB-3-I bases. The percentage of elastic deformation was calculated by dividing the elastic deformation induced by each load cycle to the total deformation (i.e., the sum of elastic and plastic deformations) at that cycle.

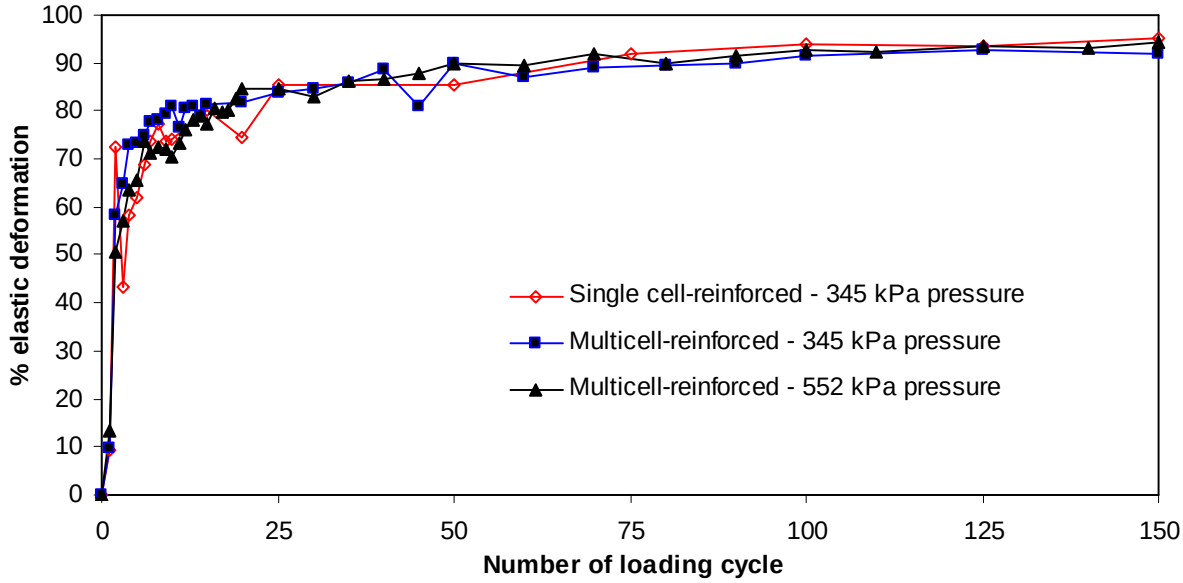

Figure 4.2.16 Percentage of elastic deformation of reinforced KR-II sands with loading cycles

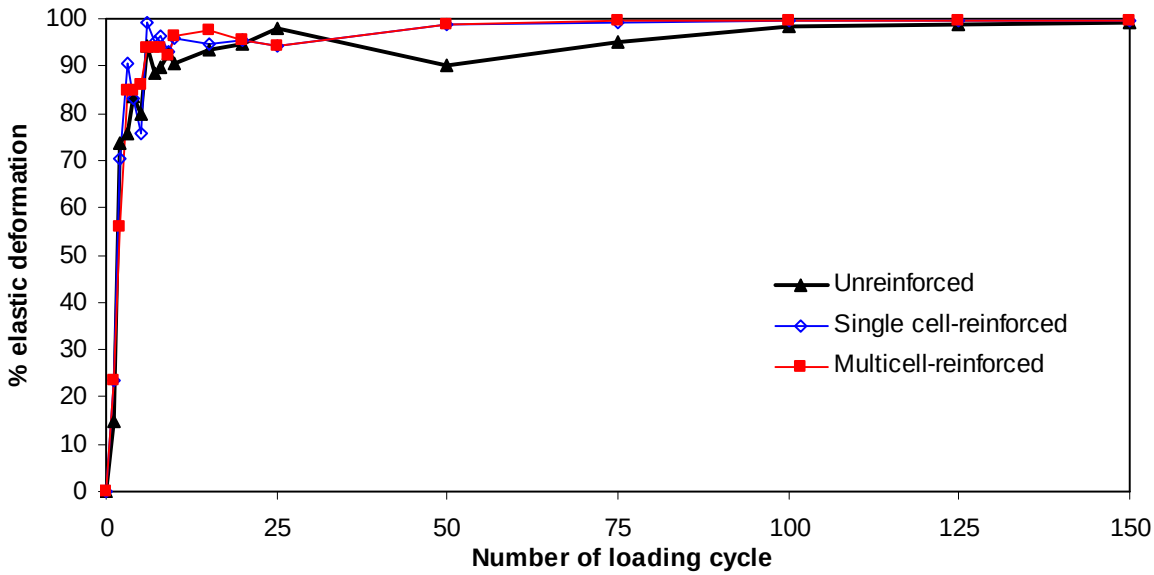

Figure 4.2.17 Percentage of elastic deformation of QW-I bases with loading cycles

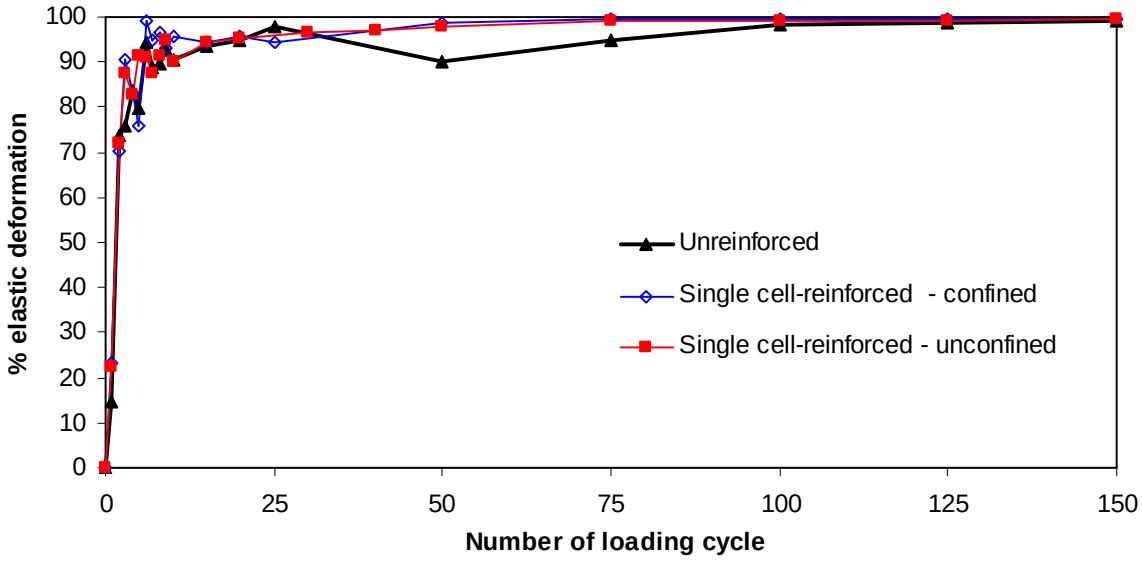

Figure 4.2.18 Percentage of elastic deformation of geocell-reinforced confined and unconfined QW-I bases with loading cycles

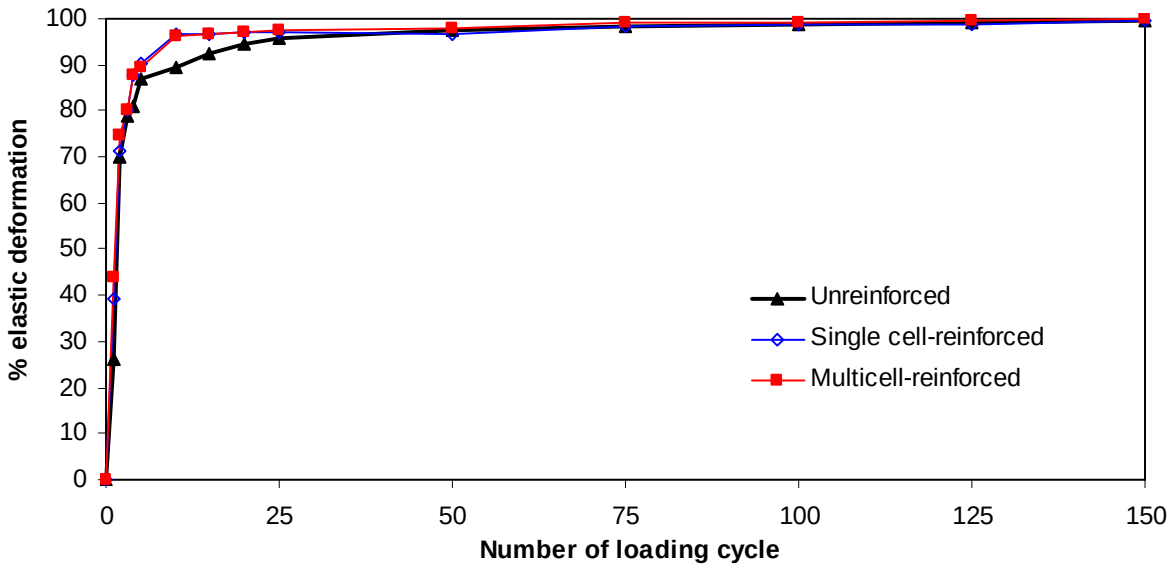

Figure 4.2.19 Percentage of elastic deformation of AB-3-I bases with loading cycles

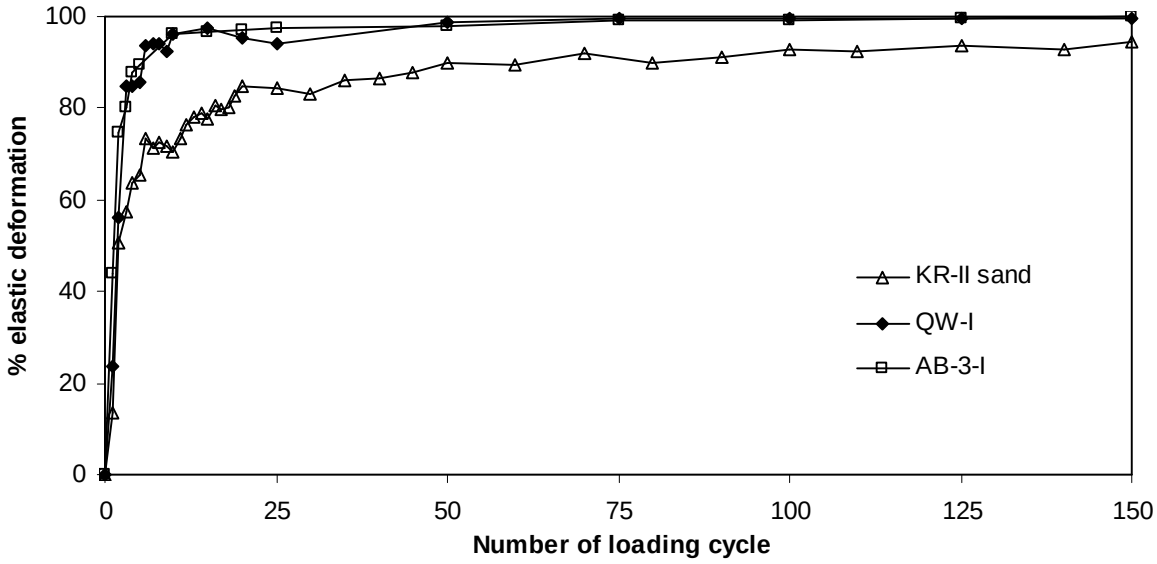

Figure 4.2.20 Percentage of elastic deformation of multiple geocell-reinforced bases with different infill materials under 552 kPa repeated loading

Figures 4.2.16 to **4.2.20** show that the percentage of elastic deformation for all the test sections increased with the number of the loading cycles. At the initial loading cycles, the plastic deformation was more pronounced, however, at around 10 cycles, the percentage of elastic deformation increased rapidly with the loading cycles and became relatively stable. After 10 cycles, the percentage of elastic deformation was more than 80% for the single NPA Type II geocell-reinforced KR-II sand and more than 95% for the NPA Type II geocell-reinforced QW-I and AB-3-I bases. At 150 loading cycles, the percentage of elastic deformation was 95.2% for the NPA Type II geocell-reinforced sand and more than 99% for the NPA Type II geocell-reinforced QW-I and AB-3-I bases. The higher percentage of elastic deformation is desirable for a longer service life of a pavement section. **Figures 4.2.16** to **4.2.20** show that geocell reinforcement increased the percentage of elastic deformation in the reinforced section as compared with the unreinforced section, especially for the sections with the KR-II sand base.

4.2.6 Traffic benefit ratio

The benefit of geocell reinforcement for extending pavement life can be evaluated using a Traffic Benefit Ratio (TBR). TBR is defined as the ratio of the number of cycles necessary to reach a given rut depth (i.e., the permanent deformation herein) for a geocell-reinforced test section to that for an unreinforced section at the same rut depth with the same section thickness and properties. The base thickness in all the test sections was 12 cm and the subgrade in the present test was a hard wood surface. Past research on other geosynthetic-reinforced bases showed that the TBR values depended on the level of permanent deformation. Since the permanent deformations of most base sections at the end of 150

loading cycles in this study were less than 4 mm, the TRB values were calculated at the permanent deformation of 3 mm. Since the unreinforced KR-II sand failed under static loading before the maximum pressure was applied, the number cycle required to reach a permanent deformation of 3 mm would be less than 1. Therefore, although the benefit of geocell reinforcement in the weak and poorly-graded KR-II sand could be very high, the TBR values for KR-II sand sections could not be calculated. **Table 4.2.1** presents the TBR values for single and multiple geocell-reinforced sections having different infill material. The TBR values were 8.0 for single geocell-reinforced QW-I, 12.0 for multiple geocell-reinforced QW-I, 8.5 for single geocell-reinforced AB-3-I, and 12.5 for multiple geocell-reinforced AB-3-I. The NPA Type II geocell-reinforced QW-I and AB-3-I bases had comparable TRB values. It should be pointed out that these TRB values were calculated to demonstrate the benefit of geocell reinforcement in pavement life, but they should not be used for design directly because actual pavement sections may be much different from the base sections in this study, for example, the bases in this study were on a firm subgrade.

Table 4.2.1 Traffic benefit ratio (TBR)

Infill material	Reinforcement type	Maximum applied pressure (kPa)	TBR compared with unreinforced case
KR-II sand	Single geocell	345	na
KR-II sand	Multi Geocell	345	na
KR-II sand	Multi Geocell	552	na
QW-I	Single geocell	552	8.0
QW-I	Multi Geocell	552	12.0
AB-3-I	Single geocell	552	8.5
AB-3-I	Multi Geocell	552	12.5

4.2.7 Summary

This section presented the results of experimental work conducted to investigate the behavior of NPA geocell-reinforced bases under repeated loading. The reinforced and unreinforced base courses with three different infill materials, Kansas River sand (KR-II sand), quarry waste (QW-I), and AB-3-I aggregates were tested under repeated loading. The experimental investigations included the effect of infill material on the performance of geocell-reinforced granular bases. The following points summarize the findings from the medium-size repeated plate loading tests.

1. NPA geocell reinforcement significantly reduced the permanent deformation after 150 cycles of loading irrespective of whether the infill material was weak or strong.
2. In case of KR-II sand after 150 loading cycles, the permanent deformation of the NPA geocell-reinforced sections was reduced by a great margin compared with the unreinforced section.
3. In case of single geocell-reinforced QW-I bases, the permanent deformation of the unreinforced section after 150 loading cycles was 50% more than that of the reinforced section. In case of AB-3-I it was 33%. Multiple geocell-reinforced sections reduced the deformation by 55% in case of QW-I and 40% in case of AB-3-I. TBR values were calculated as 8.0 and 12.0 for the single geocell-reinforced and multiple geocell-reinforced QW-I sections, respectively. Single geocell-reinforced and multiple geocell-reinforced AB-3-I sections had the TBR values of 8.5 and 12.5, respectively.
4. NPA geocell reinforcement reduced the plastic deformation in all the cases but the percentage of elastic deformation was higher in case of stronger infill materials (QW-I and AB-3-I) compared to the weaker material (KR-II sand). The improvement compared to the unreinforced case was more evident at the initial loading cycles.

5. In case of NPA geocell-reinforced KR-II sand, 80% of the total deformation was elastic after just 10 loading cycles and it reached above 95% after 150 loading cycles. In case of geocell-reinforced QW-I and AB-3-I bases, the elastic deformation after 10 cycles was above 95% over the total deformation and reached more than 99% after150 cycles. The KR-II sand had a lower percentage of elastic deformation as compared with the unreinforced and reinforced QW-I and AB-3-I bases due to its poor gradation, sub-rounded particles, and no apparent cohesion. The reinforced QW-I and AB-3-I had a higher percentage of elastic deformation than the unreinforced one due to the contribution of the NPA geocell.

CHAPTER FIVE

LARGE-SCALE PLATE LOADING TESTS

Cyclic plate loading tests were performed in a large-scale testing box (2.2 m x 2.0 m x 2.0 m high) at the University of Kansas. A total of three unreinforced and four NPA geocell-reinforced AB-3-1 sections and one unreinforced and three NPA geocell-reinforced KR-I sand over weak subgrade were investigated.

5.1 Equipments

5.1.1 The large geotechnical testing box

Figures 5.1.1 and **5.1.2** show the picture and details of the large geotechnical testing box. The box made of steel was fabricated at the geotechnical laboratory of KU. Three sides and the base of the box were fixed while the front side of the box had detachable steel channel sections of height 15 cm fixed with nuts and bolts. The detachable channel sections allowed the construction of variable thickness of the base course. The size of the box was 2.2 m x 2 m x 2 m (L x B x H). Half of the depth (1 m) of the box was be filled up by subgrade soil, the thickness of base courses varied depending upon test sections (15 cm, 23 cm, and 30 cm). The subgrade, a mixture of KR-I sand and kaolin, was prepared at about 2% CBR. Two different base materials, AB3-I and KR-I sand, were used in this study. For the AB-3-I base courses, the target CBR value was 20% while for KR-I sand base courses, the target density was 70% relative density.

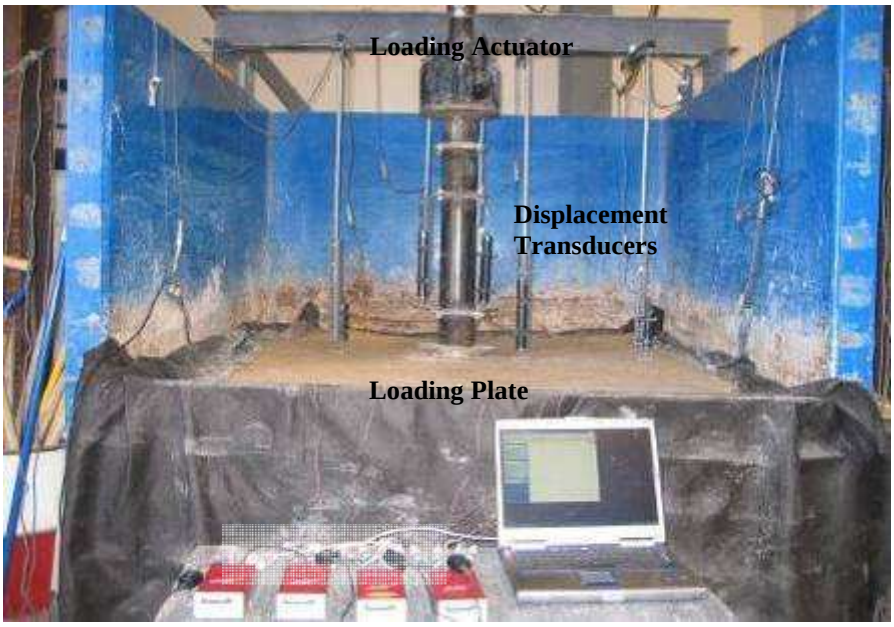

Figure 5.1.1 Large geotechnical testing box, loading actuator, and data acquisition system

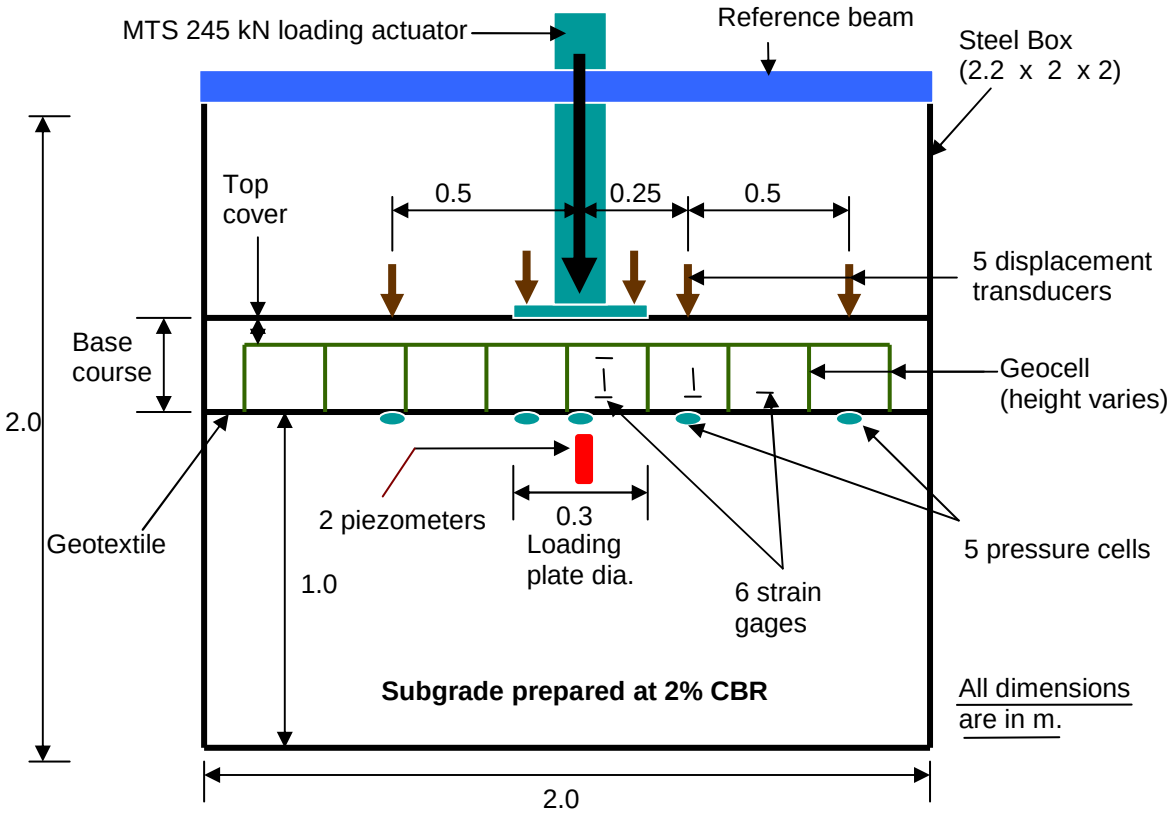

Figure 5.1.2 Schematic drawing of the large geotechnical testing box

5.1.2 MTS loading system

A servo hydraulic MTS loading system consisting of a loading frame, a hydraulic actuator, and a servo-control unit connected to both a data acquisition system and a hydraulic control valve was used to apply a cyclic load on test sections in the large geotechnical testing box. The load actuator has a 55 kip (245 kN) capacity. The cyclic load was applied to a loading plate using a computer-controlled servo hydraulic actuator, with a maximum load of 40 kN (corresponding a loading pressure of 80 psi or 552 kPa) and a minimum on 0.5 kN. The load form was applied at a frequency of 0.77 Hz as shown in **Figure 3.2.3**. MultiPurpose TestWare (MPT) software was set up to control and acquire the applied load data as well as the deformation data at the center.

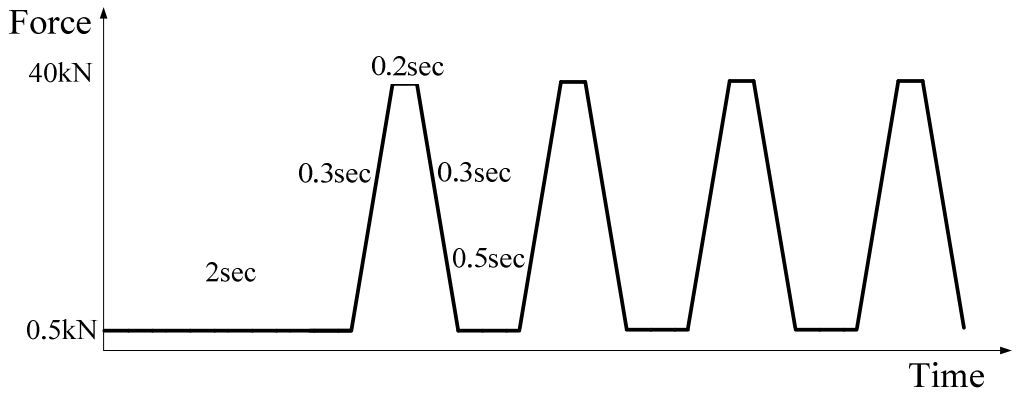

Figure 5.1.3 Cyclic loading wave form

The loading plate was connected to the actuator with arrangement as shown in **Figure 5.1.1.** **Figure 5.1.4** shows the details of the loading steel plate. The loading plate had a

diameter of 0.304 m. The steel plate was 40 mm thick including a 10 mm thick rubber base attached at the bottom to simulate rubber tire contact.

Figure 5.1.4 Picture of the loading plate

5.1.3 Data acquisition system and sensors

a) Data Recorders

The MultiPurpose TestWare (MPT) software, flexible testing software for MTS servo-hydraulic control systems, was used to apply a load, design a loading pattern, and set a displacement limit and the number of loading cycles. The MPT software was set to record applied loads and displacements at the center of the loading plate up to a total of 8,000 cycles or the maximum displacement of 85 mm whichever came first in this study. However, the measurement of stresses at the base course and subgrade interface, the displacements, pore water pressures in the subgrade, and strains in the geocell walls were made by pressure cells,

displacement transducers (LVDT), piezometers, and strain gages, respectively and recorded in external smart dynamic strain data recorders.

Four separate data recorders (smart dynamic strain recorder DC-204R) were used to record the data from all the strain gage type sensors. One of the smart dynamic strain recorders was used as a master recorder and other three served as slaves and were synchronized with the master recorder. Each of the recorders had four connection ports to the transducers. **Figure 5.1.5** shows the picture of the data recorders.

Figure 5.1.5 Picture of the data recorders

b) Earth Pressure cells

Five earth pressure cells were installed at the interface between the base and the subgrade during each test. The pressure cells used in the large box tests are shown in **Figure 5.1.6**. The portable pressure cells, KDE-500KPA, used in these tests were made of stainless steel, had a thickness of 11.3 mm, an outer diameter of 50 mm with the sensing area diameter of 46 mm, and total weight of 160 g. The pressure cells were strain gauge-type pressure cells having maximum capacity of 500 kPa, which is suitable for earth pressure measurements under dynamic loading. It had minute displacement of pressure-sensitive area due to double diaphragm structure and non linearity of 1% RO (random occurrence). The earth pressure cells were placed on the top of the subgrade before placing the base course. They were all aligned in a straight line passing through the center of the box along the width of the box as shown in **Figure 5.1.2**. Two pressure cells were placed under the loading plate, one at the center and one at the edge of the plate (12.5 cm away). Three other pressure cells were placed at 25 cm, 50 cm, and 75 cm away from the center.

c) Displacement transducers

Two displacement transducers CDP-50 and CDP-100 were used for the displacement measurement. The CDP-50 had capacity = 50 mm, sensitivity = 200 με/mm, non linearity = 0.1% random occurrence, spring force = 3.4 N, frequency response = 6 Hz, and weight = 270 g. The CDP-100 had capacity = 100 mm, sensitivity = 100 με/mm, non linearity = 0.1% random occurrence, spring force = 4.9 N, frequency response = 3 Hz, and weight = 580 g. The temperature range for both the transducers was -10^0 C to $+60^0$ C, recommended working voltage 2 V, maximum allowable voltage 10 V, and input output resistance 350 Ω.

(a) Before test **(b)** After test

Figure 5.1.6 Earth Pressure cell KDE 500 kPa

Figure 5.1.7 shows the displacement transducers used in the tests. These transducers were strain gauge-type sensors and had two maximum measurement ranges: two of them with 10 cm range placed at the center on the loading plate, one with 10 cm range placed a 25 cm away from the center, and one each of 5 cm range placed at 50 cm and 75 cm away from the center of the loading plate. Those placed away from the center were directly placed on small steel plates seated on the top of the base course. All the transducers were suspended from the reference beam fixed at the top of the large geotechnical testing box as shown in **Figure 5.1.2**. They were all aligned in a straight line along the width of the box and positioned exactly above the pressure cells placed at the subgrade-base course interface.

d) Strain gages

Figure 5.1.8 shows the strain gages used in the tests. Half-square grid general purpose strain gages were used in these tests. The strain gages had grid resistance of 120.0± 0.6 Ohms, grid length of 6.35 mm, and grid width of 3.18 mm.

Figure 5.1.7 Displacement transducer

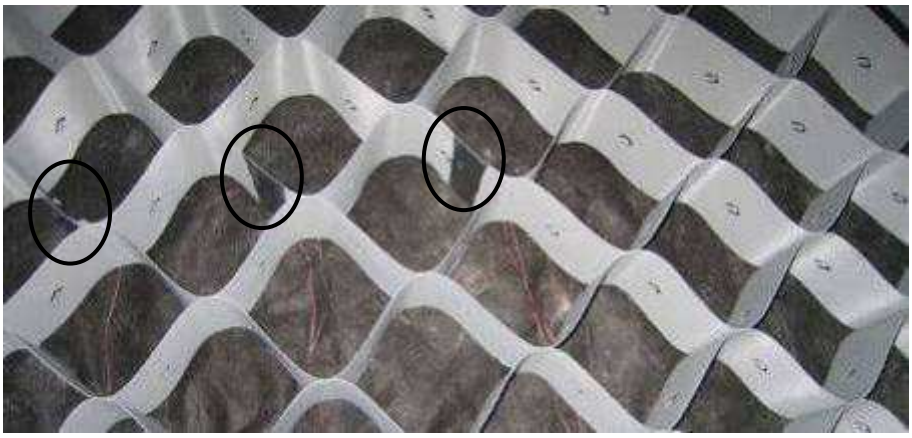

Figure 5.1.8 Strain gauge

e) Piezometer

Figure 5.1.9 shows the piezometer used in the first two tests. Two piezometers with strain gauge type-sensors with a maximum capacity of 500 kPa were used. However, since no conclusive relationship between the measured pore pressure and the cyclic loading could be established in the first two tests, they were not used in the later tests.

Figure 3.3.9 Piezometer

5.1.4 Vane shear

The hand-operated vane shear device shown in **Figure 5.1.10** was used to control the subgrade CBR value during subgrade preparation and before placing the base course. For the vane shear test, ASTM D2573-08 standard was followed. As an exact undrained shear strength value of 41 kPa corresponding to 2.0% CBR was difficult attain. A CBR value between 1.75% (35.9 kPa) and 2.10% (43.1 kPa) was accepted while preparing the subgrade.

A relationship between the undrained shear strength (c_u) in kPa and the CBR (%) value of the subgrade material was established by unconfined compression tests and laboratory CBR tests. The relationship is given in **Equation 5.1.1**.

$$CBR\,(\%) = \frac{c_u}{20.5}$$ **Equation 5.1.1**

Figure 5.1.10 Vane shear test

5.1.5 Dynamic cone penetrometer (DCP)

DCP tests were carried out at different stages of the test. In the first few tests it was used to verify the stiffness and strength of the subgrade and base course before and after the test. However, as the vane shear tests gave good results during subgrade preparation and sand cone tests were conducted to verify the density of base materials during the forensic examinations in the later tests, DCP tests were conducted to measure the CBR value of the

base course only before the test on test-ready sections. **Figure 5.1.11** shows the DCP equipment and operation. The ASTM D6951-03 standard was followed for DCP tests. The relationship between the CBR value at the depth of penetration and the penetration in inches per blow of DCP is given in **Equation 5.1.2** (Webster et al., 1992).

$$CBR(\%) = \frac{292}{(PI \times 25.4)^{1.12}} \qquad \textbf{Equation 5.1.2}$$

where PI = Penetration Index (in/blow) calculated based on the penetration per each blow.

The DCP tests were conducted at least four locations immediately before running each plate loading test so they are more representative of the final subgrade and base conditions than the vane shear tests because the vane shear tests were conducted before the placement of base courses. Therefore, in the analysis of the results of all the tests, DCP test data are used. The analysis showed minor differences in the CBR values obtained from DCP and vane shear tests for the subgrade. As the compacted base course was allowed to stay for about 24 hours before each test, the differences in the CBR values obtained from the vane shear (24 hours before) and DCP may have been caused by the result of compaction of the base course and/or the dissipation of pore water pressure over that time.

Figure 5.1.11 Dynamic cone penetration (DCP) test

5.1.6 GeoGauge

GeoGauge was used to monitor the preparation of subgrade and base courses during the first test. The GeoGauge used in these tests is shown in **Figure 5.1.12**. It was used to measure the stiffness of the base course and the subgrade. However, the test results were not consistent due to the difficulty in seating this device properly on the subgrade and base courses, so it was discarded after the first test.

5.1.7 Sand cone

Sand cone tests were performed to measure the density of compacted base course during the forensic investigation. The ASTM D1556–07 standard was followed for sand cone tests. **Figure 5.1.13** shows the picture of sand cone test being carried out on the base course after the plate loading test.

Figure 5.1.12 GeoGauge

Figure 5.1.13 Sand cone test

5.2 Test Preparation

5.2.1 Subgrade

In the test box a subgrade with target CBR value of 2% was prepared by mixing 75% KR-I sand and 25% kaolin. The subgrade material was prepared at 11.4% moisture content corresponding to 2% CBR (**Figure 3.3.4**). **Figure 5.2.1** shows the mixing of subgrade material and filling the box. The subgrade was prepared in two zones. The lower zone was 40 cm thick and compacted in two lifts (20cm thick each lift) and was not replaced during the whole study. The upper zone was 60 cm and compaction of the subgrade in this zone was done at 15 cm lifts with a total of 4 layers. The subgrade in the upper zone was replaced and re-compacted after each test. A mechanical vibratory plate compactor (**Figure 5.2.2**) was used for the compaction. Manual hand tamp (20 cm x 20 cm) was used at the corners of the box. The quantity (weight) of subgrade material for each 15 cm lift was calculated based on the density of the subgrade material at 11.4% moisture content and the volume in the box for this lift thickness. The compaction was done until the filled volume of soil reached the target thickness of 15 cm. Vane shear tests were carried out after three passes of the compaction in each lift. The next layer was placed after the vane shear value was achieved within the range mentioned in **Section 5.1.4**.

Once the CBR value of the subgrade was found satisfactory, the earth pressure cells on the top of the subgrade and the piezometers at a depth of 25 cm below the top of subgrade were installed. A layer of geotextile was placed at the interface of subgrade and base course before installing the geocell in case of geocell-reinforced sections only.

(**a**) Mixing (**b**) Filling

Figure 5.2.1 Subgrade material mixing and filling in the box

Figure 5.2.2 Vibratory plate compactor

5.2.2 Base course

Bases courses with three nominal thicknesses of 15 cm, 23 cm, and 30 cm were tested for both reinforced and unreinforced cases. AB-3-I and KR-I sand were used as the base course materials in this study. However, only 15 cm and 23 cm thick sections of KR-I sand base course were tested for the unreinforced case because they were too weak to carry the cyclic load and failed in one cycle. The quantity (weight) of base course material for each lift of compaction was calculated by multiplying the density of the material by the volume of the box to fill. The target density was 95% the maximum density for AB-3a sections and 70% relative density for KR-I sections. The base course material was filled in the box as shown in **Figure 5.2.3**. The picture of the installed geocell with fixing rebar is shown in **Figure 5.2.4** and the layout of geocell in the big box is shown in **Figure 5.2.5**.

Figure 5.2.3 Placement of base course material

The compaction in case of the 15 cm thick unreinforced AB-3-I base course section was done using the vibratory compactor in a single lift (15 cm compacted), the 23 cm thick section in two lifts of 11.5 cm each, and the 30 cm thick section in two lifts of 15 cm each. In case of the reinforced section, the material was filled loose inside the geocell and first compacted by 56 blows of standard Proctor compaction hammer in each cell (**Figure 5.2.6**). Rest of the compaction including the fill cover was done using the vibratory compactor as in case of the unreinforced section. The AB-3-I fill was compacted at 8.9% moisture content while the KR-I sand base course was compacted at 5% moisture content.

Figure 5.2.4 Geocell installed above the subgrade

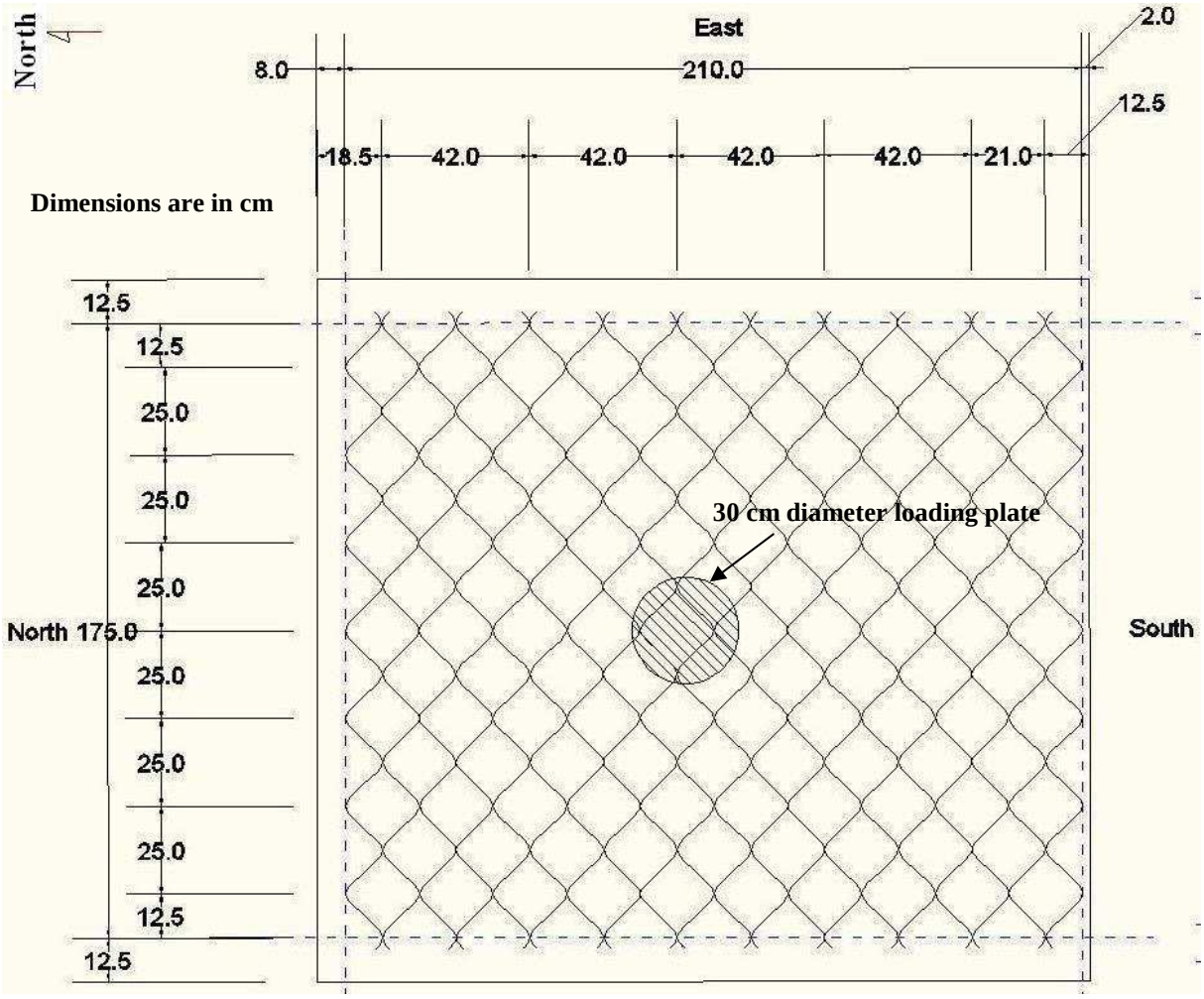

Figure 5.2.5 Plan view of the geocell layout in the big box

Figure 5.2.6 Hand compaction inside the cells

5.2.3 Test operation

The MTS hydraulic loading system as discussed in **Chapter 5.1.2** was used to apply the cyclic load on both unreinforced and reinforced bases. The cyclic loading waves were generated with a peak force of 40 kN and a trough force of 0.5 kN as shown in **Figure 5.1.3**. The instrumentation and data acquisition system included five earth pressure cells, five displacement transducers, six strain gages, and two piezometers (only used for the first two unreinforced sections).

Each cyclic plate loading test was run for a maximum displacement of 85 mm to allow sufficient margin for the rebound before a permanent deformation of 75 mm was reached. Although the MPT was set at the maximum loading cycle of 8,000, it has never been reached. All the tests stopped after the displacement limit of 85 mm was reached. All the sensor data were recorded in the smart dynamic strain recorders.

5.3 Cyclic Loading Test on AB-3-I Bases

A total of seven sections with AB-3-I base course material, that included four geocell-reinforced and three unreinforced sections, were tested. The detailed characteristics of the geocell, geotextile, subgrade, and base course materials ware discussed in **Chapter 3**. The details of test section preparation were provided in **Section 5.1**.

5.3.1 15 cm thick AB-3-I base sections

Three 15 cm thick AB-3-I base sections were tested, which included one unreinforced section and two geocell-reinforced sections. Both reinforced sections contained an infilled 10-cm high geocell and a 5-cm fill cover. The first test was carried out on the unreinforced section, followed by a reinforced section that was compacted in only one lift. The compaction in one lift with the vibratory plate compactor could not produce the desired degree of compaction for the reinforced base. To improve the degree of compaction, another 15 cm thick geocell-reinforced section was prepared in two lifts and tested. For the second reinforced section, the geocell was loosely filled and hand compaction was done in individual cells for the first lift. The remaining thickness (about half) of the base course was then compacted with the vibratory compactor. The desired degree of compaction was achieved in the second reinforced section in this way.

a) Vane shear, DCP, and sand cone tests

The results of the vane shear, DCP, and sand cone tests carried out on three test sections are given in **Table 5.3.1**. The vane shear tests were carried out before the placement

of base courses. The DCP tests were carried out after the base courses were placed and before the cyclic loading tests were started. The profiles of the calculated CBR values based on the DCP data are also shown in **Figure 5.3.1**. The average CBR values of the subgrades obtained from the vane shear tests in all three test sections were about 1.7%. The increase in the subgrade CBR values from the DCP tests may be because the measurement was taken one day after the compaction of the base course on top of the subgrade. Sand cone tests were carried out only in the reinforced sections after cyclic tests. The reinforced section compacted in a single lift had achieved only 87.3% compaction while the section compacted in two lifts achieved 94.3% compaction which is close to the target value of 95% compaction.

Table 5.3.1 Average CBR values from vane shear and DCP tests and relative compaction and moisture from sand cone tests

Test section	**Vane shear (subgrade) CBR (%)**	**DCP (subgrade) CBR (%)**	**DCP (base course) CBR (%)**	**Sand cone after test (base course)**	
				Relative compaction (%)	**Moisture content (%)**
Unreinforced	1.70	2.06	14.0	-	-
Reinforced (compacted in single lift)	1.76	2.6	13.0	87.3	9.07
Reinforced (compacted in two lifts)	1.68	2.7	20.4	94.3	8.85

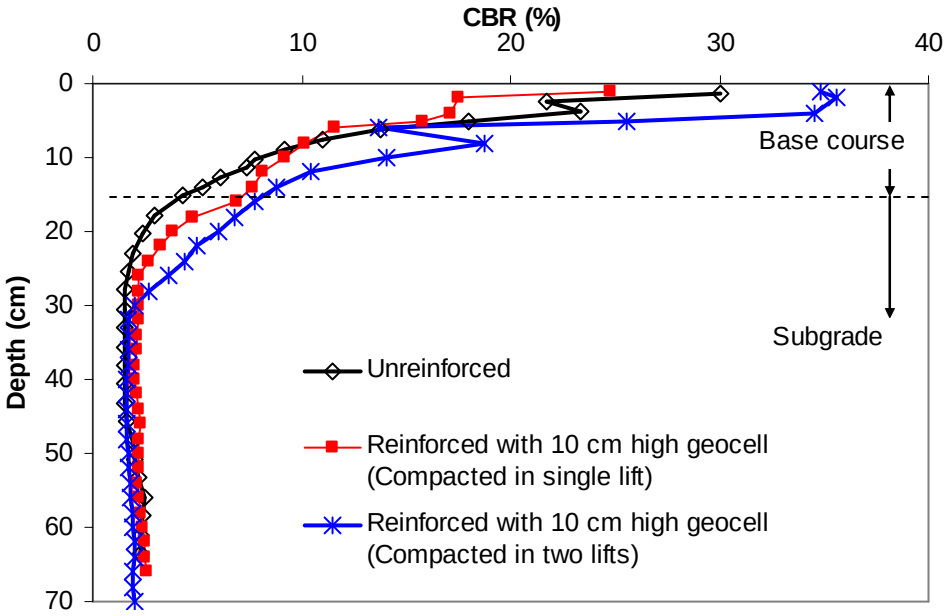

Figure 5.3.1 CBR profiles obtained from the DCP tests in 15 cm thick AB-3-I bases over weak subgrade

b) Deformed profiles

The failure criterion was set as 75 mm of permanent deformation of the base course. Failure occurred at 35 cycles for the unreinforced section, 73 cycles for the 10 cm high geocell-reinforced section with single lift compaction, and 126 cycles on the 10 cm high geocell-reinforced section with two-lift compaction. After the cyclic loading tests, all the test sections were exhumed and trenches were cut to examine the deformed profiles and geocells. The deformed profiles are plotted in **Figures 5.3.2** through **5.3.4**. **Figure 5.3.2** shows that the deformation at the interface between the base and the subgrade in the unreinforced section was within a narrower range as compared with those in the reinforced sections. The inclusion of the geocell helped distribute the deformation to a wider area in the reinforced sections. **Figure 5.3.5** shows the crack lines developed on the surface of the reinforced base after the

test. In all reinforced sections, geocells were initially laid out at 25 cm long in the seam direction and 21 cm wide in the transverse direction. Forensic tests showed that the shape and size of the cells were intact outside the loading plate. However, around the area of the loading plate, the geocells tend to turn into a circular shape; the seam side was slightly reduced and the transverse direction slightly enlarged. Welds of the geocell located under the loading plate were broken at the bottom edges. The failure crack line and forensic examination showed that the geocell-reinforced sections behaved like a beam. The beam effect of the reinforcement is illustrated in **Figure 5.3.6**. The picture of the crack lines and the geocell weld failures are shown in **Figures 5.3.7** through **5.3.10**.

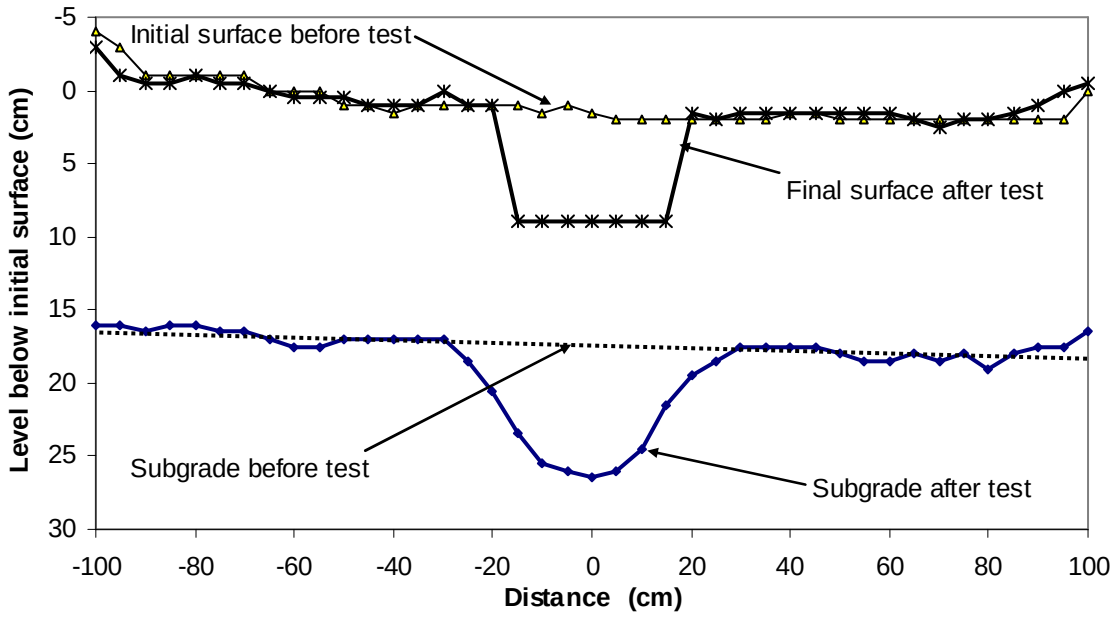

Figure 5.3.2 Profiles of the 15 cm thick unreinforced AB-3-I base section after 35 loading cycles

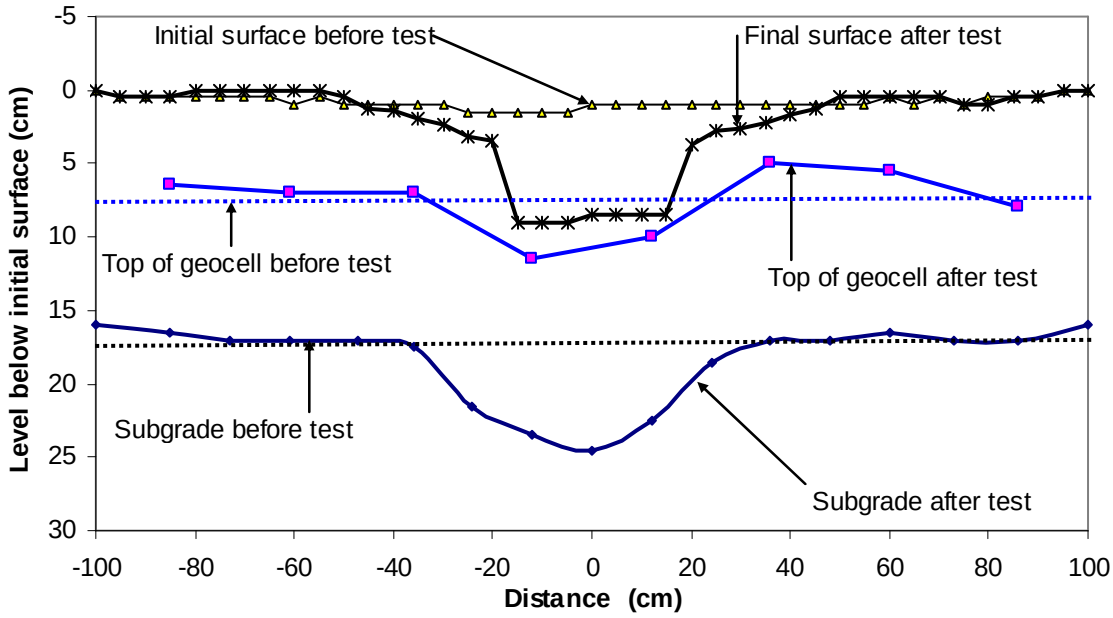

Figure 5.3.3 Profiles of the 10 cm high geocell-reinforced AB-3-I section after 73 loading cycles (the compaction of the base course was done in a single lift)

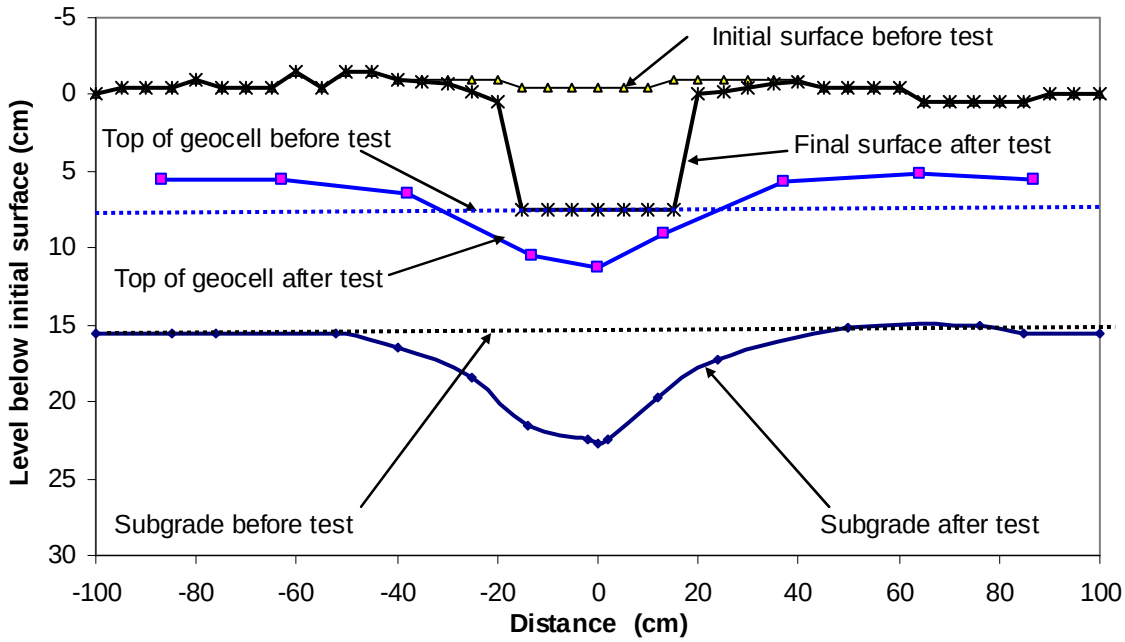

Figure 5.3.4 Profiles of the 10 cm geocell-reinforced AB-3-I base section after 126 loading cycles (the compaction of the base course was done in two lifts)

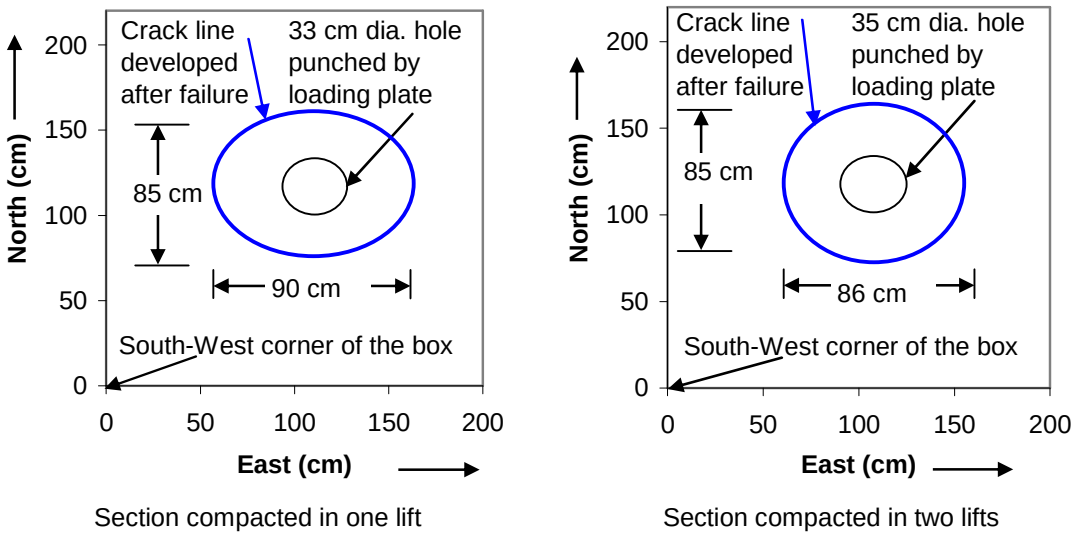

Figure 5.3.5 Surface failure patterns of the 10 cm high geocell-reinforced AB-3-I base course sections in plan

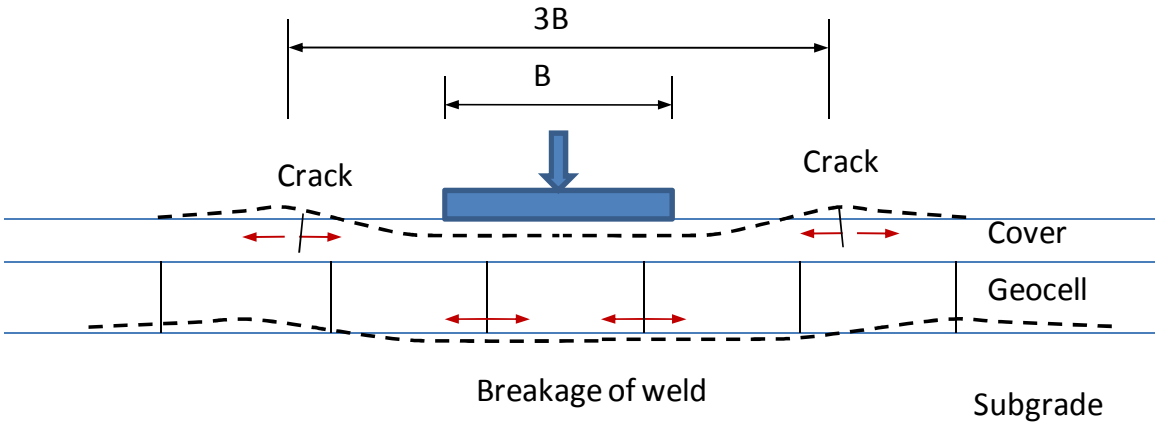

Figure 5.3.6 Beam effect observed in the geocell-reinforced sections

Figure 5.3.7 Cracks on the surface of the 10 cm high geocell reinforced AB-3-I section with single lift compaction

Figure 5.3.8 Weld failure under the loading plate observed after exhuming the section on the 10 cm high geocell reinforced section with single lift compaction

Figure 5.3.9 Cracks on the surface of the 10 cm high geocell reinforced section with two lift compaction

Figure 5.3.10 Weld failure under the loading plate observed after exhuming the section on 10 cm high geocell reinforced section with two lift compaction

c) Permanent deformation with number of loading cycles

Figures 5.3.11 through **5.3.14** show the permanent deformations at the center and 25 cm, 50 cm, and 75 cm away from the center of the loading plate at different loading cycles. In case of the unreinforced section, there was small amount of heave in all the locations away from the center. In the reinforced sections, compression was observed at 25 cm away from the center also. This phenomenon suggests that the load was distributed to a wider area in the reinforced sections.

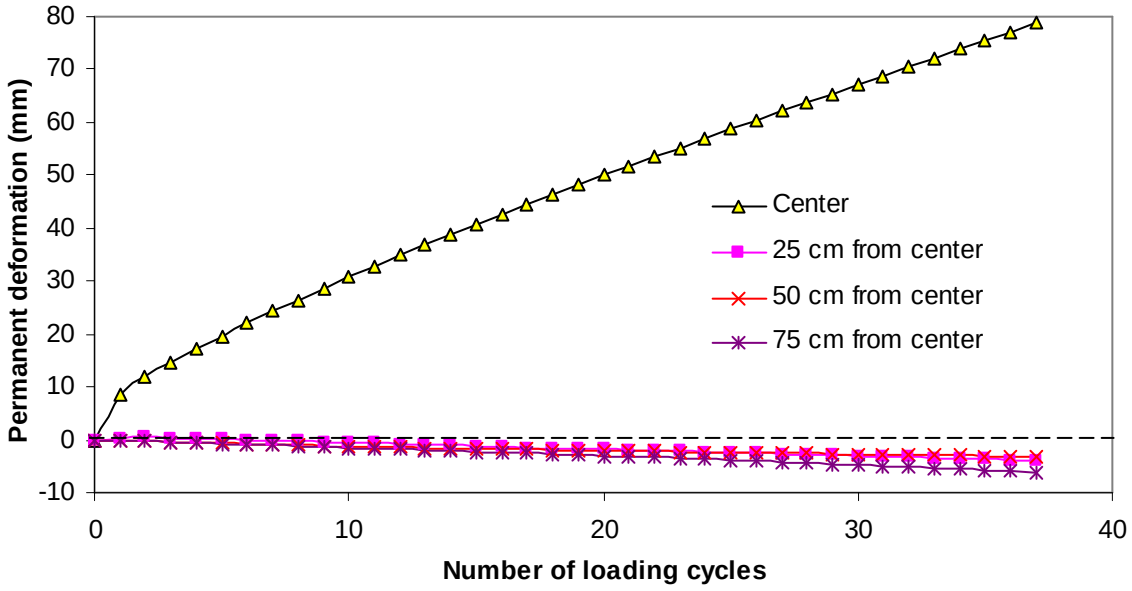

Figure 5.3.11 Permanent deformations versus the number of loading cycles for the 15 cm thick unreinforced AB-3-I base section

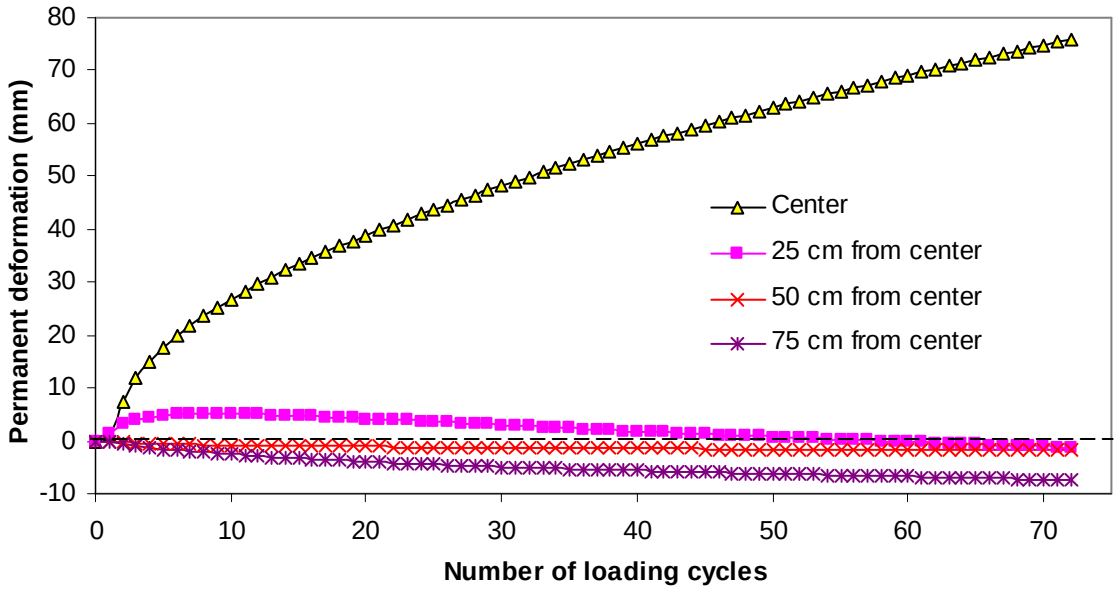

Figure 5.3.12 Permanent deformations versus the number of loading for the 10 cm high geocell-reinforced AB-3-I base section (the compaction of the base course was done in a single lift)

The comparison of permanent deformations under the loading plate in three tests is given in **Figure 5.3.14**. The benefit of geocell reinforcement is clearly evident from this comparison. For the maximum allowable permanent deformation of 75 mm, the unreinforced section lasted 35 cycles, the single lift compacted geocell-reinforced section lasted 71 cycles, and the two lift compacted geocell-reinforced section lasted 125 cycles. This result shows that the density of the base course had a significant effect on the performance of the geocell-reinforced bases and the NPA geocell reinforcement improved the performance of the section by a factor of 3.57 over the unreinforced section when a proper compaction of the base course was achieved.

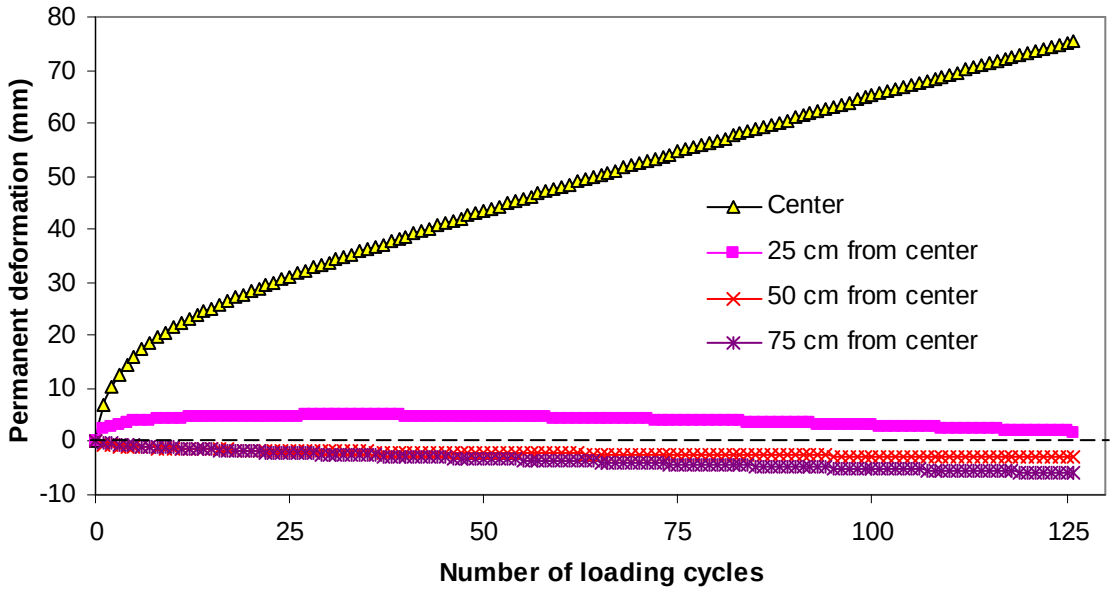

Figure 5.3.13 Permanent deformations versus the number of loading for the 10 cm high geocell-reinforced AB-3-I base section (the compaction of the base course was done in two lifts)

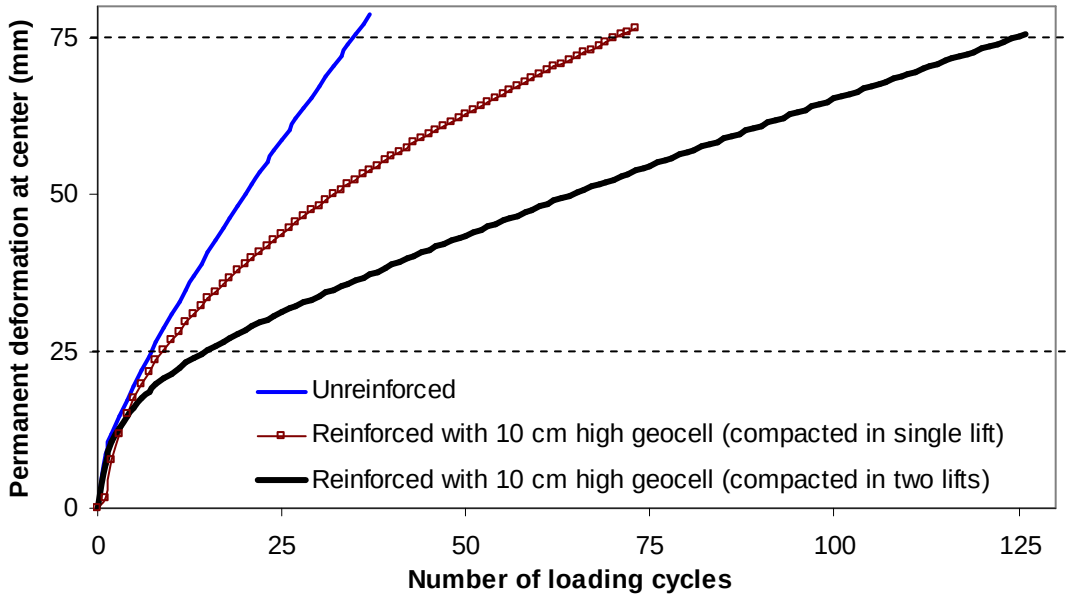

Figure 5.3.14 Comparison of the permanent deformations of unreinforced and reinforced sections at the center with 15 cm thick AB-3-I bases

Figure 5.3.15 shows the comparison of percentages of elastic deformation of three test sections at the center with 15 cm thick AB-3-I bases. The unreinforced section had only 55% of the total deformation each cycle as the elastic deformation at failure whereas the reinforced section had 95%. The plastic deformation was therefore found to decrease considerably in case of the reinforced sections.

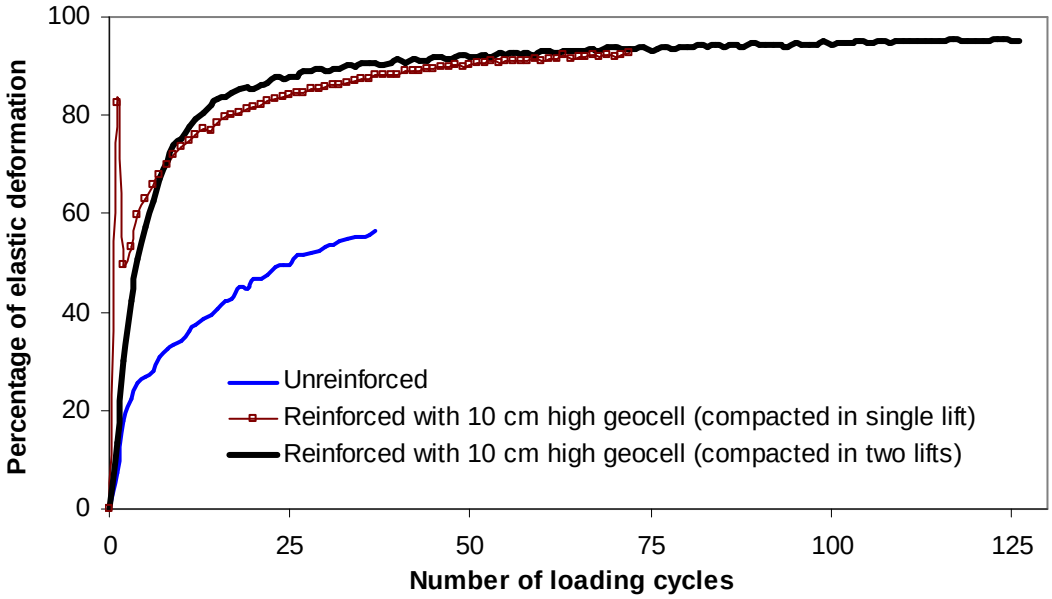

Figure 5.3.15 Percentage of elastic deformation of three test sections at the center with 15 cm thick AB-3-I bases

d) Measured vertical stresses at the subgrade-base interface

The vertical stresses at the interface of subgrade and base course were measured by the pressure cells located at five locations on a straight line passing through the center. **Figures 5.3.16** through **5.3.18** show the vertical stresses measured at the given locations with the number of loading cycles. There were some instances when one of those pressure cells

was broken. In such a case only the data from four cells are plotted at the given locations. Although the single lift-compacted NPA geocell-reinforced section failed at 73 cycles, the pressure cell located at the center did not respond after 33 cycles so the vertical stress data at the center are plotted up to 33 cycles. The measured maximum vertical stresses in all three sections occurred at the center with a magnitude of 237.6 kPa in the unreinforced section, 208 kPa in the reinforced section compacted in a single lift, and 133 kPa in the reinforced section compacted in two lifts. A comparison of the measured maximum vertical stresses under the center of the loading plate is shown in **Figure 5.3.19**. It is seen that the measured maximum vertical stresses were much lower than the applied pressure of 552 kPa on the surface. **Figures 5.3.16** and **5.3.17** also show that the measured vertical stress at the center increased with the number of passes, which is consistent with the design model proposed by Giroud and Han (2004a and b). Giroud and Han (2004a and b) considered the increase of the maximum vertical stress due to the deterioration of the base course. However, in case of the well compacted section (**Figure 5.3.18),** the maximum vertical stress started to decrease after 75 loading cycles because of the membrane effect of the reinforced base.

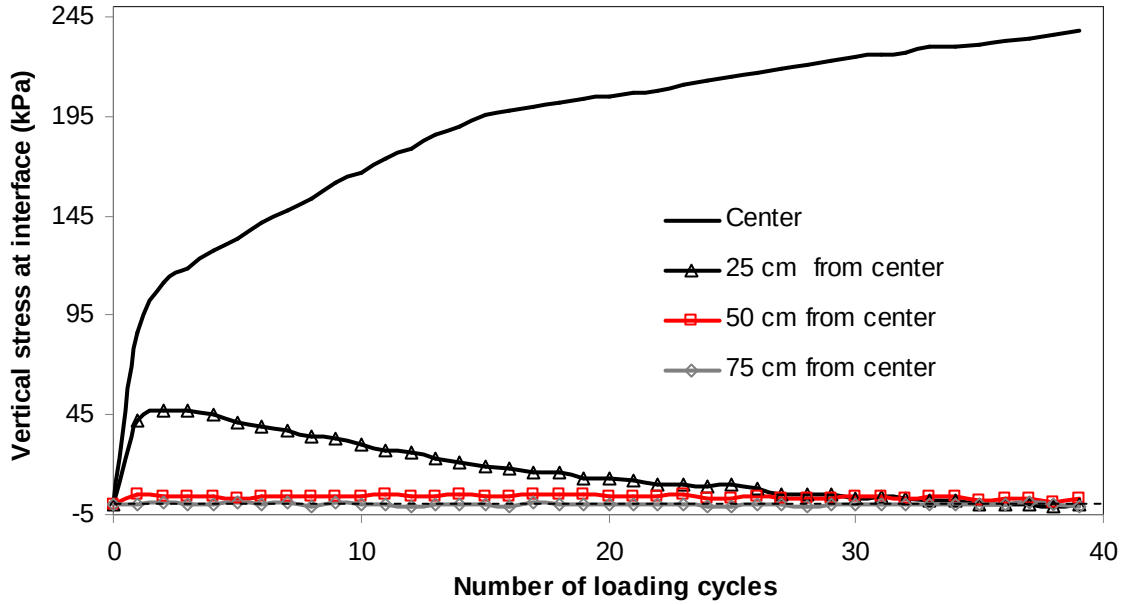

Figure 5.3.16 Measured vertical stresses at the subgrade-base interface in the 15 cm thick unreinforced AB-3-I base

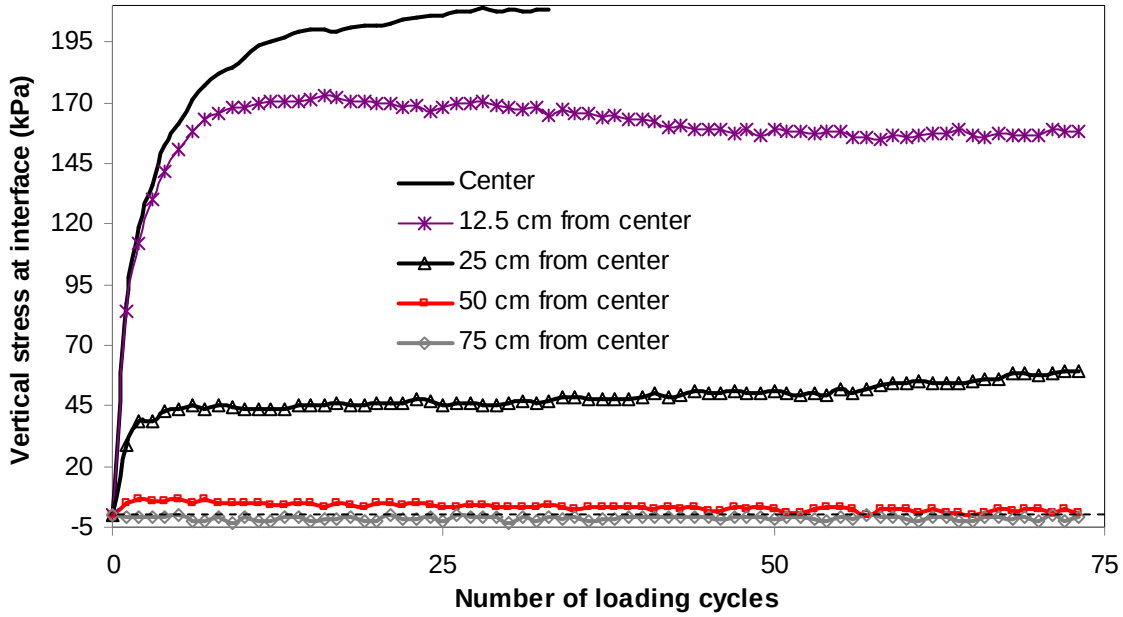

Figure 5.3.17 Measured vertical stresses at the subgrade-base interface in the 15 cm thick geocell-reinforced AB-3-I base with single lift compaction

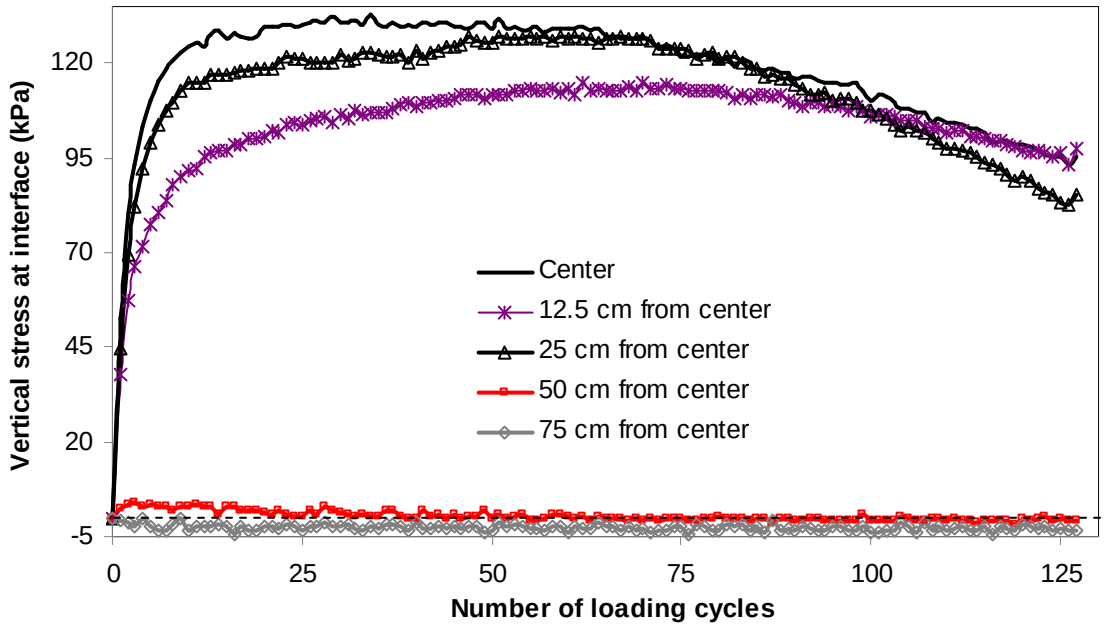

Figure 5.3.18 Measured vertical stresses at the subgrade-base interface in the 15 cm thick geocell-reinforced AB-3-I base with two lift compaction

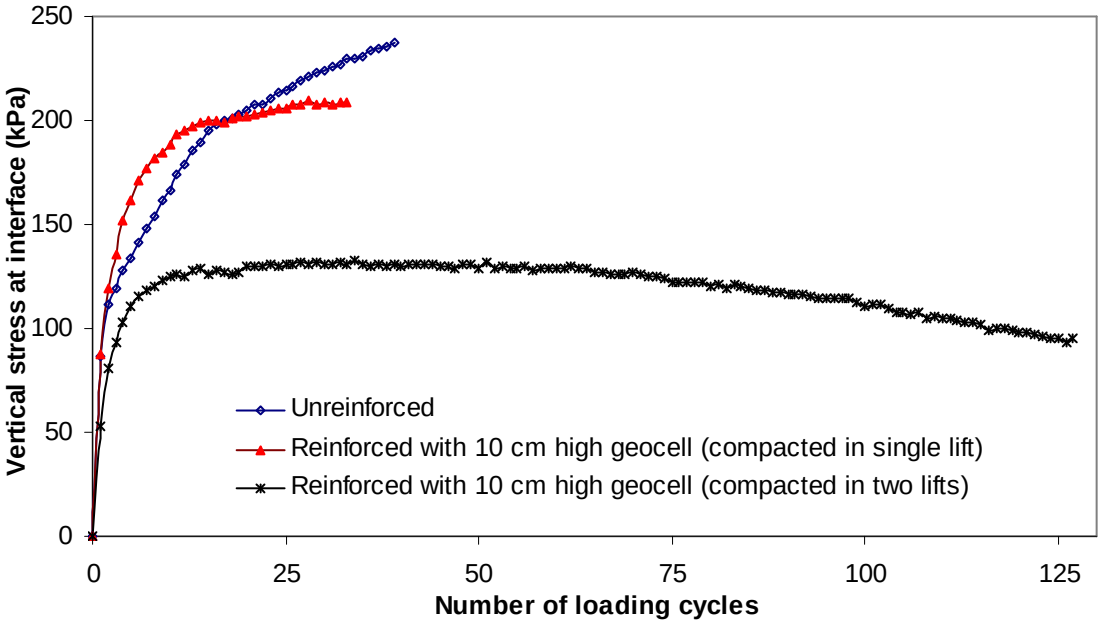

Figure 5.3.19 Comparison of the measured vertical stresses at the interface of subgrade and base at the center in three 15 cm unreinforced and reinforced AB-3-I bases

The comparison of the measured vertical stresses at the interface of subgrade and base at different locations away from center is shown in **Figure 5.3.20**. There is a significant difference in the measured vertical stresses over the number of loading cycles at 25 cm away from the center between the unreinforced and reinforced sections. The higher vertical stresses away from the center in the reinforced sections illustrate a wider stress distribution compared to the unreinforced section. The distributions of the measured vertical stresses at the first cycle, at the 39th cycle (i.e., the end of the test for the unreinforced section), and at the end of the tests for the unreinforced and reinforced sections are shown in **Figure 5.3.21**. This figure also shows a distinct difference in the stress distribution to the subgrade from the base course between unreinforced and reinforced sections. The NPA geocell-reinforced section showed a wider distribution as compared with the unreinforced section.

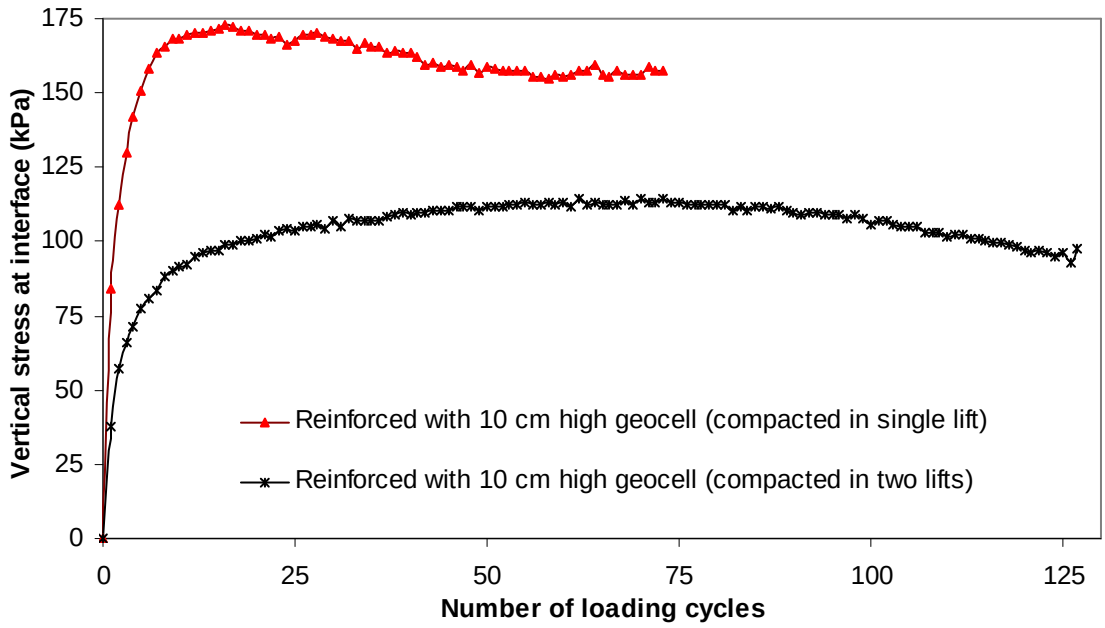

(a) 12.5 cm from the center

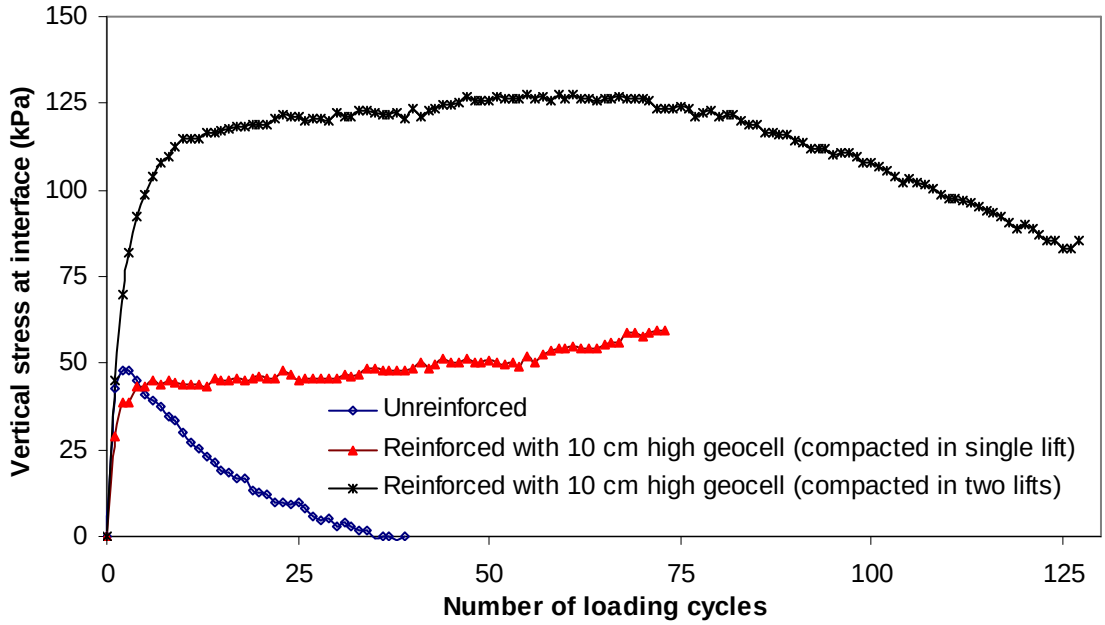

(b) 25 cm from the center

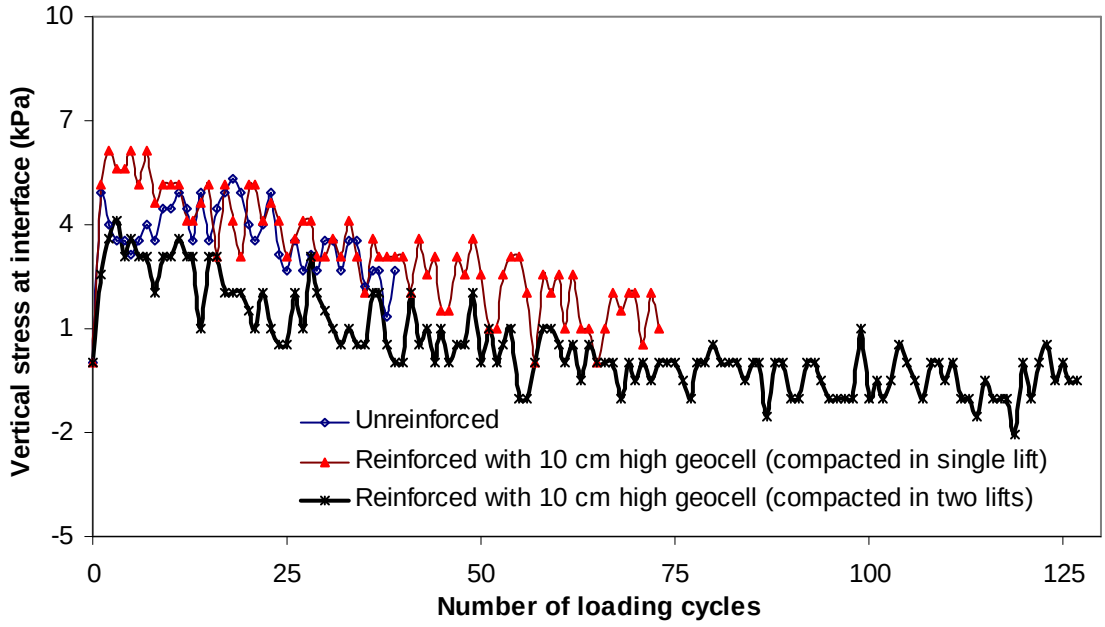

(c) 50 cm from the center

Figure 5.3.20 Comparison of the measured vertical stresses at the interface of subgrade and base at different locations away from the center in the 15 cm thick AB-3-I bases

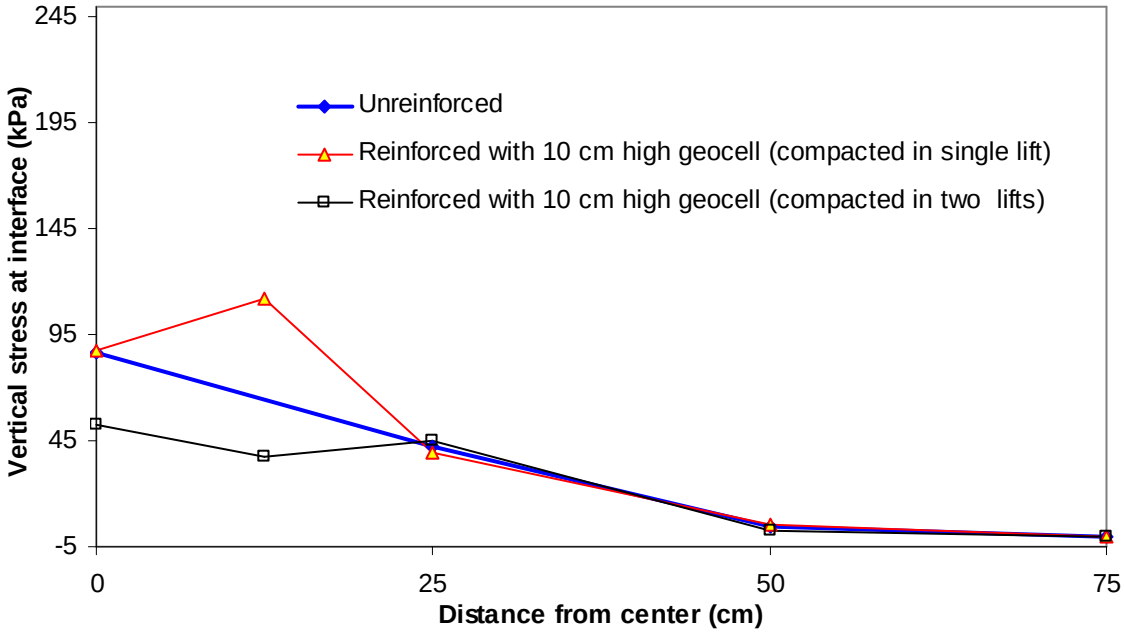

(a) Measured vertical stress at the interface at the end of first loading cycle

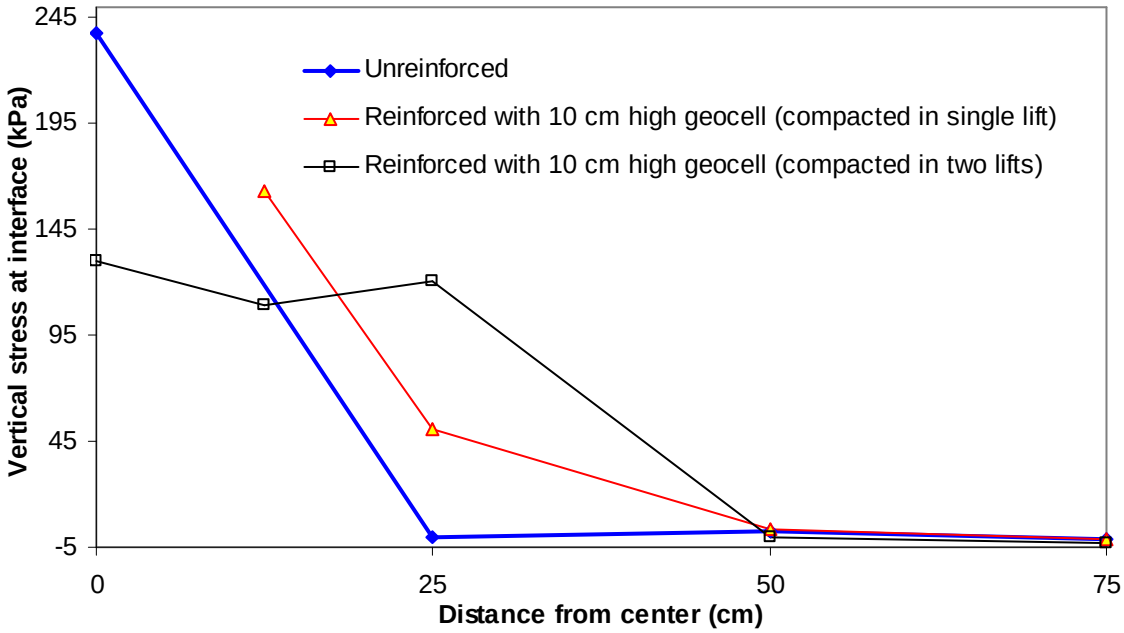

(b) Measured vertical stress at the interface at the end of 39 loading cycles

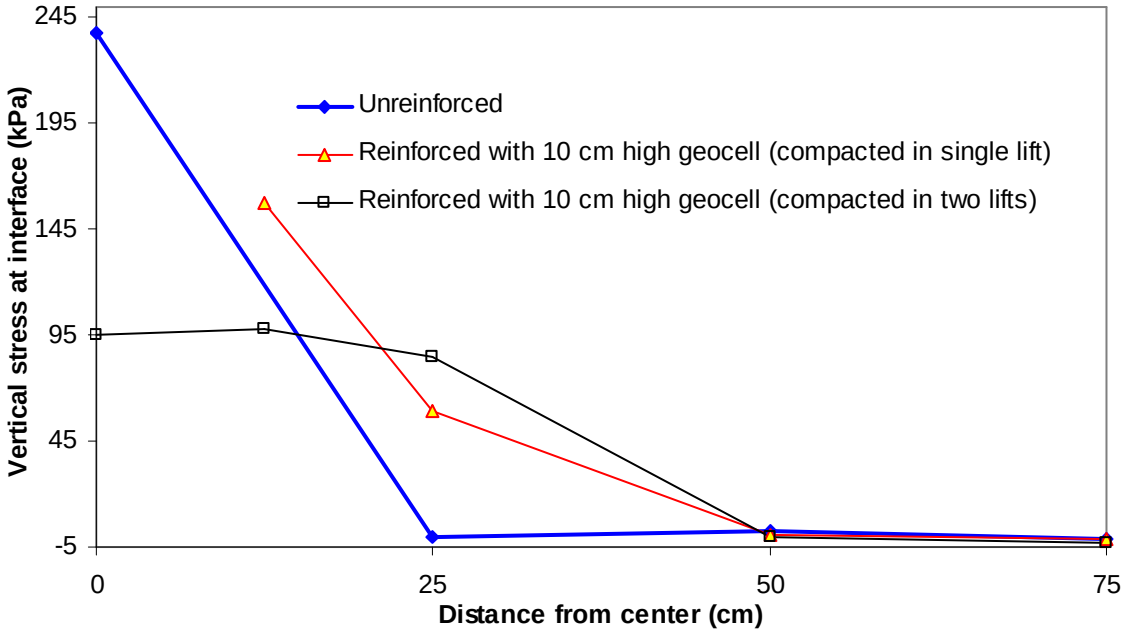

(c) Measured vertical stress at the interface at failure

Figure 5.3.21 Distributions of the measured vertical stresses at the interface of subgrade and base in the 15 cm thick unreinforced and reinforced AB-3-I bases at a given number of loading cycles

The stress distribution of the applied load through the base course can be expressed by a stress distribution angle, which can be calculated using **Equation 5.3.3**:

$$p_i = \frac{P}{\pi(r + h\tan\alpha)^2} \qquad \textbf{Equation 5.3.3}$$

where p_i = the distributed vertical stress at the center of the interface between the base course and the subgrade (kPa); P = the applied load (kN); r = the radius of the tire contact area; h = the thickness of the base course; and α = the stress distribution angle.

The calculated stress distribution angles with the number of loading cycles for three test sections are shown in **Figure 5.3.22**. This figure shows that the unreinforced and reinforced bases had similar initial stress distribution angles and decreased with the number of loading cycles at different rates. The reinforced section compacted in 2 lifts had the slowest decrease rate in the stress distribution angle followed by the reinforced section compacted in a single lift and the unreinforced base. The increase of the stress distribution angle in the reinforced section compacted in 2 lifts in the later stage was attributed to the beam effect of the geocell reinforcement. In conclusion, geocell reinforcement reduced the vertical stress by distributing the load to a wide area.

The calculated minimum stress distribution angles for the unreinforced section, the reinforced section compacted in single lift section, and the reinforced section compacted in 2 lifts were 27.5^{o}, 32.0^{o}, and 46.5^{o}, respectively.

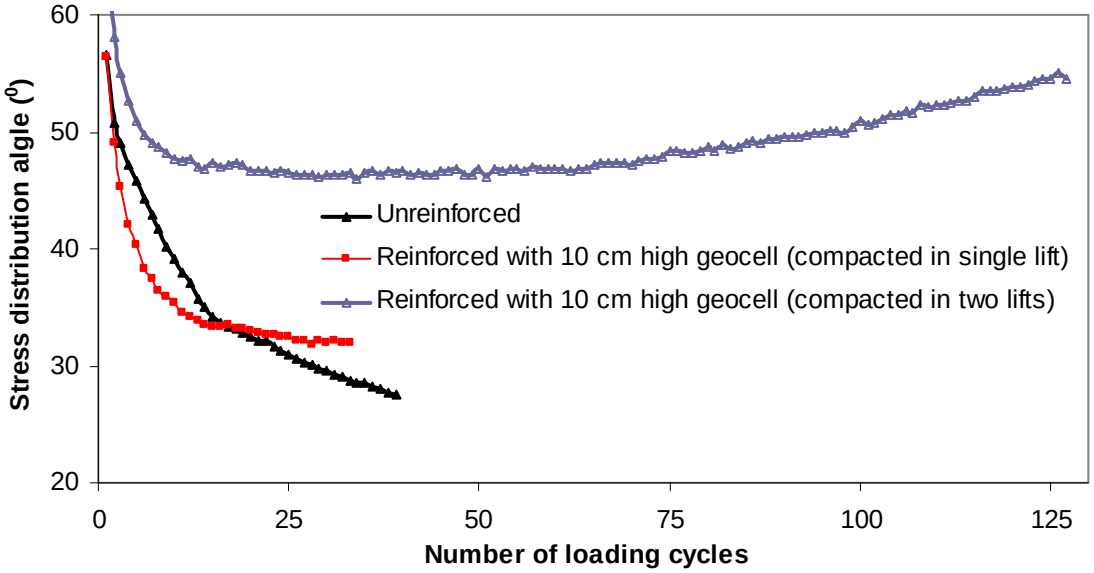

Figure 5.3.22 The calculated stress distribution angles for the 15 cm unreinforced and reinforced AB-3-I bases

5.3.2 23 cm thick AB-3-I base sections

The 23 cm thick unreinforced AB-3-I base section was compacted in two lifts of 11.5 cm each. The reinforced section had 15 cm high geocell, first loosely filled and then manually compacted in each cell individually. The second lift was placed into the remaining space of the cells left by the compaction in the first lift and above the cells as the cover layer and then compacted by the vibratory plate compactor. The thickness of the compacted cover layer was approximately 8 cm.

a) Vane shear, DCP, and sand cone tests

The results of the vane shear, DCP, and sand cone tests carried out on the subgrade and/or base courses are given in **Table 5.3.2**. The CBR profiles obtained from the DCP tests carried out on the test ready sections are also shown in **Figure 5.3.23**. The average CBR values of the subgrade obtained from vane shear tests were 1.8% for the unreinforced section and 1.75% for the reinforced section. The CBR values of the subgrade from the DCP tests on the test ready sections were 1.9% for both the unreinforced and reinforced sections. The DCP tests were conducted one day after the compaction of the base course laid on top of the subgrade. The average CBR values of the base courses were 17.3% for the unreinforced section and 18.3% for the reinforced section, respectively. Sand cone tests were carried out after the cyclic plate loading test for the reinforced and showed that the reinforced section achieved 92.8% relative compaction.

Table 5.3.2 Average CBR values from vane shear and DCP tests and relative compaction and moisture from sand cone tests

Test section	Vane shear (subgrade) CBR (%)	DCP (subgrade) CBR (%)	DCP (base course) CBR (%)	Sand cone after test (base course)	
				Relative compaction (%)	Moisture content (%)
Unreinforced	1.80	1.9	17.3	-	-
Reinforced	1.75	1.9	18.3	92.8	8.69

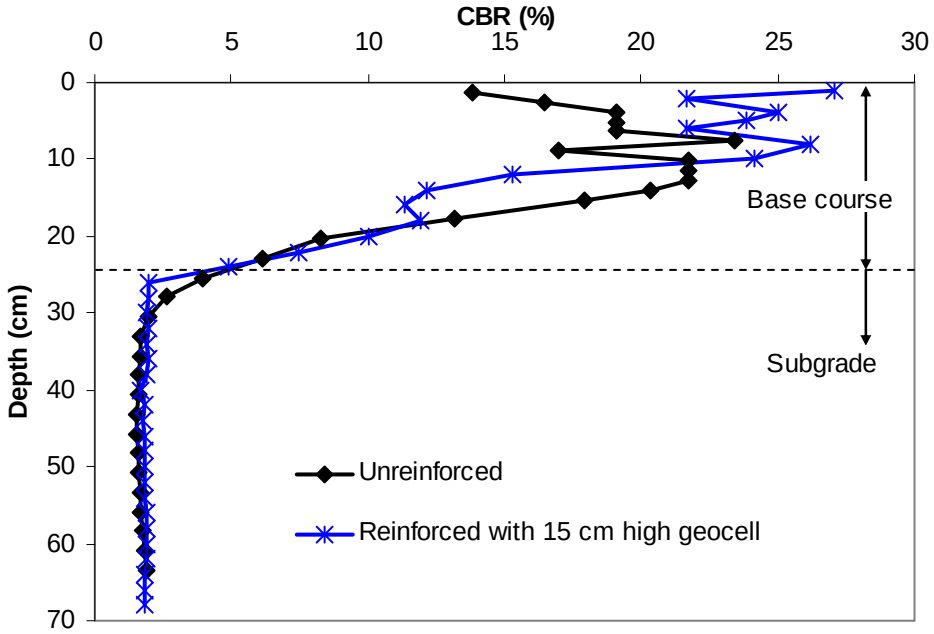

Figure 5.3.23 CBR profiles obtained from the DCP tests in 23 cm thick AB-3-I bases over weak subgrade

b) Deformed profiles

The failure criterion of 75 mm permanent deformation of the base course was reached at 62 cycles for the unreinforced section and 149 cycles for the NPA geocell-reinforced section. After the cyclic loading tests, both test sections were exhumed and trenches were cut to examine the deformed profiles and geocells. The deformed profiles are plotted in **Figures 5.3.24** and **5.3.25**. **Figure 5.3.26** shows the crack line developed on the surface of the reinforced section after the test. In the reinforced section, geocells were initially laid out at 25 cm long in the seam direction and 21 cm wide in the transverse direction. Forensic tests showed that the shape and size of the cells were intact outside the loading plate. However, around the area of loading plate, the geocells tend to take a circular shape; the seam side was slightly reduced and the transverse direction was slightly enlarged. Welds of the geocell located under the loading plate were broken at the bottom edges. One of the cells was also found vertically squeezed. The failure crack line and forensic examination showed that the geocell-reinforced sections behaved like a beam, which will be further verified by strain measurements in the geocell. The picture of the crack line and the geocell weld failures are shown in **Figures 5.3.27** and **5.3.28**.

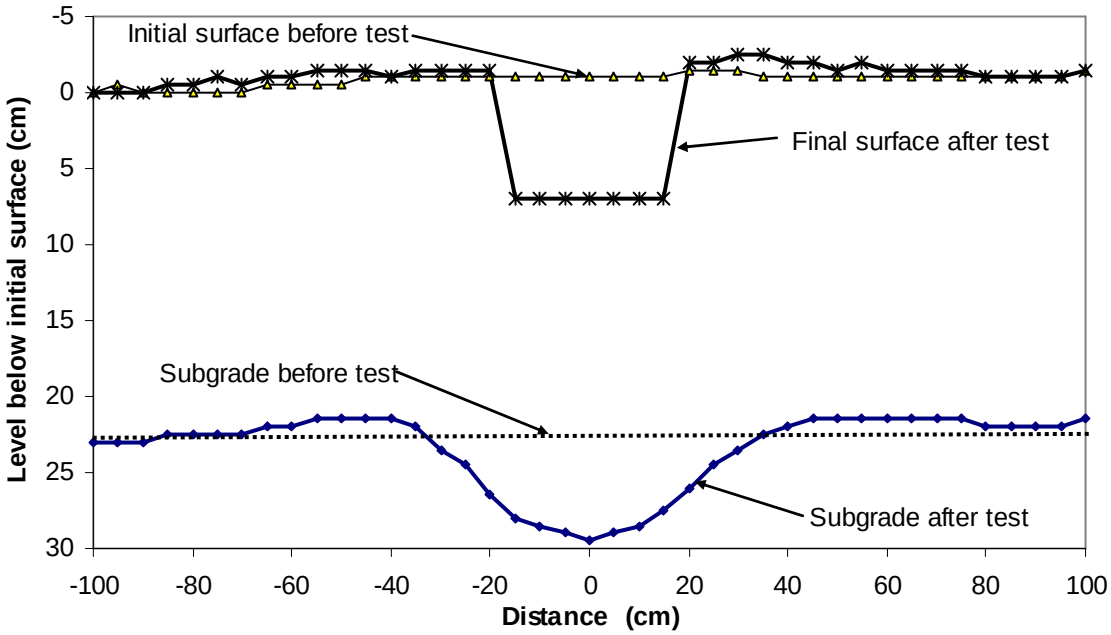

Figure 5.3.24 Profiles of the 23 cm thick unreinforced AB-3-I base section after 62 loading cycles

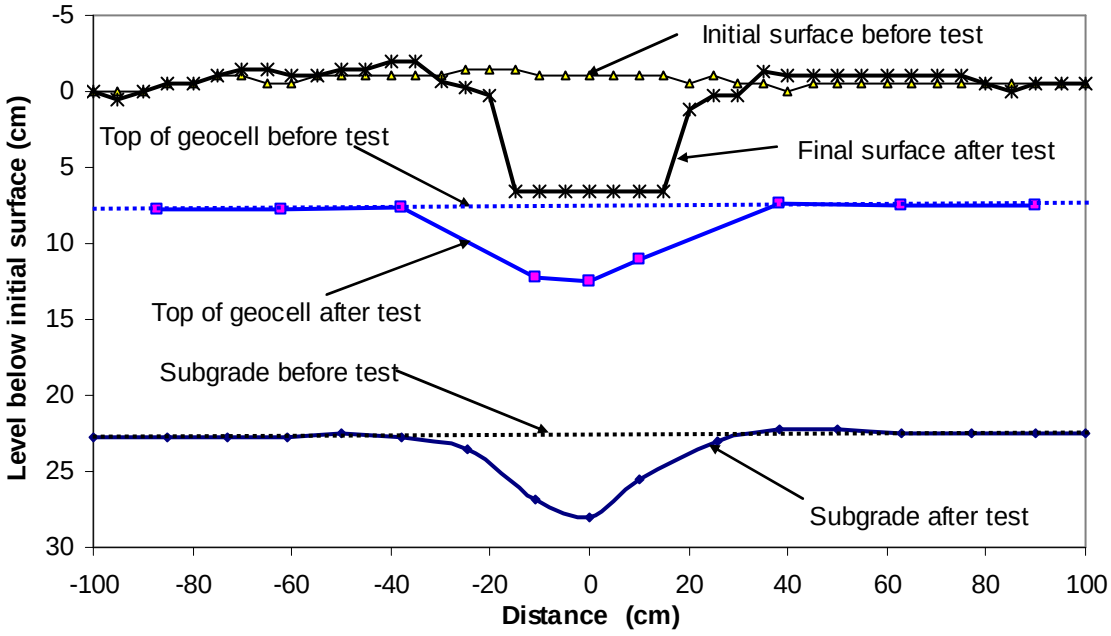

Figure 5.3.25 Profiles of the 15 cm high geocell-reinforced AB-3-I base section after 149 loading cycles

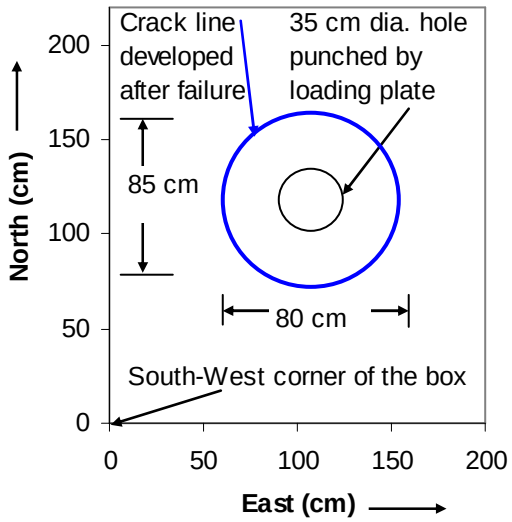

Figure 5.3.26 Surface failure pattern of the 15 cm high geocell-reinforced AB-3-I base sections in plan

Figure 5.3.27 Cracks on the surface of 15 cm high geocell reinforced AB-3-I base section

Figure 5.3.28 Weld failure under the loading plate observed after exhuming the 15 cm high geocell reinforced AB-3-I base section

c) Permanent deformations with number of loading cycles

Figures 5.3.29 through **5.3.31** show the permanent deformations at the center and 25 cm, 50 cm, and 75 cm away from the center of the loading plate at different loading cycles. For both unreinforced and reinforced sections, there was a small amount of heave in the locations of 50 cm and 75 cm away from the center. A small amount of compression was observed at 25 cm away from the center in both cases.

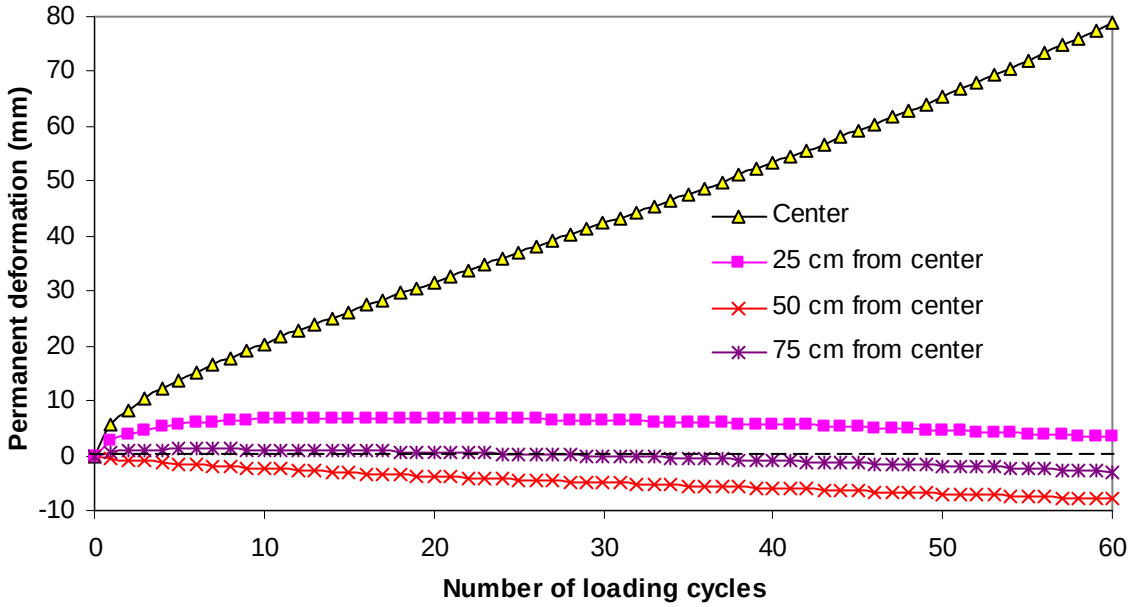

Figure 5.3.29 Permanent deformations versus the number of loading cycles for the 23 cm thick unreinforced AB-3-I base section

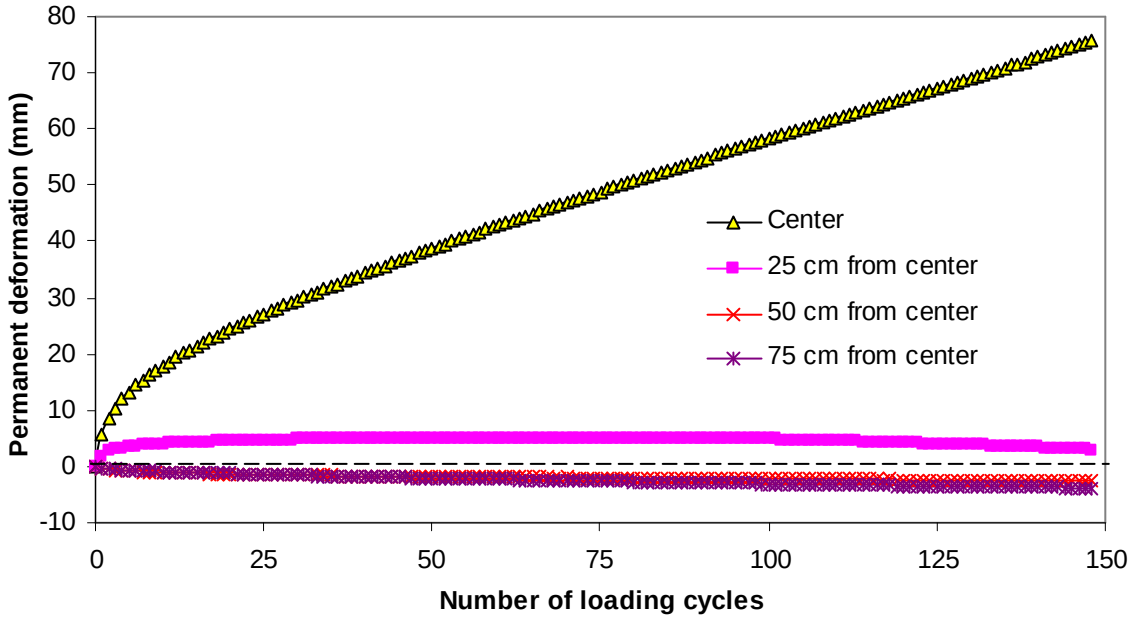

Figure 5.3.30 Permanent deformations versus the number of loading cycles for the 15 cm high geocell-reinforced AB-3-I base section

The comparison of permanent deformations for unreinforced and reinforced sections under the loading plate is given in **Figure 3.3.50**. The benefit of geocell reinforcement is clearly evident form this comparison. For the maximum allowable permanent deformation of 75 mm, the unreinforced section lasted 58 cycles and the geocell-reinforced section lasted 147 cycles. This comparison shows that the geocell reinforcement improved the performance of the section by a factor of 2.53 over the unreinforced section.

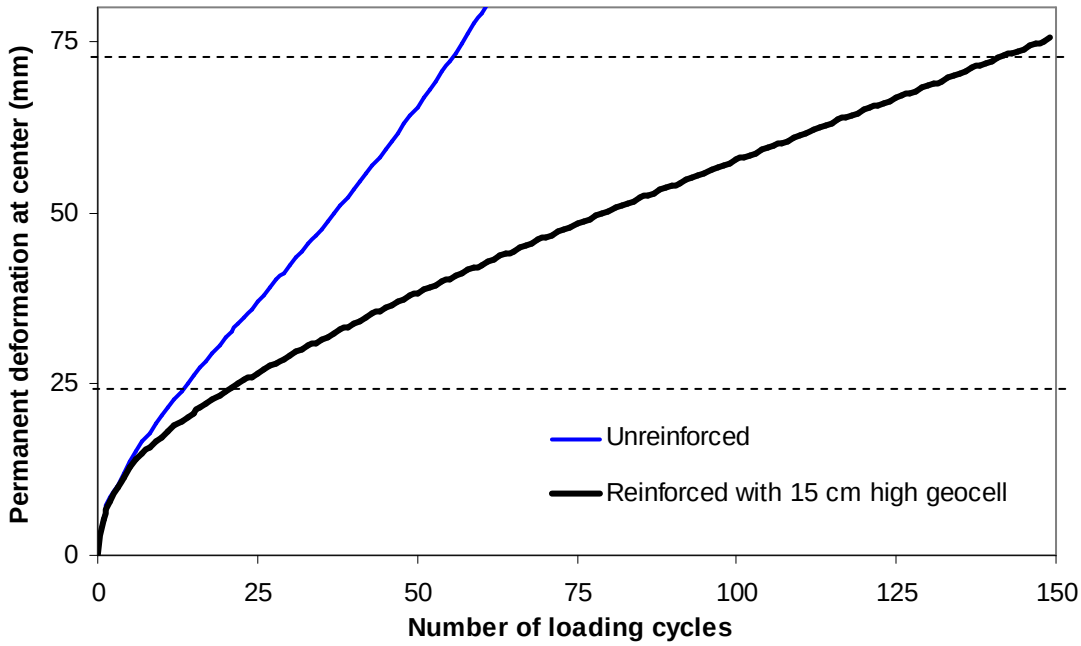

Figure 5.3.31 Comparison of the permanent deformations of unreinforced and reinforced sections at the center with 23 cm thick AB-3-I bases

Figure 5.3.32 shows the comparison of percentage of elastic deformation at the center. The unreinforced section had only 65% elastic deformation of the total deformation at failure whereas the reinforced section had 96%.

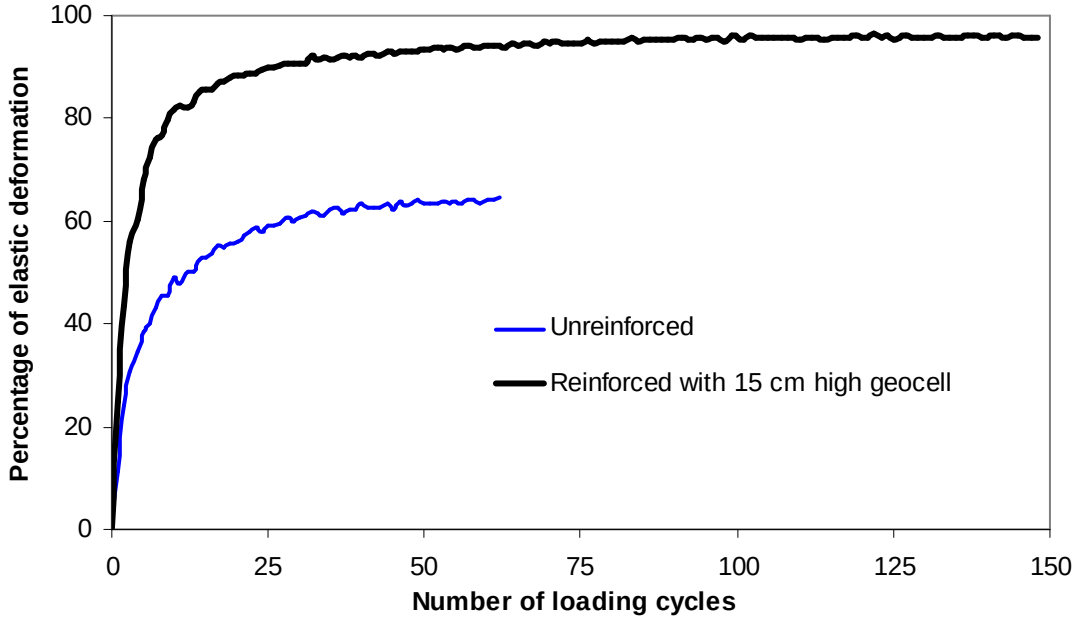

Figure 5.3.32 Percentage of elastic deformation at the center

d) Measured vertical stresses at the subgrade-base interface

The vertical stresses at the interface of subgrade and base course were measured by the pressure cells located at five locations on a straight line passing through the center. **Figures 5.3.33** and **5.3.34** show the vertical stresses measured at the given locations with the number of loading cycles. The maximum vertical stress measured at the interface under the plate was 177 kPa at 12.5 cm from the center for the unreinforced section and 165 kPa at the center for the reinforced section at failure. A comparison of the measured vertical stresses in the unreinforced and reinforced bases under the center of the loading plate is shown in **Figure 5.3.35**. It is seen that the measured vertical stresses were much lower than the applied pressure of 552 kPa on the surface. **Figures 5.3.33** and **5.3.34** also shows that the measured

vertical stress increased with the number of loading cycles, which is consistent with the design model proposed by Giroud and Han (2004a and b). Different from the 15 cm thick 10 cm high geocell-reinforced AB-3-I base, the vertical stresses did not decrease with the number of loading cycles after reaching certain values. This is because the membrane effect became less important for a thicker section.

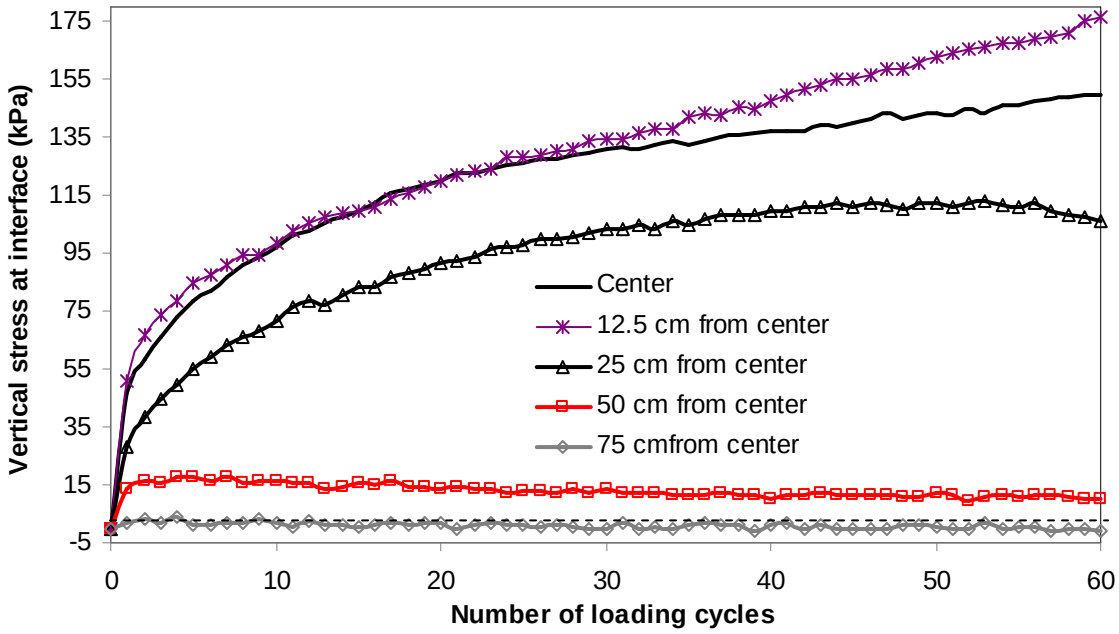

Figure 5.3.33 Measured vertical stresses at the subgrade-base interface in the 23 cm thick unreinforced AB-3-I base

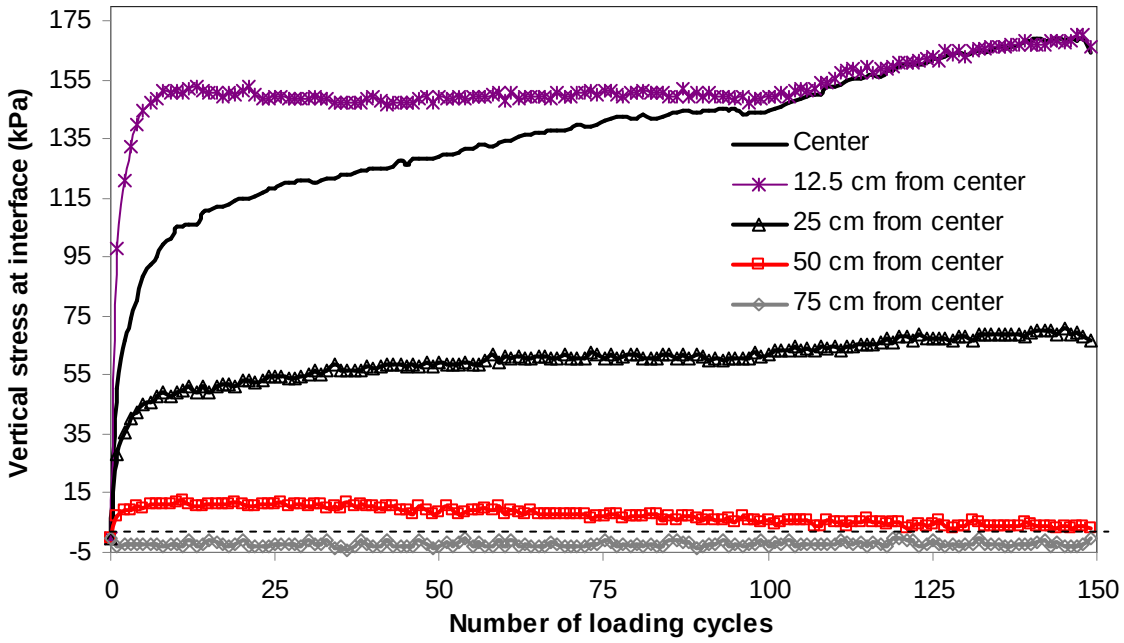

Figure 5.3.34 Measured vertical stresses at the subgrade-base interface in the 23 cm thick geocell-reinforced AB-3-I base

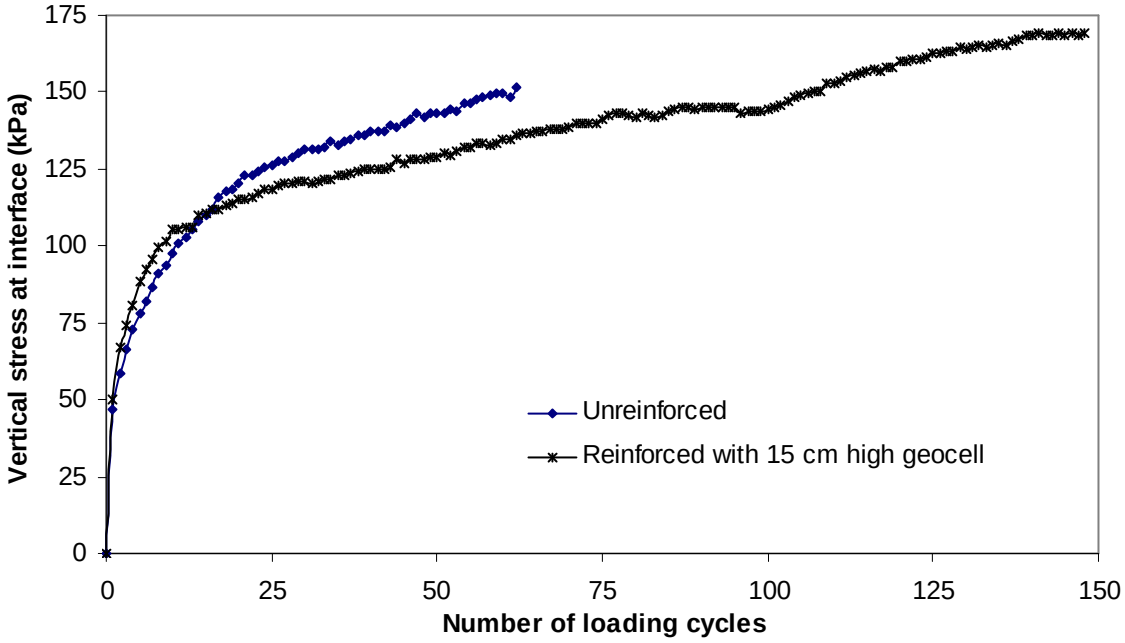

Figure 5.3.35 Comparison of the measured vertical stresses at the interface of subgrade and base at the center in 23 cm unreinforced and reinforced AB-3-I bases

The measured vertical stresses at the interface of subgrade and base at different locations away from the center in the unreinforced and reinforced sections are shown in **Figure 5.3.36**. There is a significant difference in the vertical stress measured over the number of loading cycles at 25 cm away from the center between the unreinforced and reinforced sections. The vertical stresses at the first cycle, at the 50th cycle, at the failure of the unreinforced section, and at the failure of the unreinforced and reinforced sections are shown in **Figure 5.3.37**.

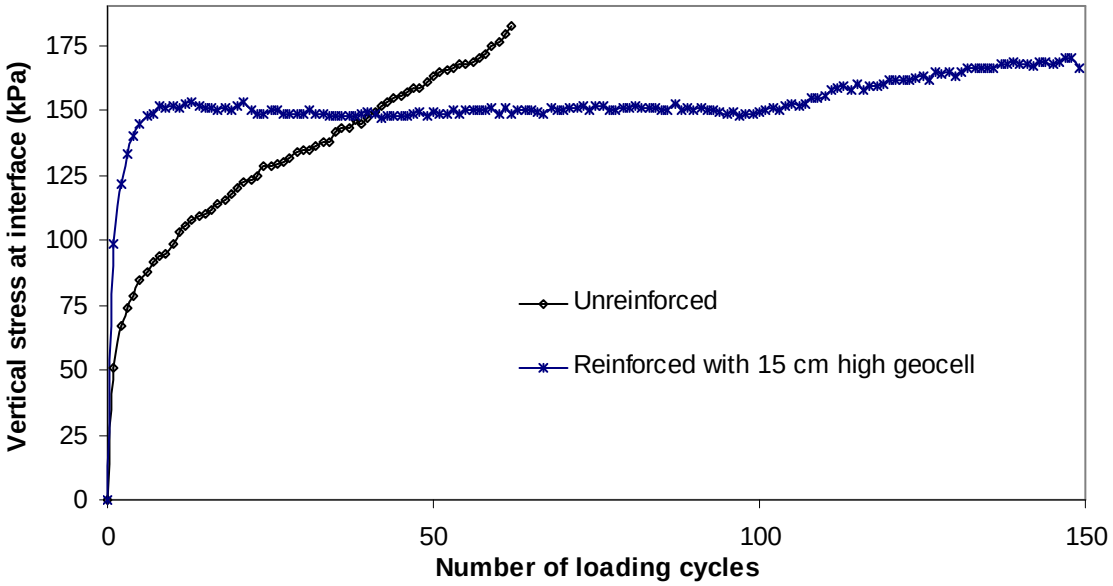

(a) 12.5 cm from the center

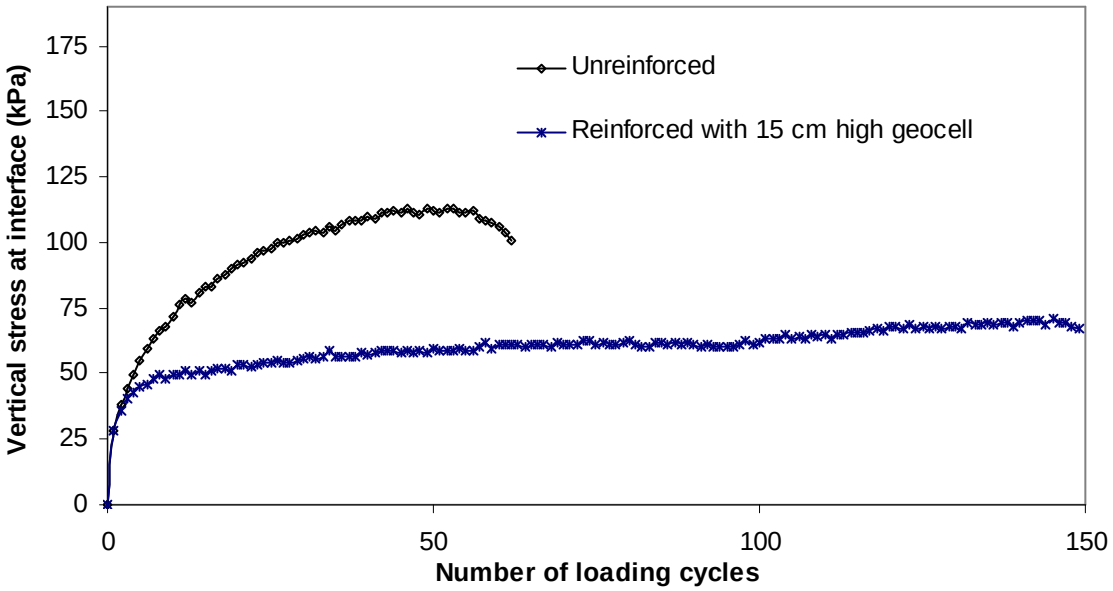

(b) 25 cm from the center

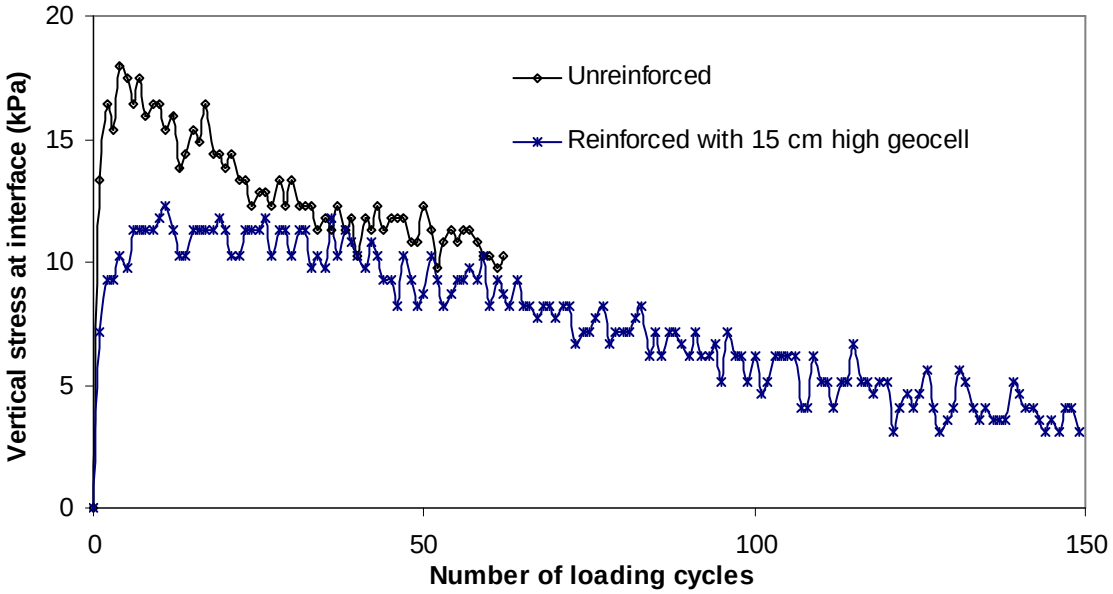

(c) 50 cm from the center

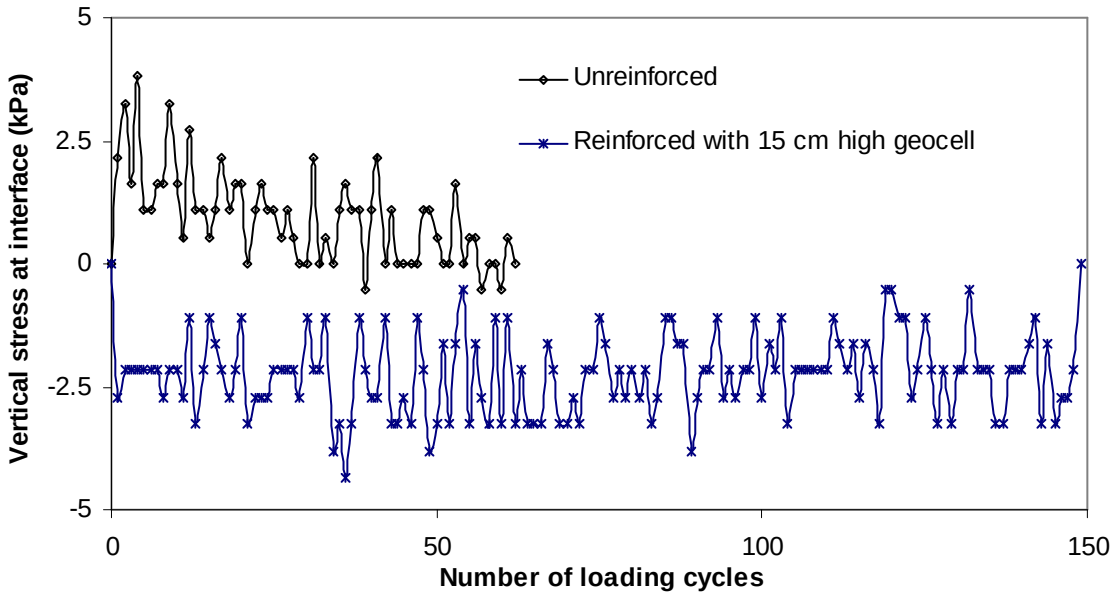

(d) 75 cm from the center

Figure 5.3.36 Comparison of the measured vertical stresses at the interface of subgrade and base at different locations away from the center in the 23 cm thick AB-3-I bases

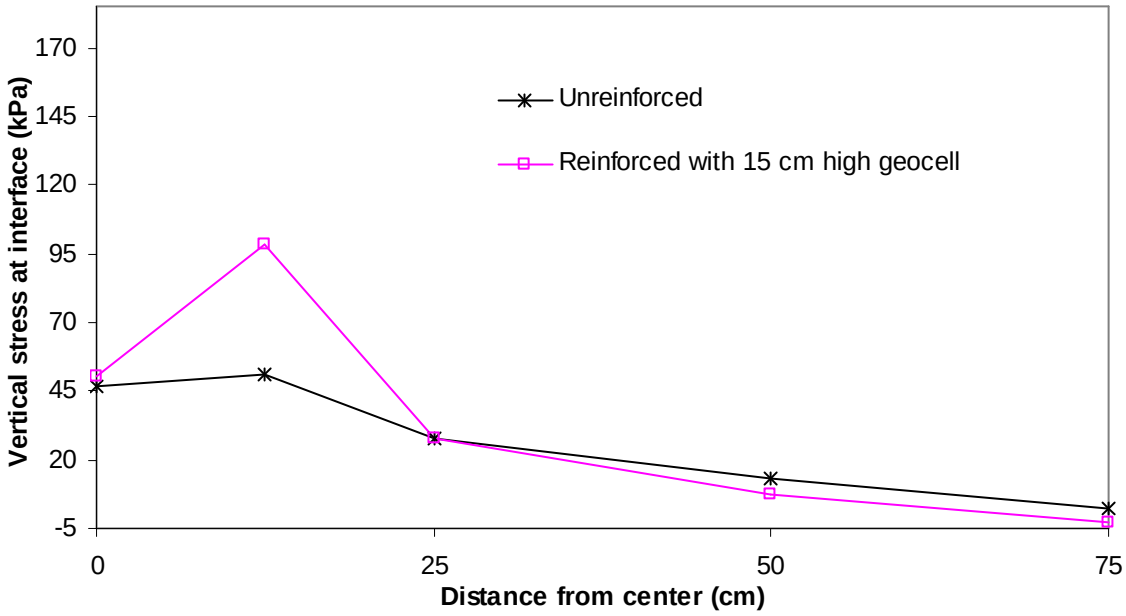

(a) Measured vertical stress at the interface at the end of first loading cycle

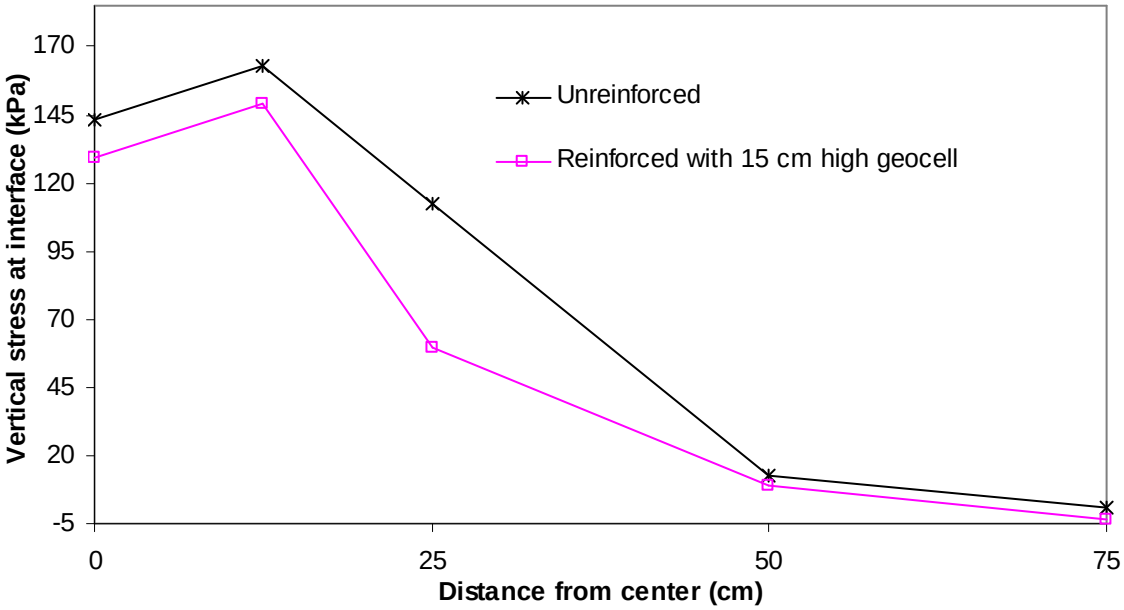

(b) Measured vertical stress at the interface at the end of 50 loading cycles

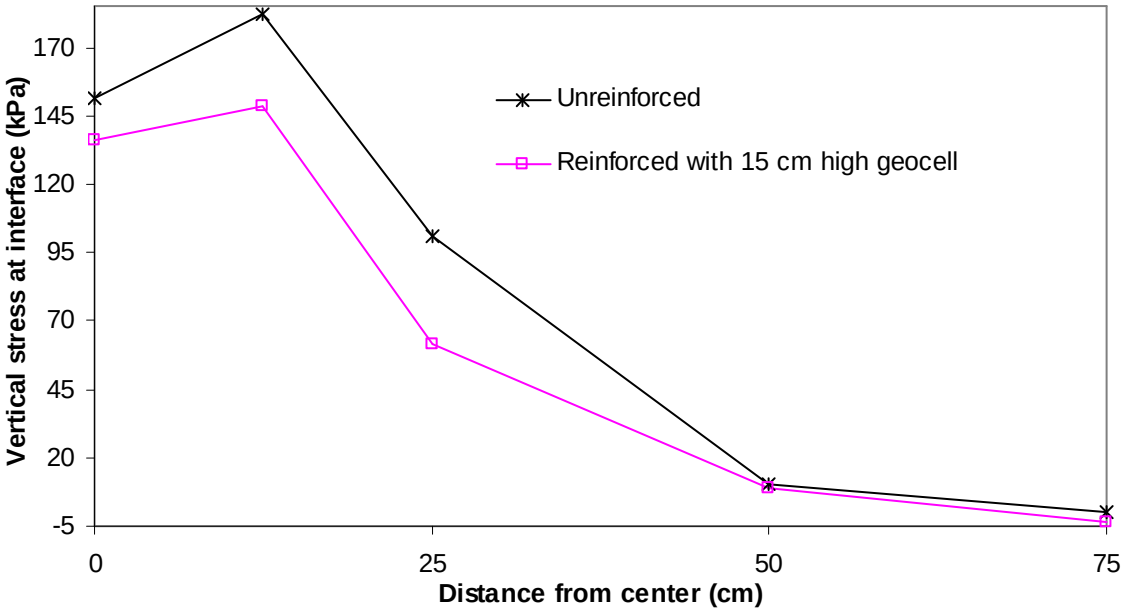

(c) Measured vertical stress at the interface at the end of 62 loading cycles

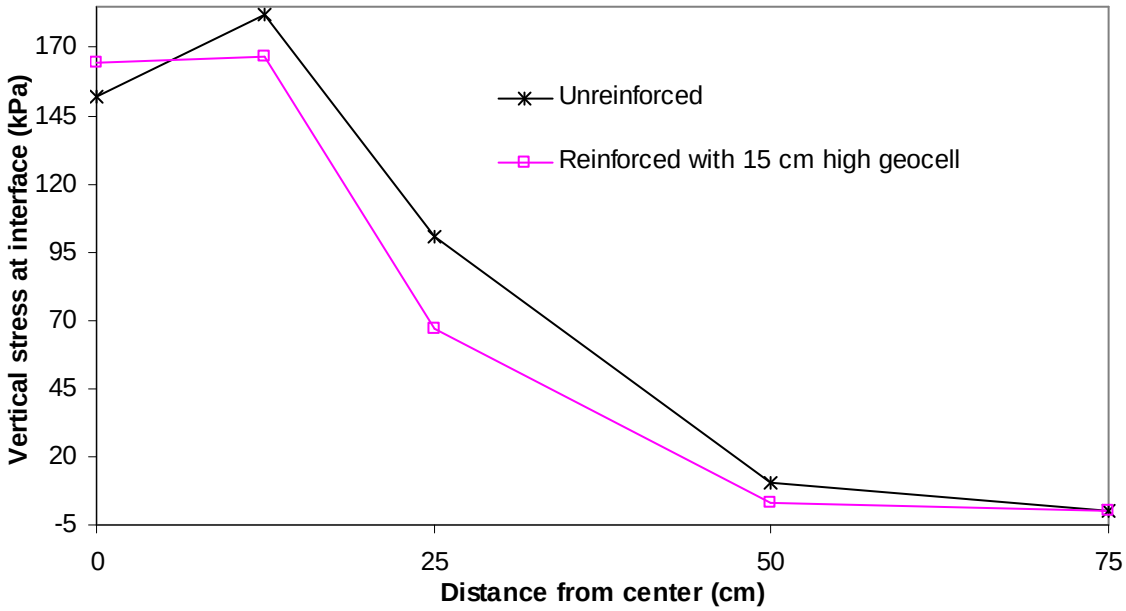

(d) Measured vertical stress at the interface at failure

Figure 5.3.37 Distributions of the measured vertical stresses at the interface of subgrade and base in the 23 cm thick unreinforced and reinforced AB-3-I bases at a given number of loading cycles

Using **Equation 5.3.3**, the stress distribution angle for each section was calculated. The calculated stress distribution angle with the number of loading cycles is shown in **Figure 5.3.38**. This comparison demonstrates that the unreinforced and reinforced sections had similar initial stress distribution angles, but the distribution angle for the reinforced section decreased more slowly that for the unreinforced section. The calculated stress distribution angles for the unreinforced and reinforced sections at 62 cycles (i.e., the end of the unreinforced section test) were 30.5^{o} and 33.4^{o}, respectively.

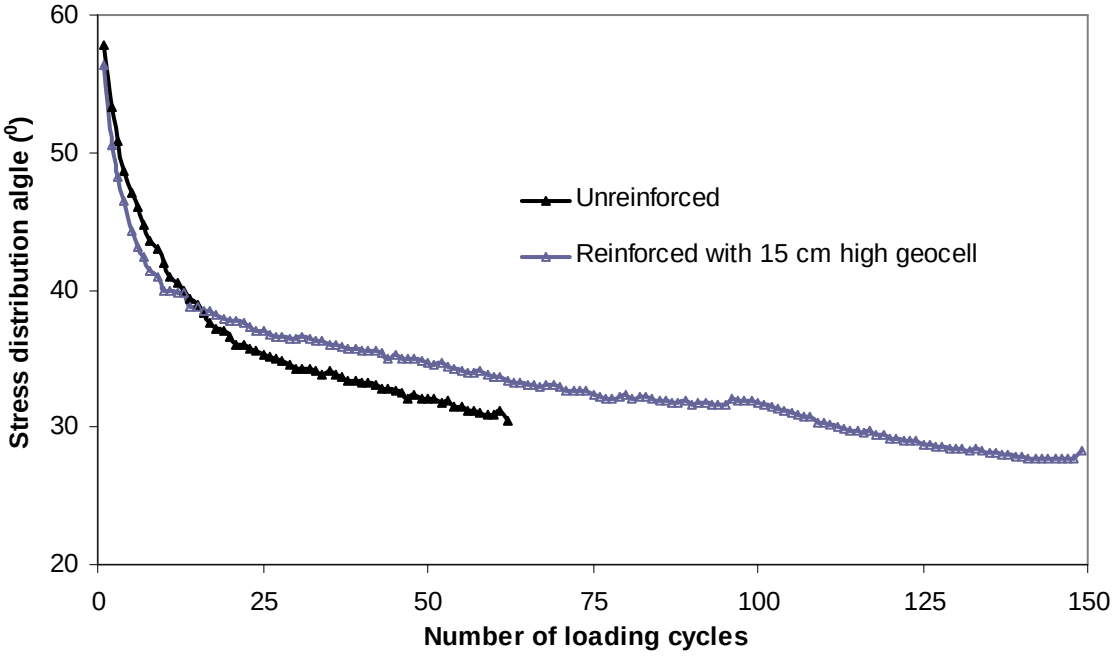

Figure 5.3.38 The calculated stress distribution angles for the 23 cm unreinforced and reinforced AB-3-I bases

e) Maximum strains in the geocell

For each test six strain gages were installed on the geocell walls. There were three gages at the central geocell located right under the loading plate, one each at the top, middle and, bottom; two gages were installed at the top and middle of the geocell wall of next adjacent geocell; and one gage was installed at the top of the cell further outside the loading plate. These strain gages were located at the center, and at 25 cm and 50 cm away from the center. The positions of the strain gages and the measured maximum strains are shown in **Figure 5.3.39**. A negative strain implies compression while a positive strain implies tension. The top of the geocell wall located at the center and the adjacent geocells showed compressive strain while the strain gage located at 50 cm away from the center had tensile strain at the top of the geocell wall. The bottom of the wall of the geocell located at the

center and middle of the wall of the adjacent geocell experienced tensile stresses. All the strain gages affixed at the top and bottom of the geocell wall measured horizontal strain while the strain gages affixed at the middle of the wall measured the vertical strains.

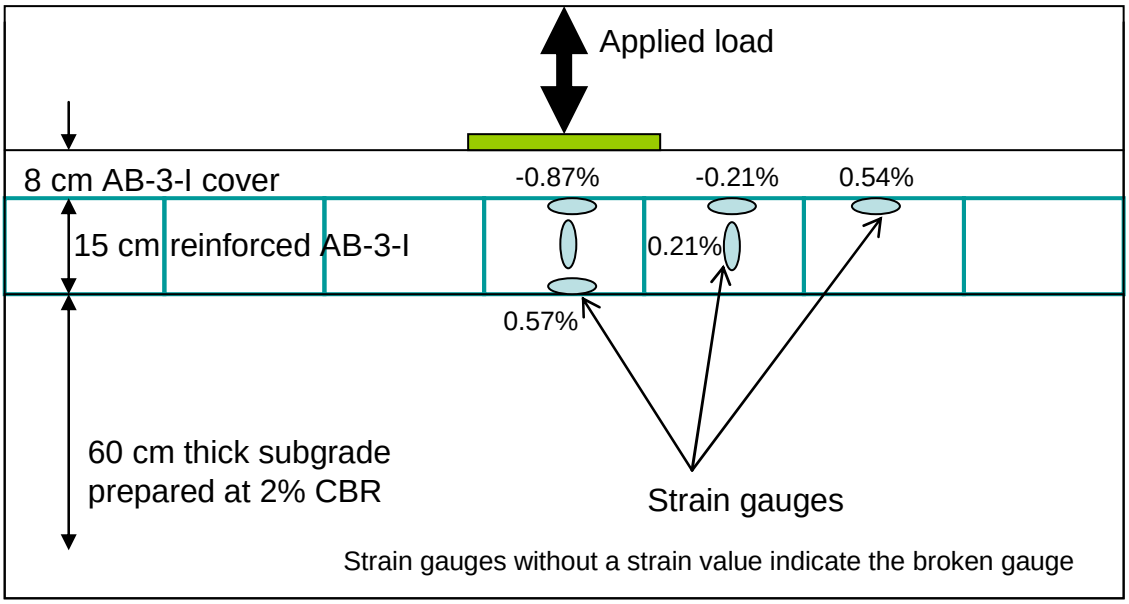

Figure 5.3.39 Measured maximum strains in the geocell in the 23 cm thick reinforced AB-3-I base

5.3.3 30 cm thick AB-3-I base sections

The 30 cm thick unreinforced AB-3-I base section was compacted in two lifts of 15 cm each. The reinforced section had two geocell layers and was prepared in the following order after the placement of the gotextile layer: 10 cm high geocell infilled with the AB-3-I aggregate, 3 cm thick AB-3-I cover, 10 cm high geocell infilled with the AB-3-I aggregate, and 7 cm thick top AB-3-I cover. The compaction was done in two lifts for each geocell layer. After placement of each geocell, it was first filled just full loosely, the fill inside the cells was manually compacted, and then additional fill including the cover material was placed and compacted using the vibratory plate compactor.

a) Vane shear, DCP, and sand cone tests

The results of the vane shear, DCP, and sand cone tests carried for the subgrade and the base courses in unreinforced and reinforced sections are given in **Table 5.3.3**. The profiles of the estimated CBR values from the DCP data are shown in **Figure 5.3.40**. The average CBR values of the subgrade obtained from vane shear tests were 1.8% for the unreinforced section and 1.65% for the reinforced section. The CBR values of the subgrade from DCP tests were 2.0% and 1.70% for the unreinforced and reinforced sections, respectively. The average CBR values of the base courses were 19.1% for the unreinforced section and 22.0% for the reinforced section. Sand cone tests carried out after the cyclic plate loading tests showed that the reinforced base achieved 94.7% relative compaction.

Table 5.3.3 Average CBR values from vane shear and DCP tests and relative compaction and moisture from sand cone tests

Test section	Vane shear (subgrade) CBR (%)	DCP (subgrade) CBR (%)	DCP (base course) CBR (%)	Sand cone after test (base course)	
				Relative compaction (%)	Moisture content (%)
Unreinforced	1.80	2.0	19.1	-	-
Reinforced section	1.65	1.7	20.6	94.7	8.89

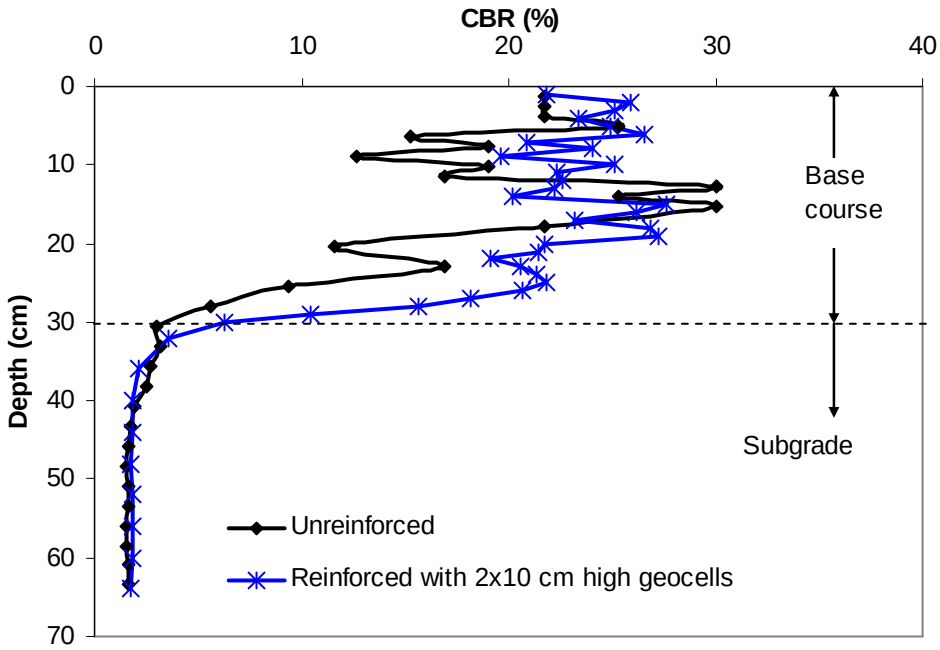

Figure 5.3.40 CBR profiles obtained from the DCP tests in 30 cm thick AB-3-I bases over weak subgrade

b) Deformed profiles

The failure criterion of 75 mm permanent deformation of the base course was reached at 123 cycles for the unreinforced AB-3-I base section and 1299 cycles for the 2x10 cm high geocell-reinforced AB-3-I base section. After the cyclic plate loading tests, all the test sections were exhumed and trenches were cut to examine the deformed profiles and geocells. The deformed profiles are plotted in **Figures 5.3.41** and **5.3.42**. **Figure 5.3.43** shows the crack line developed on the surface of the reinforced section after the test. In the reinforced section, geocells were initially laid out at 25 cm long in the seam direction and 21 cm wide in the transverse direction. Forensic tests showed that the shape and size of the cells were intact outside the loading plate. However, same as the 15 cm and 23 cm thick reinforced sections the geocells in the 30 cm thick reinforced section under the area of loading plate tend to take a circular shape; the seam side was slightly reduced and the transverse direction slightly enlarged. Welds of the geocell located under the loading plate were broken at the bottom edges after the test. The failure crack line and forensic examination showed that the geocell-reinforced sections behaved like a beam. **Figure 5.3.44** shows the exhumed cross-section of the unreinforced section. **Figure 5.3.45** shows the surface deformation of the reinforced section after the test. **Figure 5.3.**46 shows the deformed geocell after the test.

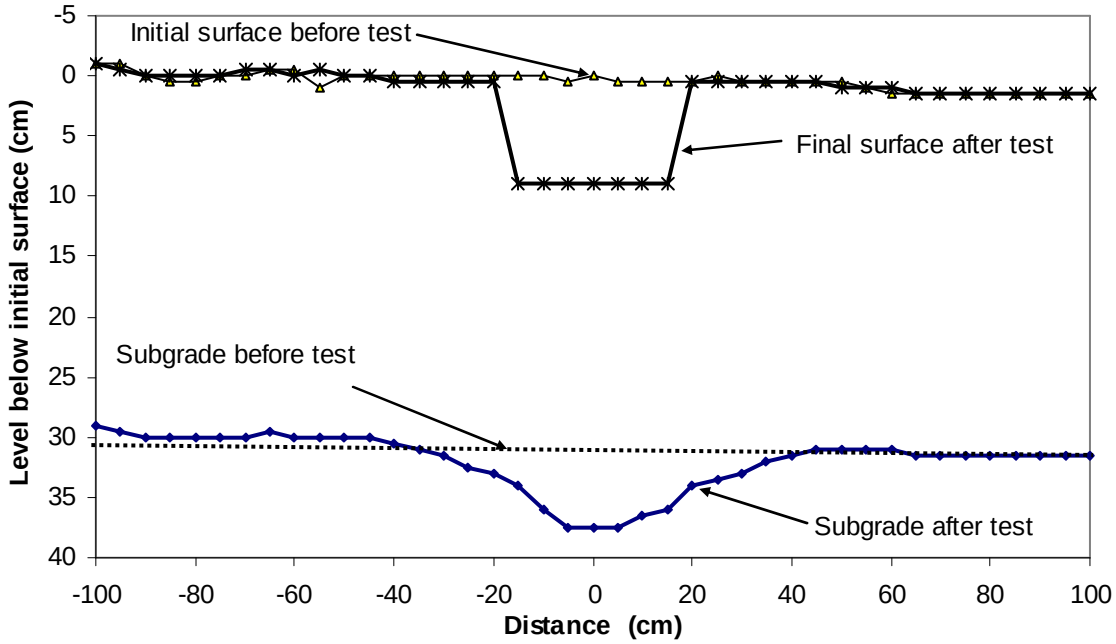

Figure 5.3.41 Profiles of the 30 cm thick unreinforced AB-3-I base section after 130 loading cycles

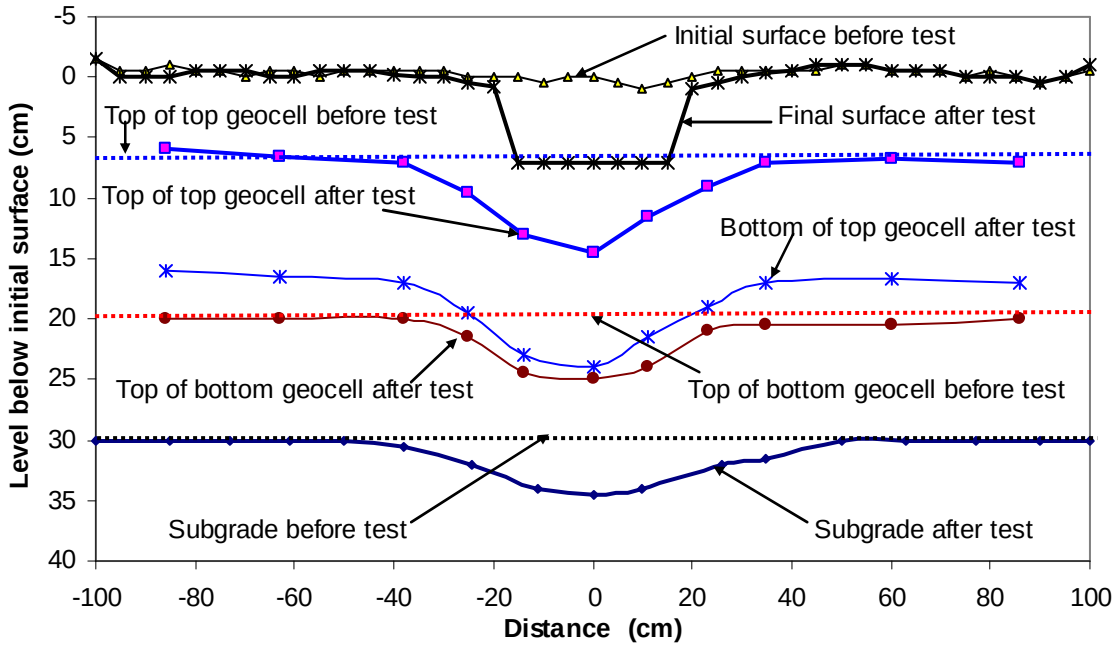

Figure 5.3.42 Profiles of the 2x10 cm high geocell-reinforced AB-3-I base section after 1385 loading cycles

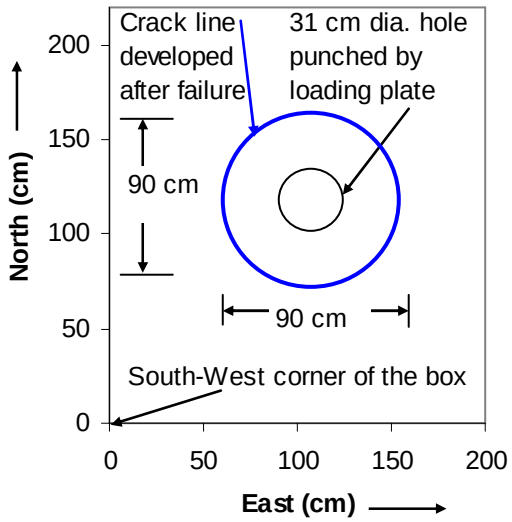

Figure 5.3.43 Surface failure Pattern of the 2x10 cm geocell-reinforced AB-3-I sections in plan

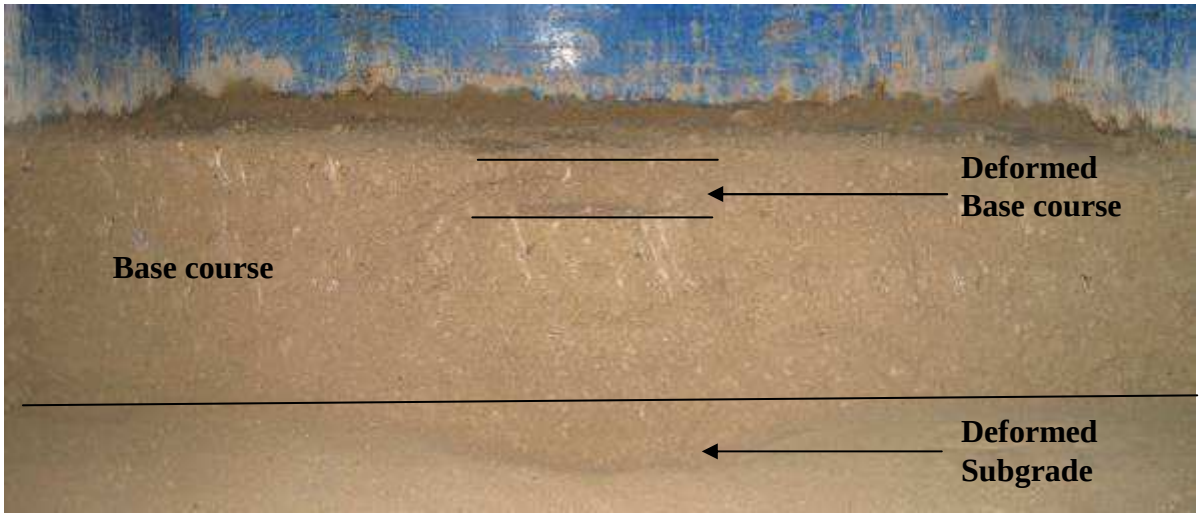

Figure 5.3.44 Exhumed cross section of the 30 cm thick unreinforced AB-3-I base section

Figure 5.3.45 Surface deformation of the 30 cm thick reinforced AB-3-I base section after the test

Figure 4.3.46 Deformed geocells in the 30 cm thick reinforced AB-3-I base section under the loading plate

c) Permanent deformations with the number of loading cycles

Figures 5.3.47 through **5.3.49** show the permanent deformations of the unreinforced and NPA geocell-reinforced AB-3-I bases at the center and 25 cm, 50 cm, and 75 cm away from the center of the loading plate at different loading cycles. In the unreinforced section, there was a small amount of heave at the locations of 50 cm and 75 cm away from the center. A small amount of compression was observed at 25 cm away from the center in both the cases.

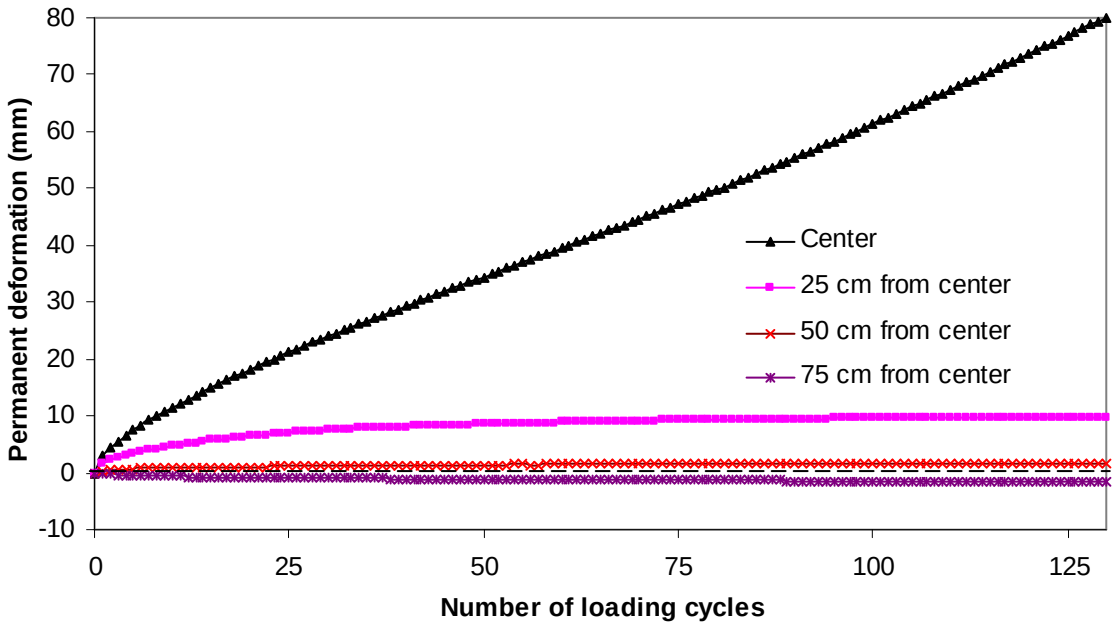

Figure 5.3.47 Permanent deformations versus the number of loading cycles for the 30 cm thick unreinforced AB-3-I base section

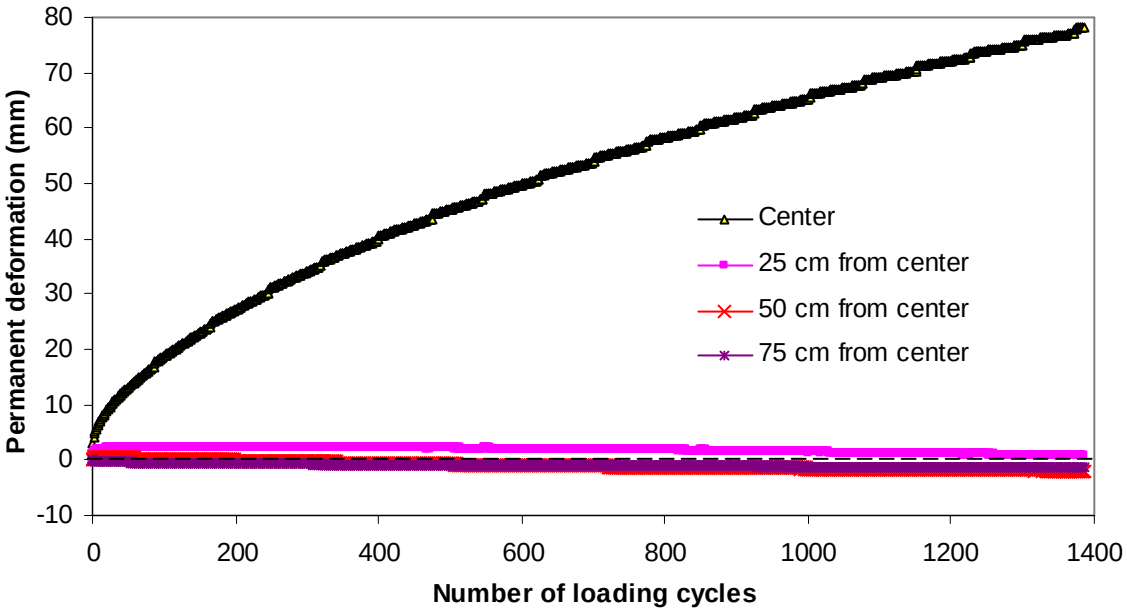

Figure 5.3.48 Permanent deformations versus the number of loading cycles for the 2x10 cm high geocell-reinforced AB-3-I base section

The comparison of permanent deformations of the unreinforced and reinforced sections under the loading plate is given in **Figure 5.3.48**. The benefit of geocell reinforcement is clearly evident form this comparison. At the permanent deformation of 75 mm, the unreinforced section lasted for 123 cycles while the NPA geocell-reinforced section lasted for 1299 cycles. In other words, the geocell reinforcement improved the performance of the test section by a factor of 10.6 over the unreinforced section.

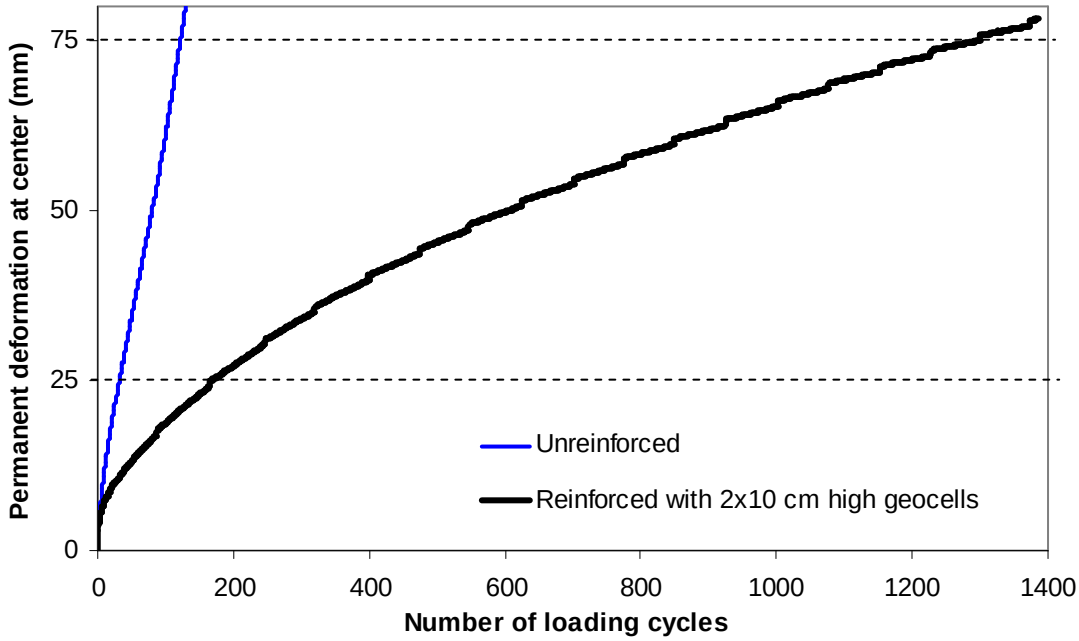

Figure 5.3.49 Comparison of the permanent deformations of unreinforced and reinforced sections at the center with 30 cm thick AB-3-I bases

Figure 5.3.50 shows the percentages of elastic deformation at the center of the unreinforced and reinforced sections. The unreinforced section had only 87% of the total deformation each cycle as the elastic deformation at the end of the test whereas the reinforced section had 99%.

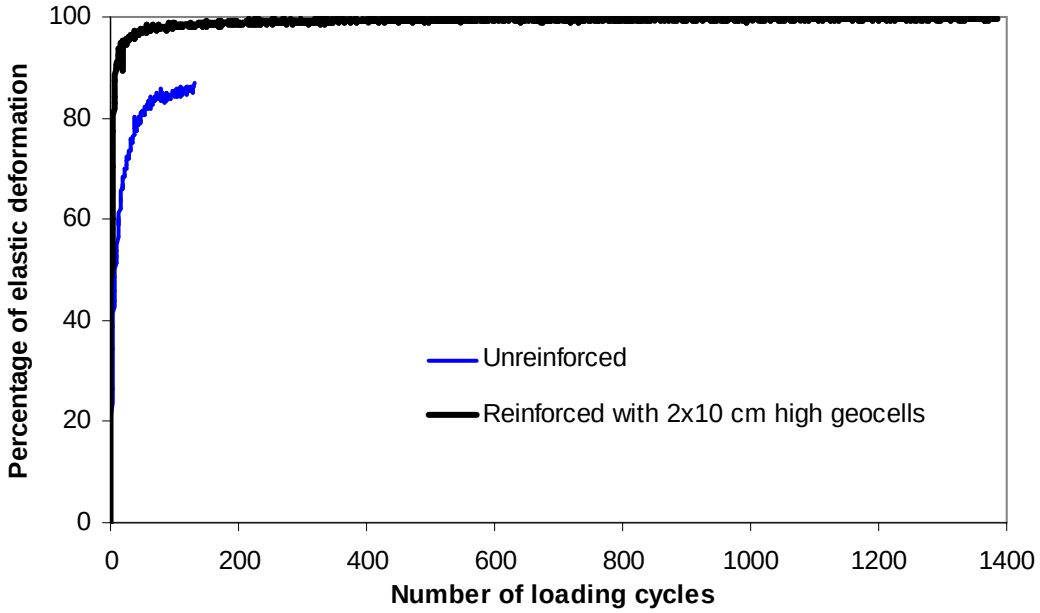

Figure 5.3.50 Percentage of elastic deformation at the center

d) Measured vertical stresses at the subgrade-base interface

The vertical stresses at the interface of subgrade and base course were measured by the pressure cells located at five locations on the straight line passing through the center. **Figures 5.3.51** and **5.3.52** show the measured vertical stresses at the given locations with the number of loading cycles. The measured vertical stress at the center was 145 kPa for the unreinforced section and 125 kPa for the reinforced section. The measured vertical stresses in the unreinforced and reinforced sections under the center of the loading plate are shown in **Figure 5.3.53**. It is seen that the measured vertical stresses at the interface were much lower than the applied pressure of 552 kPa on the surface. The increase of the vertical stress at the interface in the reinforced section was much slower than that in the unreinforced section, which is consistent with the design model proposed by Giroud and Han (2004a and b).

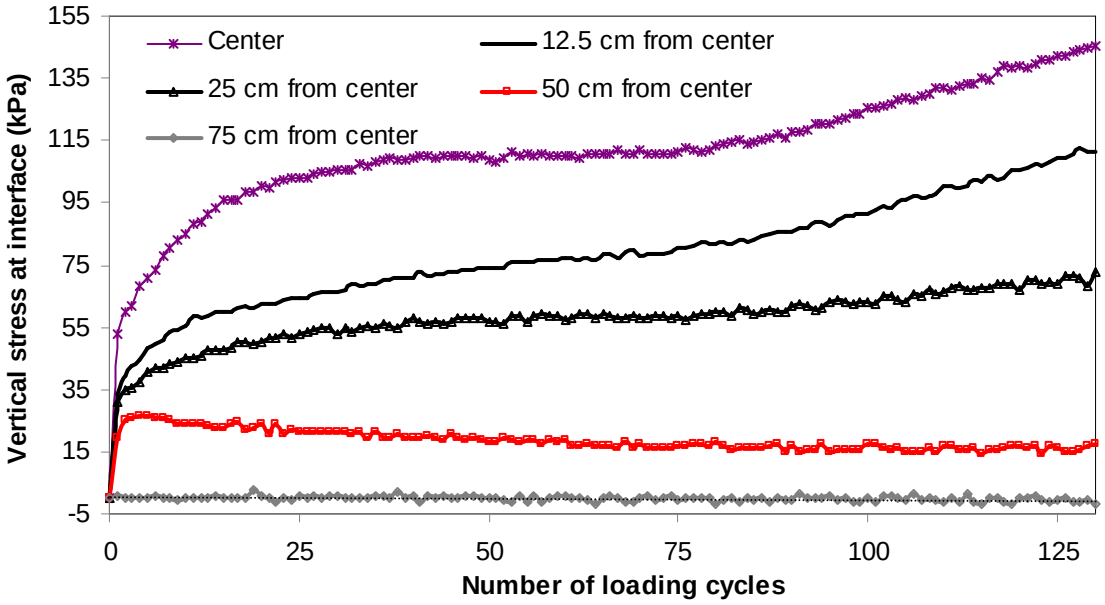

Figure 5.3.51 Measured vertical stresses at the subgrade-base interface in the 30 cm thick unreinforced AB-3-I base

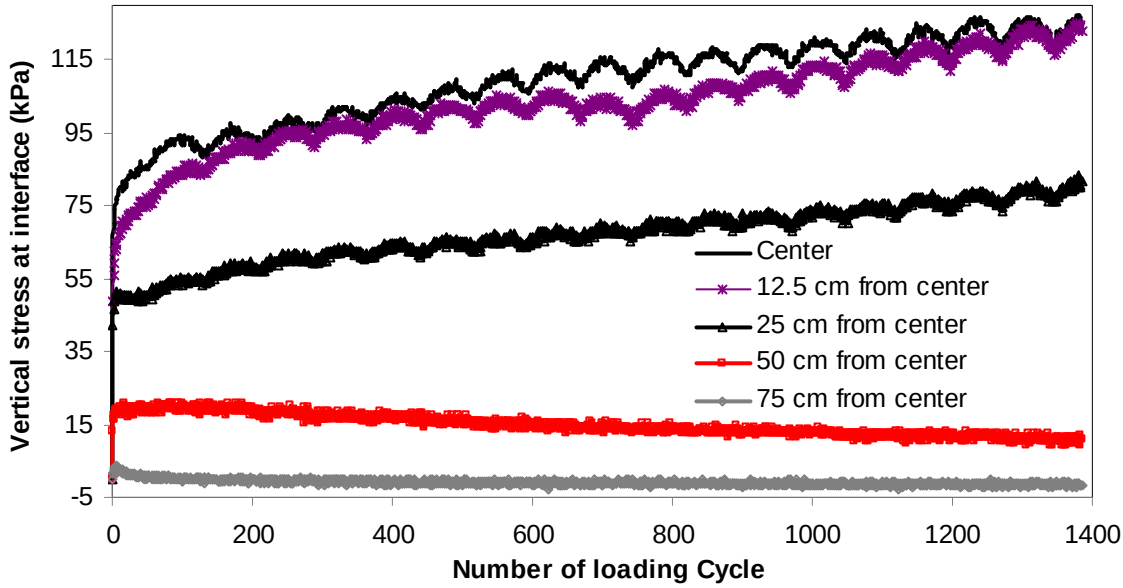

Figure 5.3.52 Measured vertical stresses at the subgrade-base interface in the 30 cm thick geocell-reinforced AB-3-I

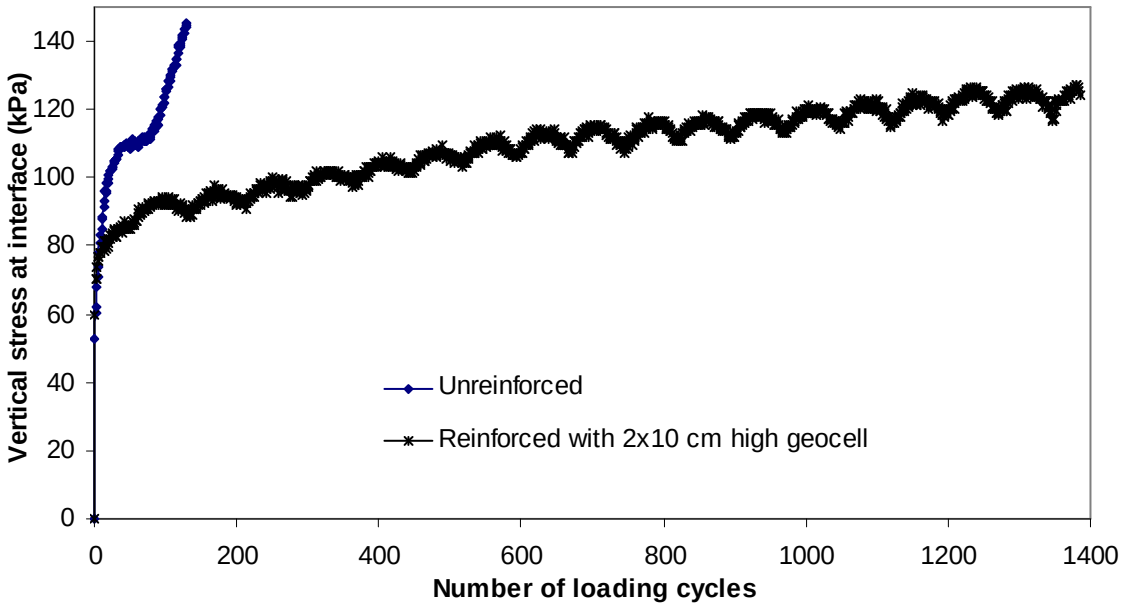

Figure 5.3.53 Comparison of the measured vertical stresses at the interface of subgrade and base at the center in 30 cm unreinforced and reinforced AB-3-I bases

The measured vertical stresses at the interface of subgrade and base at different locations away from the center are shown in **Figure 5.3.54**. There is a significant difference in the vertical stress measured over the number of loading cycles at 25 cm away from the center between the unreinforced and reinforced sections. The vertical stresses at the first cycle, the 50th cycle, and the 100th cycle, the end of the test for the unreinforced and reinforced sections are shown in **Figure 5.3.55**.

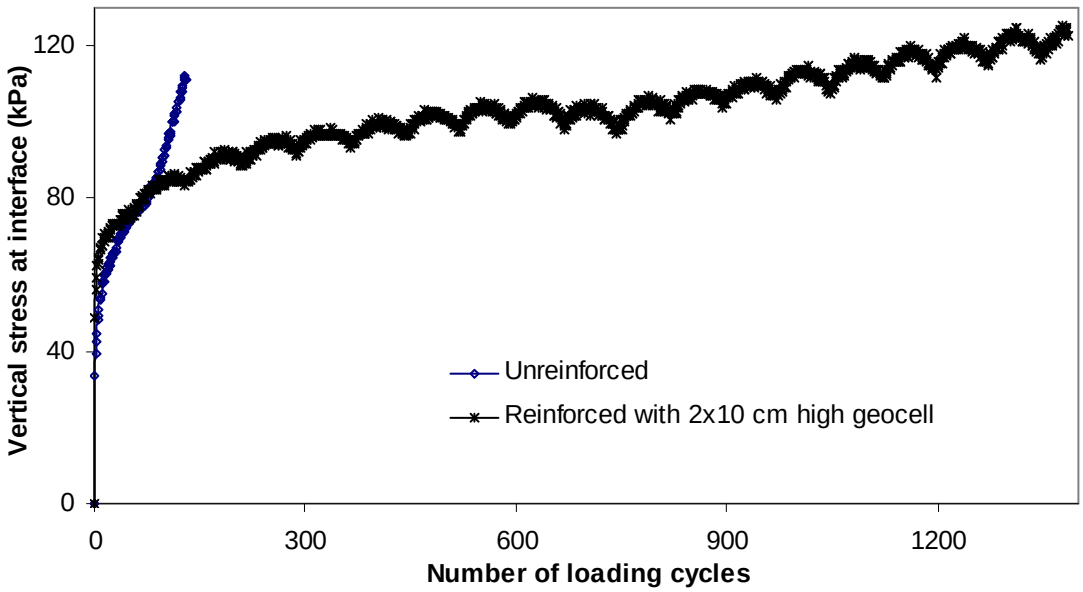

(a) 12.5 cm from the center

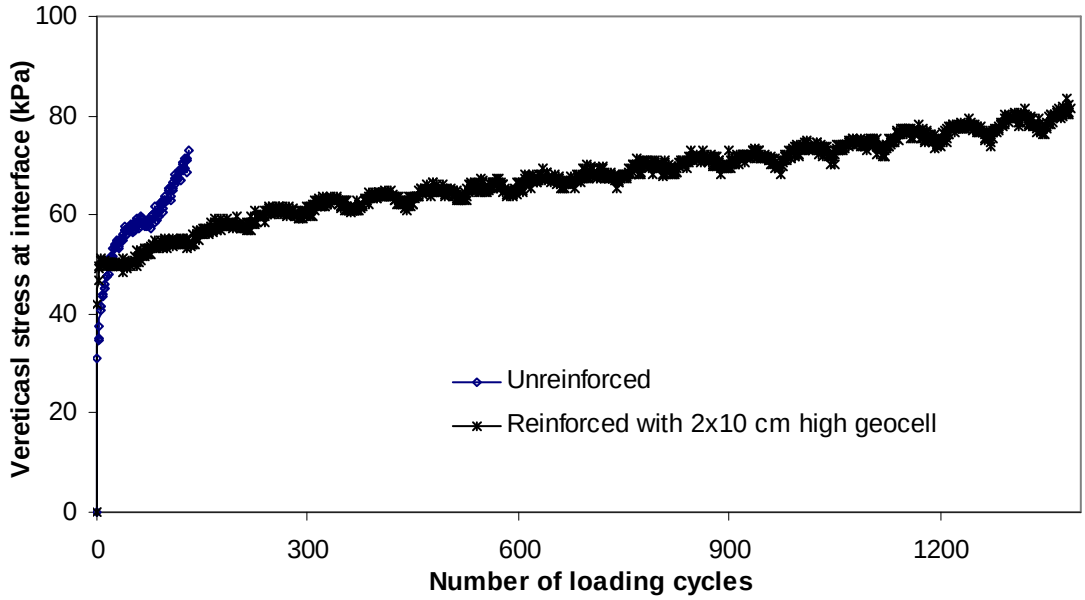

(b) 25 cm from the center

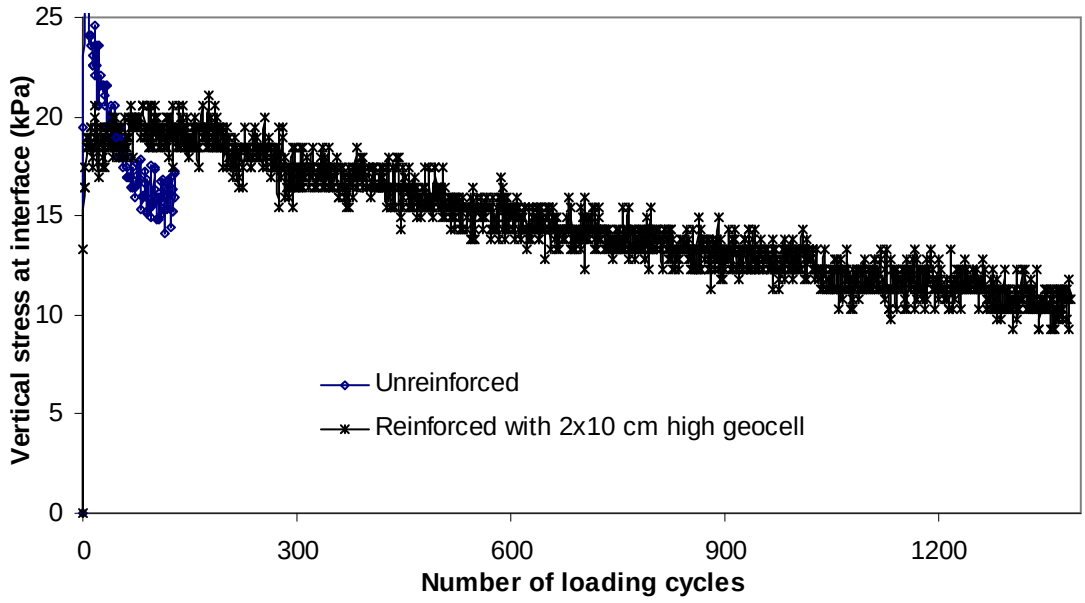

(c) 50 cm from the center

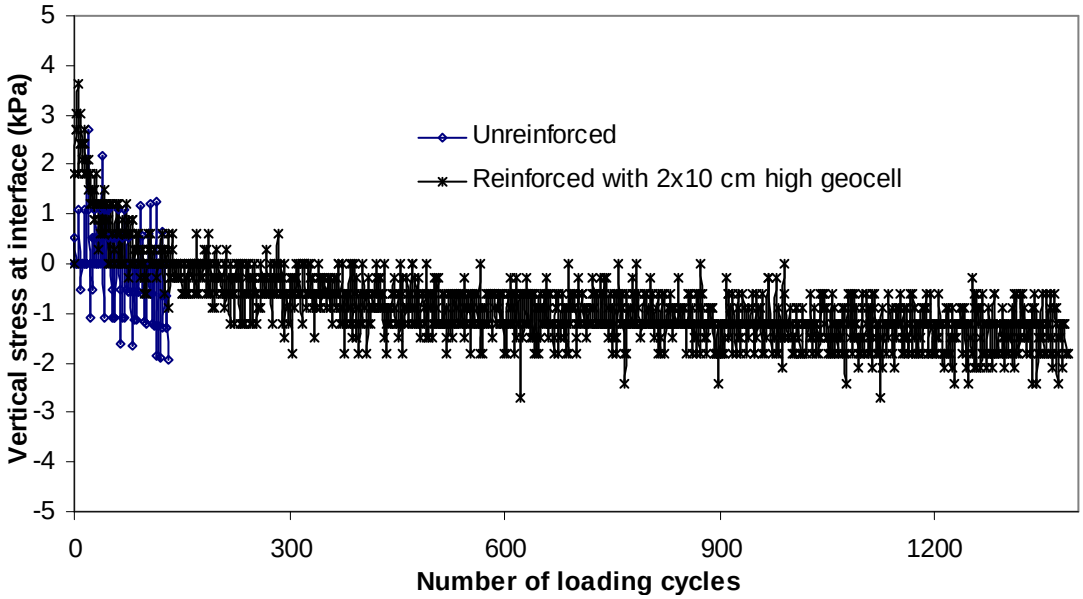

(d) 75 cm from the center

Figure 5.3.54 Comparison of the measured vertical stresses at the interface of subgrade and base at different locations away from the center in the 30 cm thick AB-3-I bases

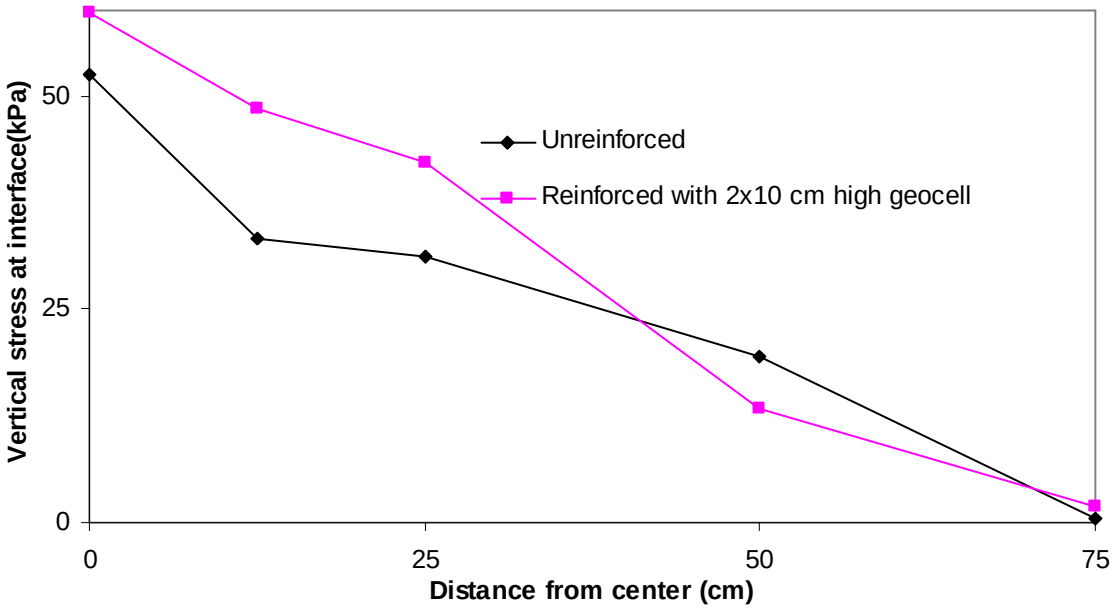

(a) Measured vertical stress at the interface at the end of first loading cycle

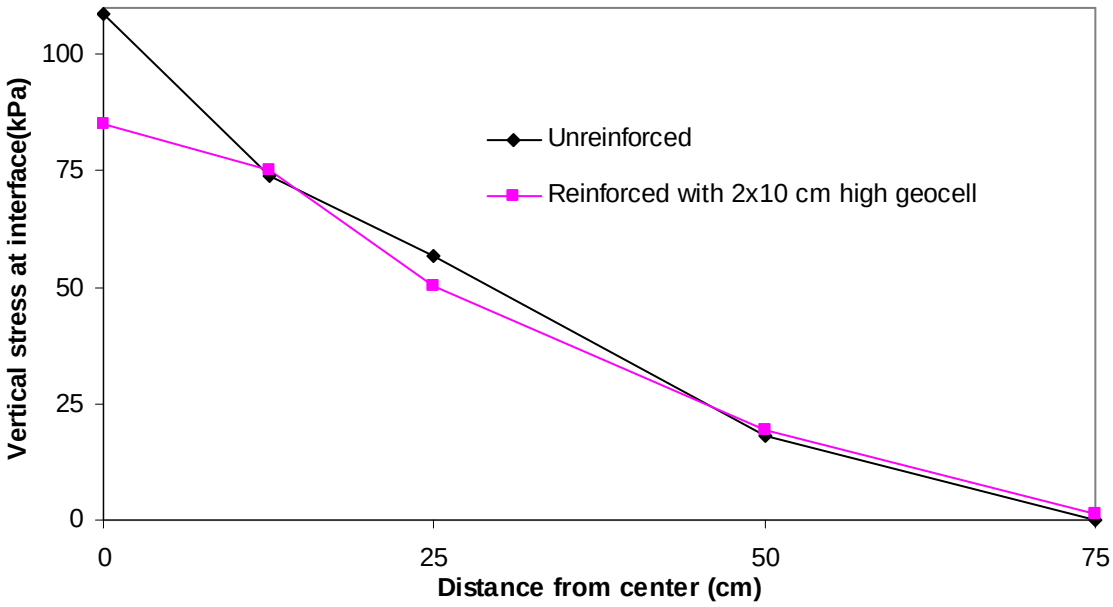

(b) Measured vertical stress at the interface at the end of 50 loading cycle

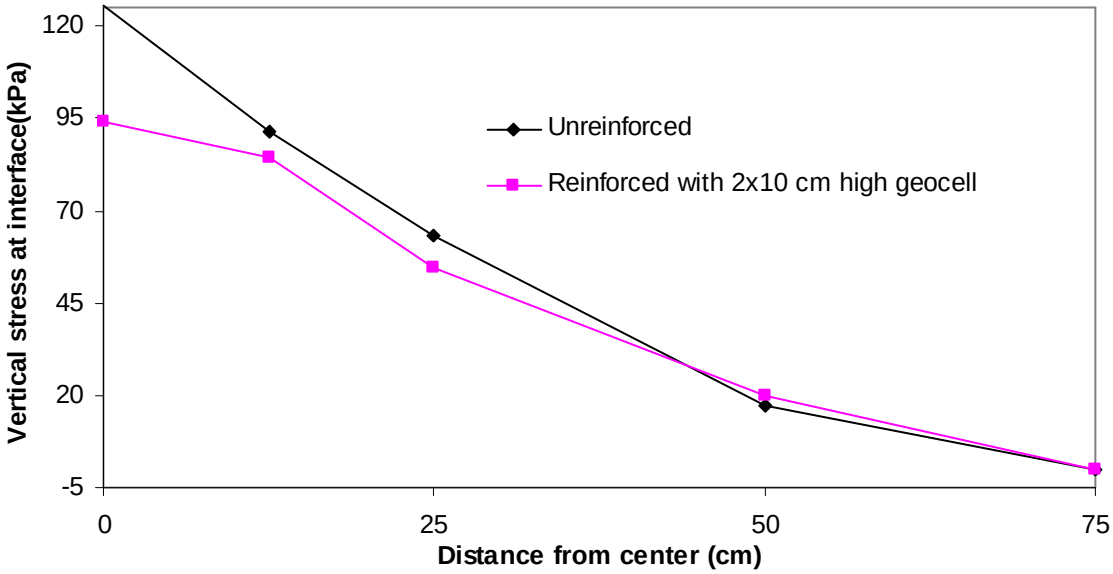

(c) Measured vertical stress at the interface at the end of 100 loading cycle

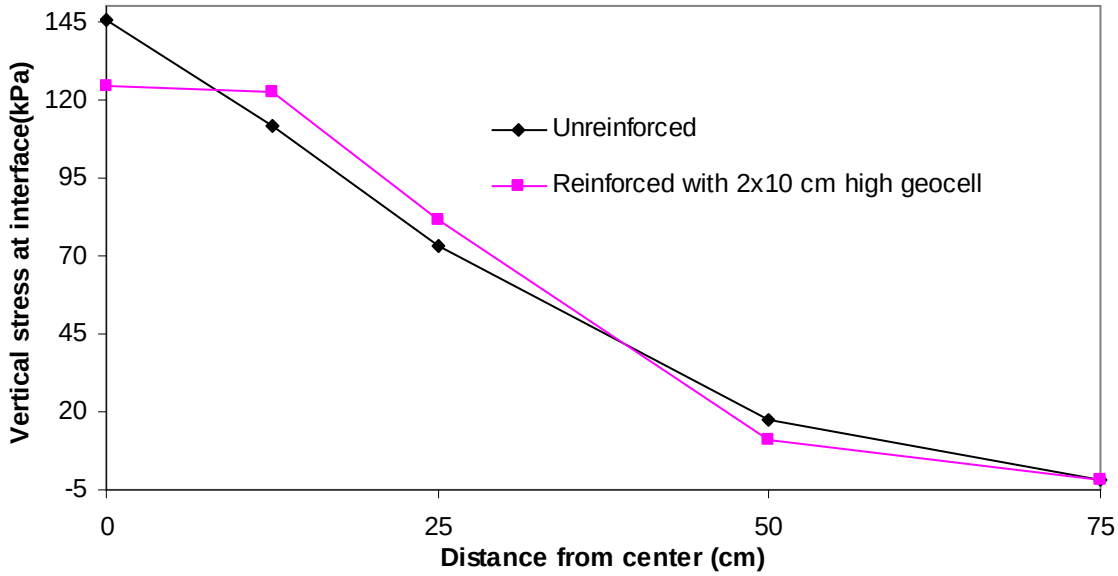

(d) Measured vertical stress at the interface at failure

Figure 5.3.55 Distributions of the measured vertical stresses at the interface of subgrade and base in the 30 cm thick unreinforced and reinforced AB-3-I bases at a given number of loading cycles

The calculated stress distribution angle with the number of loading cycles is shown in **Figure 5.3.56**. This comparison demonstrates that the geocell reinforcement slowed down the reduction of the stress distribution angle with the number of loading cycles.

The calculated stress distribution angles for the unreinforced and reinforced sections at the cycle corresponding to the end of the unreinforced section test were 25.3^{o} and 36.3^{o}, respectively.

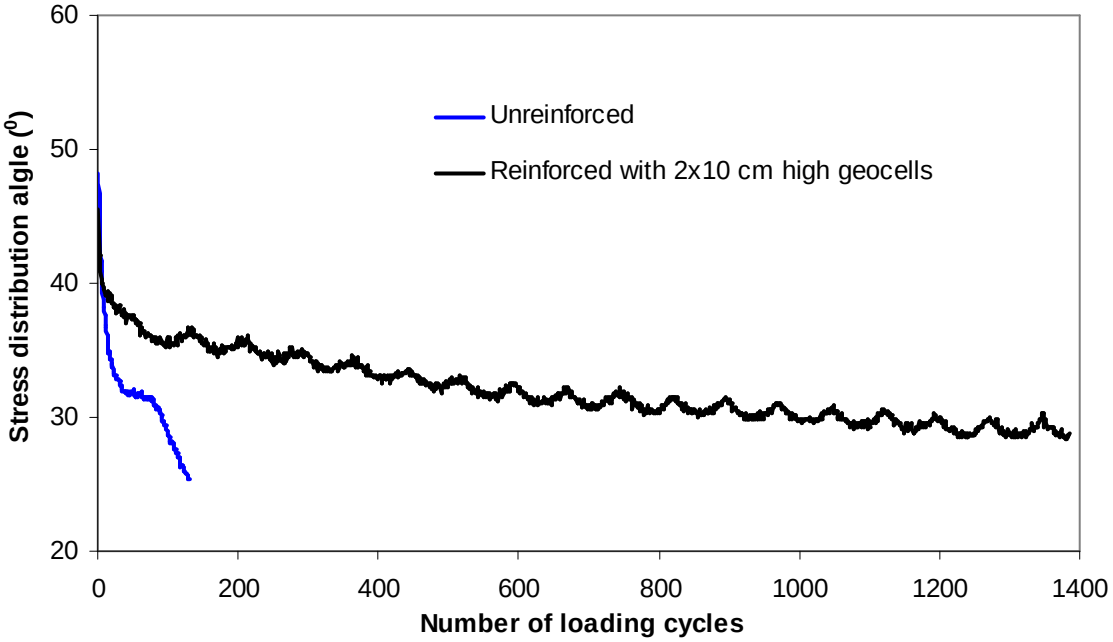

Figure 5.3.56 The calculated stress distribution angles for the 30 cm unreinforced and reinforced AB-3-I bases

e) Maximum strain in the geocell

Six strain gauges were installed on the geocell walls in each geocell layer. There were three gauges on the central geocell located right under the loading plate, one each at the

top, middle, and bottom of the geocell. Two gauges were installed at the top and middle of the geocell wall of the next adjacent geocell. One gauge was installed at the top of the cell further outside the loading plate. These strain gauges were located at the center, and 25 cm and 50 cm away from the center. Since there were only six connection points available for strain gauges on the data recorders, only six of the strain gauges were recorded during the entire test period; however, the initial and final strains were measured for other strain gauges. All the strain gauges affixed horizontally at the top and bottom of the geocell wall measured horizontal strains while the strain gauges affixed vertically at the middle of the wall measured the vertical strains. The positions of the strain gauges and the measured maximum values of strains in the geocell are shown in **Figure 5.3.57**.

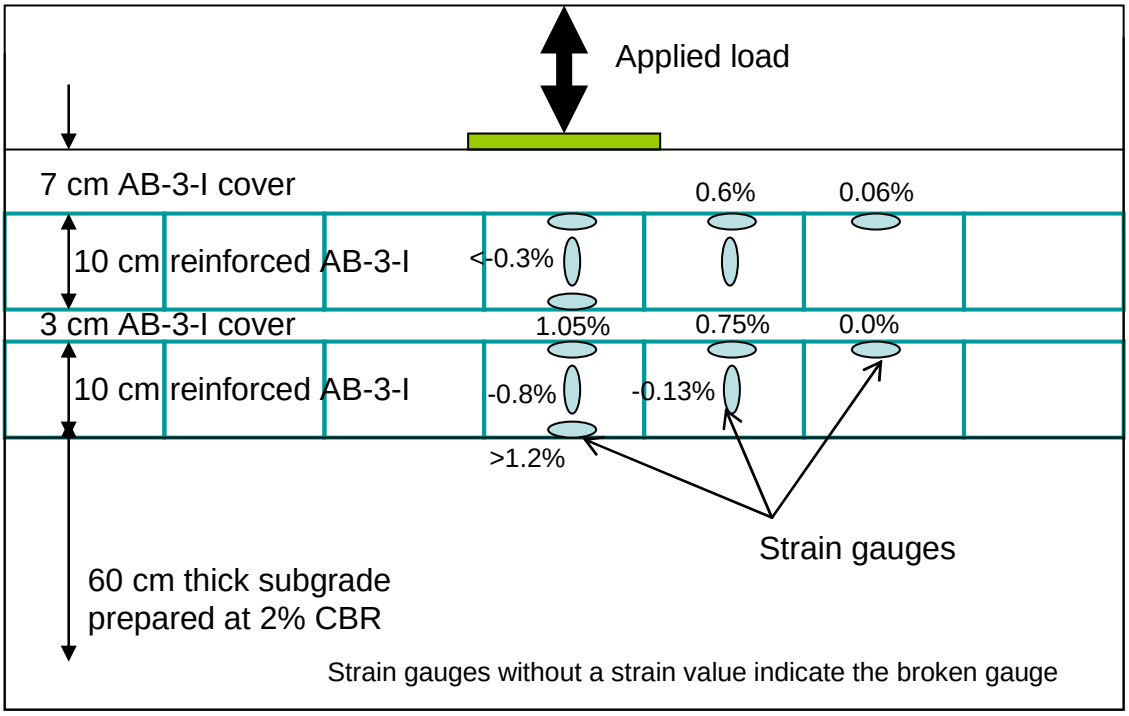

Figure 5.3.57 Measured maximum strains in the geocell in the 30 cm thick reinforced AB-3-I base

As shown in **Figure 5.3.57,** compressive strains were measured by all the vertical strain gauges, irrespective of whether they were on the top or bottom geocell layer. All the horizontal strain gauges experienced tensile stresses, the highest being at the bottom of the lower layer of geocell located right under the loading plate.

5.4 Cyclic Loading Tests on KR-I Sand Bases

Five cyclic plate loading tests on unreinforced and NPA geocell-reinforced KR-I sand bases (two unreinforced and three unreinforced) were performed. In all the test sections, an AB-3-I top cover was used. For the 15, 23, and 30 cm thick sections, 5, 8, and 7 cm top AB-3-I covers were used. As described in **Section 5.2,** the KR-I sand was compacted to 70% relative density and the AB-3-I cover was compacted to 95% relative compaction on the drier side of the compaction curve. The 15 cm thick unreinforced section failed at the very first cycle and did not even reach the maximum applied load of 522 kPa while the 23 cm thick unreinforced section failed at the second cycle. They both failed due to the weak sand base under low confinement. The 30 cm thick unreinforced section was not tested because it was expected to fail in the same way as other two unreinforced sections. Since the difference in the performance of the 15 cm and 23 cm thick unreinforced sections is minor, the test results of the 23 cm thick unreinforced section were presented and compared with those of the geocell-reinforced sections.

a) Vane shear, DCP, and sand cone tests

The results of the vane shear, DCP, and sand cone tests on the unreinforced and reinforced sections are given in **Table 5.4.1**. The profiles of the DCP data on the test sections are shown in **Figure 5.4.1**. The average CBR values of the subgrade obtained from the vane shear tests were 1.78% in the 23 cm thick unreinforced section, 1.70% in the 15 cm thick geocell-reinforced section, 1.60% in the 23 cm thick geocell-reinforced section, and 1.67% for in 30 cm thick geocell-reinforced section. The CBR values of the subgrade estimated from DCP tests were 2.2%, 2.3%, 1.6%, and 1.9% in the 23 cm thick unreinforced section, the 15 cm thick reinforced section, the 23 cm thick reinforced section, and the 30 cm thick reinforced section, respectively. The average CBR values of the KR-I sand bases estimated from the DCP data were 2.0% in the 23 cm thick unreinforced section, 4.0% in the 15 cm thick reinforced section, 2.9% in the 23 cm thick reinforced section, and 4.7% in the 30 cm thick reinforced section. The CBR values of the AB-3-I top cover estimated from the DCP data were 10.5% for the 23cm thick unreinforced section, 16.3% for the 15 cm thick reinforced section, 14.4% for the 23 cm thick reinforced section, and 14.0% for the 30 cm thick reinforced section. Sand cone tests were carried out after each cyclic plate loading test and showed that the 23 cm thick unreinforced section achieved 89.5% relative compaction. The 15 cm thick reinforced section, the 23 cm thick reinforced section, and the 30 cm thick reinforced section had 90.5%, 95.5%, and 95% relative compaction, respectively.

Table 5.4.1 Average CBR values from vane shear and DCP tests and relative compaction and moisture from sand cone tests

Test section	Vane shear subgrade	DCP subgrade	DCP (base course)		Sand cone after test KR-I sand layer	
			AB-3-I cover	KR-I sand		
	CBR (%)	CBR (%)	CBR (%)	CBR (%)	Relative compaction (%)	Moisture content (%)
Unreinforced (15 cm thick)	1.85	1.99	13.9	0.78	86.0	4.99
Unreinforced (23 cm thick)	1.78	2.2	10.5	2.0	89.5	4.84
Reinforced (15 cm thick)	1.75	2.3	16.3	4.0	95.5	4.18
Reinforced (23 cm thick)	1.60	1.6	14.4	2.9	90.5	5.31
Reinforced (30 cm thick)	1.67	1.9	14.0	4.7	95.0	4.43

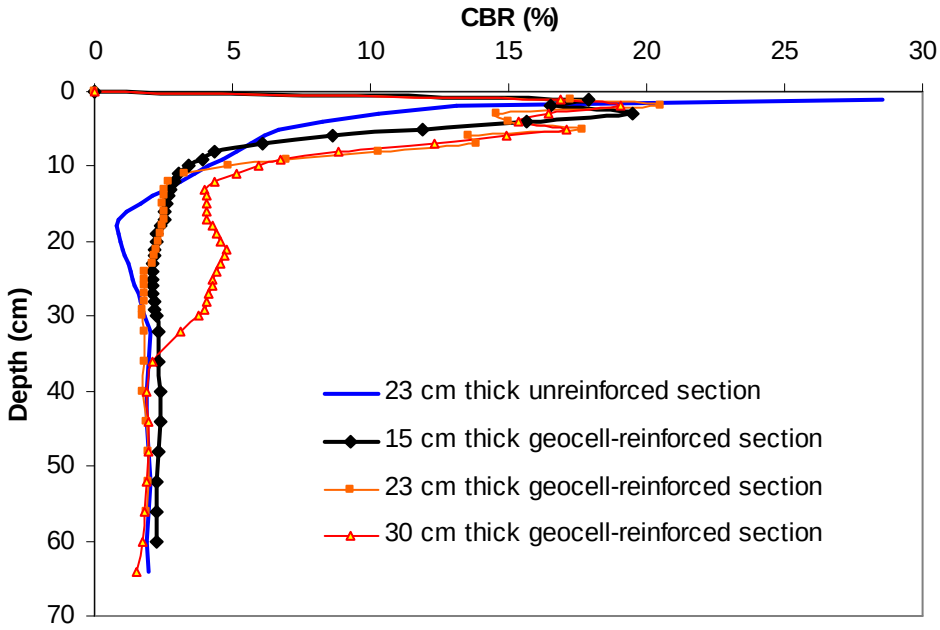

Figure 5.4.1 CBR profiles obtained from the DCP tests in KR-I bases over weak subgrade

b) Deformed profiles

The number of loading cycles reaching 75 mm permanent deformation was reached at 2 cycles for the 23 cm unreinforced 23 cm thick unreinforced section, 26 cycles for the 15 cm thick geocell-reinforced section, 18 cycles for the 23 cm thick geocell-reinforced section, and 228 cycles for the 30 cm cm thick geocell-reinforced (including two 10 cm high geocells) section. After all the cyclic plate loading tests, all the test sections were exhumed and trenches were cut to examine the deformed profiles and geocells. The deformed profiles are plotted in **Figures 5.4.2** through **5.4.5**. Forensic tests showed that the shape and size of the cells were intact outside the loading plate. However, the geocells under the area of the loading plate were found to change their shape into a circular shape; the seam side was slightly reduced and the transverse direction was slightly enlarged. Welds of the geocell located under the loading plate were broken at the bottom edges in all three reinforced

sections. For the 15 and 23 cm thick geocell-reinforced sections, the geocells were also compressed in the vertical direction. However, the weld failure and the compression of geocells were not observed in the 30 cm thick geocell-reinforced section. There were no distinct crack lines observed away from the center in the 15 cm and 23 cm thick geocell-reinforced sections; however, there was a distinct line of crack in the 30 cm thick geocell-reinforced section. The pictures of these test sections are shown in **Figures 5.4.6** through **5.4.12**.

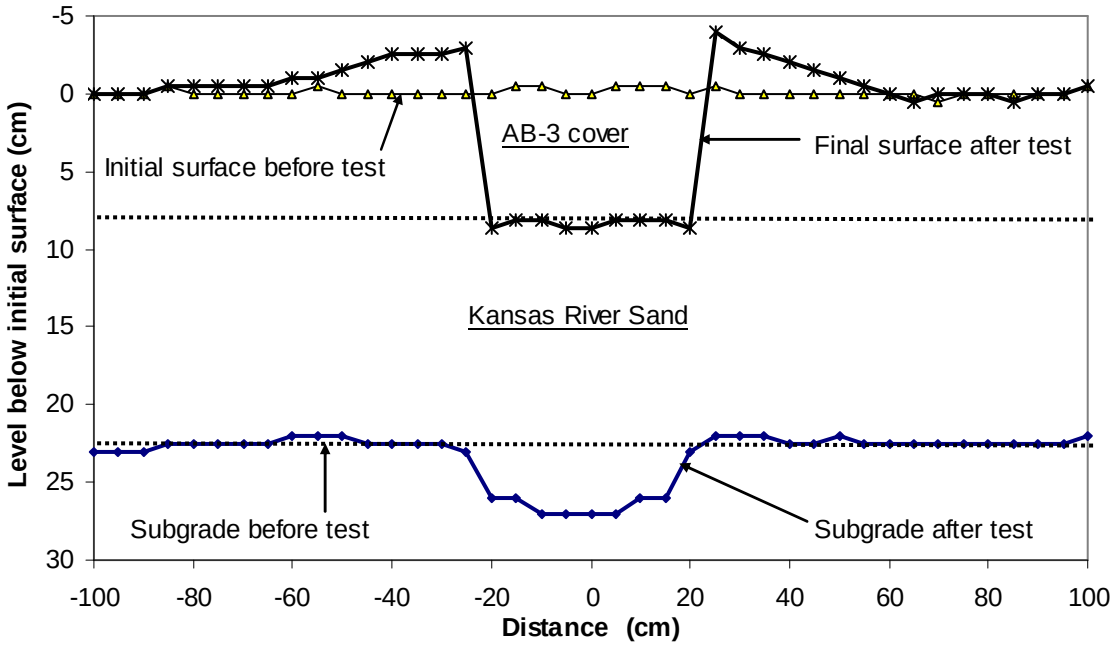

Figure 5.4.2 Profile of the 23 cm thick unreinforced KR-I sand base section after 2 loading cycles

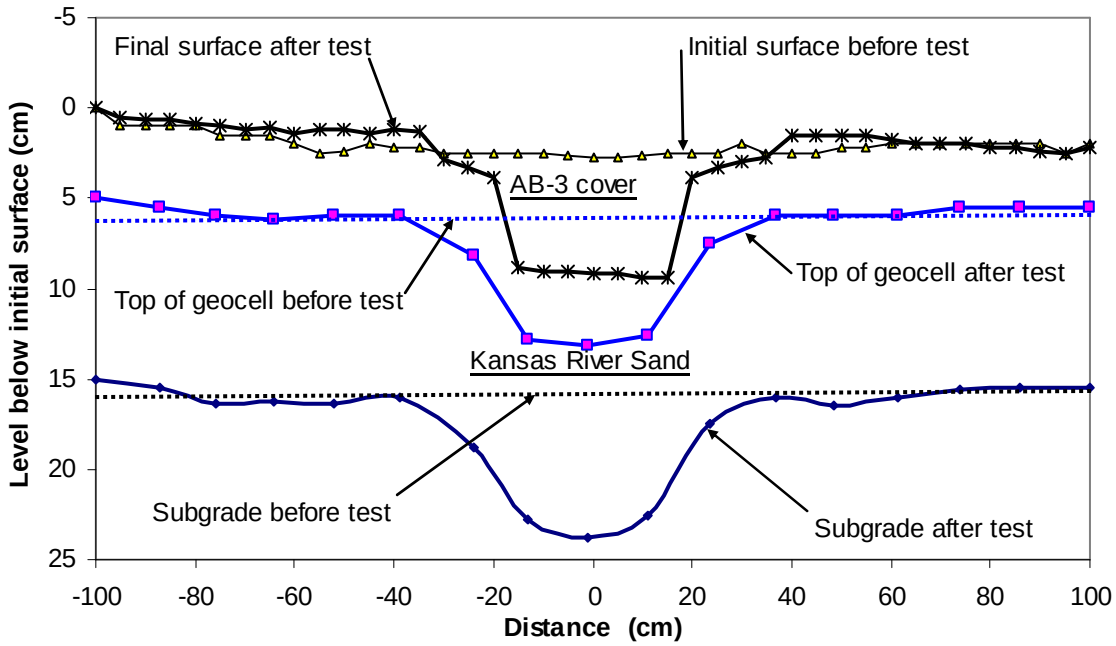

Figure 5.4.3 Profile of the 10 cm high geocell-reinforced KR-I sand base section after 26 loading cycles

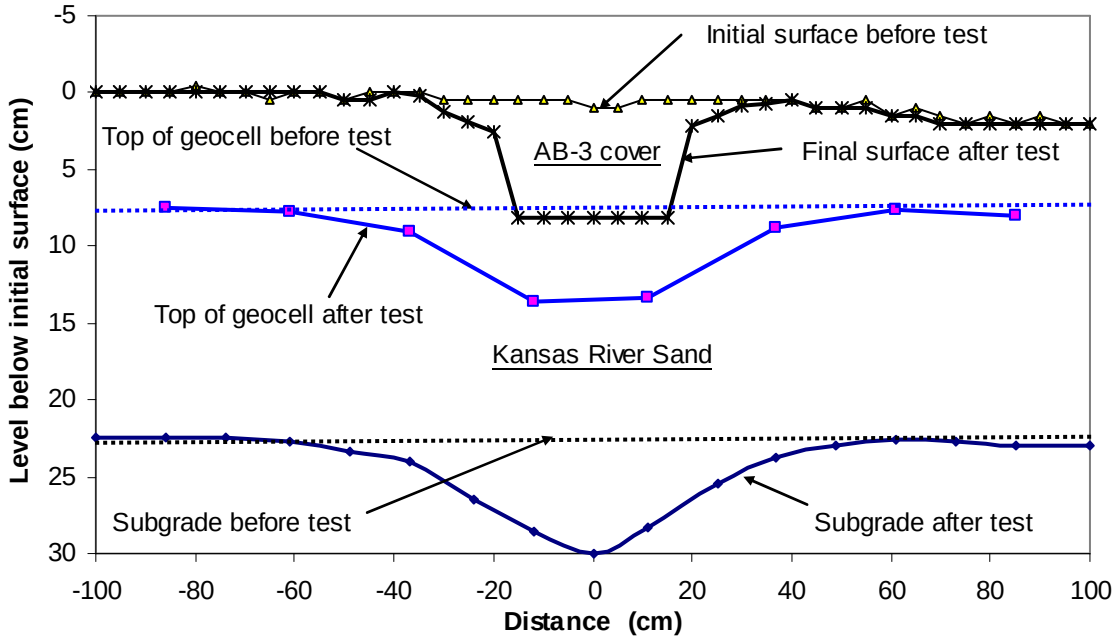

Figure 5.4.4 Profile of the 15 cm high geocell-reinforced KR-I sand base section after 18 loading cycles

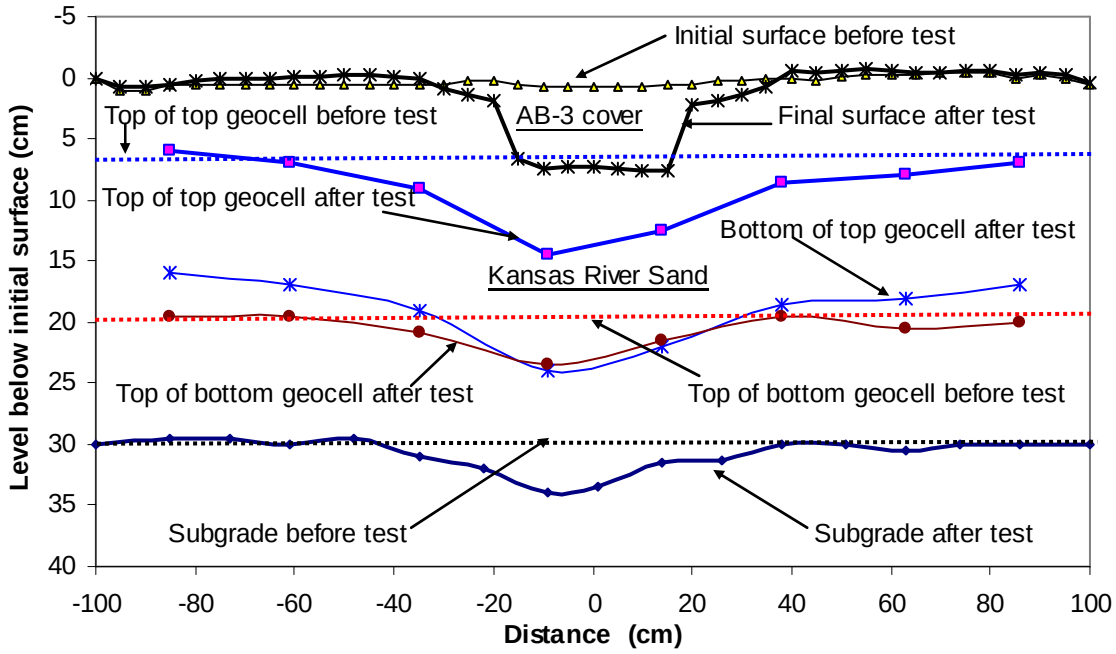

Figure 5.4.5 Profile of the 2x10 cm high geocell-reinforced KR-I sand base section after 228 loading cycles

Figure 5.4.6 Unreinforced section under the plate after failure

Figure 5.4.7 10 cm high geocell-reinforced 15 cm thick section after failure

Figure 5.4.8 Weld failure under the loading plate in case of 10 cm high geocell-reinforced 15 cm thick section

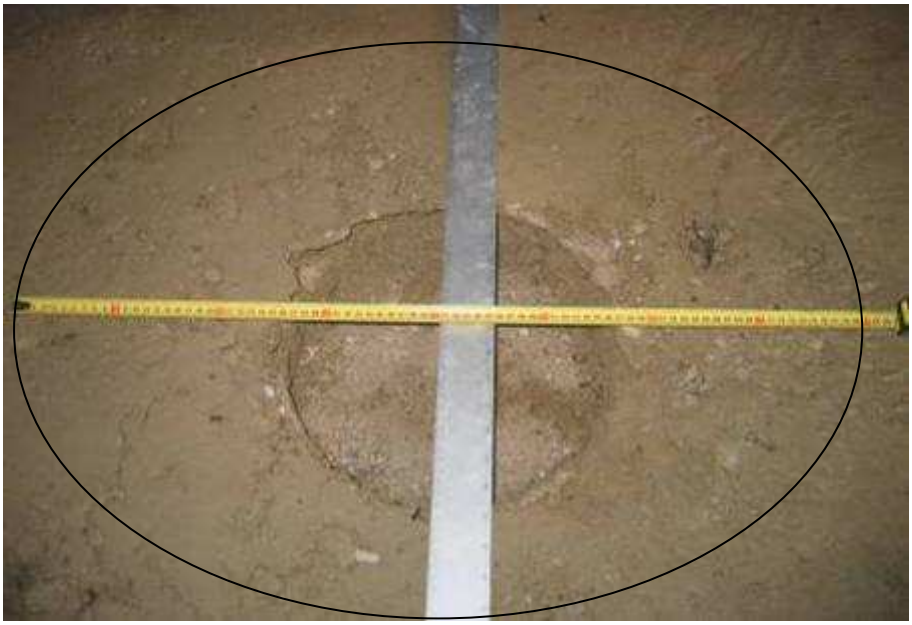

Figure 5.4.9 15 cm high geocell-reinforced 23 cm thick section after failure

Figure 5.4.10 Weld failure under the loading plate in case of 15 cm high geocell-reinforced 23 cm thick section

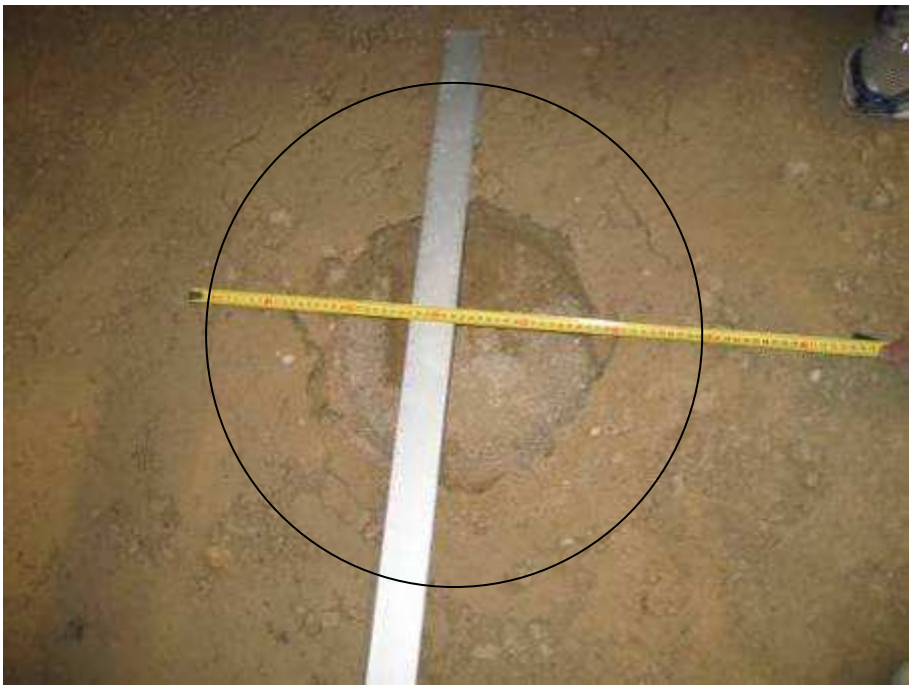

Figure 5.4.11 2x10 cm high geocell-reinforced 30 cm thick section after failure

Figure 5.4.12 Weld failure under the loading plate in case of 2x10 cm high geocell-reinforced 30 cm thick section

c) Permanent deformations with the number of loading cycles

Figures 5.4.13 through **5.4.16** show the permanent deformations of the unreinforced and reinforced sections at the center and 25 cm, 50 cm, and 75 cm away from the center of the loading plate at different loading cycles. In the 23 cm thick unreinforced section, there was a significant amount of heave at the locations of 25 cm and 50 cm away from the center, but there was no deformation at 75 cm away form the center. The significant amount of heave resulted from the failure of the sand base. In all the reinforced sections, a small amount of compression was observed at 25 cm away from the center and heaving was observed at 50 cm and 75 cm away from the center.

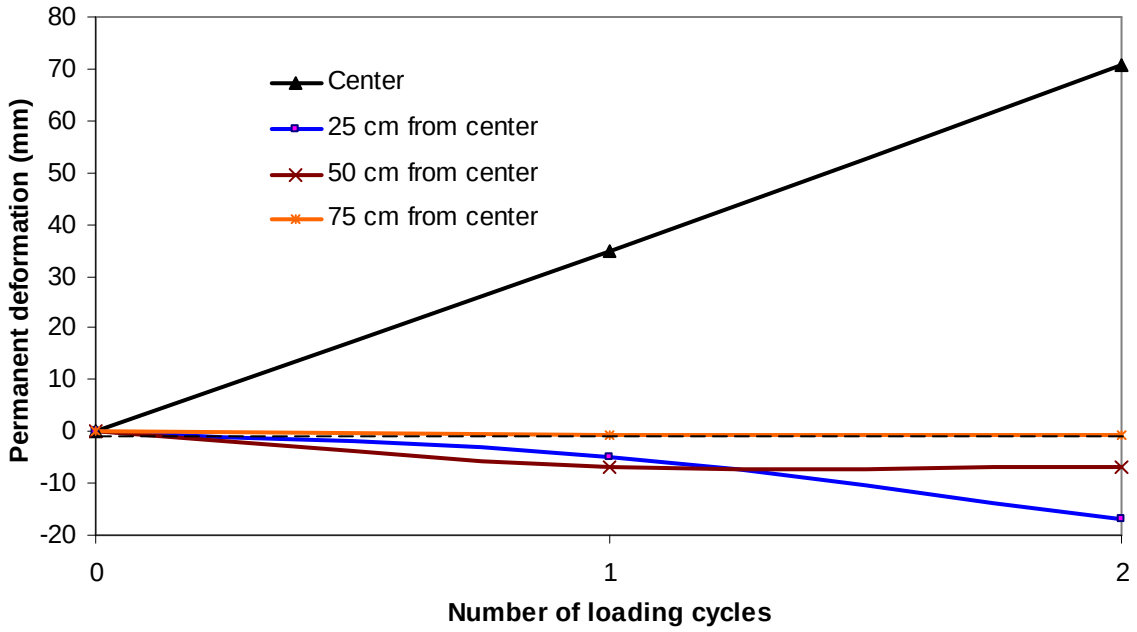

Figure 5.4.13 Permanent deformations versus the number of loading cycles for the 23 cm thick unreinforced KR-I sand base section

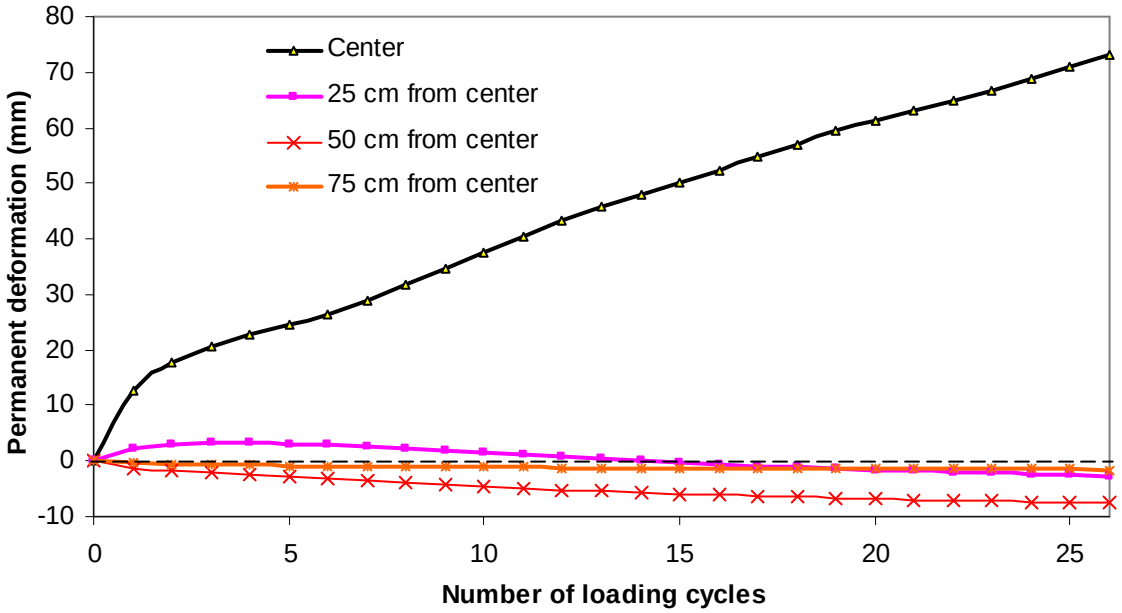

Figure 5.4.14 Permanent deformations versus the number of loading cycles for the 10 cm high geocell-reinforced KR-I sand base section

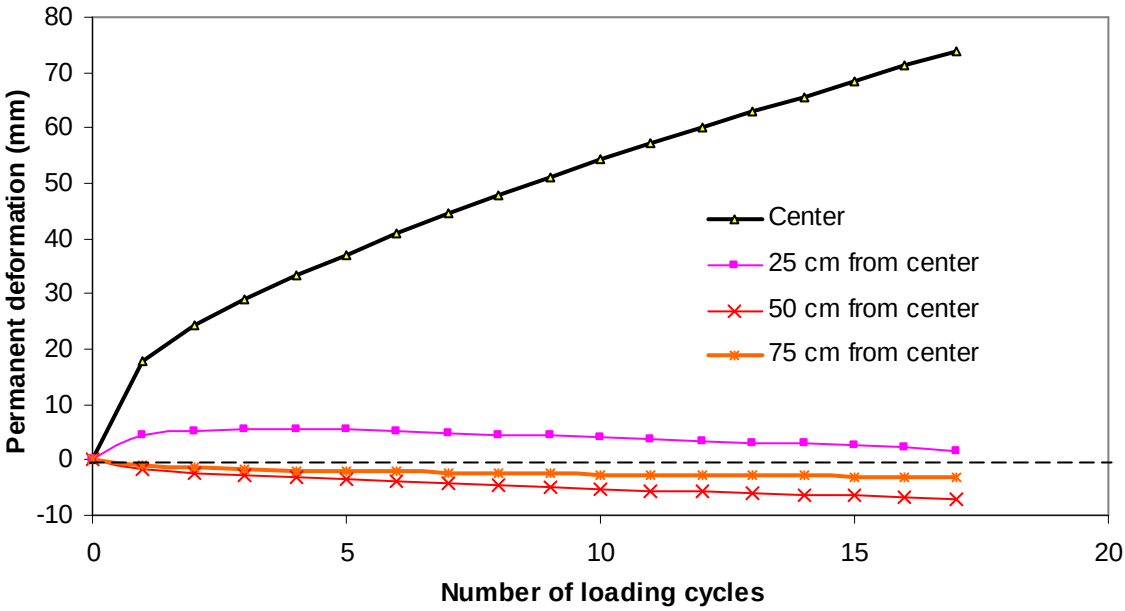

Figure 5.4.15 Permanent deformations versus the number of loading cycles for the 15 cm high geocell-reinforced KR-I sand base section

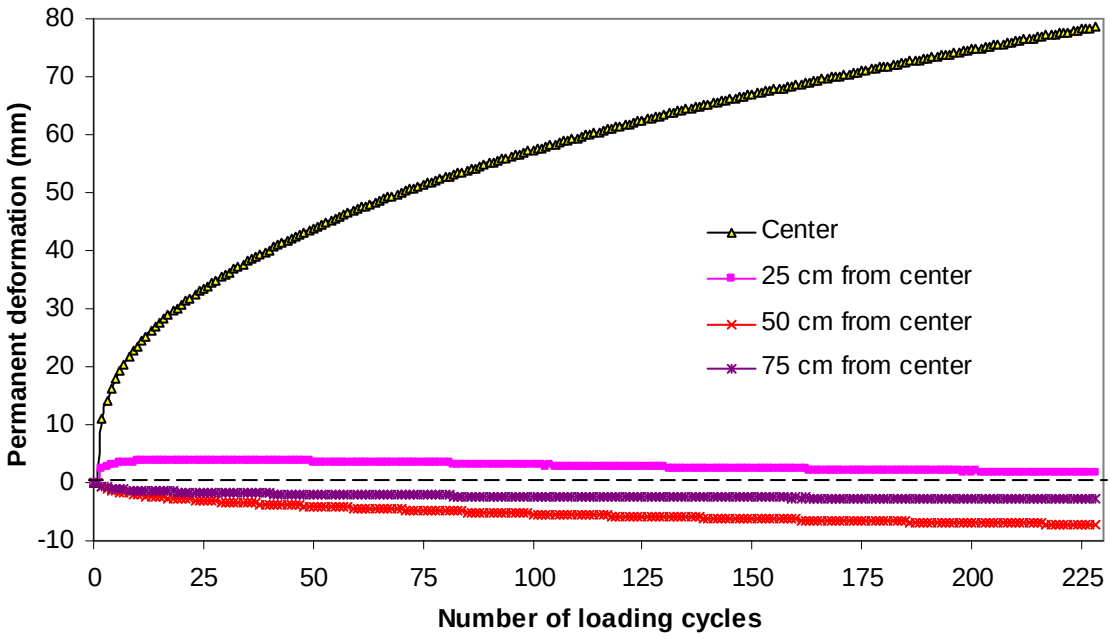

Figure 5.4.16 Permanent deformations versus the number of loading cycles for the 30 cm high geocell-reinforced KR-I sand base section

The comparison of permanent deformations of the unreinforced and reinforced sections under the loading plate is given in **Figure 5.4.17**. The benefit of geocell reinforcement is clearly evident form this comparison. At the permanent deformation of 75 mm, the 23 cm thick unreinforced base section lasted for just 2 cycles while the 15 cm, 23 cm, and 30 cm thick NPA geocell-reinforced base sections lasted for 26, 18, and 228 cycles, respectively. This result shows that the geocell reinforcement improved the performance of the base section by a factor of 9 to 114 over the unreinforced section.

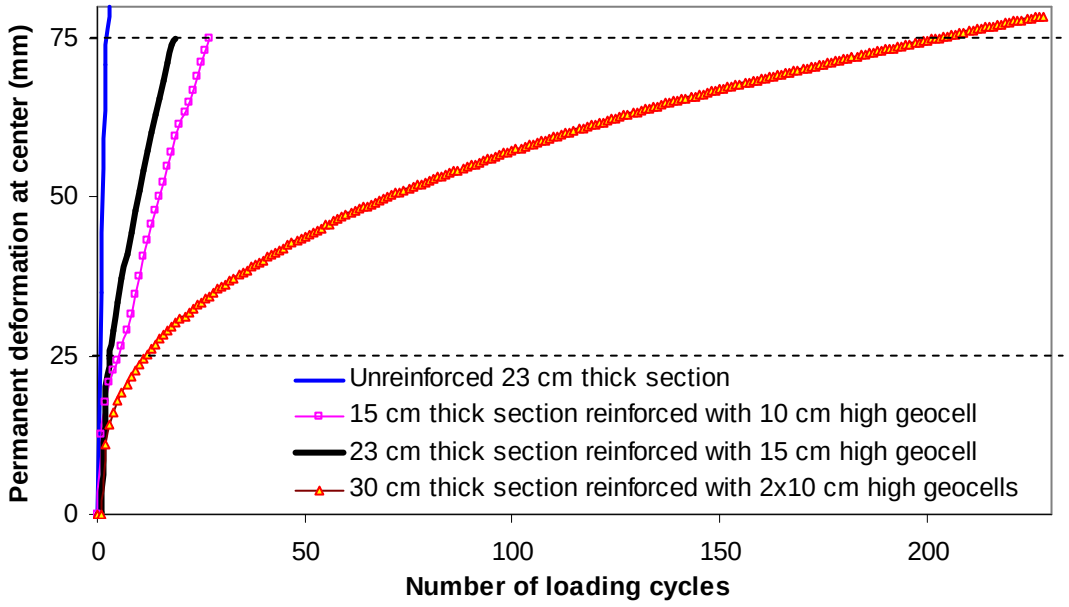

Figure 5.4.17 Comparison of the permanent deformations of unreinforced and reinforced sections at the center with KR-I sand bases

Figure 5.4.18 shows the comparison of percentages of elastic deformation of the unreinforced and reinforced base sections at the center. The unreinforced section had only 4.6% elastic deformation of the total deformation per each cycle at the end of the test whereas the reinforced sections had 78.8 to 99.3% elastic deformation.

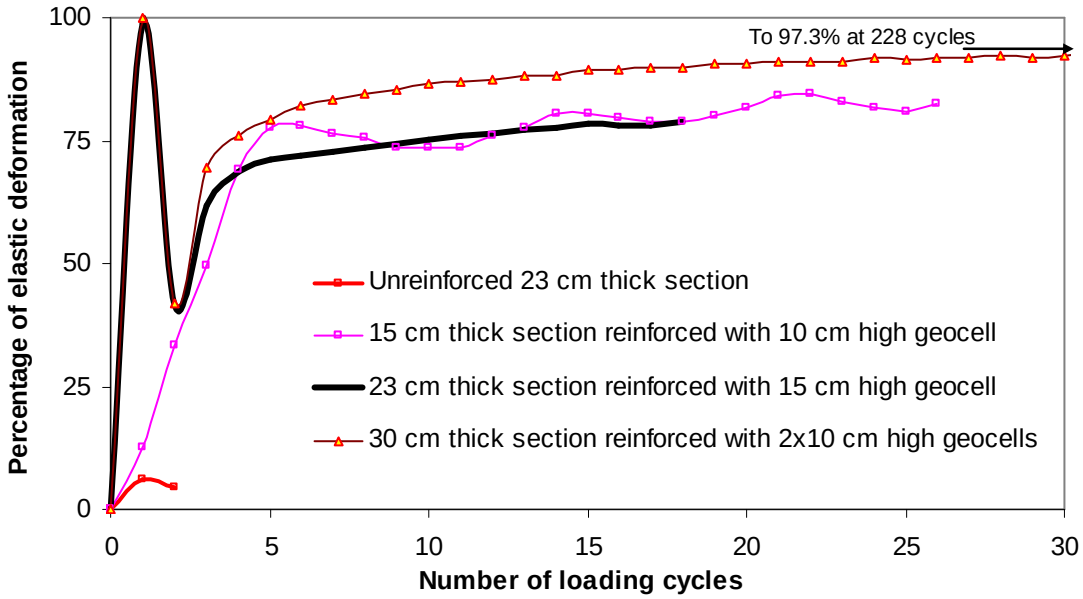

Figure 5.4.18 Percentage of elastic deformation at the center

d) Measured vertical stresses at the subgrade-base interface

The vertical stresses at the interface of subgrade and base course were measured by the pressure cells located at five locations on the straight line passing through the center. **Figures 5.4.19** through **5.4.22** show the vertical stresses measured at the given locations of the interface with the number of loading cycles. The vertical stresses measured at the center of the 23 cm thick unreinforced section and the 15 cm, 23 cm, and 30 cm thick NPA geocell-reinforced sections were 509 kPa, 261 kPa, 205 kPa, and 140 kPa, respectively. The measured vertical stresses at the interface under the center of the loading plate on the unreinforced and reinforced bases are shown in **Figure 5.4.23**. It is shown that the measured vertical stress in the unreinforced section was close to the applied pressure of 552 kPa on the surface while those in the reinforced section were much lower than the applied pressure.

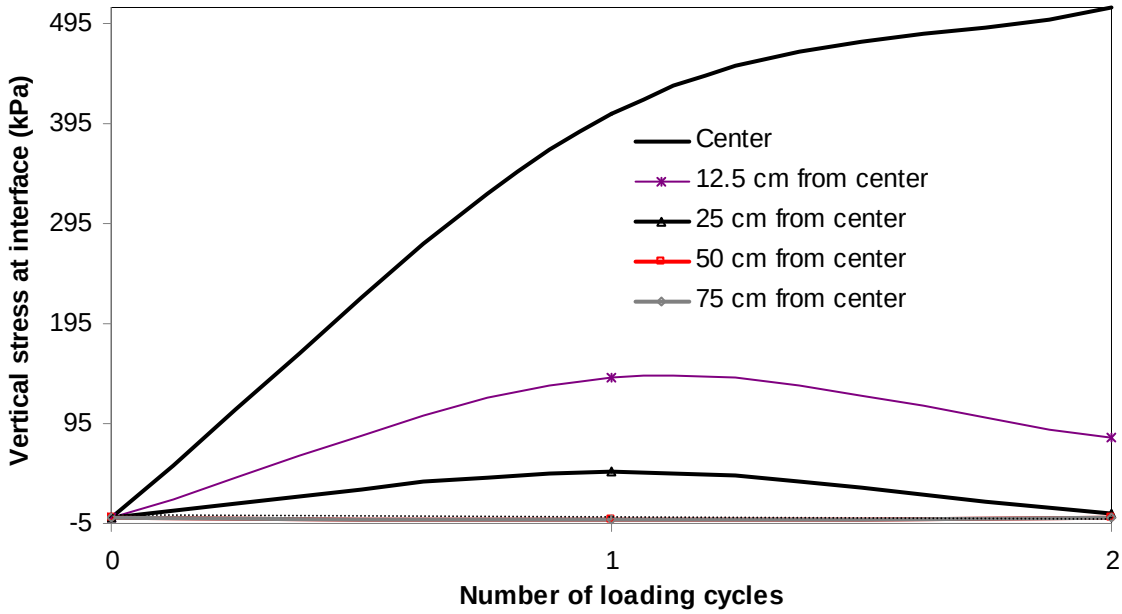

Figure 5.4.19 Measured vertical stresses at the subgrade-base interface in the 23 cm thick unreinforced KR-I sand base

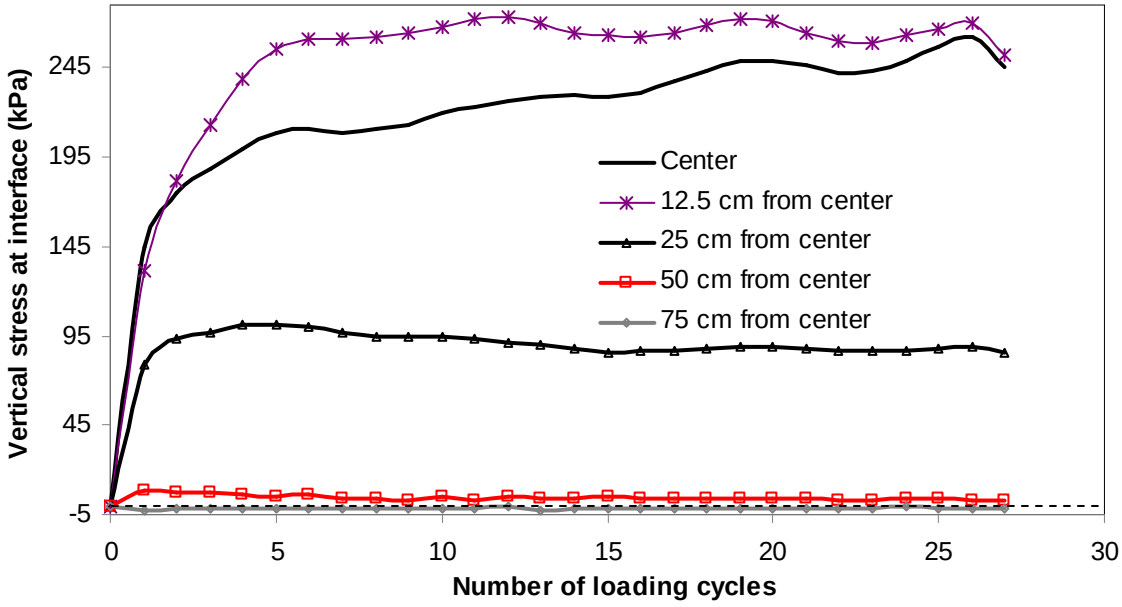

Figure 5.4.20 Measured vertical stresses at the subgrade-base interface in the 15 cm thick geocell-reinforced KR-I sand base

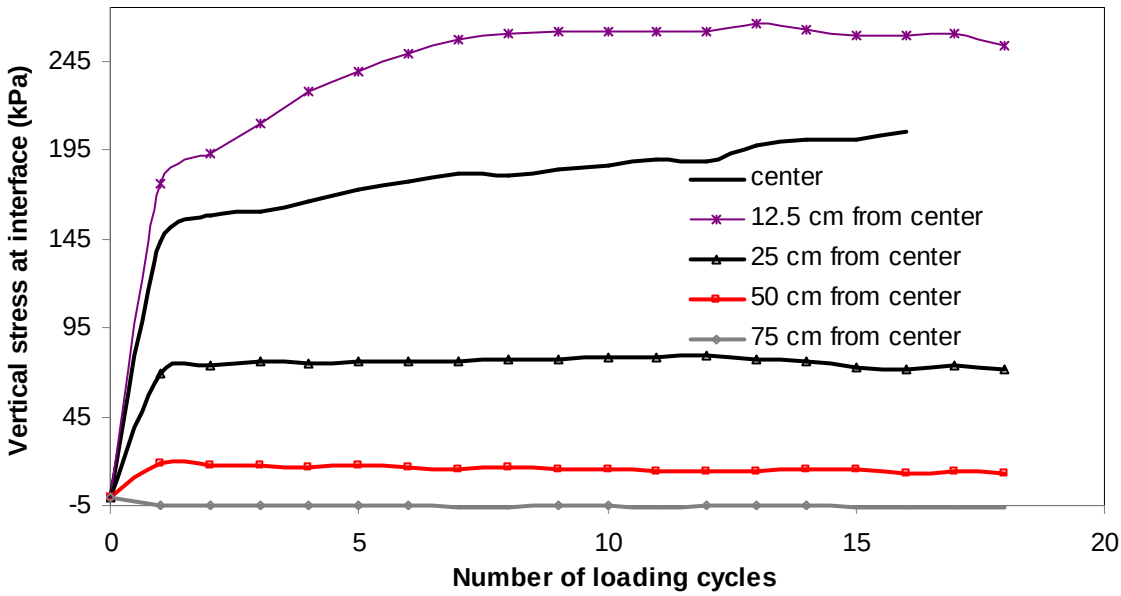

Figure 5.4.21 Measured vertical stresses at the subgrade-base interface in the 23 cm thick geocell-reinforced KR-I sand base

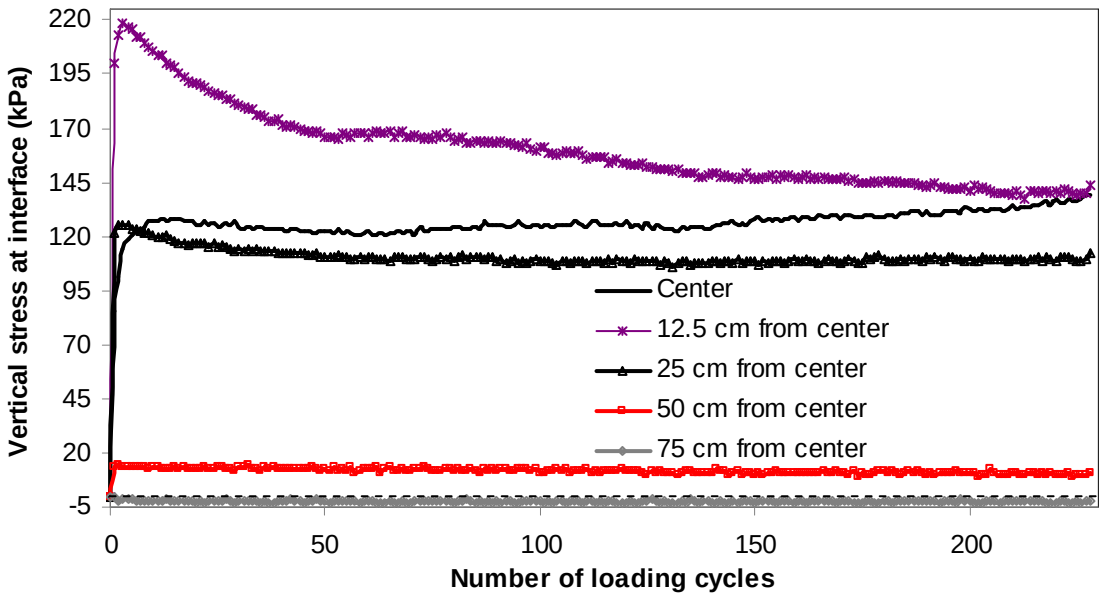

Figure 5.4.22 Measured vertical stresses at the subgrade-base interface in the 30 cm thick geocell-reinforced KR-I sand base

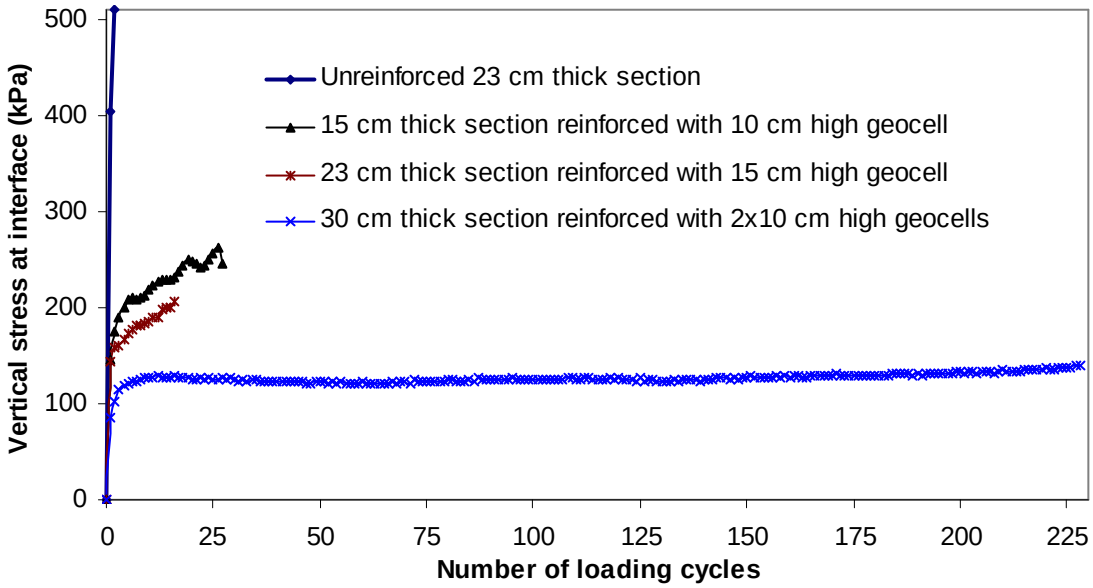

Figure 5.4.23 Comparison of the measured vertical stresses at the interface of subgrade and base course at the center in unreinforced and reinforced KR-I sand section

The measured vertical stresses at the interface of subgrade and base at different locations away from the center are shown in **Figure 5.4.24**. The vertical stresses at the first cycle, 10th cycle, and at the end of the tests for the unreinforced and reinforced sections are shown in **Figure 5.4.25**.

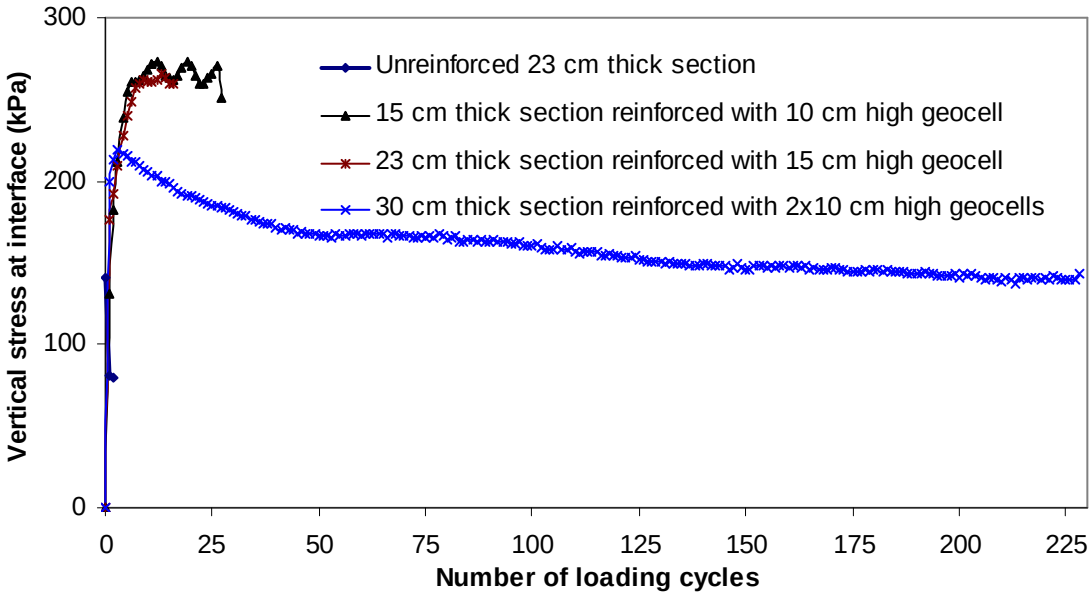

(a) 12.5 cm from the center

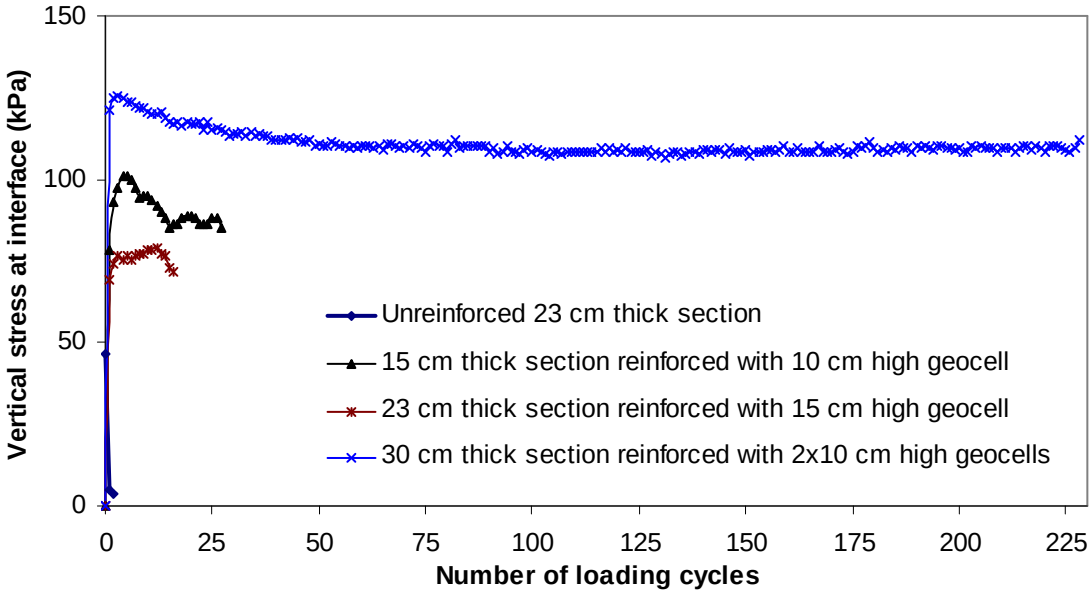

(b) 25 cm from the center

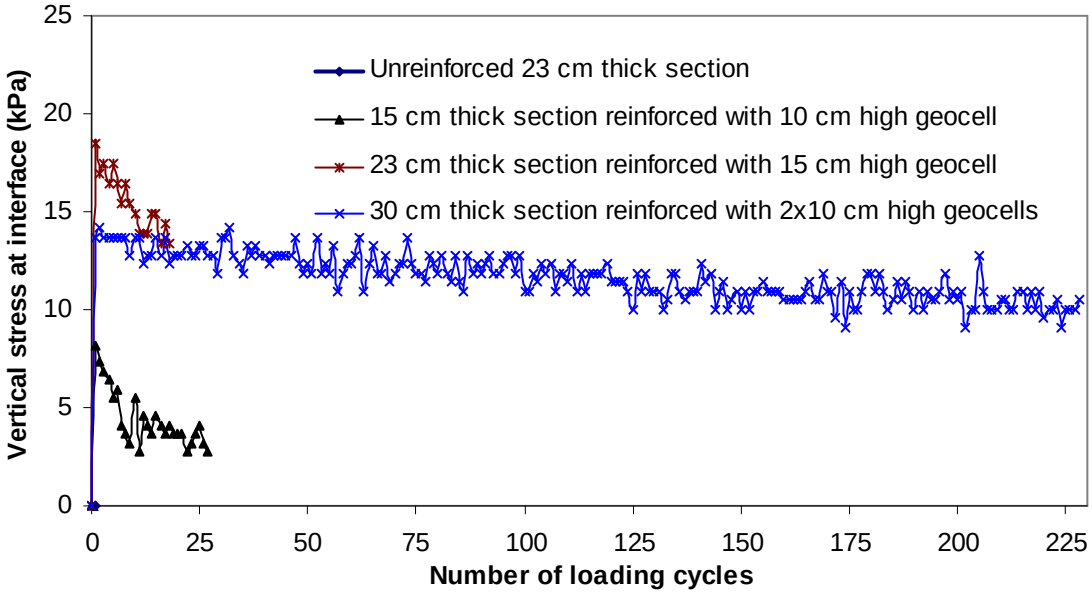

(c) 50 cm from the center

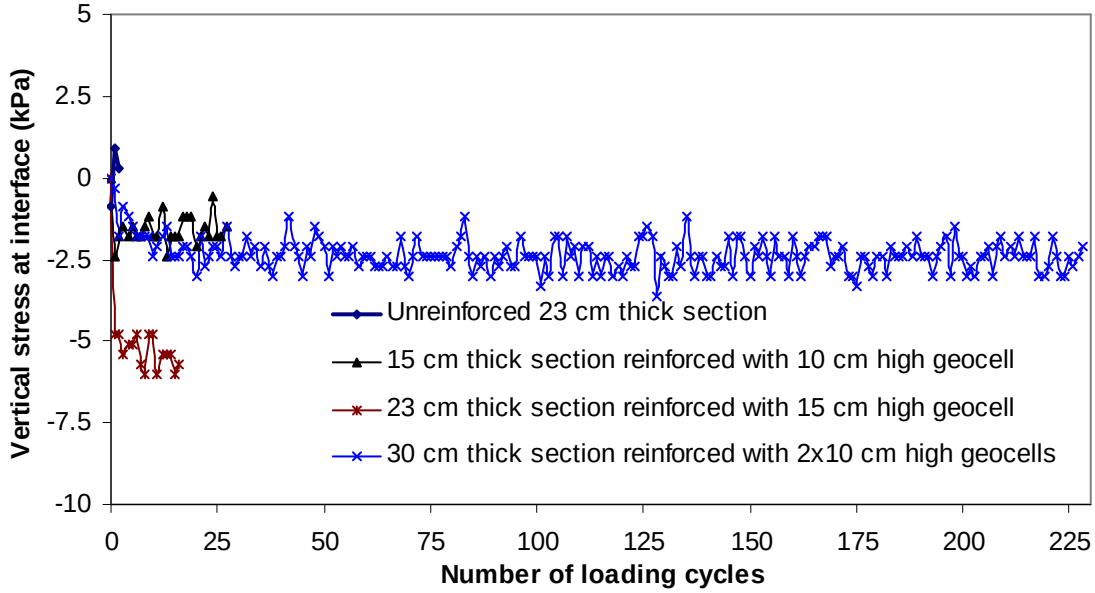

(d) 75 cm from the center

Figure 5.4.24 Comparison of the measured vertical stresses at the interface of subgrade and base at different locations away from the center KR-I sand bases

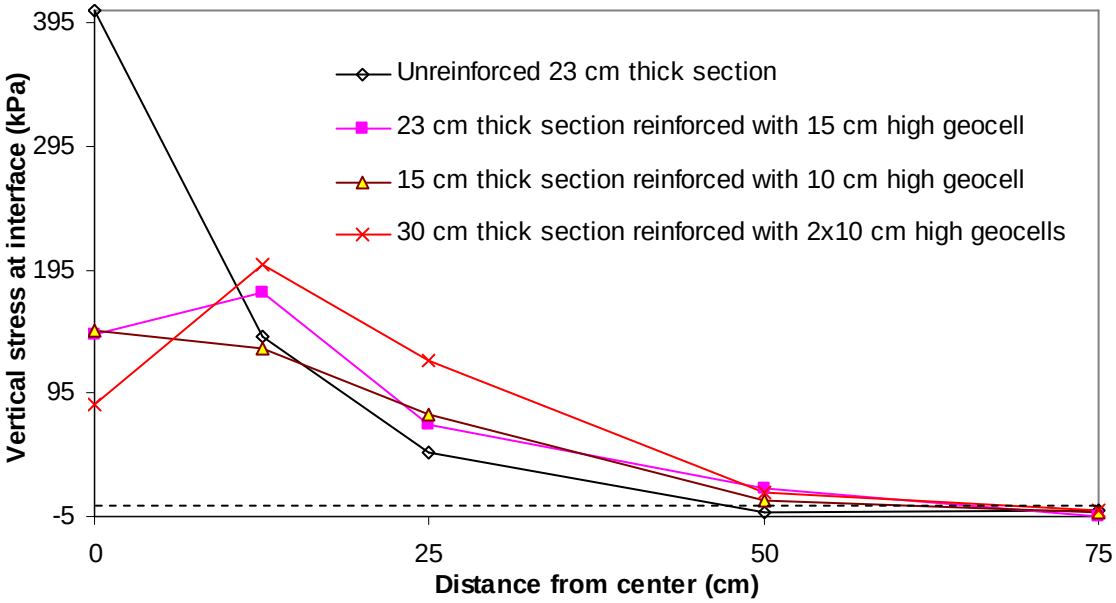

(a) Measured vertical stress at the interface at the end of first loading cycle

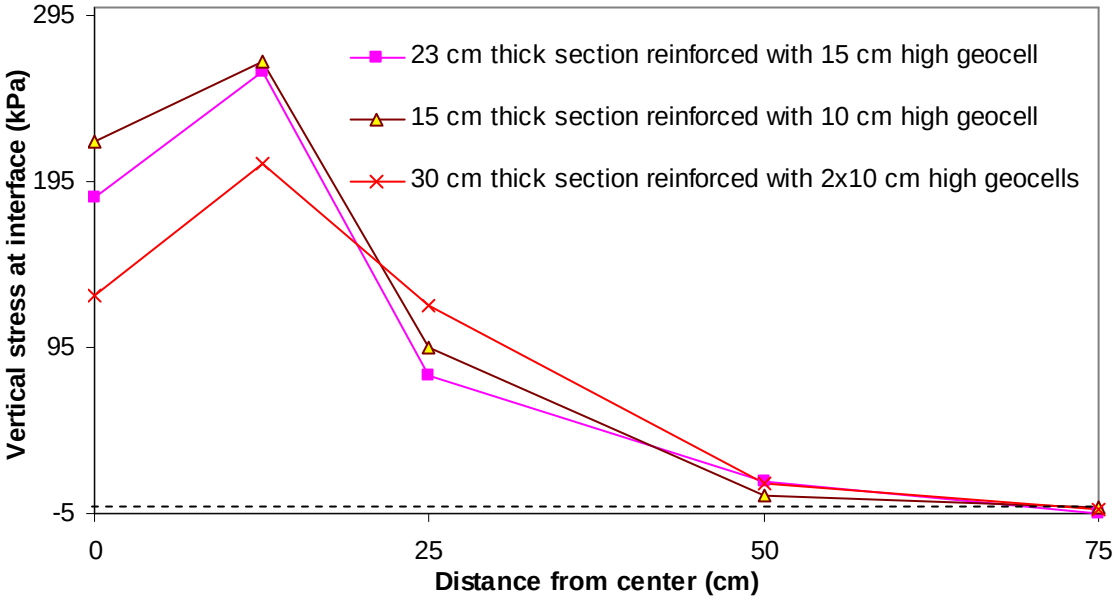

(b) Measured vertical stress at the interface at the end of 10 loading cycles

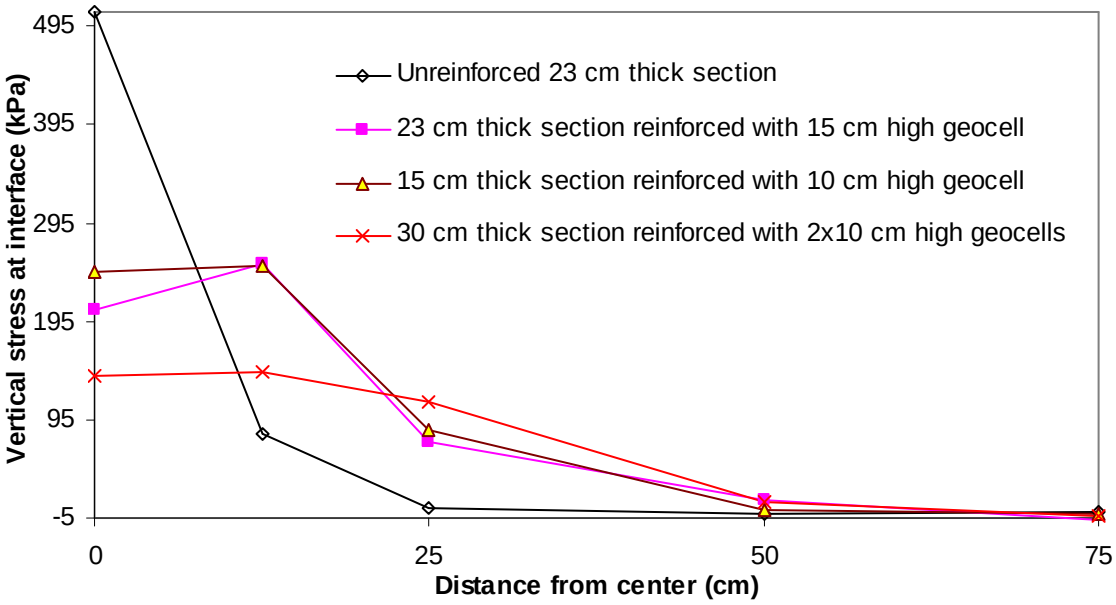

(c) Measured vertical stress at the interface at failure

Figure 5.4.25 Distributions of the measured vertical stresses at the interface of subgrade and base in the KR-I sand bases at a given number of loading cycles

The calculated stress distribution angles for the unreinforced and reinforced sections with the number of loading cycles are shown in **Figure 5.4.26**. The calculated stress distribution angle for the unreinforced section at the end of the test was 1.5^{o}. The calculated stress distribution angles for the 15 cm, 23 cm, and 30 cm thick NPA geocell-reinforced sections at the cycle corresponding to the end of the unreinforced section test were 37.6^{o}, 29.6^{o}, and 33.5^{o}, respectively. This comparison demonstrates that geocell reinforcement reduced the vertical stress by distributing the load to a wide area.

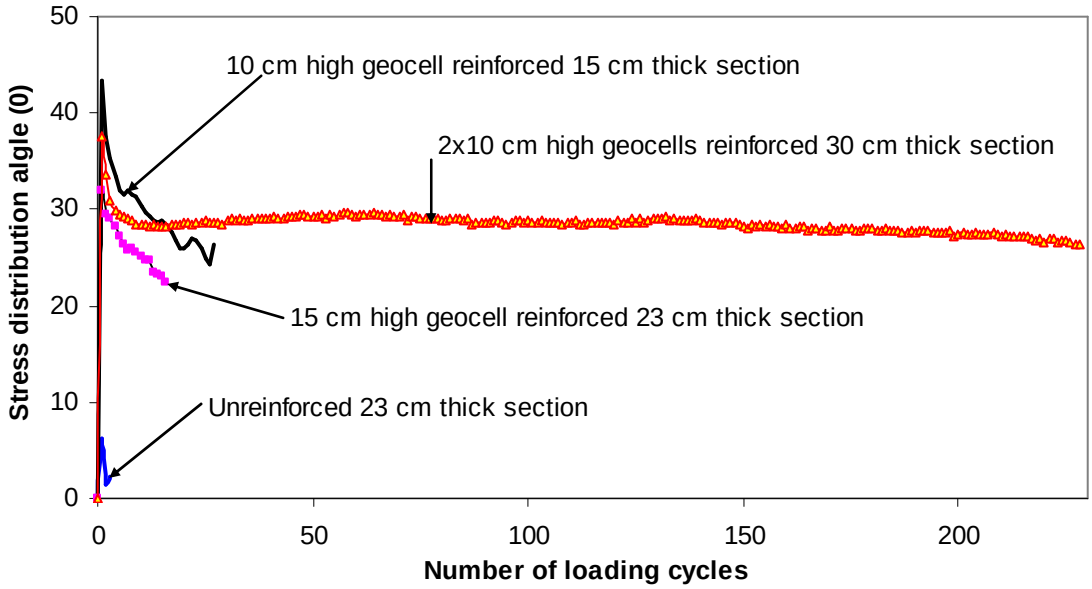

Figure 5.4.26 The calculated stress distribution angles for the unreinforced and reinforced KR-I sand bases

e) Maximum strain in geocell reinforcement

In each one layer geocell-reinforced test section, six strain gauges were installed on the geocell walls while in the double layer geocell-reinforced section six strain gauges were affixed on each layer of geocell. In each geocell layer, there were three strain gauges at the central geocell located right under the loading plate (one each at the top, middle, and bottom); two gauges at the top and middle of the geocell wall in the next adjacent geocell; and one gauge at the top of the cell further outside the loading plate. The strain gauges were located at the center, and at 25 cm and 50 cm away from the center. As already mentioned in Section 5.3.3e, only six of the strain gauges were recorded during the entire test period; however, the initial and final strains were measured for other strain gauges. The positions of the strain gauges and the measured maximum strains are shown in **Figures 5.4.27** through **5.4.29**. All

the strain gauges affixed at the top and bottom of the geocell wall measured horizontal strains while the strain gauges affixed at the middle of the wall measured the vertical strains.

In the 15 cm thick NPA geocell-reinforced section (**Figure 5.4.27**), the maximum horizontal tensile strain (>2.1%) was recorded at the bottom of the geocell located right under the loading plate. The compressive strains were recorded in the vertical direction and on the top of the geocell wall at the center. At the top of the wall of the geocell located at 50 cm away from the center, a tensile strain was recorded.

In the 23 cm thick NPA geocell-reinforced section (**Figure 5.4.28**), the maximum horizontal tensile strain (>2.1%) and the maximum compressive strain (<-2.1%) were recorded at the bottom and middle of the geocell, respectively, located right under the loading plate. The compressive strains were recorded in the vertical direction and on the top of the geocell wall at the center. At the top of the wall of the geocell located at 25 and 50 cm away from the center, tensile strains were recorded.

Figure 5.4.29 shows that compressive strains were measured at all the vertical strain gauges measuring in the 30 cm thick NPA geocell-reinforced section, irrespective of whether they were on the top or bottom geocell layer. Most of the horizontal strain gauges experienced tensile stresses except the one at the top of the upper layer geocell wall located under the loading plate.

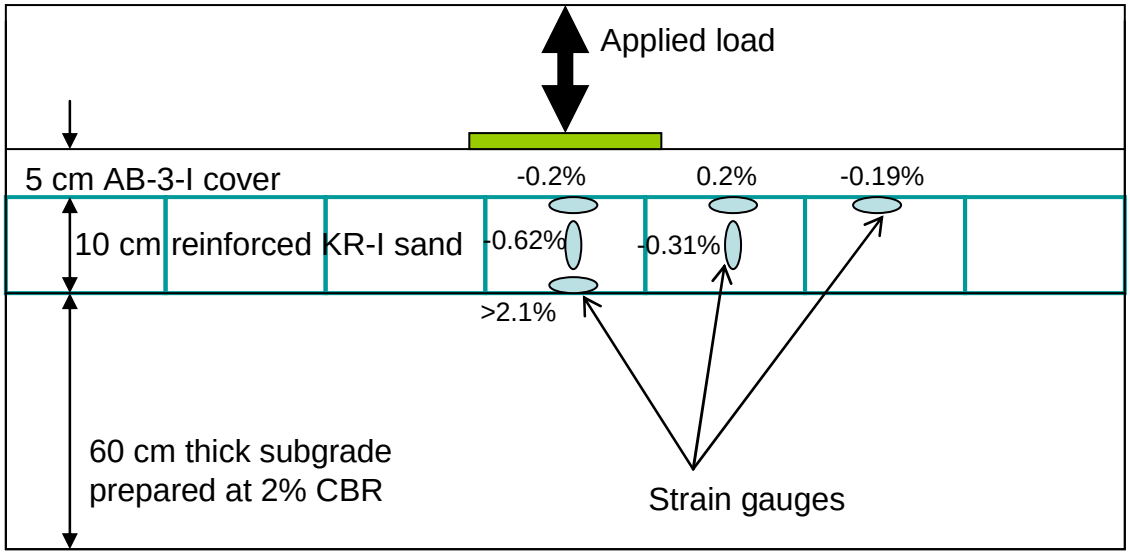

Figure 5.4.27 Measured maximum strains in the geocell in the 15 cm thick reinforced KR-I sand base

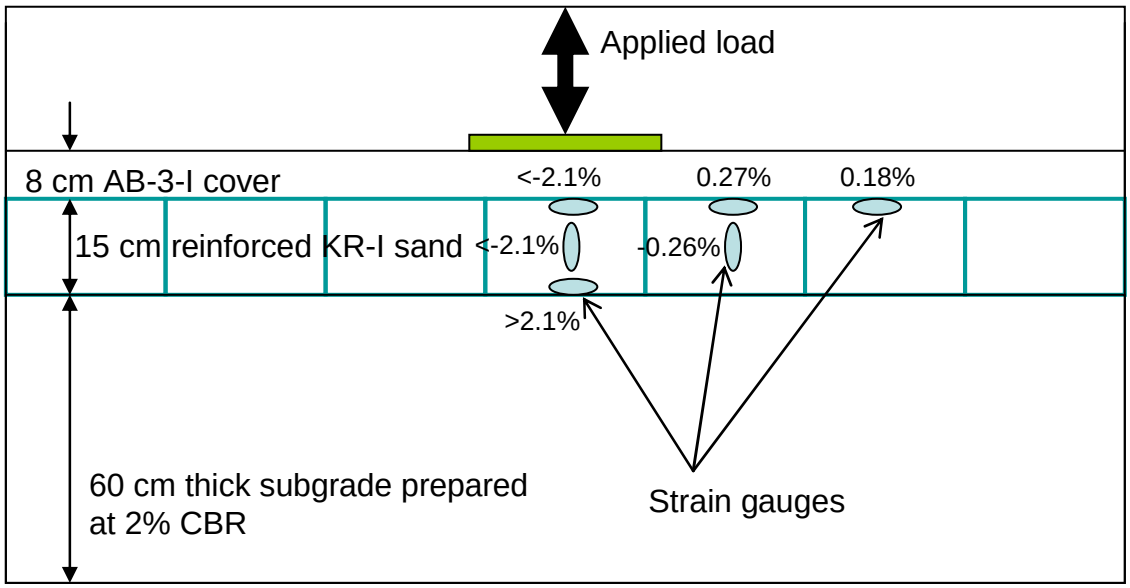

Figure 5.4.28 Measured maximum strains in the geocell in the 23 cm thick reinforced KR-I sand base

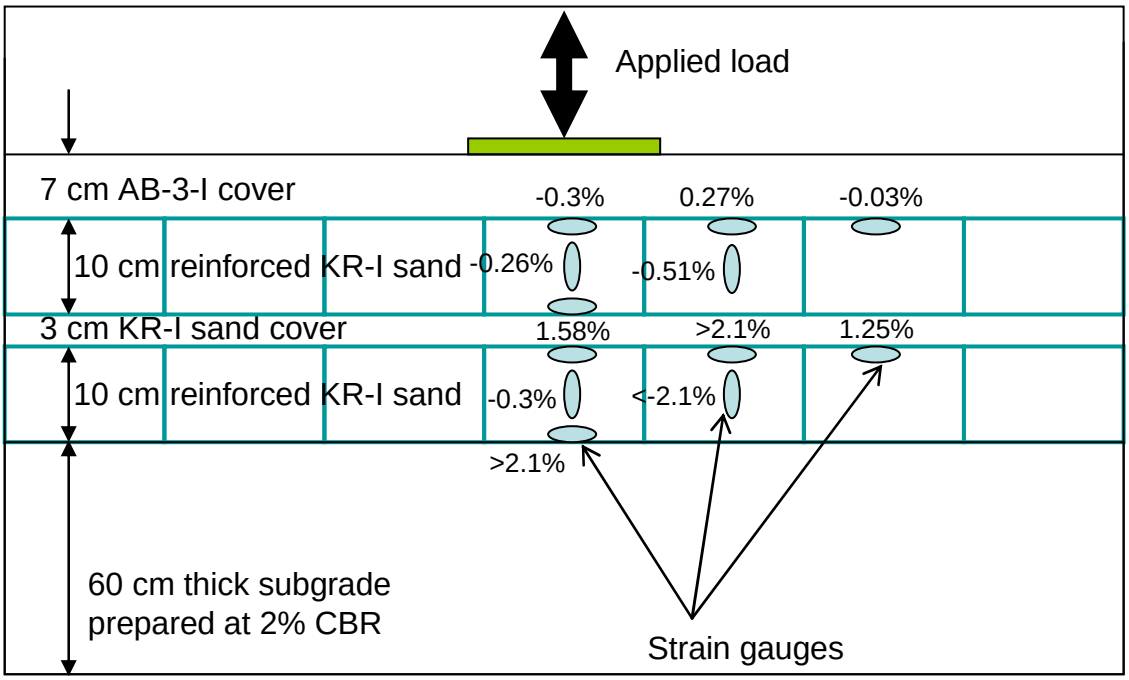

Figure 5.4.29 Measured maximum strains in the geocell in the 30 cm thick reinforced KR-I sand base

5.5 Discussion

5.5.1 Modulus of subgrade

Four cyclic plate loading tests on the subgrade (without a base course) at different magnitudes of applied loads were carried out in the big box to calculate the resilient modulus of the subgrade. All the four tests were run until a fairly constant modulus value was reached. The resilient modulus of the subgrade was calculated using **Equation 5.5.1** (Harr, 1996) and plotted in Figure **5.5.1**.

$$E_{sg} = \frac{p_i BI\left(1-\nu_{sg}{}^2\right)}{\delta} \qquad \textbf{Equation 5.5.1}$$

where, δ = the elastic deformation on each loading cycle; p_i = the applied vertical stress on the subgrade (kPa); ν_{sg} = Poisson's ratio of the subgrade (chosen as 0.5 for this study); B = the diameter of the loading plate (0.3 m); I = the displacement influence factor (0.88); E_{sg} = the resilient modulus of the subgrade. As a rigid plate was used to apply the load in this study, a factor of 0.79 suggested by Yoder and Witczak (1975) was used to correct the calculated resilient moduli into those corresponding to a flexible loading condition (such as tire contact). The resilient moduli obtained at the applied loads of 4 kN, 8 kN, 12 kN, and 16 kN were 25.96 MPa, 29.5 MPa, 27.5 MPa, and 31.8 MPa, respectively. Therefore, the average resilient modulus of the subgrade was 28.7 MPa. The resilient modulus obtained using **Equation 5.5.2** suggested by the Transportation and Road Research Laboratory (TRRL) on NCHRP 1-37A Design Guide (2002) is 27.5 MPa, which is very close to the result obtained from this laboratory study. Therefore, **Equation 5.5.2** was used to calculate the modulus ratio of base to subgrade.

$$M_r = 2555(CBR)^{0.64} = E_{sg} \text{ (psi)} \qquad \textbf{Equation 5.5.2}$$

where M_r = the resilient modulus of the subgrade in psi.

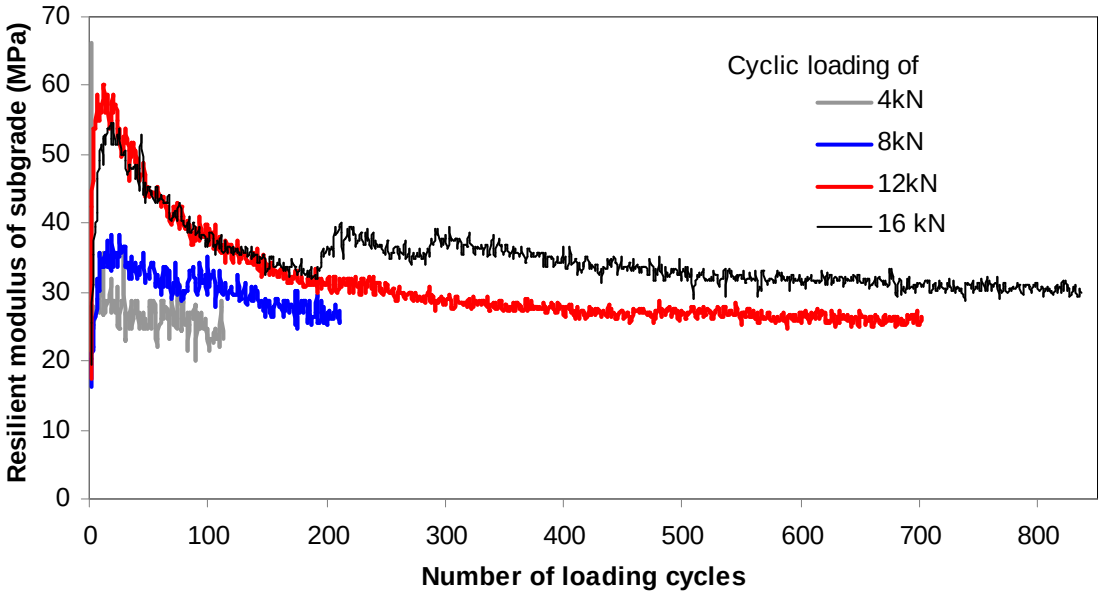

Figure 5.5.1 Calculated subgrade resilient moduli at different applied loads with the number of loading cycles

5.5.2 Modulus of base course

The test sections discussed above are a two-layer system made up of the base course and the subgrade. A two-layer system can be transformed to an equivalent one-layer homogenous system by using Odemark's method (Ullidtz, 1987). Based on Boussinesq's solution given in **Equation 5.5.3** and using the measured vertical stresses, the equivalent thickness of a homogenous layer, h_e, can be calculated:

$$\sigma_c = p\left[1 - \frac{h_e^3}{\left(r^2 + h_e^2\right)^{1.5}}\right] \qquad \textbf{Equation 5.5.3}$$

where σ_c = the vertical stress at the interface between the base course and the subgrade in kPa measured during the test; p = the contact pressure applied at the surface in kPa; and r = the radius of the equivalent tire contact area (m).

The modulus of subgrade (E_{sg}) obtained from **Equation 5.5.2** and the equivalent thickness of the homogenous layer (h_e) obtained from **Equation 5.5.3** can be input into **Equation 5.5.4** to estimate the modulus of the base course (E_{bc}):

$$h_e = h\left[\frac{E_{bc}\left(1-\nu_{bc}^2\right)}{E_{sg}\left(1-\nu_{sg}^2\right)}\right]^{\frac{1}{3}} \qquad \textbf{Equation 5.5.4}$$

where h = the thickness of the base course;; ν_{bc} = Poisson's ratio of the base course (0.3 was chosen in this study); and ν_{sg} = Poisson's ratio of subgrade (0.5 was chosen in this study).

Figures 5.5.2 through **5.5.5** show the calculated resilient moduli of the base course plotted against the number of loading cycles for all the tests carried out in the big geotechnical box in this study. The test results show that the moduli of the base courses decreased with an increase of the number of load cycles. The reduction of the resilient modulus of the base course was attributed to the deterioration of the base quality. The test results show that the deterioration of base moduli was slowed down by NPA geocell reinforcement irrespective of the infill material. The increase in the modulus in case of a weak base course material, such as KR-I sand, was significant.

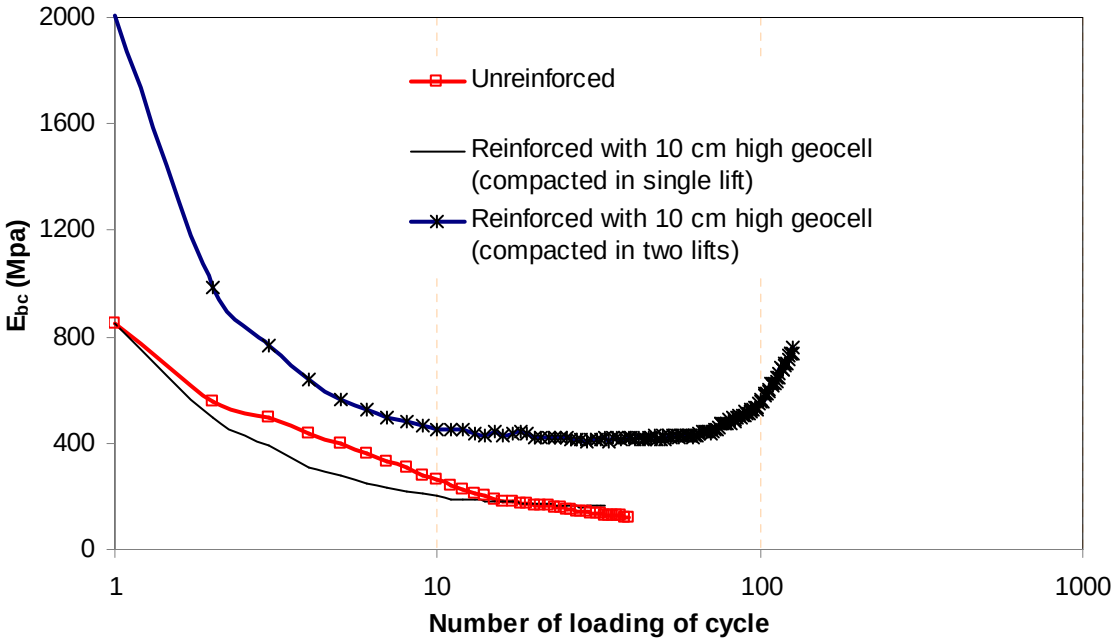

Figure 5.5.2 Calculated resilient moduli of the 15 cm thick AB-3-I base courses

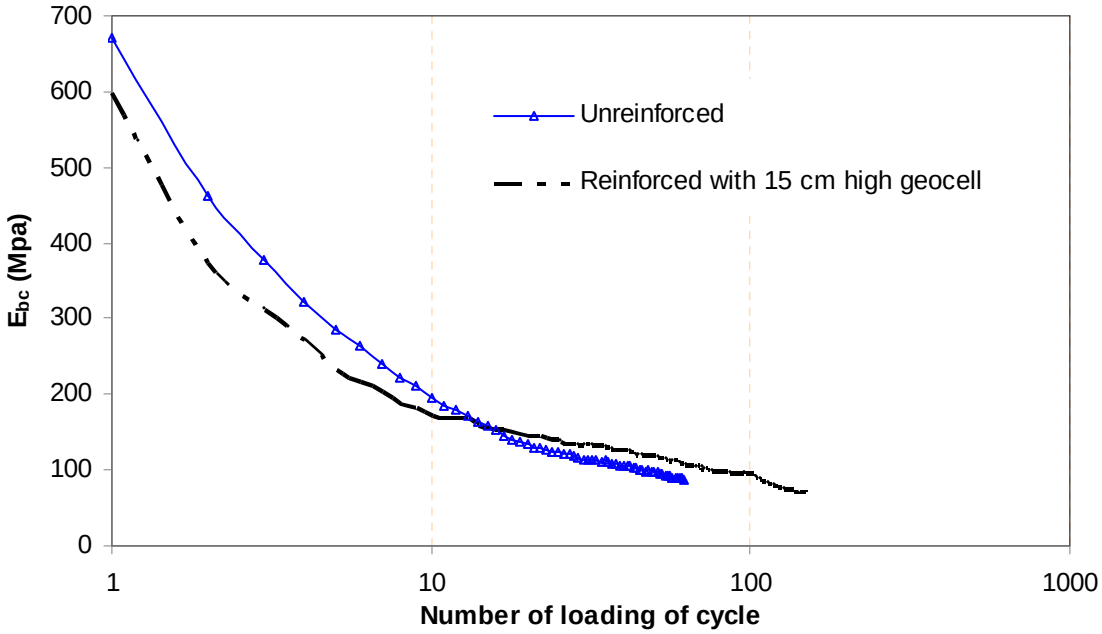

Figure 5.5.3 Calculated resilient moduli of the 23 cm thick AB-3-I base courses

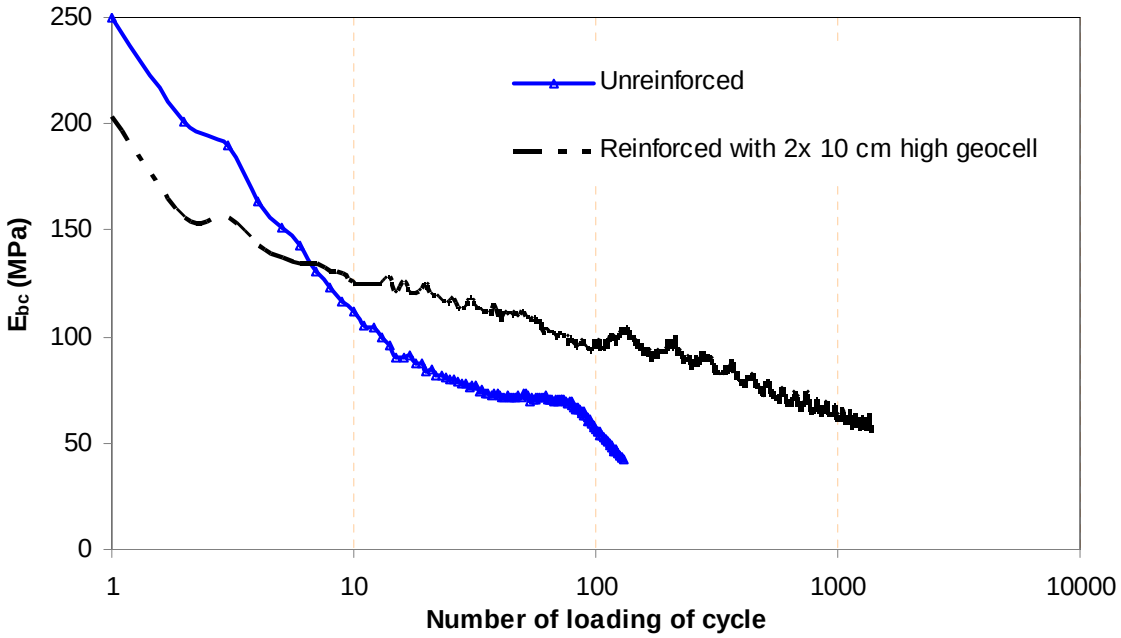

Figure 5.5.4 The calculated resilient moduli of the 30 cm thick AB-3-I base courses

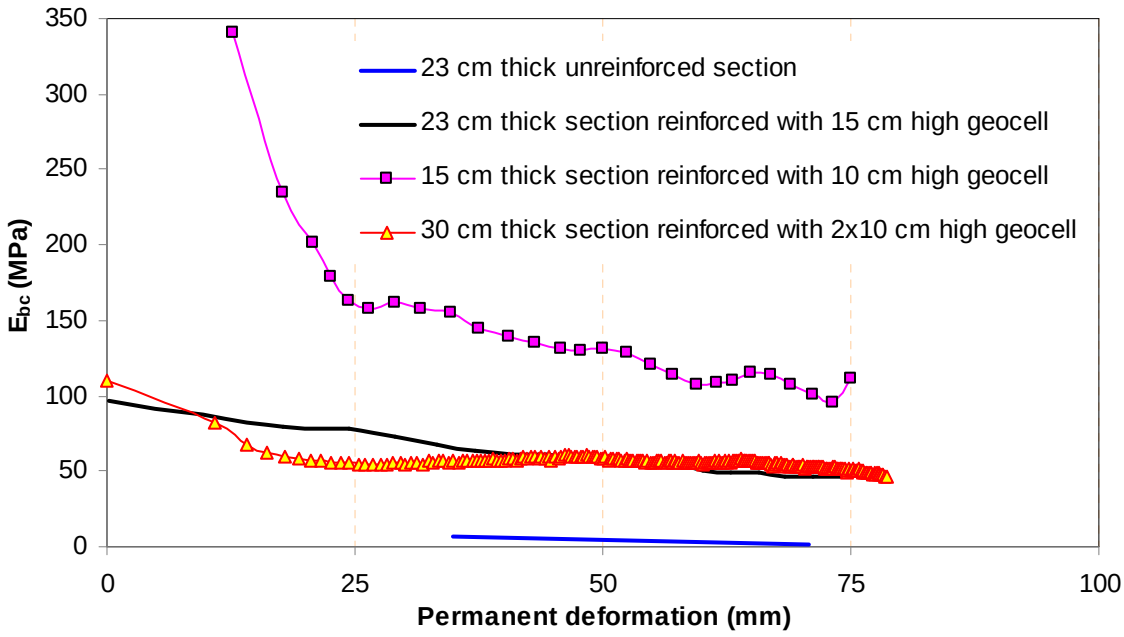

Figure 5.5.5 The calculated resilient moduli of the KR-I sand base courses

5.5.3 Improvement factor

Improvement factor herein is defined as the ratio of the number of loading cycles required to reach a permanent deformation of 75 mm on an NPA geocell-reinforced section to that on an unreinforced section with the same base thickness. The improvement factors for the 15 cm, 23 cm, and 30 cm NPA geocell-reinforced AB-3-I bases were 3.6, 2.5, and 10.4, respectively. The improvement factors for the 15 cm, 23 cm, and 30 cm thick NPA geocell-reinforced KR-I sand sections were 26, 9, and 114 as compared with the 23 cm thick unreinforced section since unreinforced sand bases failed at the similar number of load cycles regardless of their base thicknesses.

5.6 Summary

This section provides a summary of the results of the experimental work conducted to investigate the behavior of NPA geocell-reinforced bases under cyclic loading in the large geotechnical box. Seven tests on the unreinforced and reinforced base courses with AB-3-I aggregates and five tests on the unreinforced and reinforced KR-I sand base courses were conducted. The experimental investigations included the study of the effect of NPA geocell-reinforcement on the performance of the base courses. Following conclusions can be drawn from this experimental study:

1. NPA geocell reinforcement significantly improved the strength and life of the unpaved road sections constructed in the laboratory. Primarily the performance of a test section was evaluated in terms of the number of load cycles sustained by that section until the maximum permanent deformation of 75 mm was reached. There was improvement by geocell reinforcement irrespective of the base material, but the

improvement was more pronounced when a weak granular base course (KR-I sand) was used.

2. The NPA geocell reinforcement reduced vertical stresses transferred to the subgrade and increased the stress distribution angle.
3. The cracks developed on the surface at the time of the section failure were attributed to the beam effect caused by the NPA geocell reinforcement. The crack lines had a diameter of approximately three times that of the loading plate.
4. All the NPA geocell-reinforced sections had higher percentages of elastic deformation as compared with the unreinforced sections. Thinner and weaker sections had the higher improvement in this regard. All the reinforced sections achieved more than 90% elastic deformation at the end of the tests.
5. The calculated resilient moduli showed that the base courses in all the test sections irrespective of the base material deteriorated under cyclic loading; but the rate of deterioration was significantly reduced by NPA geocell reinforcement.
6. In the thinner sections, the failure mode of geocell was the weld failure in the cells located right under the loading plate. However, the weld failure was not observed in the 30 cm thick two-layer NPA geocell-reinforced section. The weld failure in some sections disconnected the honeycomb structure of the geocell rendering the cells to behave individually which in turn restricted the beam effect.

Compaction of the reinforced base courses was one of the challenging problems during the test preparation. To achieve the required degree of compaction, the infill materials in the individual geocells were compacted with compaction rammers.

CHAPTER SIX

ACCELERATED MOVING WHEEL TESTS

Full-scale moving wheel tests were conducted to evaluate the effect of novel polymeric alloy geocell (NPA) reinforcement on the performance of low-volume unpaved roads over weak subgrade using the accelerated pavement testing (APT) facility at Kansas State University (KSU). The objectives of the full-scale moving wheel tests were to evaluate the benefits of geocells as base reinforcement with different infill materials and base thicknesses and to obtain performance data for the development of a design method for geocell-reinforced bases over weak subgrade. This chapter documents the accelerated moving wheel tests carried out using the APT facility.

There were totally 16 sections investigated, 4 sections each prepared in 4 tests. Among the 16 road sections tested, there were seven RAP sections, four AB-3 sections, four KR sand sections, and one QW section. AB-3-II, QW-II, and RAP-I as base materials were used in the first test; AB-3-II, and RAP-I in the second test; and AB-3-II, RAP-II in the third test, and KR-I sand in the fourth test. The properties of all the materials used in these tests have been discussed in detail in **Chapter 3**. Although different road sections were tested in each test run, the analysis of the test results are divided into three major groups in this dissertation. The first group compares the results of the first test that includes an unreinforced control section of AB-3-II and four NPA geocell reinforced sections of AB-3-II, QW-II, and RAP-I materials. The second group compares four AB-3-II sections from three different tests. Seven road sections with RAP-I and RAP-II are compared separately in the third group. The test results of KR-I sand were reported by Yang (2010); therefore, they are not repeated herein.

6.1 Facility and Equipment

The test facilities at the University of Kansas (KU) and Kansas State University (KSU) were used for this research. The material properties of subgrade and base courses were determined at the KU Geotechnical Laboratory while the moving wheel tests and insitu testing were carried out at the APT facility of KSU. The laboratory material tests included sieve analysis, standard Proctor compaction, and CBR tests. The insitu tests included dynamic cone penetration (DCP) tests, vane shear tests, nuclear gauge tests, sand cone tests, light falling weight deflectometer (LFWD) tests, and falling weight deflectometer (FWD) tests.

The APT machine has a 12.8 m long reaction frame and a full-scale, 80 kN single axle with dual tires. The load is controlled by hydraulic pressure. The dual-wheel axle assemblies with air-bag suspension are belt-driven using a 20 HP electric motor and a variable frequency drive controls wheel motion. The test pit of the APT facility was 6.1 m long, 4.9 m wide, and 1.8 m deep. The tire pressure used for these tests was 552 kPa. The width of dual tires is approximately 0.55 m from edge to edge. The frequency of wheel moving was 0.167 Hz (i.e., 6 sec/pass) and the wheels were run at a speed of 11.3 km/hr within the test pit. In this research, the test pit was divided into four sections of equal dimensions in plan, each section having a length of 3.05 m and a width of 2.45 m. **Figure 6.1.1** shows the plan of the APT test pit and **Figure 6.1.2** shows the picture of the APT facility. The subgrade consisted of A-7-6 soil and was compacted to simulate a field condition of CBR value at about 3%. A non-woven geotextile was placed at the subgrade-base interface as a separator in case of the geocell-reinforced sections.

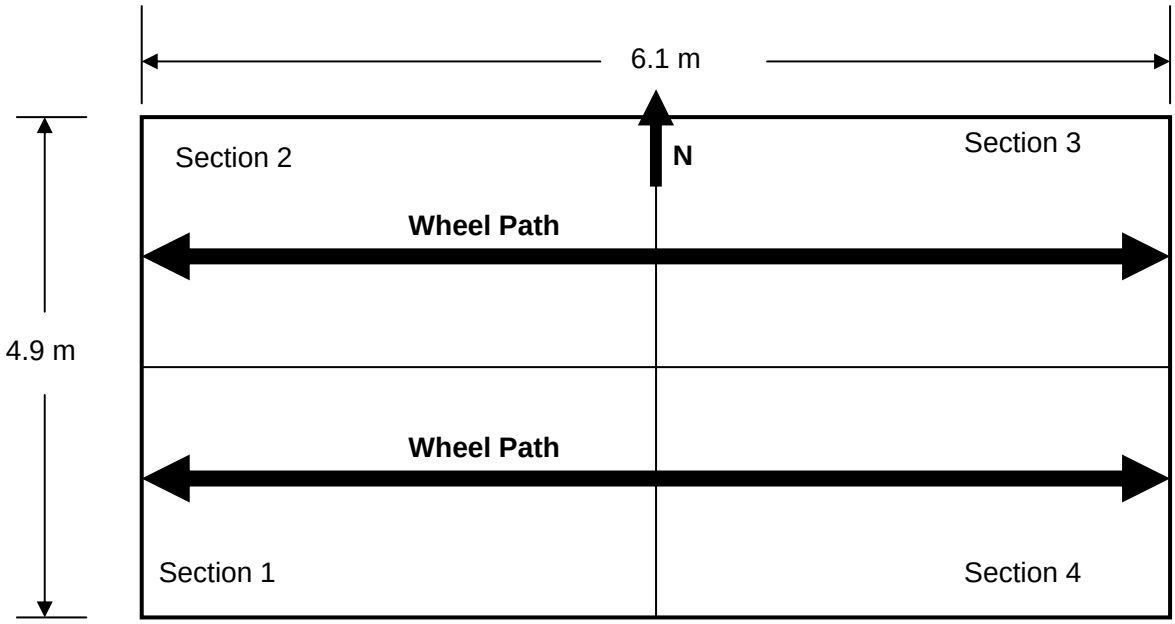

Figure 6.1.1 Plan of test sections at the APT facility

Figure 6.1.2 Accelerated pavement testing (APT) facility at KSU

6.2 Test Preparation

The 1.8 m deep test pit was filled with the subgrade material A-7-6 soil and compacted with a jumping jack compactor. It was found very difficult to attain the CBR value of 3%. Later a vibratory compactor (CAT CS54) was used to compact the subgrade and the desired CBR of 3% was achieved at 21% moisture content. This CBR was achieved at 26% moisture content in the laboratory. Monitoring of the CBR was done by both DCP and vane shear tests at every layer of subgrade compaction. **Figure 6.2.1** shows the subgrade prepared for the first test with the pressure cells installed. One layer of non-woven geotextile was placed on top of the subgrade for geocell-reinforced sections. The subgrade was covered with a geotextile and the steel bars were stationed for geocell installation as shown in **Figure 6.2.2**. Geocells for all the tests were equipped with strain gauges at specified locations. **Figure 6.2.3** shows the geocells installed in the reinforced sections and the unreinforced control section in the first test. Placement of infill materials QW-II and RAP-I are shown in **Figures 6.2.4** and **6.2.5**. **Figures 6.2.6, 6.2.7,** and **6.2.8** show the leveling and compaction processes of the base courses. The target density of the base courses of all the test sections was 95% the maximum dry density determined by the standard Proctor tests. Field compaction was done in the wet side of the optimum in the first test and the dry side in the second and third tests. Only a vibratory compactor was used to compact the base courses in the first test except the QW-II section where additional jumping jack compaction was applied. A 4-ton roller compactor (**Figures 6.2.7)** was used for the second and third tests.

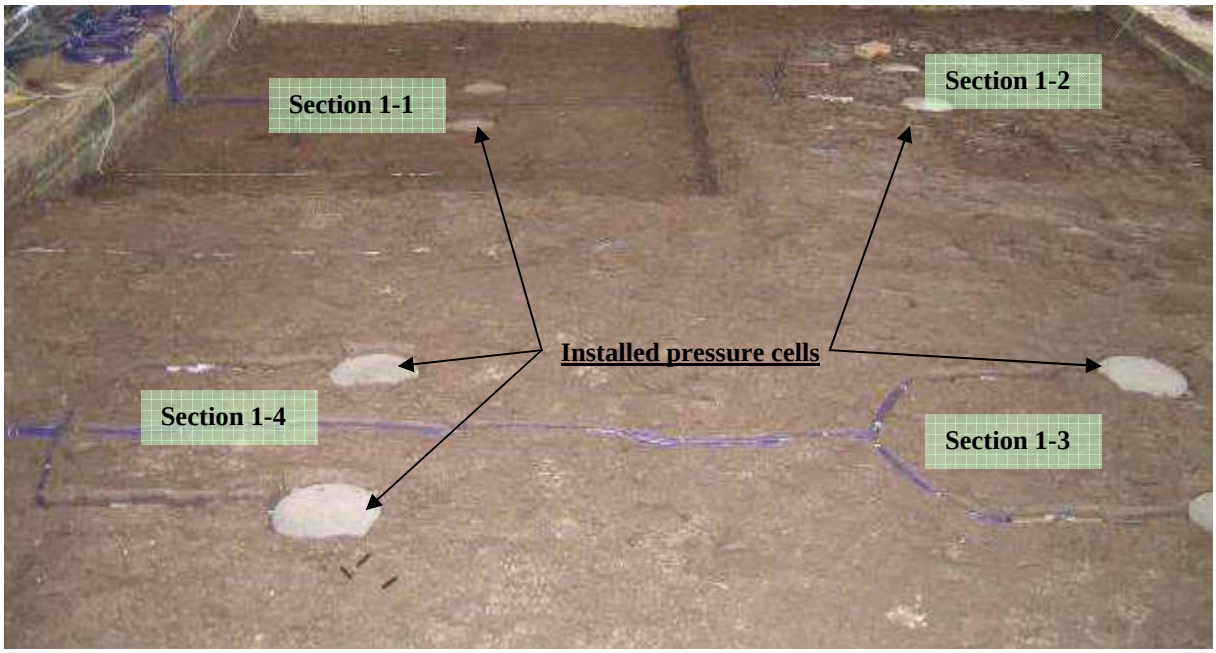

Figure 6.2.1 Prepared subgrade for four test sections with 8 installed pressure cells

Figure 6.2.2 Geotextile and steel bars stationed for geocell installation

Figure 6.2.3 Geocell installed before filled with infill material

Figure 6.2.4 Filling of QW-II in the geocell

Figure 6.2.5 Sieving of the RAP-I through a 5 cm mesh size sieve for placement

Figure 6.2.6 Leveling of the base course material

Figure 6.2.7 Compaction with a roller compactor (used in the second and third tests)

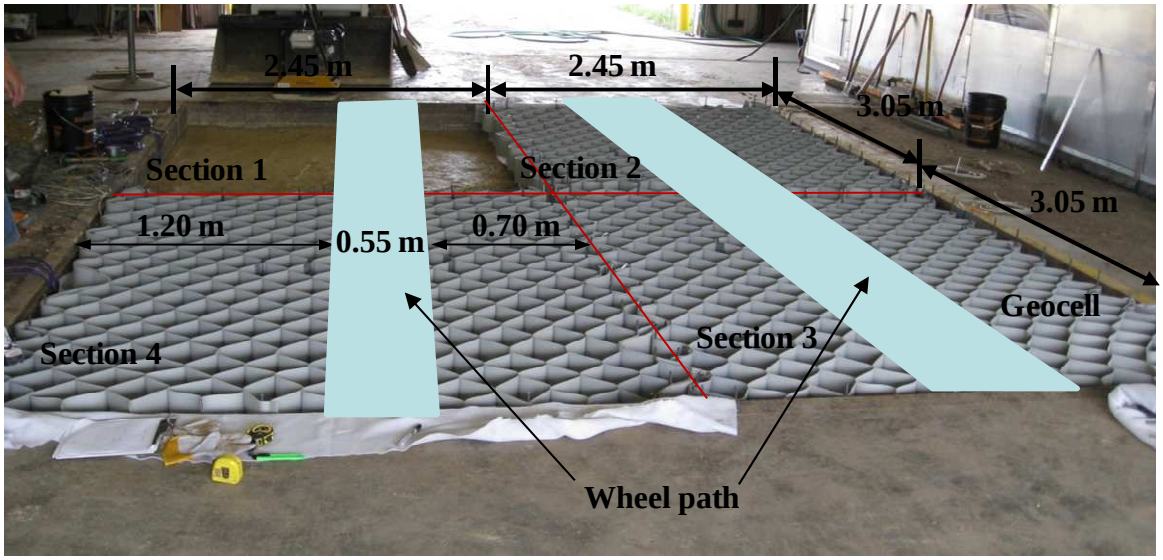

a) Geocell-installed in Section 1-2, 1-3, and 1-4

b) Test ready sections

Figure 6.2.8 Plan layout of the test sections in the first test

Vane shear, dynamic cone penetrometer (DCP), nuclear gauge, light falling weight deflectometer (LFWD), and falling weight deflectometer (FWD) tests were performed to evaluate the density and stiffness of the base courses. However, the FWD data were not reliable because the difficulties in setting up the device and conducting the tests on the unpaved surface. So, the LFWD and FWD data are not analyzed here. Sand cone tests were performed after each moving wheel test was completed.

Vane shear tests were carried out to ensure the uniformity of the subgrade CBR values during the preparation of subgrade. The target CBR value was 3%. Dynamic Cone Penetrometer (DCP) tests were carried out to estimate the CBR values of the subgrade and base courses. The density was checked by a nuclear gauge before each test. **Figures 6.2.9** show the picture of a nuclear gauge used for the density measurements. For rut measurement,

initial top surfaces at two locations were measured for each section as the references. Earth pressures on the top of the subgrade and strains in the geocell were measured by earth pressure cells and strain gauges using the data acquisition system. The test sections were exhumed after each test for forensic analysis and profiling.

Figures 6.2.9 Nuclear gauge

6.3 Test Sections

The tests at the APT facility were carried out in four stages and a total of 16 sections were investigated. **Table 6.3.1** shows the details of each test section except the KR-I sand sections reported by Yang (2010).

The arrangements of four sections in the first test are shown in **Figure 6.3.1**. The road sections in this test were prepared with the base course materials of QW-II, RAP-I, and

AB-3-II. Section 1-1 was 30 cm thick unreinforced AB-3-II base course; Section 1-2 was 17 cm thick QW-II base course reinforced with 15 cm high NPA geocell; Section 1-3 was 17 cm thick RAP-I base course reinforced with 15 cm high NPA geocell; and Section 1-4 was 17 cm thick AB-3-II base course reinforced with 15 cm high NPA geocell. The base thickness of the reinforced sections included 2 cm top fill cover with the same material as the infill one.

The arrangements of four sections in the second test are shown in **Figure 6.3.2**. The road sections in this test were prepared with RAP-I and AB-3-II base materials. Section 2-1 was 30 cm thick unreinforced RAP-I base course; Section 2-2 was 17 cm thick AB-3-II base course reinforced with 10 cm high NPA geocell; Section 2-3 was 17 cm thick RAP-I base course reinforced with 10 cm high NPA geocell; and Section 2-4 was 30 cm thick RAP-I base course reinforced with two layers of 10 cm high NPA geocells. The thickness of the reinforced sections included 7 cm top cover. In Section 2-4, a cover of 3 cm thick RAP-I was also provided on top of the bottom layer geocell before installing the top layer reinforcement.

Table 6.3.1 Details of all test sections

Test #	Section 1	Section 2	Section 3	Section 4
1	Section 1-1 AB-3-II Unreinforced 30 cm thick	Section 1-2 QW-II 15 cm geocell +2 cm cover	Section 1-3 RAP-I 15 cm geocell +2 cm cover	Section 1-4 AB-3a 15 cm geocell +2 cm cover
2	Section 2-1 RAP-I Unreinforced 30 cm thick	Section 2-2 AB-3-II 10 cm geocell +7 cm cover	Section 2-3 RAP-I 10 cm geocell +7 cm cover	Section 2-4 RAP-I 10 cm geocell + 3 cm cover +10 cm geocell + 7 cm cover
3	Section 3-1 RAP-II Unreinforced 25 cm thick	Section 3-2 RAP-II 10 cm thick base +10 cm geocell +5 cm cover	Section 3-3 RAP-II 10 cm thick base +7.5 cm geocell +7.5 cm cover	Section 3-4 AB-3-II 10 cm thick base +10 cm geocell +5 cm cover

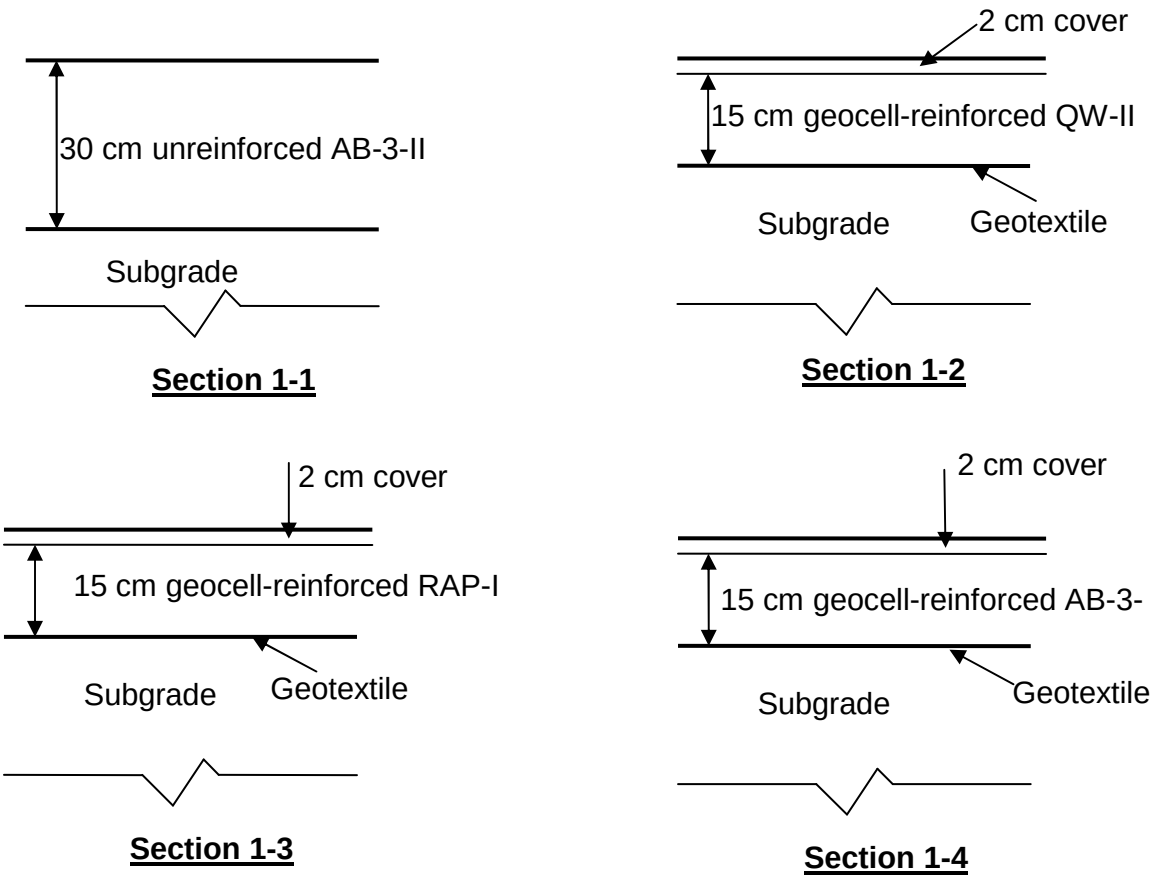

Figure 6.3.1 Nominal dimensions of the test sections in the first test

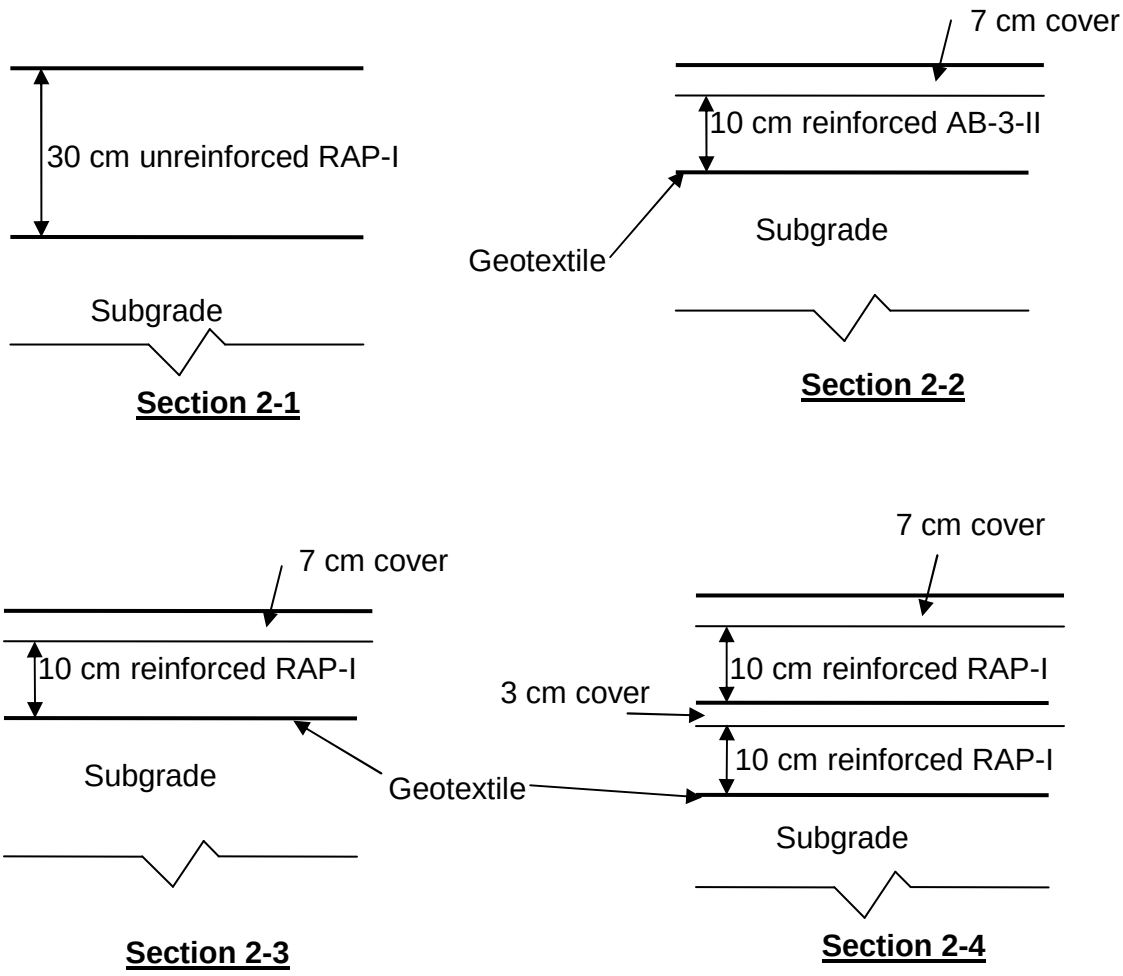

Figure 6.3.2 Nominal dimensions of the test sections in the second test

The arrangements of four sections in the third test are shown in **Figure 6.3.3**. The road sections in this test were prepared with RAP-I and AB-3-II base materials. Section 2-1 was 30 cm thick unreinforced RAP-I base course; Section 2-2 was 17 cm thick AB-3-II base course reinforced with 10 cm high geocell; Section 2-3 was 17 cm thick RAP-I base course reinforced with 10 cm high geocell; and Section 2-4 was 30 cm thick RAP-I base course reinforced with two layers of 10 cm high geocells. The thickness of reinforced sections included 7 cm top cover. In case of the two layer reinforcement in Section 2-4 a cover of 3

cm thick RAP-I was also provided on top of the bottom layer geocell before installing the top layer reinforcement.

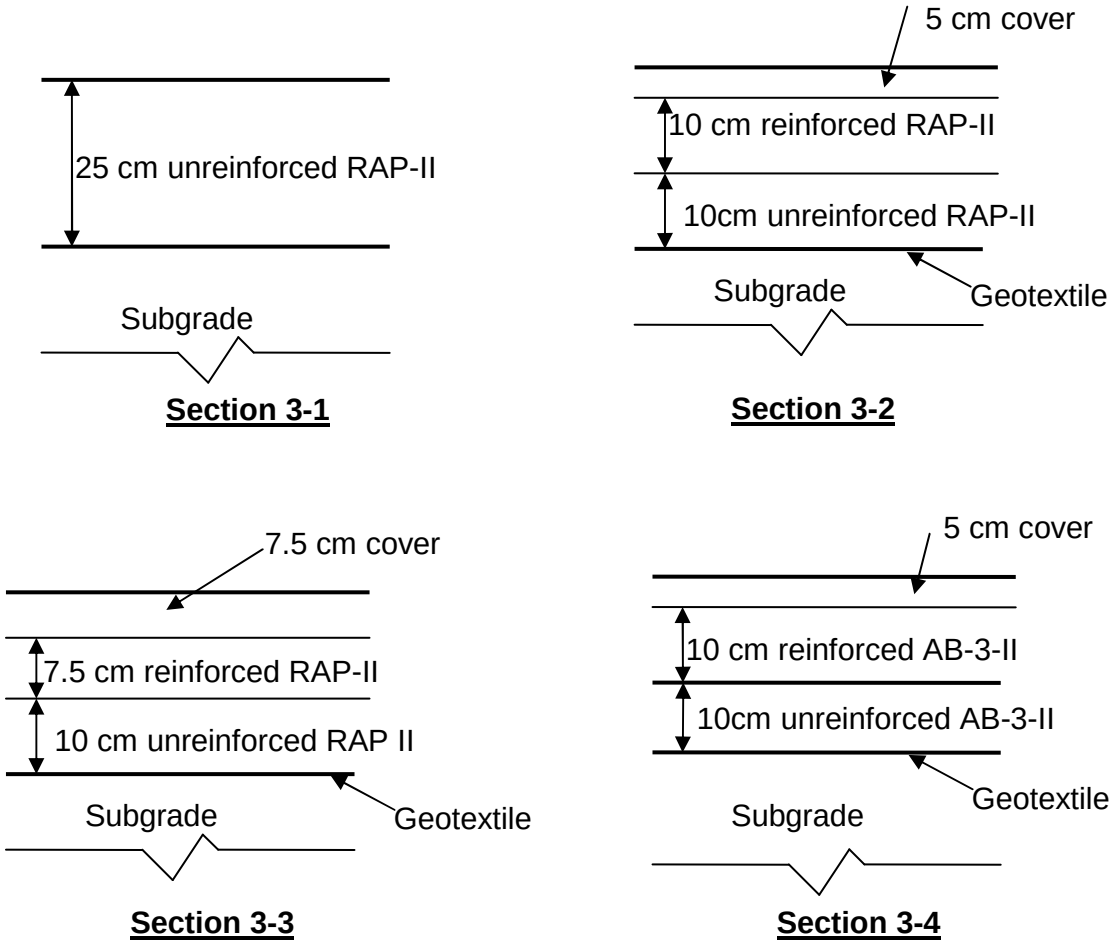

Figure 6.3.3 Nominal dimensions of the test sections in the third test

In the proceeding sections three separate studies are presented by comparing the road sections from different tests. The first test is included in **Section 6.4** for the study on different infill materials; the entire RAP sections are analyzed in **Section 6.5**; and all sections with AB-3-II are analyzed in **Section 6.6**.

6.4 Road Sections with Different Base Course Materials

6.4.1 Test sections

The results of DCP, nuclear gauge, and sand cone tests carried out on the finished subgrade and base course of the four test sections are given in **Table 6.4.1**.

The desired density of the base courses was 95% of the maximum dry density. It was specified that the compaction should be performed within the range of ±2% to the optimum moisture content. The actual compaction was ended with the wet side of the optimum moisture content, but within the range of 2%. The control section was compacted in two lifts, i.e., 15 cm each lift while the reinforced sections were compacted in one lift. A nuclear gauge was used to monitor the level of compaction and density measurement during each lift of the compaction. DCP tests were carried out to estimate the CBR values of the test-ready sections (including the base and the subgrade) using **Equation 5.1.2**. The DCP test results are plotted in **Figure 6.4.1**, which shows that the CBR values of the base course in Section 1-1 (the control section) were higher than those in other three reinforced sections.

Table 6.4.1 Measured average CBR values from DCP tests and compaction values from nuclear gage and sand cone tests

Test Method	Sections	1-1	1-2	1-3	1-4
DCP (subgrade)	CBR (%)	2.4	1.9	2.2	2.2
DCP (base course)	CBR (%)	22.6	9.2	7.5	9.2
Nuclear gauge test on base course before test	Compaction (%)	90	98	87	86
Sand cone test on the wheel path after the moving wheel test	Compaction (%)	86	NA	100	83
Sand cone test outside the wheel path after the moving wheel test	Compaction (%)	83	93	88	80

The same procedure was followed to compact the base courses in all the four sections. The nuclear gauge tests showed the final relative compaction before the test was 90% at Section 1-1, 98% at Section 1-2, 87% at Section 1-3, and 86% on Section 1-4. The sand cone tests after the moving wheel test found the compaction of 86% at Section 1-1, 93% at Section 1-2, 88% at Section 1-3, and 80% on Section 1-4 outside of the wheel path. Although the same compaction procedure was adopted for all the sections, DCP results showed that the average CBR value of the base course was 22.6% at Section 1-1 (the control section), 9.2% at Section 1-2, 7.5% at Section 1-3, and 9.2% at Section 1-4. In the control section, a CBR value of 39% was measured at a depth of about 25 cm from the surface. The control section (Section 1-1) therefore had the higher CBR values than those at other three reinforced sections.

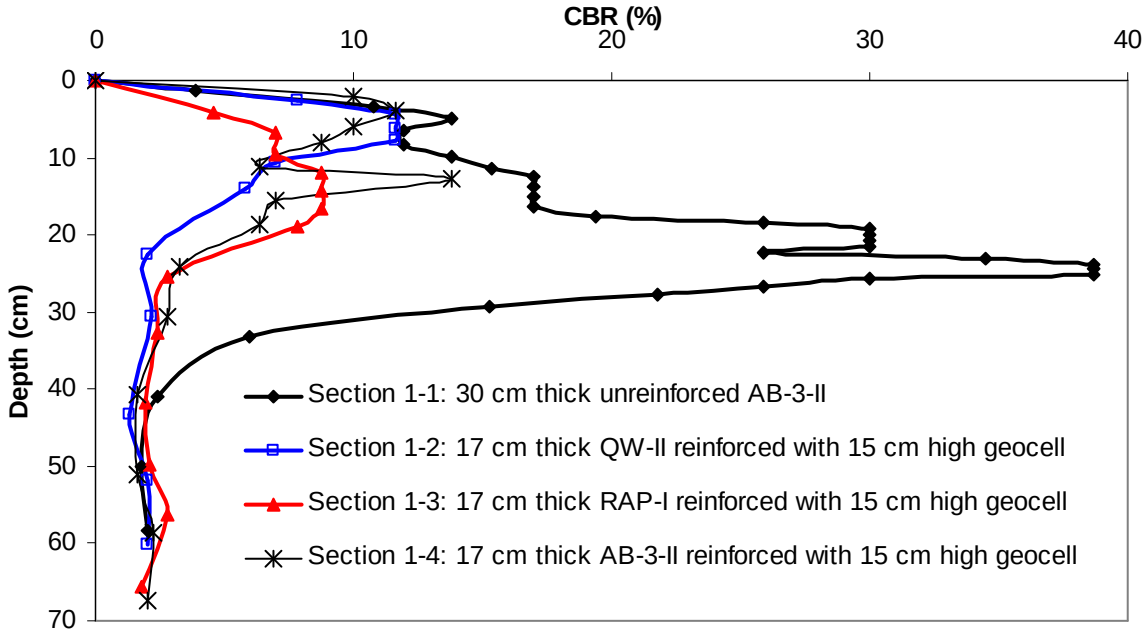

Figure 6.4.1 CBR profiles obtained from DCP tests in the moving wheel test No. 1

6.4.2 Rut depths

All four sections were subjected to the same moving wheel load. The rut depths are plotted against the number of wheel passes for all four sections in **Figure 6.4.2**. However, the rut depths in these sections developed at different rates. For example, the rut depth in the reinforced QW-II section (Section 1-2) increased rapidly within the first few passes and obvious heave around the wheel path was observed. At 50 passes, the measured rut depth was approximately 7 cm. The rut depth was measured from the peak to trough around the rut. It can be concluded that the QW-II at wet of the optimum moisture content was not strong enough to directly sustain the traffic loading. For unpaved roads, typically allowable rut depths are 75 to 100 mm (Giroud and Han, 2004a and b). The moving wheel test was

terminated at 305 passes because three out of four sections reached more than 13-cm rut depth. The number of 305 passes is small if these sections are used for local roads. However, it may be acceptable that they are used for temporary roads, haul roads, and construction platforms. Since the QW-II section had excessive rut depths, the QW-II and control sections were refilled during the test. Rut measurements on these two sections were not made after 205 passes.

Figure 6.4.2 shows that the reinforced QW-II section had the largest rut depth among all the test sections while the NPA geocell-reinforced RAP-I section had the smallest rut depth. Even though the NPA geocell-reinforced AB-3-II section had a thinner base thickness, it had a smaller rut depth than the unreinforced AB-3-II section. This result demonstrated that NPA geocell reinforcement reduced the rut depth compared to the unreinforced section. The reinforced AB-3-II and RAP-I bases had the same thickness, however, the reinforced RAP-I base had a smaller rut depth than the reinforced AB-3-II especially at a larger number of passes. Visual observations showed that the reinforced RAP-I base course was more stable than the reinforced AB-3-II base under the traffic loading.

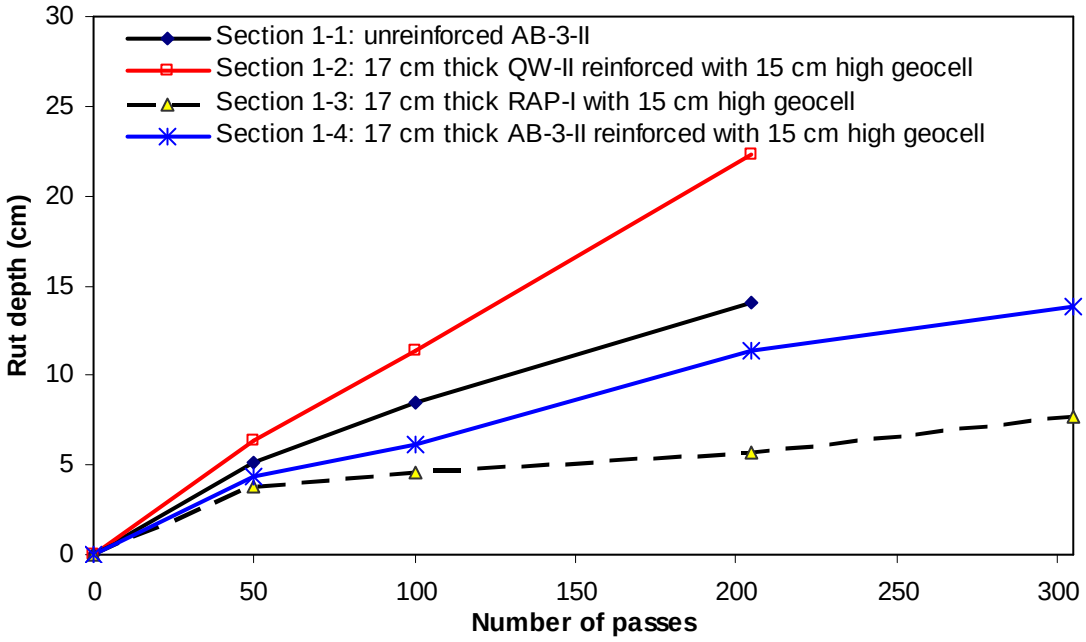

Figure 6.4.2 Rut depth versus number of passes of test sections in the moving wheel test No.1

6.4.3 Deformed profiles

After the moving wheel test, all the test sections were exhumed and trenches were cut to examine the deformed profiles and geocells. In all reinforced sections, geocells were initially laid out at 25 cm long in the traffic direction and 21 cm wide in the transverse direction. Forensic tests showed that the shape and size of the cells were intact outside the wheel path. However, under the wheel path, the average size was found to be 23.5 cm long in the traffic direction and 21.5 cm wide in the transverse direction. Some welds of the geocell in Sections 1-2 and 1-3 were broken at the edge of the wheel path. **Figure 6.4.3** through **6.4.10** show the profiles of the test sections before and after the moving wheel test and the pictures of the sections after the test. The profiles are presented at the bottom (also the top of the subgrade) and top of the NPA geocell for the reinforced sections but at the top

of the subgrade for the unreinforced section. Due to excessive rut and heave in Section 1-2 (the QW-II section), the exhumation of Sections 1-2 and 1-3 in the same path were conducted before re-filling (i.e., after 205 passes). Other two sections were exhumed after 305 passes. Patterns of rut and heave are clearly seen in all sections. It is shown that the volumes of rut and heave were close for all the sections due to incompressibility of the subgrade.

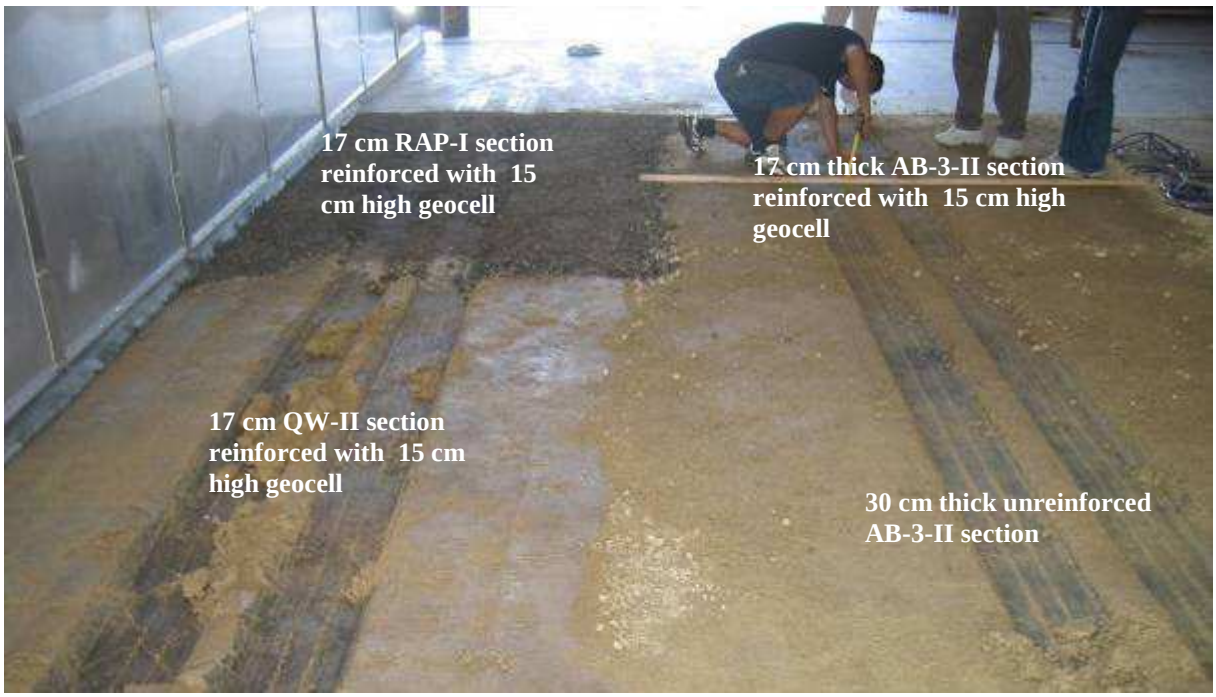

Figure 6.4.3 All four sections after the moving wheel test No. 1

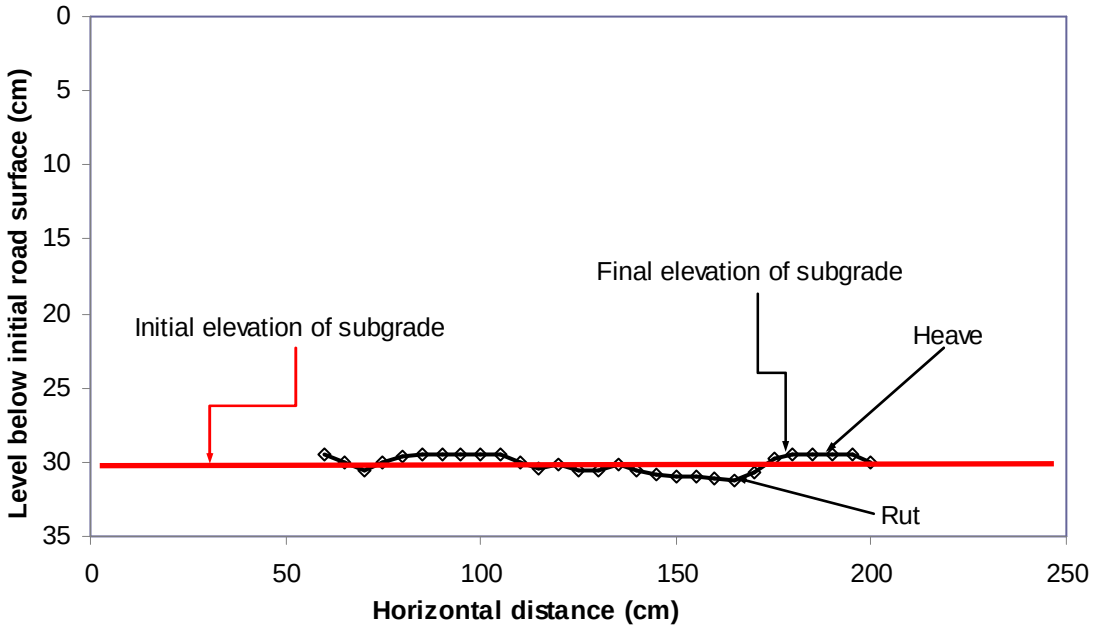

Figure 6.4.4 Initial and final subgrade profiles of control section 1-1- after 305 passes

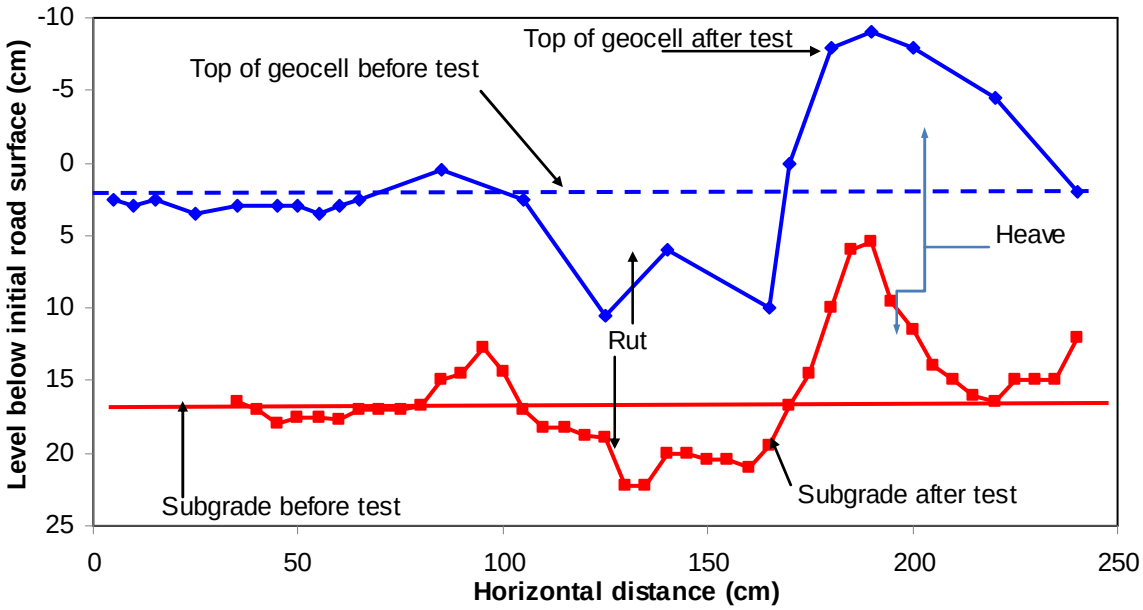

Figure 6.4.5 Initial and final profiles of geocell-reinforced QW-II section 1-2 after 205 passes

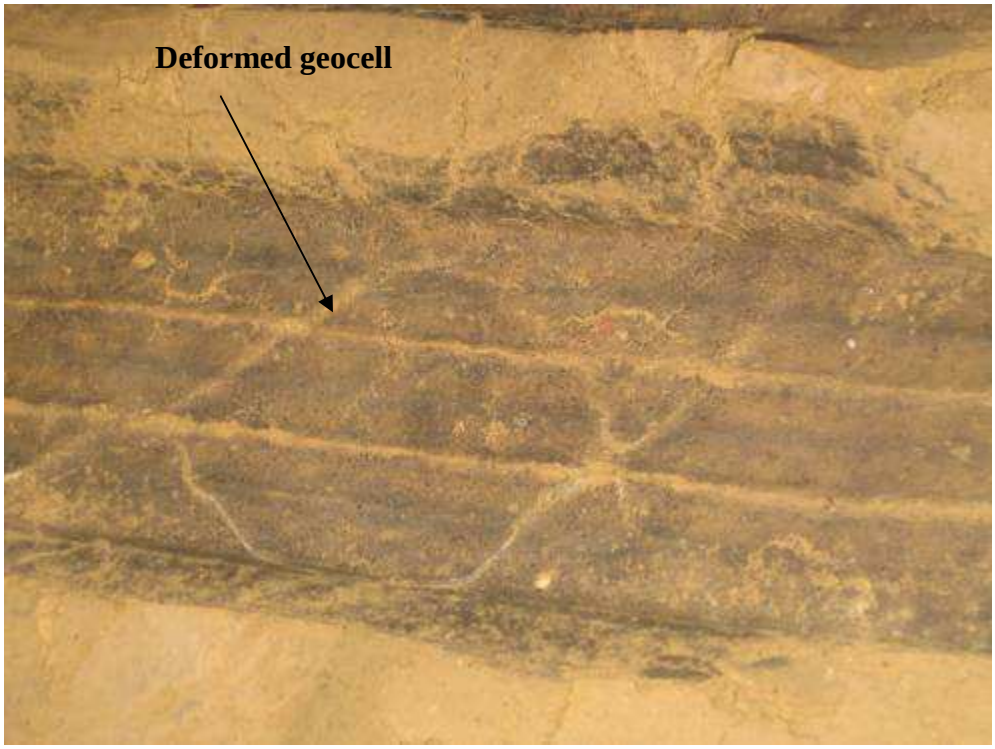

Figure 6.4.6 Deformed geocell in reinforced QW-II section 1-2

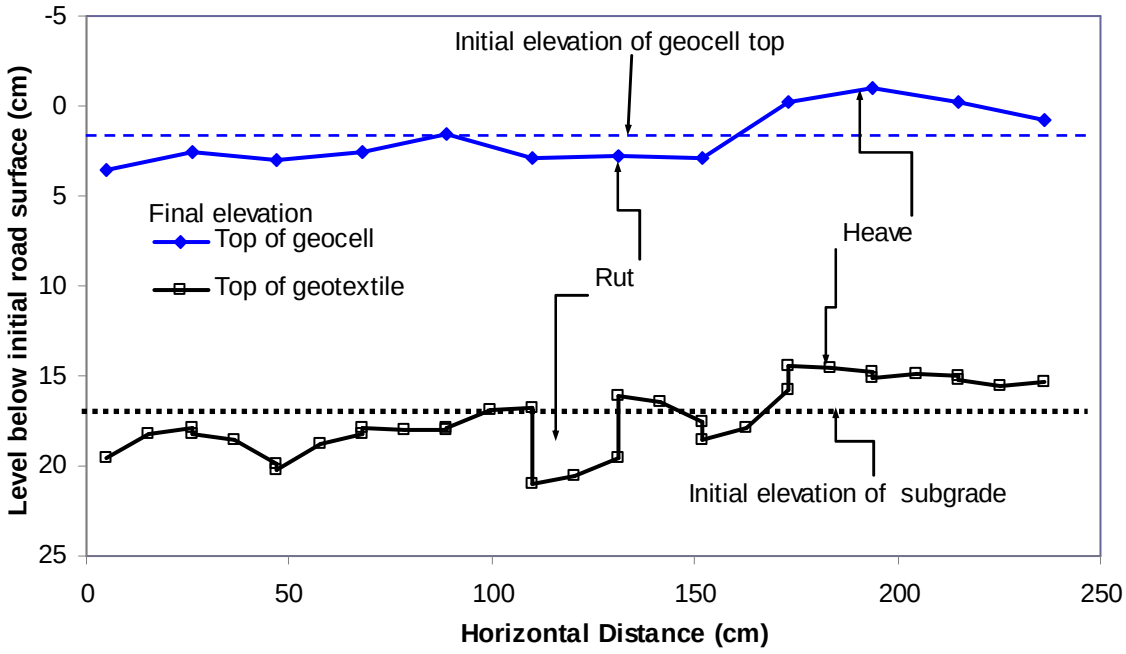

Figure 6.4.7 Initial and final profiles of reinforced RAP-I section 1-3 after 205 passes

Figure 6.4.8 Deformed geocell in reinforced RAP-I section 1-3 after 205 passes

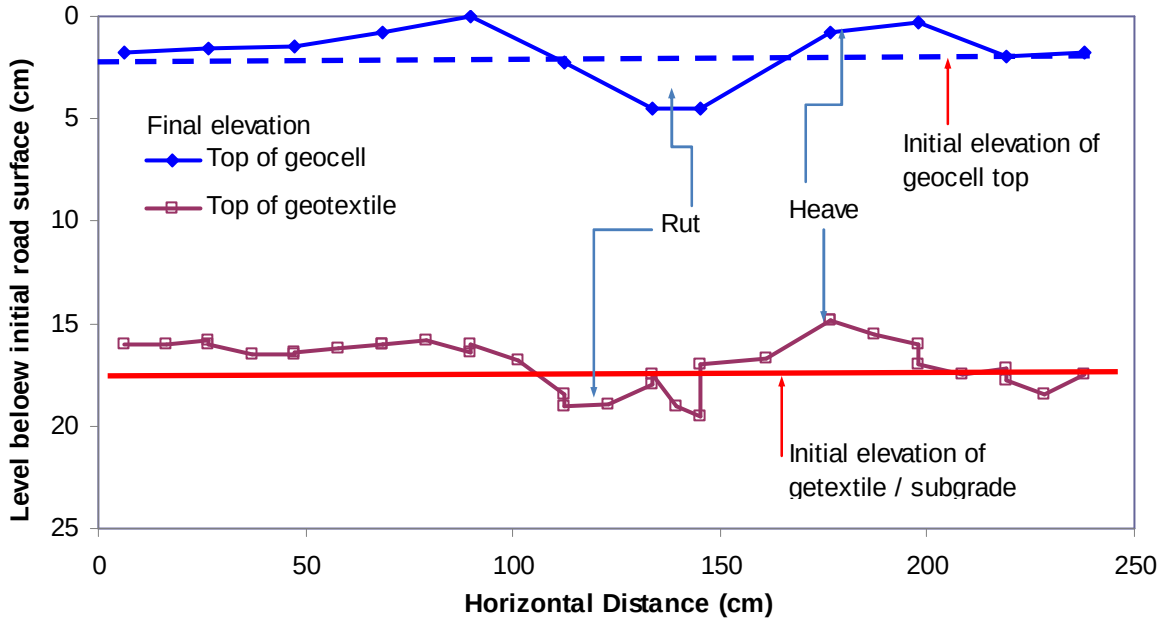

Figure 6.4.9 Initial and final profiles of reinforced AB-3-II section 1-4 after 305 passes

Figure 6.4.10 Deformed geocell in reinforced AB-3-II Section 1-4 after 305 passes

6.4.4 Vertical stresses

Vertical stresses transmitted to the subgrade were measured by the pressure cells located at the subgrade-base interface as shown in **Figure 6.4.11**. It is seen that the measured vertical stresses were much lower than the tire pressure of 552 kPa applied on the road surface. **Figure 6.4.11** also shows that the measured vertical stresses increased with the number of passes. This trend is consistent with the design model proposed by Giroud and Han (2004a and b). Even though the control section had a base thickness of 30 cm compared to 17 cm in the NPA geocell-reinforced AB3-II section, their measured vertical stresses were close. This comparison demonstrates that NPA geocell reinforcement reduced the vertical stress by distributing the load to a wide area. The distribution angles after 100 passes for

different sections can be calculated from **Figure 6.4.11** using **Equation 5.3.3**. The calculated stress distribution angles for the tests sections are given in **Table 6.4.2**. The control section had the highest stress distribution angle followed by the QW-II section, the RAP-I section, and the AB-3-II sections, respectively. Therefore, the reinforced AB-3-II section had the largest stress distribution angle among all the sections. Even though the reinforced QW-II section did not perform well due to the failure of the base course itself, it had a higher stress distribution angle than that of the control section.

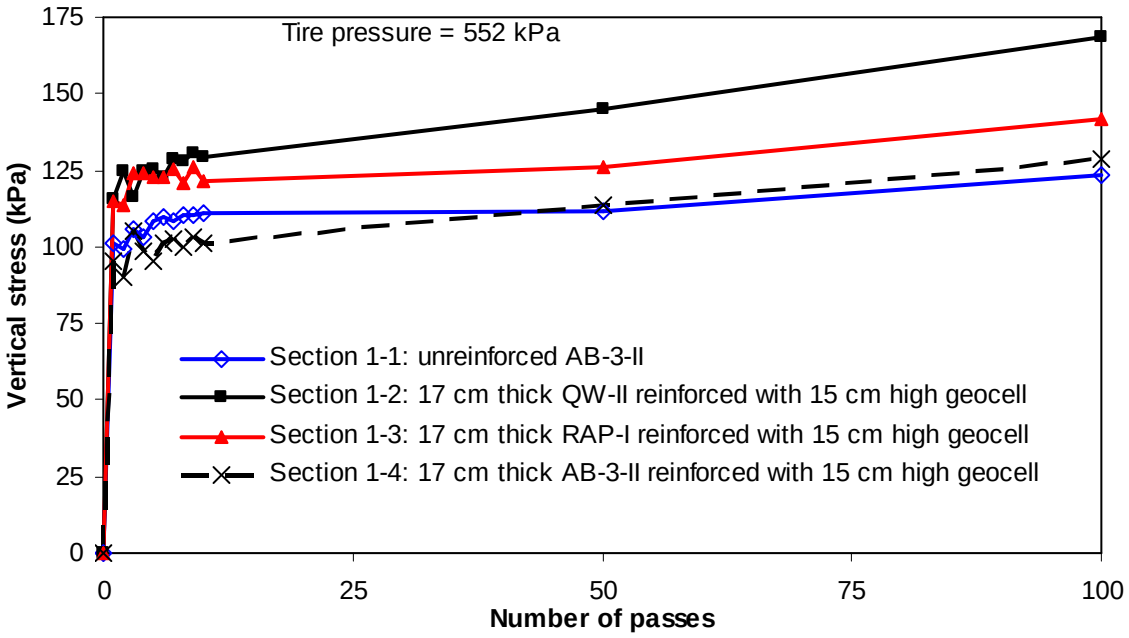

Figure 6.4.11 Measured vertical stresses at the subgrade-base interface

Table 6.4.2 Stress distribution angle

Base course sections above the subgrade		Vertical stress	Distribution angle
Section	**Section detail**	**(kPa)**	**(degrees)**
1-1	30 cm thick unreinforced AB-3-II	123	29
1-2	17 cm thick reinforced QW-II with one layer of 15 cm high geocell	168	36
1-3	17 cm thick reinforced RAP-I with one layer of 15 cm high geocell	141	41
1-4	17 cm thick reinforced AB-3-II with one layer of 15 cm high geocell	128	43

6.4.5 Maximum strains in geocells

Five strain gauges were affixed on the geocell walls in each reinforced section. All the strain gauges were affixed horizontally at the middle of the geocell walls. **Figures 6.4.12** through **6.4.14** show that one strain gauge was affixed under the wheel path while one each was affixed on the walls of the two consecutive geocells located outside on both sides of the wheel path perpendicular to the direction of wheel motion. The maximum measured strains under the wheel path are given in **Table 6.4.3**.

At the time of running the test, as shown in **Figures 6.4.12** through **6.4.14,** only one strain gauge in Section 1-2, three strain gauges in Section 1-3, and two strain gauges in Section 1-4 were functional. The available data show that all the geocells affixed with strain gauges experienced tensile strains and the maximum strain was measured right under the wheel path.

Table 6.4.3 Recorded maximum tensile strains in different reinforced sections

Base course sections above the subgrade		Maximum recorded tensile strain
Section	**Section detail**	**(%)**
1-2	17 cm thick reinforced QW-II with one layer of 15 cm high geocell	NA (strain gauge broken)
1-3	17 cm thick reinforced RAP-I with one layer of 15 cm high geocell	0.40
1-4	17 cm thick reinforced AB-3-II with one layer of 15 cm high geocell	0.39

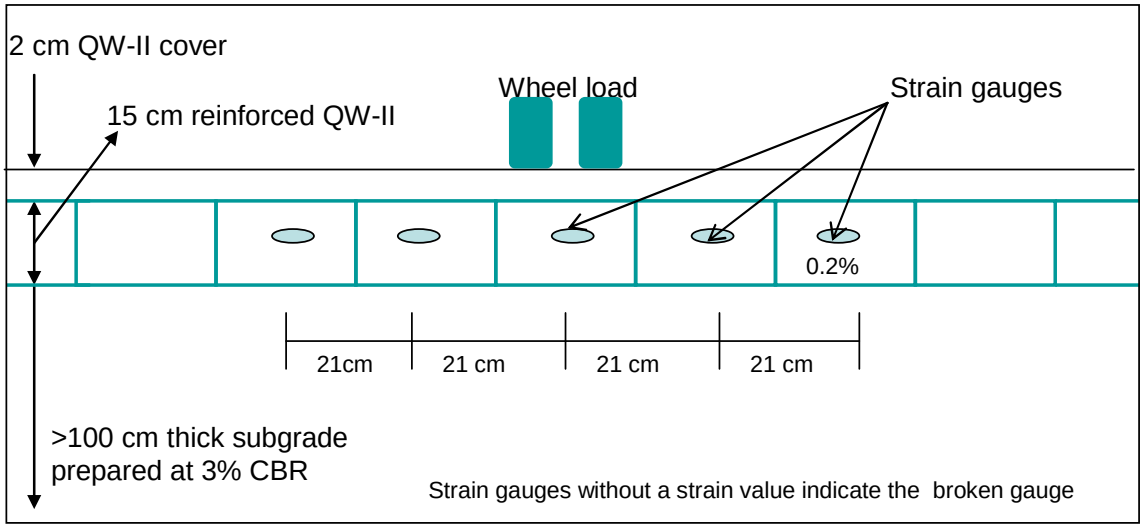

Figure 6.4.12 Measured maximum strain at shown location in Section 1-2

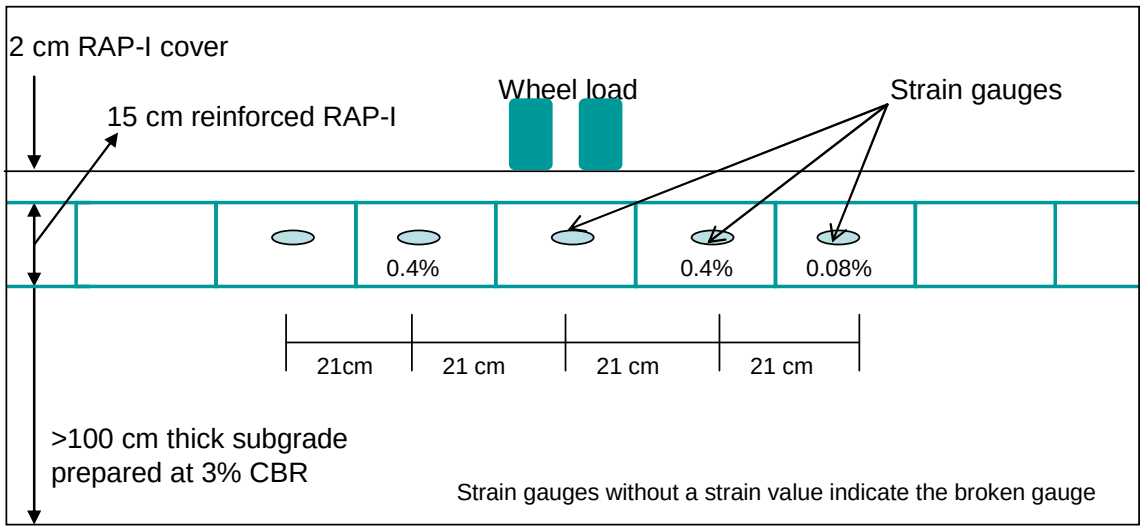

Figure 6.4.13 Measured maximum strains at shown locations in Section 1-3

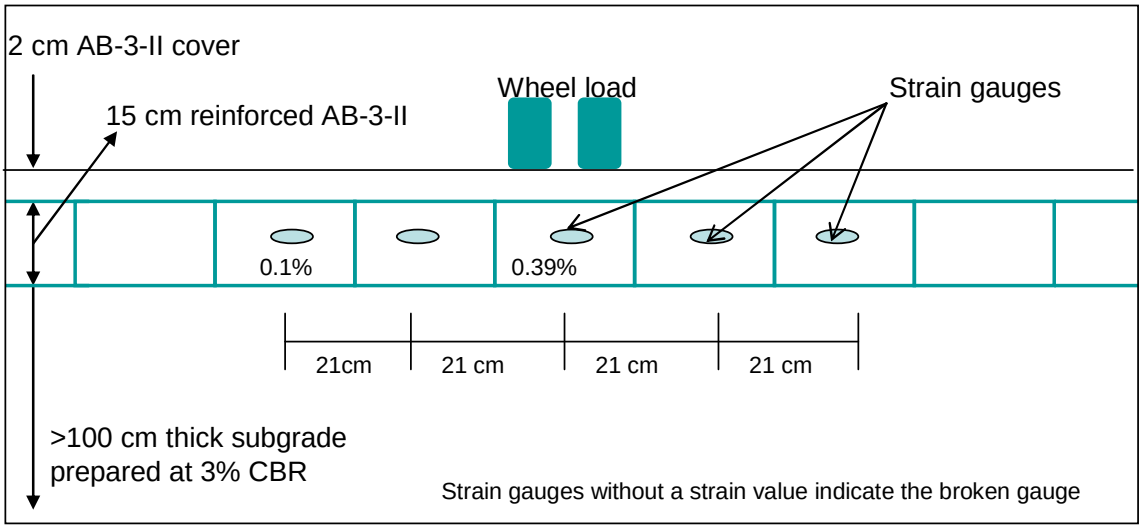

Figure 6.4.14 Measured maximum strains at shown locations in Section 1-4

6.4.6 Summary

As discussed before, the geocell reinforcement can provide lateral confinement, beam effect, and wider stress distribution to the subgrade. These mechanisms ultimately contribute to the reduction of base and subgrade deformations that result in a reduced rut depth on the surface. It is clearly evident from the results of the moving wheel tests that NPA geocell reinforcement of the base courses improved the strength and life of the unpaved sections except for the QW-II section. Based on the rut data in **Figure 6.4.2**, NPA geocell reinforcement not only saved 13 cm of base material but also increased the life of the unpaved road when compared with the control section by 3.5 times for the reinforced RAP-I section and by 1.5 times for the reinforced AB-3-II section at a rut depth of 7.5 cm.. The benefit could have been more pronounced if a similar level of compaction was achieved in all the sections. As shown in **Figure 6.4.1**, the control section had the highest CBR values among the four sections.

As the stress distribution angle was higher for the reinforced QW-II section, the initial failure was within the base course including the breakage of the welds. The failed weld connection rendered the geocell as a single unit rather than a monolithic honeycombed structure. It is also seen from **Figure 3.4.11** that QW-II had more than 10% fines, which made it sensitive to moisture. In other words, QW-II compacted at wet of optimum was too weak to support the traffic loading. Due to deterioration of the base course, the vertical stress increased rapidly at the beginning as shown in **Figure 6.4.11** and caused the subgrade to fail.

The NPA geocell reinforcement increased the stress distribution angle by 13.4^{o} for the reinforced AB-3-II section, by 11.6^{o} for the reinforced RAP-I section, and by 6.5^{o} for the reinforced QW-II section, when compared with the control section.

6.5 Road Sections with RAP Base Course Materials

6.5.1 Test sections

This section discusses a total of seven geocell-reinforced and unreinforced RAP sections tested under moving wheel loading. The seven RAP sections from three different tests (Section 1-3, Section 2-1, Section 2-3, Section 2-4, Section 3-1, Section 3-2, and Section 3-3) are chosen to study the behavior of the geocell reinforcement in RAP and discussed here. Section 1-3 was tested in the first test, Sections 2-1, 2-3, and 2-4 were tested in the second test, and Sections 3-1, 3-2, and 3-3 were tested in the third test. RAP-I was used as the base course material in Sections 1-3, 2-1, 2-3, and 2-4. RAP-II was used in Sections 3-1, 3-2, and 3-3. The properties of these materials are discussed in **Chapter 3**. Section 2-1 was used as a control section for the test with RAP-I while Section 3-1 was used as a control section for the test with RAP-II. All of the sections had same subgrade material (A-7-6 soil) prepared at target CBR value of 3%. The base course of Section 2-1 was 30 cm thick unreinforced RAP-I; Section 1-3 was 17 cm thick RAP-I reinforced with 15 cm high geocell; Section 2-3 was 17 cm thick RAP-I reinforced with 10 cm high geocell; and Section 2-4 was 30 cm thick RAP-I reinforced with two layers of 10 cm thick geocell. Similarly, Section 3-1 was 25 cm thick unreinforced RAP-II; Section 3-2 was 25 cm thick RAP-II reinforced with 10 cm high geocell; and Section 3-3 was 25 cm thick RAP-II reinforced with 7.5 cm high geocell. The details of these test sections are given in **Table 6.3.1** and in **Figures 6.3.1** through **6.3.3**.

A vibratory compactor was used to compact the subgrade and base courses in case of Section 1-3 with RAP-I. A 4-ton roller was used for base course compaction in case of all other sections with RAP-I and RAP-II. The subgrade was prepared at approximately 21% moisture content and compacted until a CBR value of about 3% was achieved. Vane shear,

DCP, nuclear gauge tests were performed to evaluate the density and stiffness of the base courses. Sand cone tests were performed after each test for forensic evaluation.

The results of the vane shear, DCP, nuclear gage, and sand cone tests carried out on the finished subgrade and base course of the four tests are given in **Table 6.5.1**. The average CBR values obtained from the vane shear tests on the ready-to-work subgrade were 3.4% at Section 2-1, 3.4% at Section 1-3, 3.1% at Section 2-3, 3.7% at Section 2-4, 3.2% at Section 3-1, 3.1% at Section 3-2, and 3.2% at Section 3-3. The desired density of the base courses was 95% of the maximum dry density. The compaction was performed on the dry side of the compaction curve within the range of 2% to the optimum moisture content except for Section 1-3 which was compacted on the wet side within the range of 2%. The control sections (Sections 2-1 and 3-1) were compacted in two lifts, i.e., 15 cm (RAP-I) or 12.5 cm (RAP-II) each lift while the reinforced sections were compacted in one lift. In case of Sections 3-2 and 3-3 each geocell was filled just full and compacted with hand tamping compaction before applying the roller compactor. A nuclear gauge was used to monitor the level of compaction and density measurement during the compaction. DCP tests were carried out to estimate the CBR values of the test-ready sections (including the base and the subgrade) using the **Equation 5.1.2**. The DCP test results are plotted in **Figures 6.5.1** and **6.5.2** for sections with RAP-I and RAP-II, respectively. **Figure 6.5.1** shows that the CBR value of the base course in Section 2-1 (the control section for RAP-I) was much higher than the other three reinforced sections. However, the sections with RAP-II, where the 4-ton roller compaction was used, did not show such differences in CBR values.

Table 6.5.1 Measured average CBR values from DCP tests and compaction values from nuclear gauge and sand cone tests

Test method	Sections	2-1	1-3	2-3	2-4	3-1	3-2	3-3
DCP (subgrade)	CBR (%)	3.8	2.2	2.5	3.3	3.1	3.1	2.9
DCP (base course)	CBR (%)	23.2	7.5	7.2	14.7	14.0	15.4	15.0
Nuclear gauge test on base course before test	Compaction (%)	90	87	87	86	94	93	94
Sand cone test on the wheel path after the moving wheel test	Compaction (%)	101	100	95	99	108	101	97
Sand cone test outside of the wheel path after the moving wheel test	Compaction (%)	86	88	86	92	104	92	87

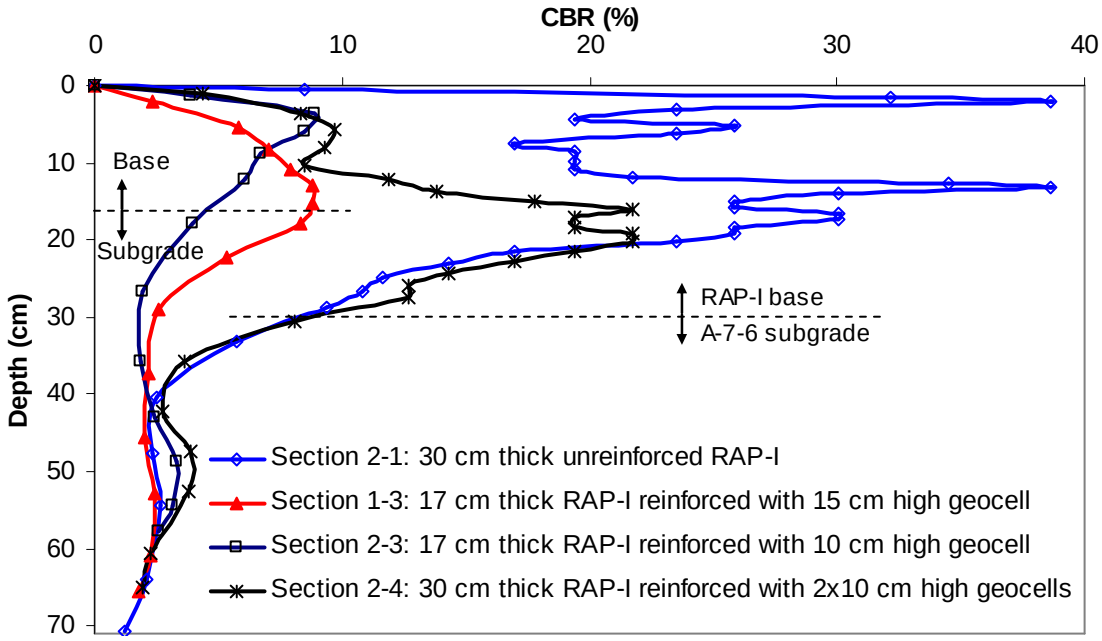

Figure 6.5.1 CBR profiles from DCP tests for the sections tested with RAP-I base courses

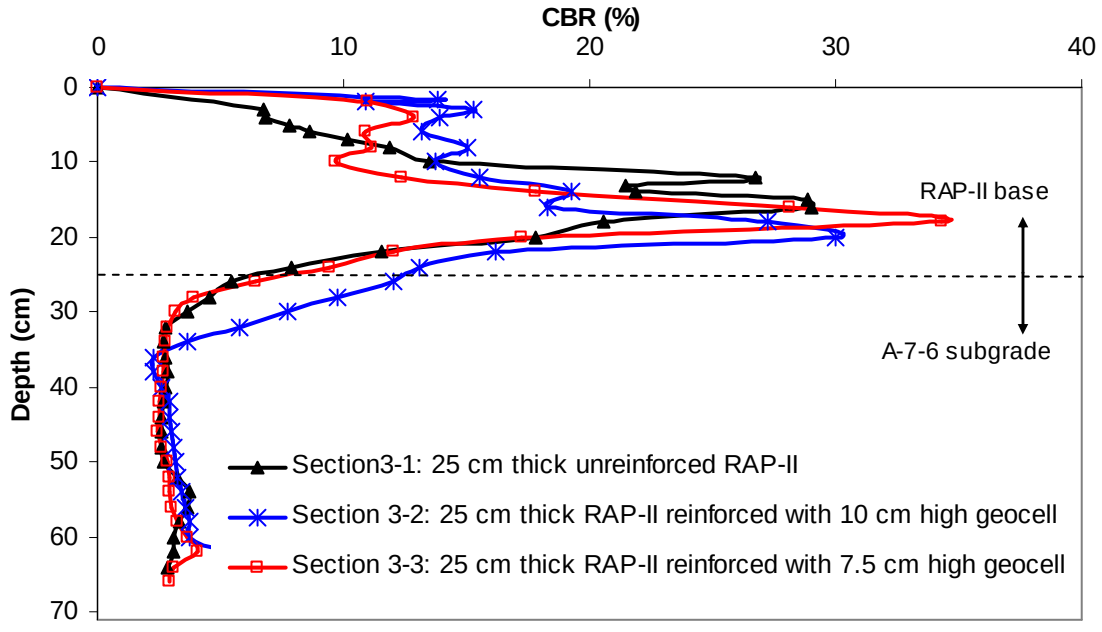

Figure 6.5.2 CBR profiles from DCP tests for the sections tested with RAP-II base courses

Approximately the same kind of compaction was applied to the base courses in all the four sections with RAP-I. The nuclear gauge tests showed the final relative compaction before the test was 90% at Section 2-1, 87% at Section 1-3, 87% at Section 2-3, and 86% at Section 2-4. The sand cone tests after the moving wheel test found the relative compaction of 86% at Section 2-1, 88% at Section 1-3, 86% at Section 2-3, and 92% at Section 2-4 measured outside the wheel paths. These sand cone test results confirmed the results obtained by the nuclear gauge tests. Under the wheel path, however, the sand cone tests showed that the relative compaction was 101% at Section 2-1, 100% at Section 1-3, 95% at Section 2-3, and 99% at Section 2-4. Therefore, densification of base courses happened during trafficking. Although approximately equal amount of compaction effort was applied in all the sections, DCP results showed that the average CBR value of the base course was 23.2% at Section 2-1 (the control section), 7.5% at Section 1-3, 7.2% at Section 2-3, and 15% at Section 2-4. In the control section, a CBR value of 39% was measured at a depth of about 5 and 15 cm from the surface. The control section therefore had higher CBR values than those at other three sections. **Figure 6.5.1** also shows that the average CBR values of the subgrade in Sections 2-1, 1-3, 2-3, and 2-4 were 3.8%, 2.2%, 2.5%, and 3.3%, respectively.

Since the degree of compaction achieved with the vibratory compactor was not consistent, it was decided to use a 4-ton roller compactor for tests with RAP-II. The nuclear gauge tests showed the final relative compaction before the test was 94% at Section 3-1, 93% at Section 3-2, and 94% at Section 3-3. The sand cone tests after the moving wheel test found the compaction of 104% at Section 3-1, 92% at Section 3-2, and 87% at Section 3-3 measured outside the wheel path. Under the wheel path the relative compaction was 108% at Section 3-1, 101% at Section 3-2, and 97% at Section 3-3. Again, densification of base courses happened during trafficking but less than that for RAP-I. Unlike the case of RAP-I, DCP results showed that the average CBR value of the base course was about 18 % for all three

RAP-II sections. **Figure 6.5.2** shows that the average CBR values of the subgrade in Sections 3-1, 3-2, and 3-3 were 3.1%, 3.1%, and 2.9%, respectively. During the testing, surface deformations, vertical stresses at the interface of subgrade and base, and horizontal strains in geocell walls were also monitored.

6.5.2 Rut depths

Since the objective of the tests was to evaluate the effect of geocell reinforcement on RAP as a base course material, comparisons are made separately for RAP-I and RAP-II. All seven test sections were subjected to the same moving wheel load from the APT, however, the rut depths in these sections developed at different rates.

For example, the rut depths in the NPA geocell-reinforced RAP-I sections (Sections 1-3 and 2-3) increased rapidly within the first few passes and obvious heave around the wheel path was observed. At 50 passes, the measured rut depths were approximately 7 cm. The rut depth was measured from the peak to trough around the rut. The moving wheel test was terminated at 300 passes for Sections 1-3 and 2-3 because the rut depth was more than 7.5 cm. Rut measurements on Sections 1-3 and 2-3 were not made after 300 passes. Sections 2-1 (unreinforced) and 2-4 (2-layer NPA geocell-reinforced section) were tested for 40,000 passes. The rut data are plotted against the number of wheel passes for all four sections as shown in **Figure 6.5.3**. Since the numbers of passes for these four test sections are very different, they were grouped into two plots for clarity.

Figure 6.5.3 shows that the 17 cm thick NPA geocell-reinforced RAP-I section with 10 cm high geocell (Section 2-3) had the largest rut depth followed by the 17 cm NPA geocell-reinforced RAP-I section with 15 cm high geocell (Section 1-3) among all the test

sections while the unreinforced 30 cm RAP-I section (Section 2-1) had the smallest rut depth. The better performance of the unreinforced section is due to the higher degree of compaction achieved for its base course compared to other sections. **Figure 6.5.3** also illustrates that after a certain number of wheel passes in Section 2-4, the base course achieved a higher degree of compaction and the rut development followed a similar trend as in case of the stronger base course of Section 2-1. Although a thicker base course with RAP-I showed better performance, the results of the tests with RAP-I were inconclusive in terms of rut depths due to the inconsistent CBR values of the bases.

The tests with RAP-II were carried out for 15,000 wheel passes and the rut data are presented in **Figure 6.5.4**. All three test sections had the same total base thickness but different reinforcement arrangements. It is shown that the section with one layer of 10 cm high geocell performed the best but, the section with one layer of 7.5 cm high geocell did not show much benefit compared with the unreinforced section. Among the three RAP-II sections, the unreinforced RAP-II section (Section 3-1), the reinforced section with 7.5 cm high geocell (Sections 3-3), and the reinforced section with one layer of 10 cm high geocell (Sections 3-2) reached 7.5 cm rut depth at 1200, 1450, and 1950 passes, respectively. In case of tests with RAP-II, since all the test sections had the same overall base course thickness and similar degree of compaction including the average CBR values, a comparison of these sections gives better knowledge on the effect of geocell reinforcement. Traffic benefit ratio (TBR), calculated as the ratio of the number of passes for the reinforced section to that for the unreinforced section reaching 7.5 cm rut is 1.62 for the reinforced section with one layer of 10 cm high geocell and 1.21 for the reinforced section with one layer of 7.5 cm high NPA geocell.

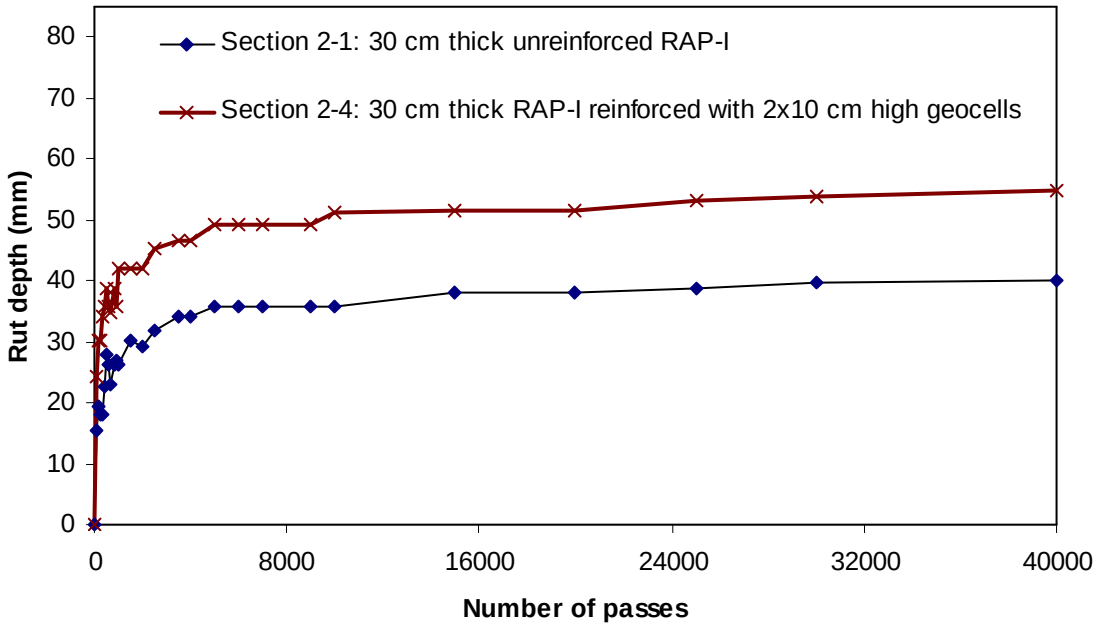

(a)

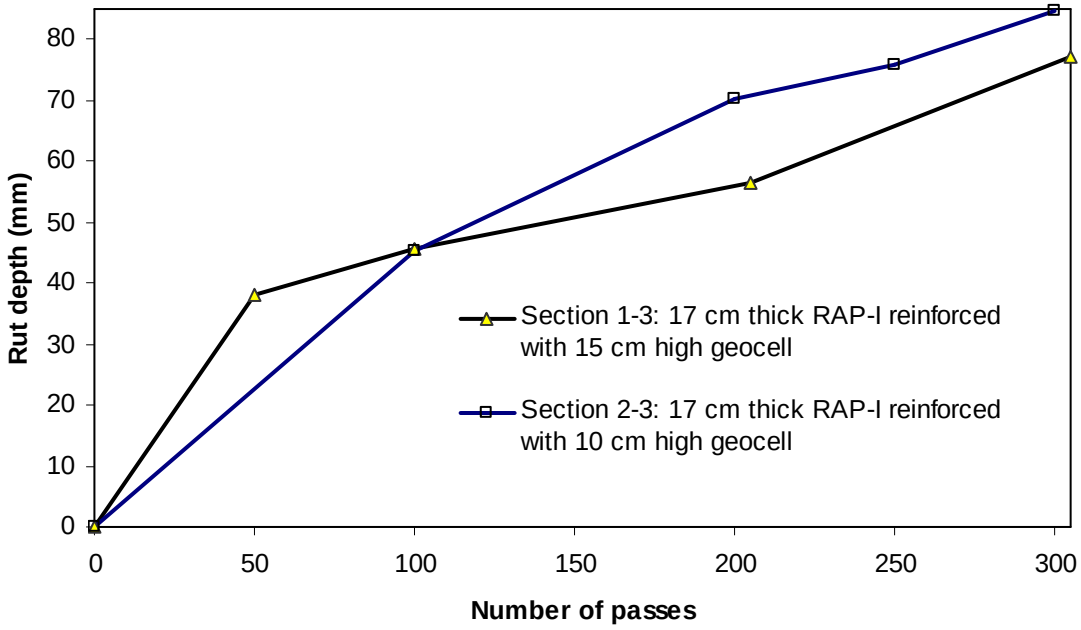

(b)

Figure 6.5.3 Rut depths versus number of passes in RAP-I sections

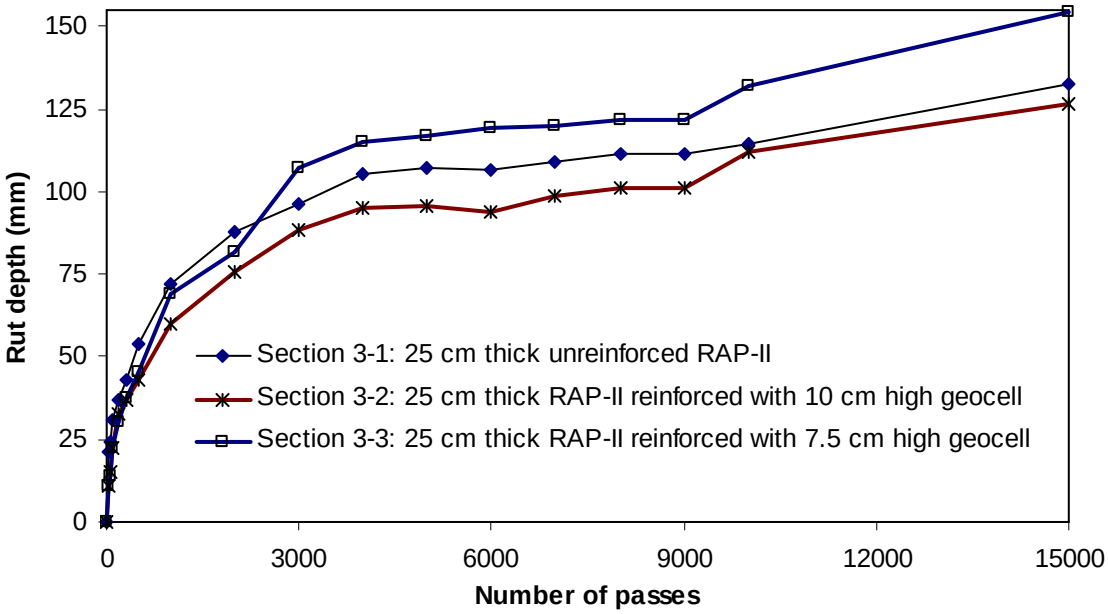

Figure 6.5.4 Rut depths versus number of passes in RAP-II sections

6.5.3 Deformed profiles

After each moving wheel test, all the test sections were exhumed and trenches were cut to examine the deformed profiles of the subgrade and geocells. In all reinforced sections with RAP-I, geocells were initially laid out at 25 cm long in the traffic direction and 21 cm wide in the transverse direction. Forensic tests showed that the shape and size of the cells were intact outside the wheel path. However, under the wheel path, the average size was found to be 23.5 cm long in the traffic direction and 21.5 cm wide in the transverse direction. Some welds of the geocell in Sections 1-3 and 2-3 were broken at the edge of the wheel path due to excessive deformations. To avoid this problem in Sections 3-2 and 3-3, geocells were laid out at 25 cm long in the transverse direction and 21 cm wide in the traffic direction. The deformed profiles and picture of Section 1-3 are shown in Figures **6.4.7** and **6.4.8**. **Figures**

6.5.5 through **6.5.20** show the pictures and the deformed profiles of the other test sections before and after the moving wheel tests.

The profiles are presented at the bottom (also the top of the subgrade) and top of the geocell for the reinforced sections but at the top of the subgrade for the unreinforced section. Due to excessive rut and heave in Sections 1-3 and 2-3, the exhumation of these sections was conducted before re-filling (i.e., after 305 passes). Some top base course surfaces were disturbed during moving the test facility for rut measurements and refilling; therefore, they were not reported. Patterns of rut and heave in the base courses and subgrade are clearly seen in all the sections. It is interesting to note that the rut depths and heaves at different depths in each section were similar in magnitude. The heights of the geocells were maintained approximately constant during the tests. This phenomenon demonstrates the benefit of the NPA geocell confinement.

The top surface profiles of Section 2-1 in **Figure 6.5.5** and Section 2-4 in **Figure 6.5.9** after the test could not be measured as the sections were refilled and leveled on top to run additional passes after other sections in that particular test set deformed excessively. Section 3-1 was also re-filled after other sections had excessive deformations but as it was not leveled, the top surface after the test (15,000 passes) was measured to show the representative shape of the profile only.

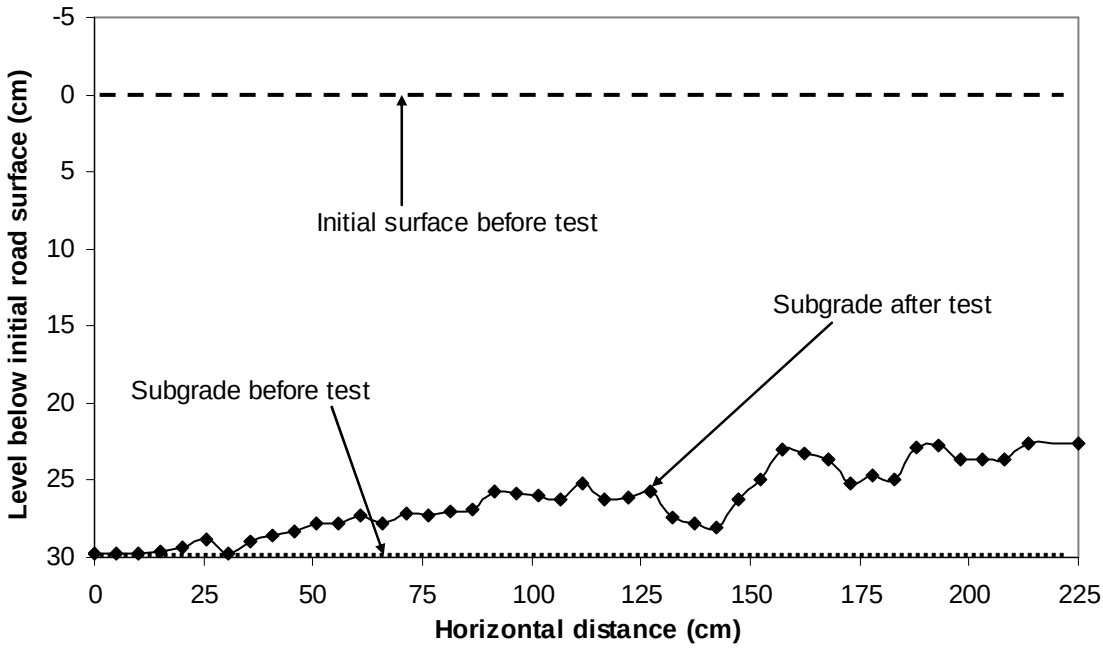

Figure 6.5.5 Deformed profiles of Section 2-1 (RAP-I) after 40,000 passes

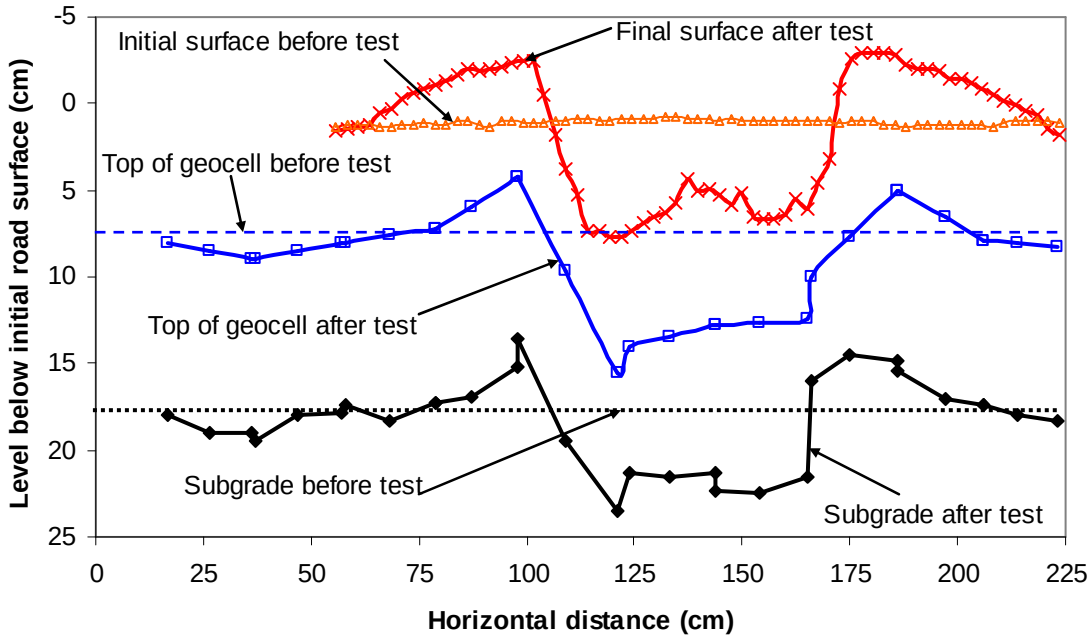

Figure 6.5.6 Deformed profiles of Section 2-3 (RAP-I) after 305 passes

Figure 6.5.7 Deformed wheel path of Section 2-3 (RAP-I) after 100 passes

Figure 6.5.8 Exposed wheel path of Section 2-3 (RAP-I) after 100 passes

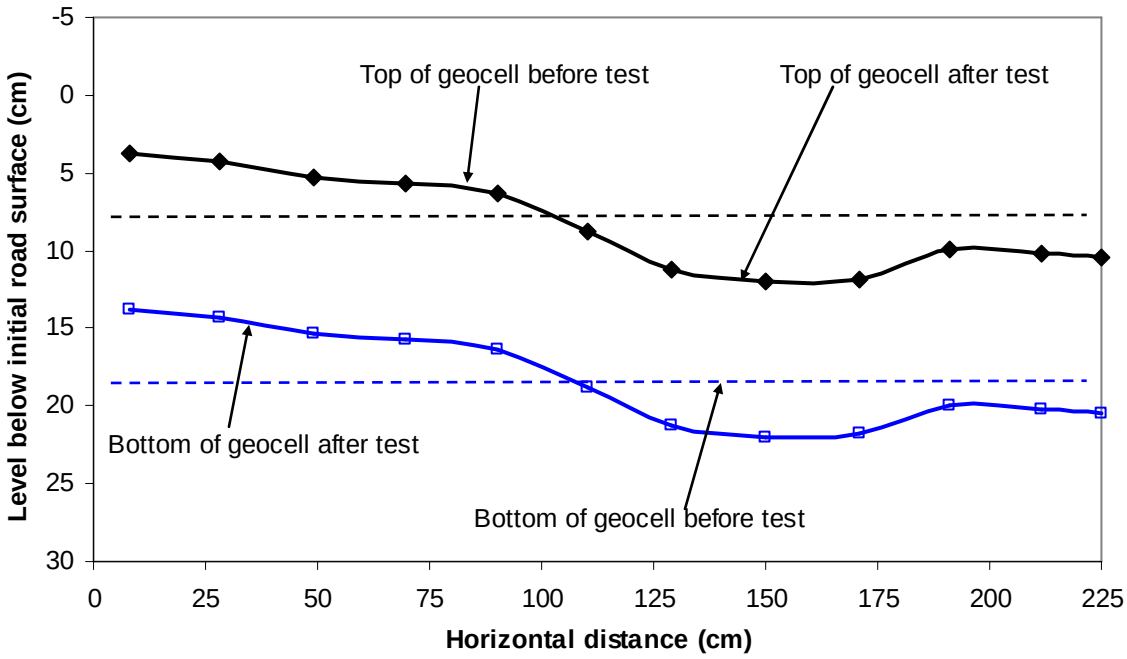

Figure 6.5.9 Deformed profiles of top layer geocell in Section 2-4 (RAP-I) after 40,000 passes

Figure 6.5.10 Deformed wheel path of Section 2-4 (RAP-I) after 100 passes

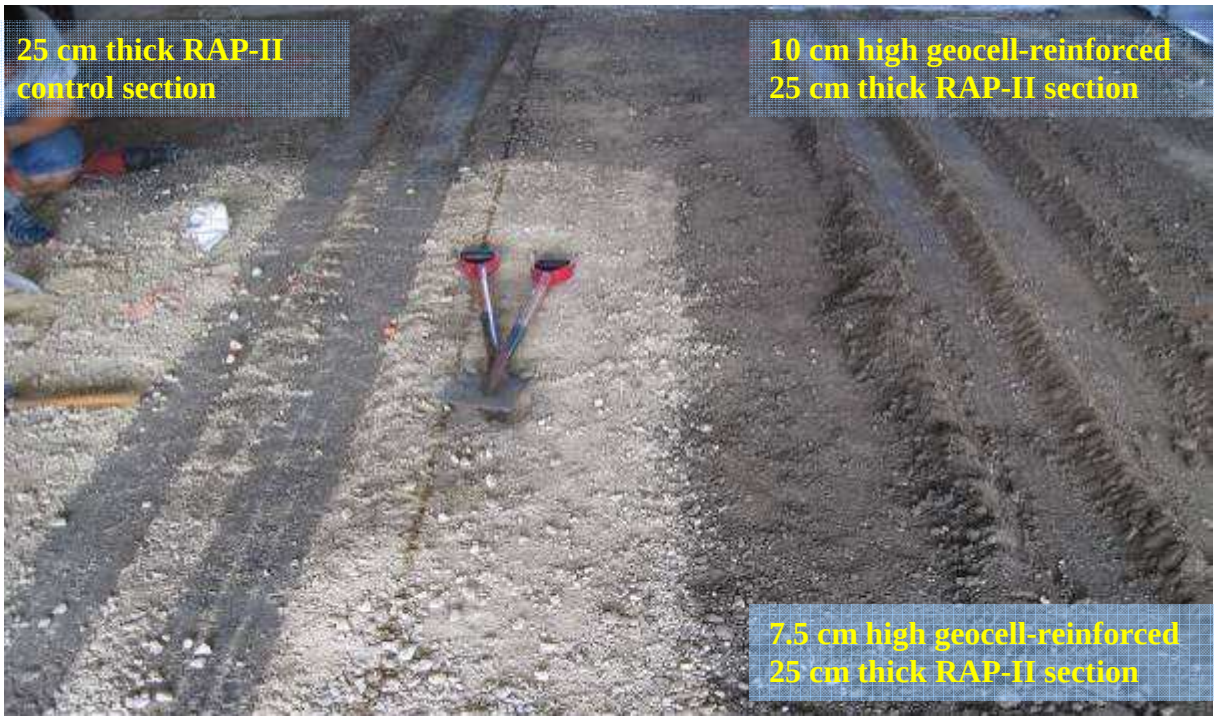

Figure 6.5.11 Three RAP –II sections after 15,000 passes

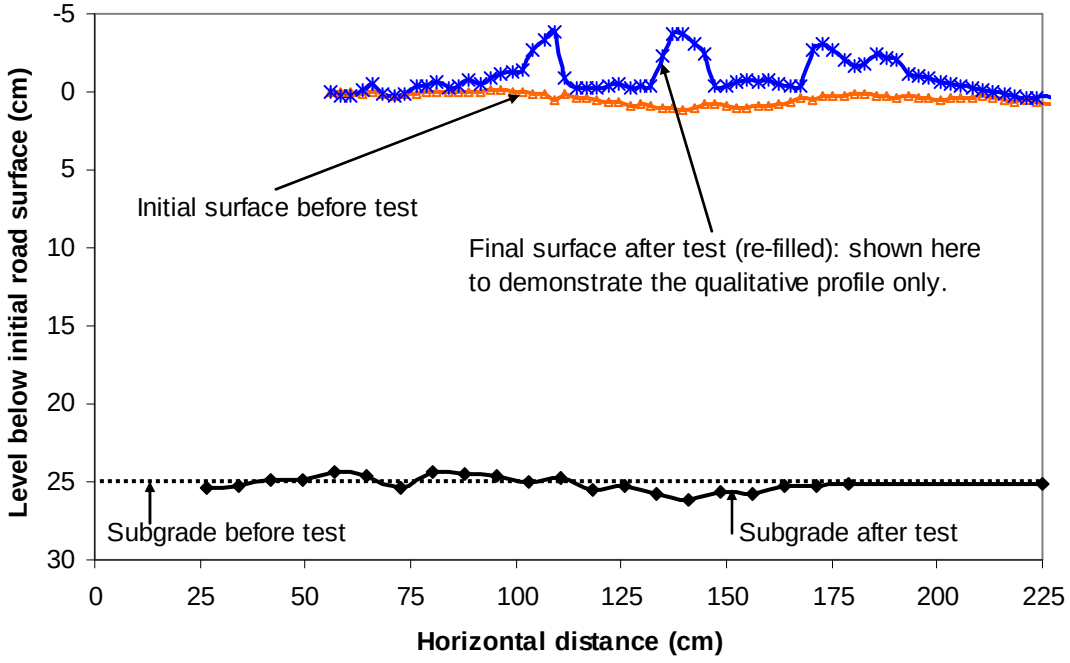

Figure 6.5.12 Deformed profiles of Section 3-1 (RAP-II) after 15,000 passes

Figure 6.5.13 Deformed wheel path of Section 3-1 (RAP-II) after 100 passes

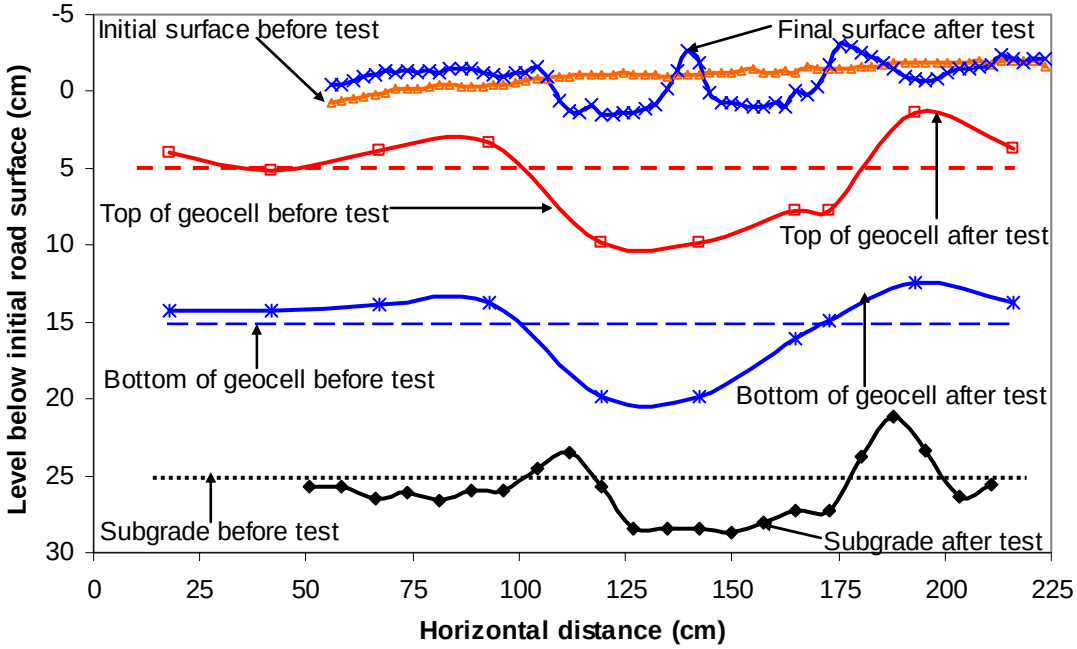

Figure 6.5.14 Deformed profiles of Section 3-2 (RAP-II) after 15,000 passes

Figure 6.5.15 Deformed shape and weld failure of Section 3-2 (RAP-II) after 15000 passes

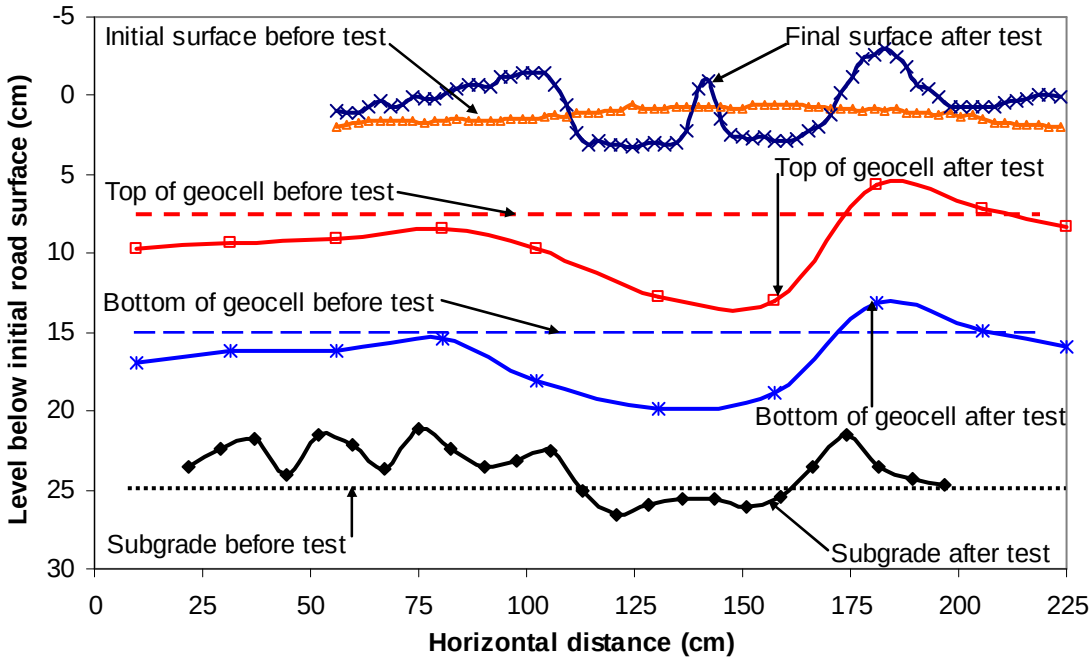

Figure 6.5.16 Deformed profiles of Section 3-3 (RAP-II) after 15,000 passes

Figure 6.5.17 Deformed wheel path of Section 3-3 (RAP-II) after 100 passes

6.5.4 Vertical stresses

Vertical stresses transmitted to subgrade were measured by the pressure cells placed at the subgrade-base interface along the wheel path. The measured peak vertical stresses at number of passes are shown in **Figures 6.5.18** for RAP–I and **6.5.19** for RAP–II. It is seen that the measured vertical stresses at the interface between base course and subgrade in all seven tests were much lower than the tire pressure of 552 kPa applied on the road surface. It is interesting to note that the measured vertical stresses for the unreinforced sections increased with the number of passes and then approached to constant values; however, those for the reinforced sections generally decreased with the number of the passes and then approached constant values even though there were some variations. This phenomenon demonstrates the beam effect of geocell-reinforced bases.

The stress distribution angles were calculated from **Figures 6.5.18** for RAP–I and **6.5.19** for RAP–II using **Equation 5.3.3** with the measured peak vertical stresses and are given in **Table 6.5.2**.

The calculated stress distribution angles of two geocell-reinforced RAP-I base course sections (Sections 2-3 and 2-4) showed only a marginal increase but the reinforced section with one layer of 15-cm high geocell (Section 1-3) showed an increase of 7^o over the unreinforced section (Section 2-1). As pointed out earlier, the base in the unreinforced section (Section 2-1) had much higher CBR values than other reinforced sections thus having a high distribution angle. If the unreinforced section had the same percent of compaction and CBR values as the reinforced sections, the increase in the stress distribution angle by geocell reinforcement would be more significant.

In case of the test sections with RAP-II, which had the same base thickness of 25 cm and percent of compaction, the measured vertical stresses at the interface between subgrade and base were much lower in the geocell-reinforced sections than those in the unreinforced section. **Table 6.5.2** shows that the geocell-reinforced sections (Sections 3-2 and 3-3) had the stress distribution angles of 7^o and 10^o higher than the unreinforced section (Section 3-1). This increase in the stress distribution angles for the reinforced sections demonstrates that geocell reinforcement reduced the vertical stress by distributing the load to a wider area at the interface.

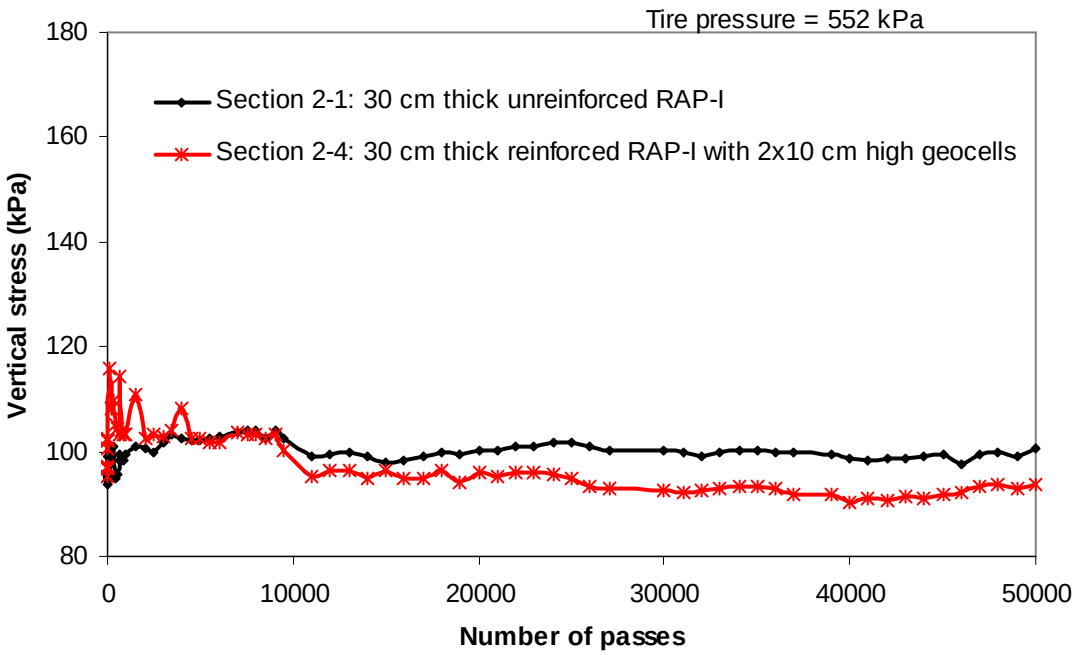

(a)

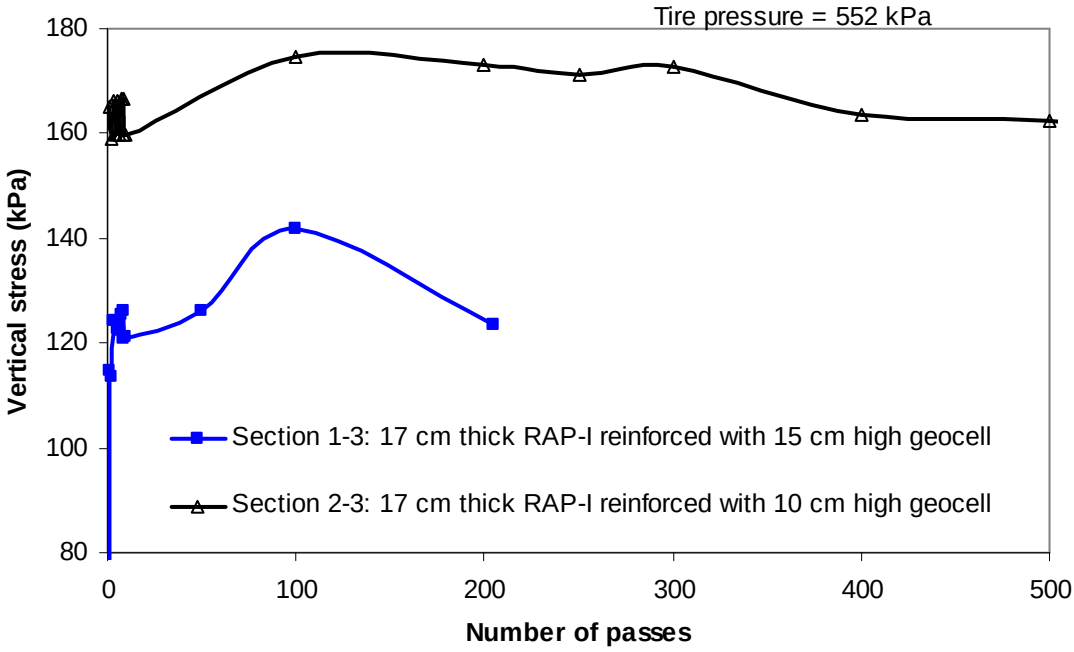

(b)

Figure 6.5.18 Measured vertical stresses at the subgrade-base interface in the RAP-I test sections

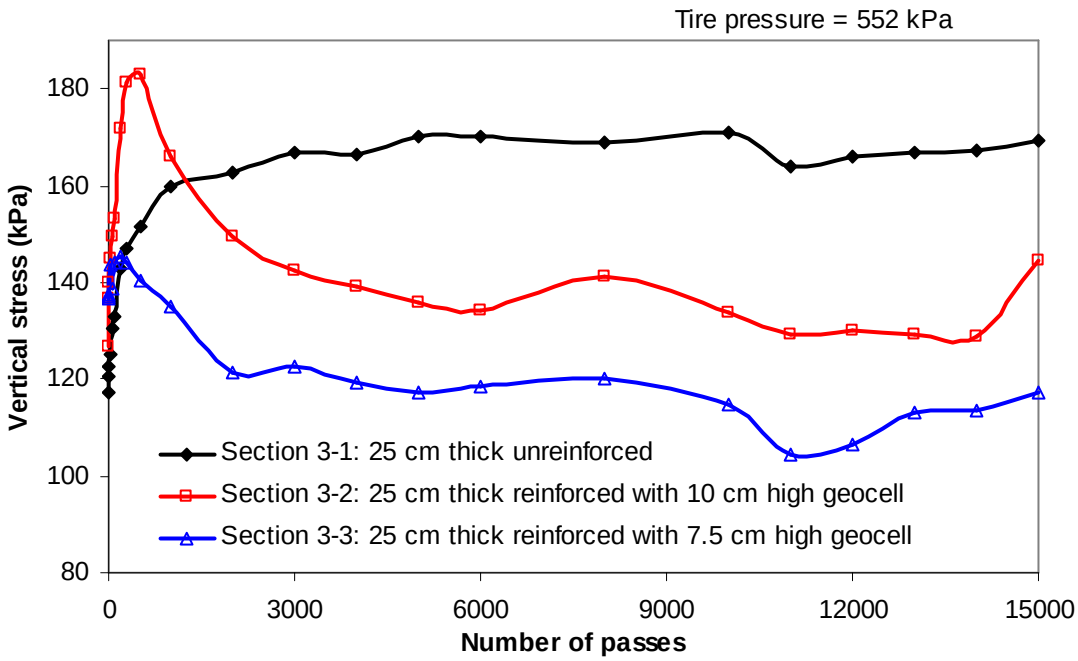

Figure 6.5.19 Measured vertical stresses at the subgrade-base interface in the RAP-II test sections

Table 6.5.2 Stress distribution angles for different test sections

Base course sections above the subgrade		Vertical stress	Distribution angle
Section	**Section detail**	**(kPa)**	**(degrees)**
2-1	30 cm thick unreinforced RAP-I	101	34
1-3	17 cm thick reinforced RAP-I with one layer of 15 cm high geocell	141	41
2-3	17 cm thick reinforced RAP-I with one layer of 10 cm high geocell	172	35
2-4	30 cm thick reinforced RAP-I with two layers of 10 cm thick geocell	93	36
3-1	25 cm thick unreinforced RAP-II	169	26
3-2	25 cm thick reinforced RAP-II with one layer of 10 cm high geocell	129	33
3-3	25 cm thick reinforced RAP-II with one layer of 7.5 cm high geocell	114	36

6.5.5 Maximum strains in geocells

Strain gauges were attached on the walls of the geocells in all the reinforced sections to measure the strain developments in the geocells as explained in **Section 6.4.5**. There were five strain gauges in each geocell-reinforced section and they were placed horizontally on the geocell walls underneath and outside the wheel path. The details of the placement of the strain gages can be found in **Figures 6.4.13**, and **6.5.20** through **6.5.23**. The maximum

tensile strains recorded on the cells were located right under the wheel path. The recorded maximum strain in each section is given in **Table 6.5.3**.

At the time of running the test, **Figures 6.4.13,** and **6.5.20** through **6.5.23** show some of the strain gages were not functional. The available data show that all the geocells located under the wheel path experienced tensile strain and the geocells adjacent to the central geocell experienced tensile strain in general with one exception in case of Section 3-3. Similarly, in general, the strain gages located on the outer geocells (42 cm to 50 cm outside the center of the wheel path) experienced a small compressive strain.

Table 6.5.3 Recorded maximum tensile strains in different reinforced sections

Base course sections above the subgrade		Maximum recorded tensile strain
Section	**Section detail**	**(%)**
1-3	17cm thick reinforced RAP-I with one layer of 15 cm high geocell	0.4
2-3	17 cm thick reinforced RAP-I with one layer of 10 cm high geocell	0.52
2-4	30 cm thick reinforced RAP-I with two layers of 10 cm high geocell	0.52
3-2	25 cm thick reinforced RAP-II with one layer of 10 cm high geocell	0.3
3-3	25 cm thick reinforced RAP-II with one layer of 7.5 cm high geocell	1.29

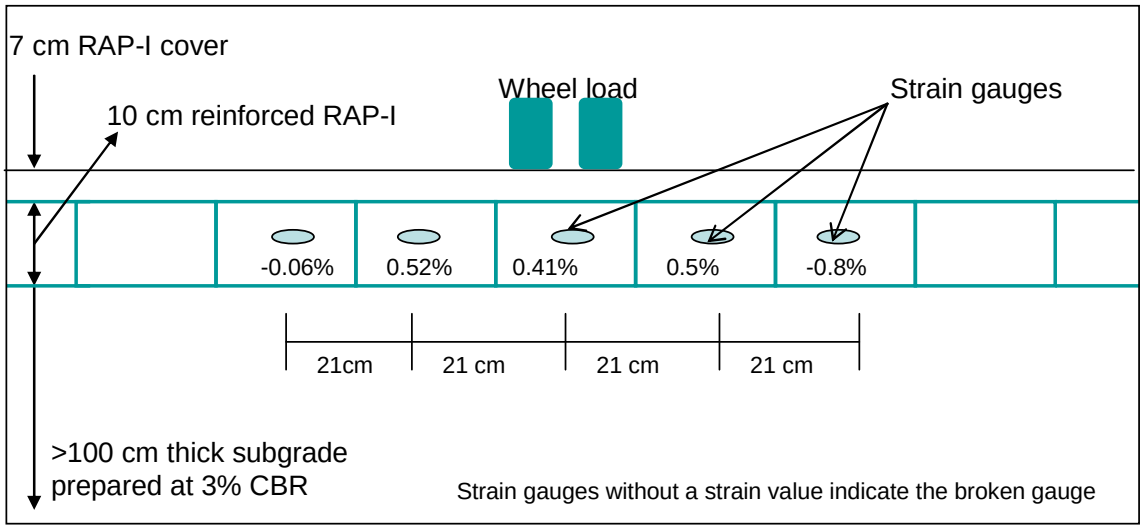

Figure 6.5.20 Measured maximum strains at shown locations in Section 2-3

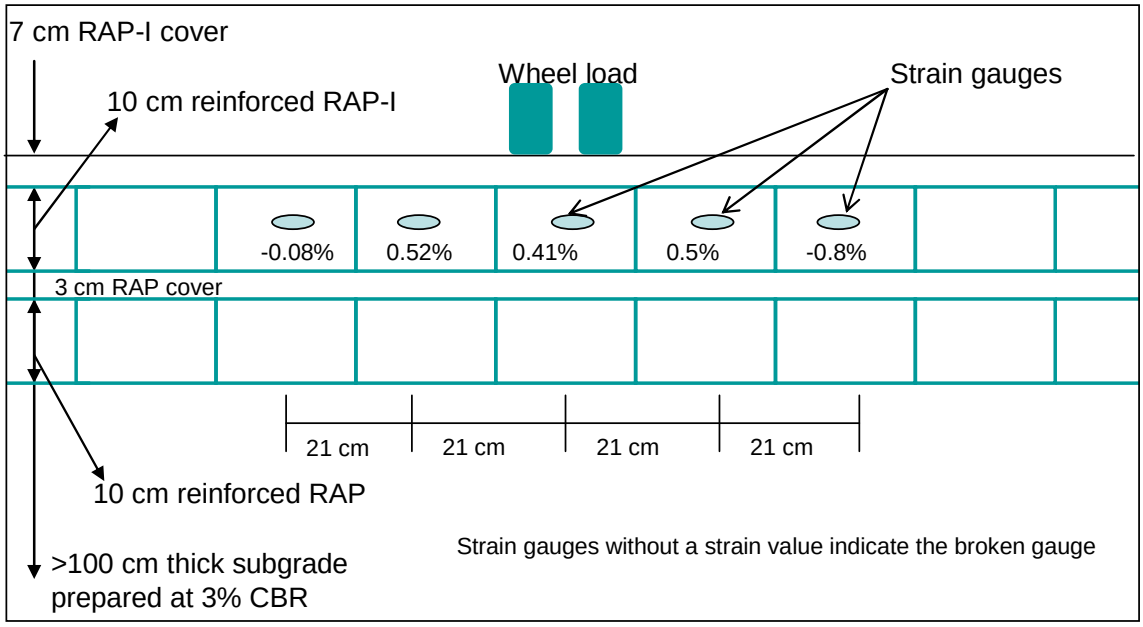

Figure 6.5.21 Measured maximum strains at shown locations in Section 2-4

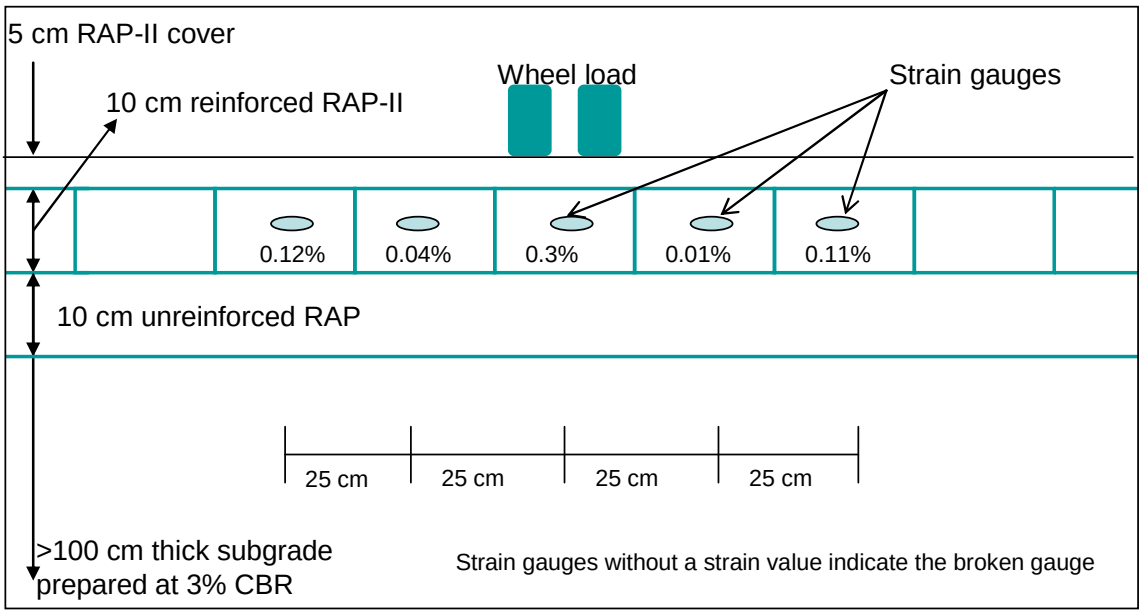

Figure 6.5.22 Measured maximum strains at shown locations in Section 3-2

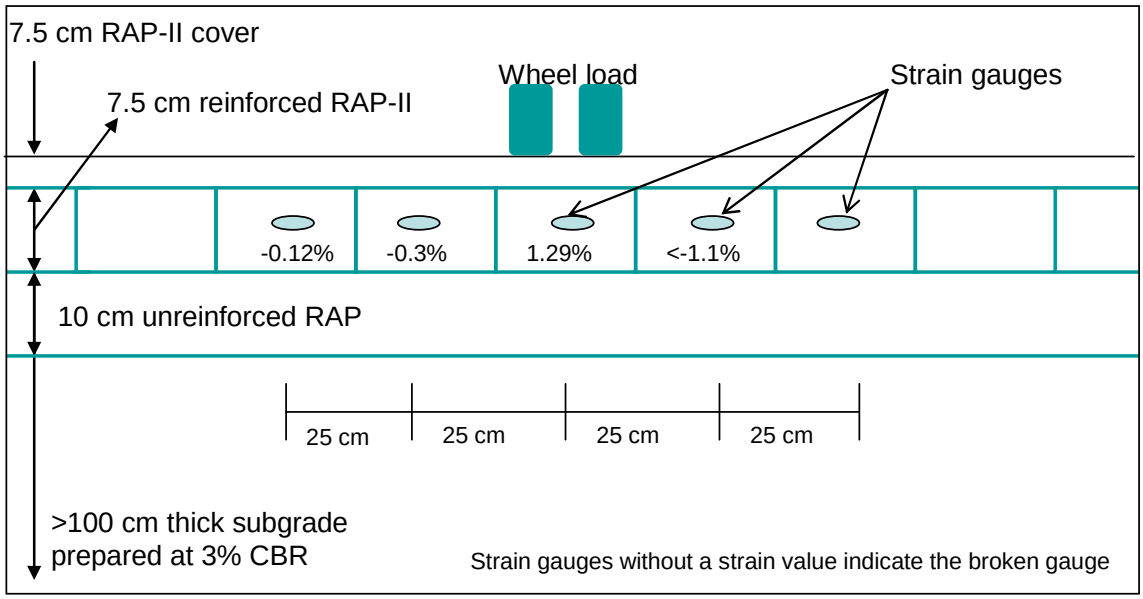

Figure 6.5.23 Measured maximum strains at shown locations in Section 3-3

6.5.6 Summary

The above test results show that although similar procedures were followed in the preparation of test sections with RAP-I and RAP-II, only the tests with RAP-II produced conclusive results. The inconclusive results in case of tests with RAP-I can be attributed to the differential degree of compaction achieved by the vibratory plate compactor at different test sections. **Figure 6.5.1** clearly shows that the base course in Section 2-1 had a much higher average CBR value (23.2%) than other reinforced sections (i.e., approximately 3.1, 3.3, and 1.5 times as those in Sections 1-3, 2-3, and 2-4, respectively). The comparison of the results of sand cone tests under and outside the wheel path after the test as discussed earlier confirmed that the base courses were further densified during trafficking, especially for RAP-I. Such a vibratory plate compactor is rarely used in the field to compact geocell-reinforced bases; therefore, these results are not further discussed in this section. However, one important lesson learned from this moving wheel test is that less compacted geocell-reinforced bases would minimize the benefit of geocell confinement, which should be avoided in the field.

When the 4-ton roller compactor was used, comparatively consistent compaction was achieved in all three sections of RAP-II as shown in **Figure 6.5.2**. The test results with RAP-II clearly demonstrated the benefits of geocell reinforcement of RAP base courses both in terms of rut depth and stress distribution to the interface between subgrade and base course. Therefore, it can be concluded that in addition to geocell reinforcement, compaction plays a vital role in overall performance of the geocell-reinforced unpaved road sections.

The test results with RAP-II suggest that the height of geocell reinforcement played an important role in the performance of the geocell-reinforced road section. Based on the rut data in **Figure 6.5.4**, NPA geocell reinforcement increased the life of the unpaved road. A

geocell with a height higher than 10 cm may be beneficial to the confinement, however, it may make the compaction more difficult. Therefore, a compromise in the selection of cell height has to be made to achieve the optimum performance. Further research is needed to evaluate the effect of cell height on the degree of compaction of base courses.

It is clearly evident from the results of the moving wheel tests that NPA geocell reinforcement reduced the vertical stresses at the interface between subgrade and base course. This reduction is attributed to the mechanisms of increased base stiffness due to lateral confinement, beam effect, and wider stress distribution. **Table 6.5.2** shows that the stress distribution angles were higher for all the reinforced sections than the unreinforced sections. NPA geocell reinforcement increased the stress distribution angle by 7^o and 10^o for the reinforced RAP-II sections when compared with the unreinforced section.

The visual observations during tests and exhumations after tests suggested that the cover thickness is important for the protection of geocells. In Section 1-3, 2 cm RAP-I cover was used above the geocell. The thin cover disappeared during the test due to compression of the base course and shoveling of the moving wheel. The top of the geocell was exposed after a certain number of passes. This problem was minimized when a thicker fill cover (5 or 7.5 cm thick) was used. The forensic test showed that in the section which had a thin cover, the welds connecting the geocells failed or were opened under the wheel path. The breakage of connecting welds was also observed in case of thinner sections (e.g. Section 1-3 and 2-3) under excessive deformations. The failed weld connection rendered the geocell as a single unit rather than a monolithic honeycombed structure thus minimizing the benefit of the geocell confinement.

This test has demonstrated that the Recycled asphalt pavement (RAP) materials can be used as infill materials in geocells for base courses in unpaved roads as a sustainable alternative.

6.6 Road Sections with AB-3-II Base Course Material

6.6.1 Test sections

There were four base course sections (Sections 1-1, 1-4, 2-2, and 3-4) of AB-3-II tested in course of three tests. Since the Sections 1-1 and 1-4 from the first test have already been discussed in **Section 6.4,** further discussion and analysis on these two sections are limited to only comparison with Section 2-2 from the second test and Section 3-4 from the third test. The details of these sections are given in **Table 6.3.1** and shown in **Figures 6.3.1** through **6.3.3**. The subgrade of material A-7-6 soil was prepared for all test sections as discussed in **Section 6.2**. The properties of the AB-3-II material were discussed in **Chapter 3**.

The 30 cm thick unreinforced Section 1-1 was used as the control section for the comparison. The Section 1-4 was 17 cm thick reinforced with 15 cm high NPA geocell and 2 cm top cover; Section 2-2 was 17 cm thick reinforced with 10 cm high NPA geocell and 7 cm top cover; Section 3-4 was 25 cm thick reinforced with 10 cm high NPA geocell but had 10 cm thick AB-3-II bottom cushion and 5 cm top cover.

The results of DCP, nuclear gage, and sand cone tests carried out on the finished subgrade and base courses of the four tests are given in **Table 6.6.1**. The DCP carried out on the test ready sections are shown in **Figure 6.6.1**. The average CBR value obtained from DCP tests show that the subgrade on all three tests was prepared at about 2.1% to 3.2%. The higher CBR value in the Section 1-1 was achieved because the compaction in this section was done in two lifts compared to the single lift in case of Section 1-4. Section 3-4 also had the higher CBR values because it was compacted effectively in three layers; first under the geocell, second inside the geocell with hand tamping and the third again with the roller

compactor on top surface. Sections 1-1 and 1-4 were compacted using the vibratory plate load compactor while Section 2-2 was compacted with the roller compactor. In case of Section 3-4, the first 10 cm base course was compacted without any reinforcement then the geocell was laid out. Each cell was separately compacted by hand tamping before placing the 5 cm thick top cover which was again compacted with the roller compactor. From the DCP test data, the CBR values of the test ready Sections 1-1, 1-4, 2-2, and 3-4 were 22.6%, 8.8%, 13.8%, and 20.9%, respectively. Nuclear gauge was used to monitor the compaction of the base course. The degrees of compaction achieved on the test ready sections based on nuclear gauge data were 90%, 86%, 98%, and 95% for Sections 1-1,1-4, 2-2, and 3-4, respectively. Sand cone tests were carried out after the moving wheel test at two different locations on each section, one at the wheel path and the other outside. The results show a higher degree of compaction under the wheel path suggesting that the densification happened in the base course during the moving wheel test.

Table 6.6.1 Measured average CBR values from DCP tests and compaction values from nuclear gage and sand cone tests

Test Method	Sections	1-1	1-4	2-2	3-4
DCP (subgrade)	CBR (%)	2.4	2.1	3.2	2.7
DCP (base course)	CBR (%)	22.6	8.8	13.8	20.9
Nuclear gauge test on base course before the moving wheel test	Compaction (%)	90	86	97.7	94.6
Sand cone test under the wheel path after the moving wheel test	Compaction (%)	86	83	88	96
Sand cone test outside the wheel path after the moving wheel test	Compaction (%)	83	80	83	86

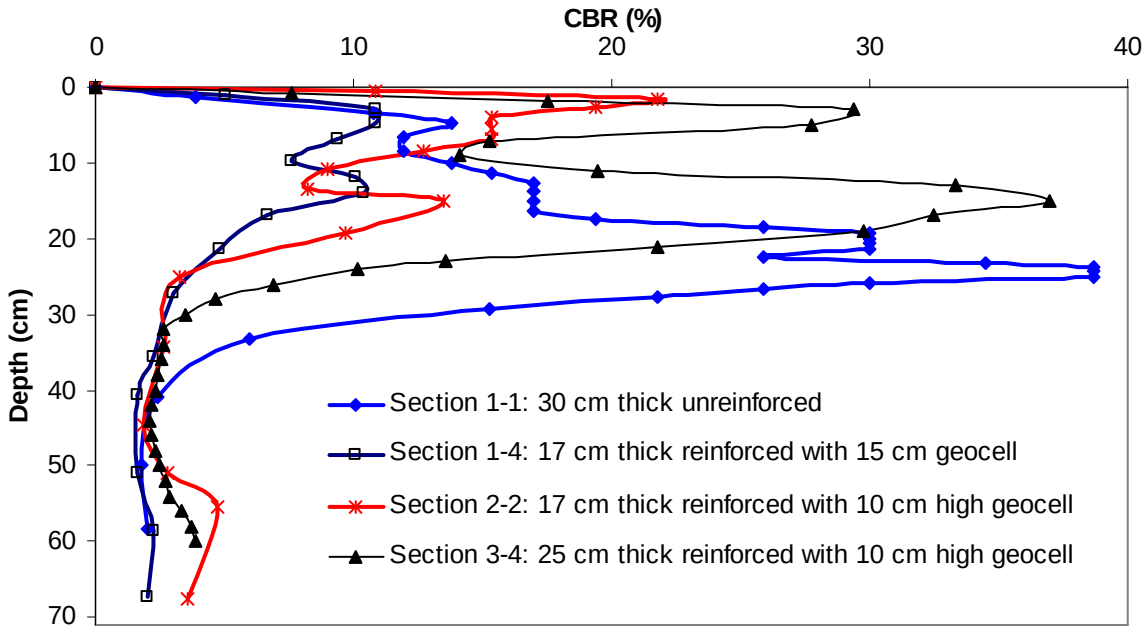

Figure 6.6.1 CBR values obtained from DCP tests in AB-3-II bases

6.6.2 Rut depths

Figure 6.6.2 shows that the unreinforced AB-3-II section (Section 1-1) had the largest rut depth among all the test sections while the geocell-reinforced 25 cm thick AB-3-II section (Section 3-4) had the smallest rut depth. Even though all the NPA geocell-reinforced sections had a thinner base thickness, they had smaller rut depth than the unreinforced section. This result demonstrated that NPA geocell reinforcement reduced the rut depth compared to the unreinforced section.

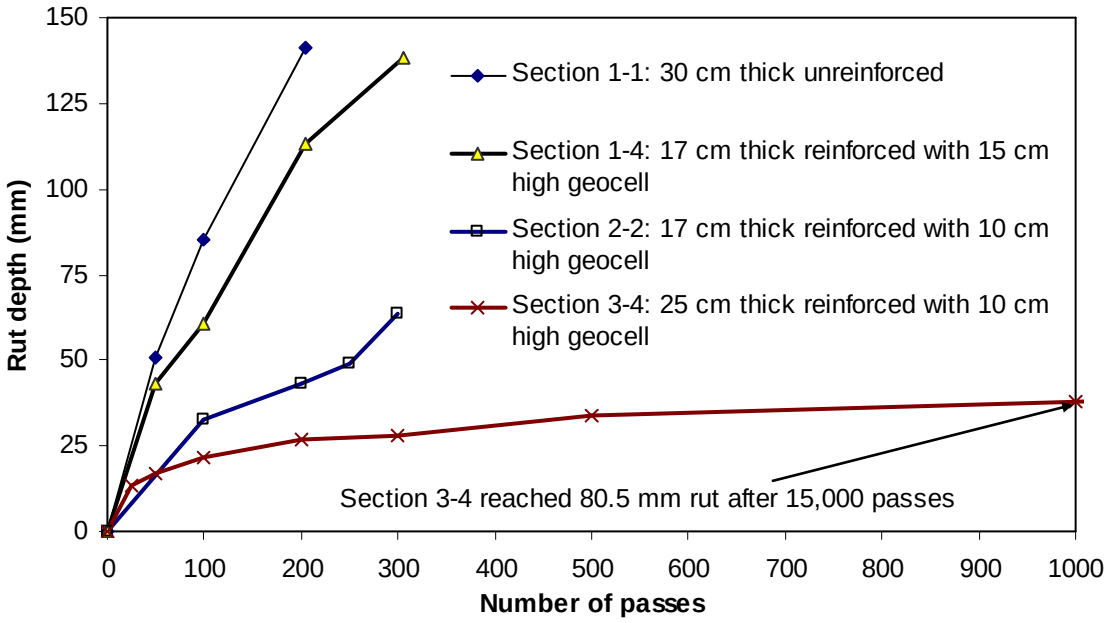

Figure 6.6.2 Rut depth versus number of passes for AB-3-II sections

6.6.3 Deformed profiles

As mentioned before after each test, all the test sections were exhumed and trenches were cut to examine the deformed profiles and geocells. In all reinforced sections, geocells

were initially laid out at 25 cm long in the traffic direction and 21 cm wide in the transverse direction. Forensic tests showed that the shape and size of the cells were intact outside the wheel path. However, under the wheel path, the average size was found to be 23.5 cm long in the traffic direction and 21.5 cm wide in the transverse direction. Breakage of welds along the wheel path was observed only in Section 2-2. **Figures 6.4.4** and **6.4.9** show the deformed profiles of Sections 1-1 and 1-4 before and after the moving wheel test. **Figures 6.6.3** through **6.6.8** show the deformed profiles and pictures of Sections 2-2 and 3-4. The profiles are presented at the bottom (also the top of the subgrade) and top of the geocell for the reinforced sections but at the top of the subgrade for the unreinforced section. **Figure 6.6.5** shows the failure of weld at the edge of the wheel path in Section 2-2. After the failure of weld, the contribution of the geocell outside the wheel path was minimized. To avoid this situation, geocells were laid out with the seam side perpendicular to the wheel path in the third test (Section 3-4).

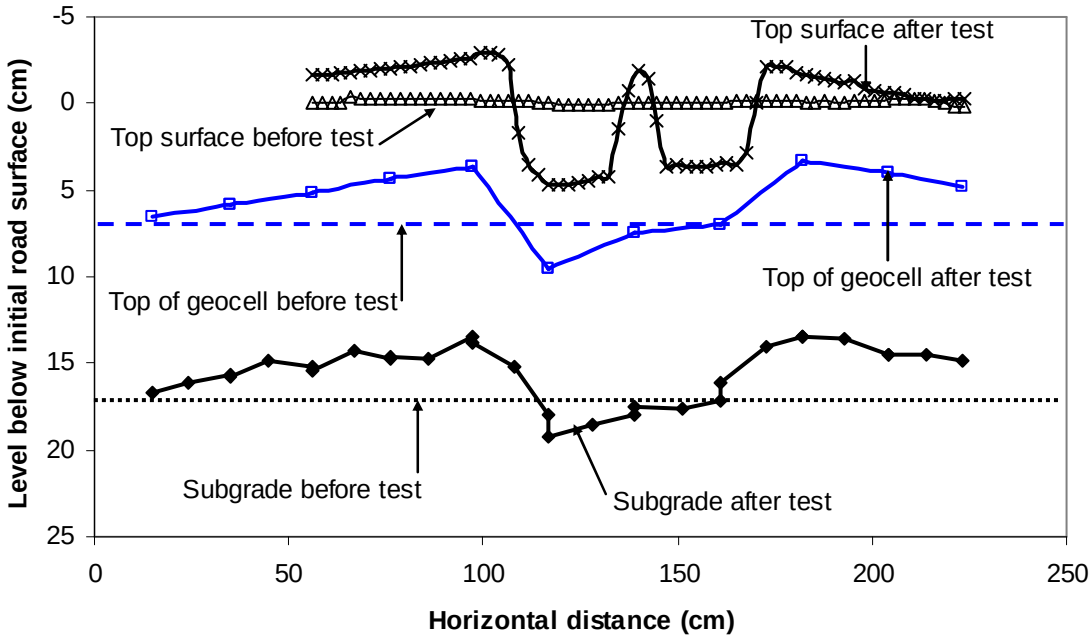

Figure 6.6.3 Profiles of Section 2-2 after 100 passes

Figure 6.6.4 Wheel paths of Section 2-2 after 100 passes

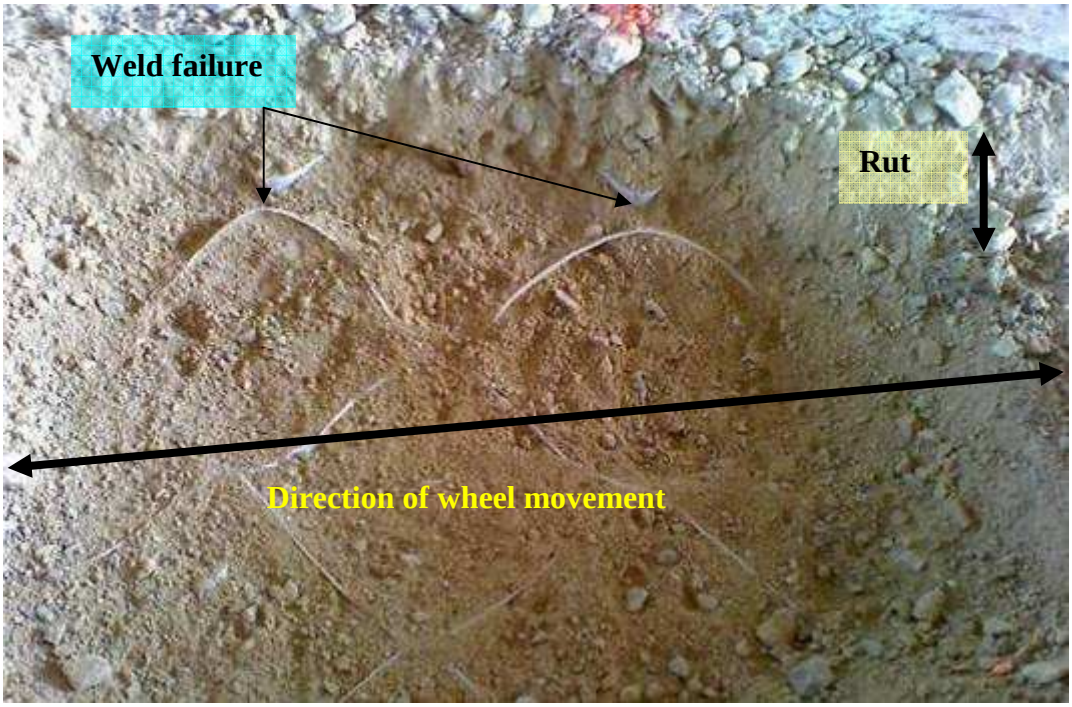

Figure 6.6.5 Exhumed Section 2-2

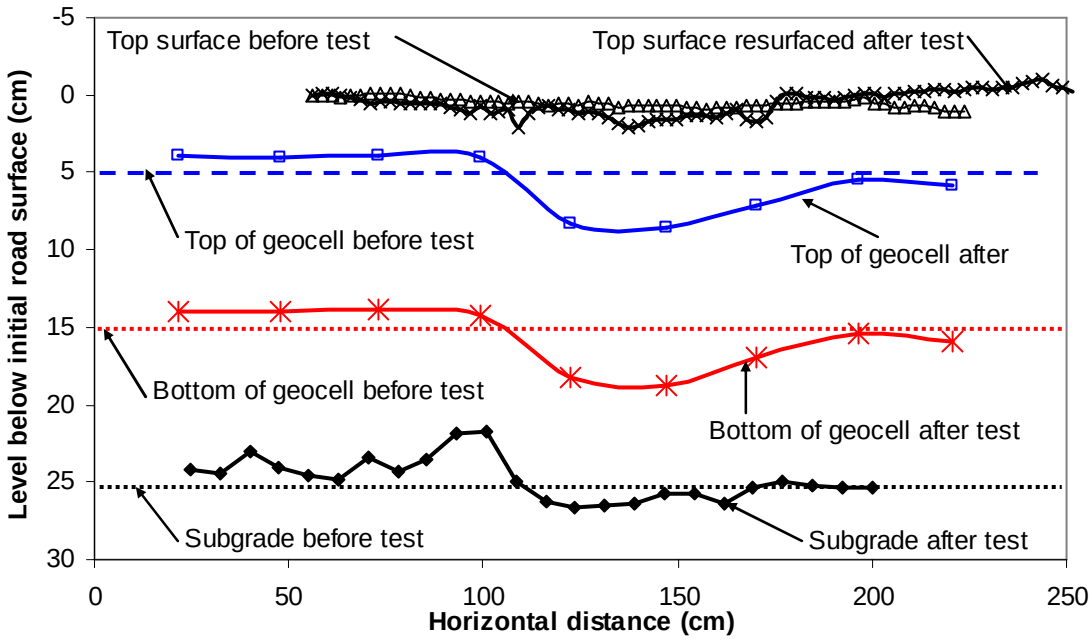

Figure 6.6.6 Profiles of Section 3-4 after 100 passes

Figure 6.6.7 Wheel path of Section 3-4 after 100 passes

Figure 6.6.8 Exhumed Section 3-4

6.6.4 Vertical stresses

The vertical stresses at the interface of subgrade and base course were measured by the earth pressure cells located under the wheel path. **Figures 6.6.9** shows the measured maximum vertical stresses with the number of wheel passes. The maximum stresses measured in all the sections were much lower than the applied tire pressure of 552 kPa om the surface. After 205 passes, the vertical stresses measured in Sections 1-1 and 1-4 were 98 kPa and 117 kPa, respectively. At the end of 50,000 passes, the maximum stress measured in Section 2-2was 168 kPa. At the end of 15,000 passes, the maximum stress measured in Section 3-4 was 120 kPa.

The stress distribution angles calculated using **Equation 5.3.3** for all four test sections are given in **Table 6.6.2**. This comparison demonstrates that geocell reinforcement reduced

the vertical stress by distributing the load to a wide area. The section with higher geocell height (15 cm) had the highest distribution angle of 43^0.

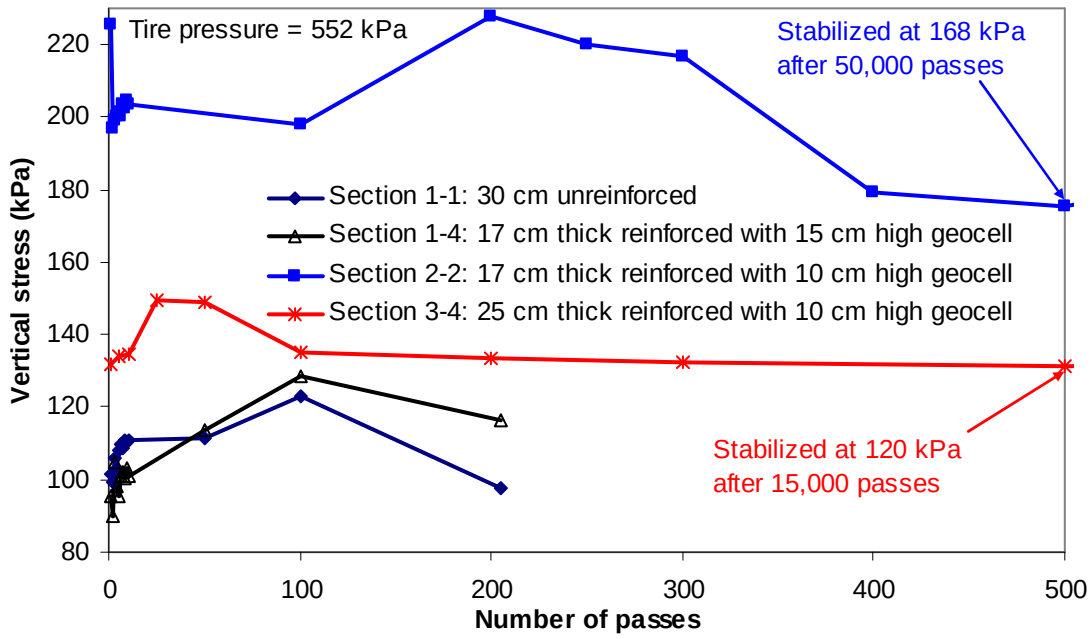

Figure 6.6.9 Measured vertical stresses at the interface between subgrade and base for AB-3-II test sections

Table 6.6.2 Stress distribution angle

Base course sections above the subgrade		Vertical stress	Distribution angle
Section	**Section detail**	**(kPa)**	**(degrees)**
1-1	30 cm thick unreinforced AB-3-II	123	29
1-4	17 cm thick reinforced AB-3-II with one layer of 15 cm high geocell	128	43
2-2	17 cm thick reinforced AB-3-II with one layer of 10 cm high geocell	168	36
3-4	25 cm thick reinforced AB-3-II with two layers of 10 cm high geocell	120	35

6.6.5 Maximum strains in geocells

Strain gauges were attached on the walls of the geocells in all the reinforced sections as explained in **Section 6.4.5**. The details of the placement of the strain gages can be found in **Figures 6.4.12**, **6.4.14**, **6.6.10,** and **6.6.11**. The maximum tensile strains recorded on the cells were located right under the wheel path. The recorded maximum strain in each section is given in **Table 6.6.3**.

At the time of running the test, as shown in **Figures 6.4.12**, **6.4.14**, **6.6.10,** and **6.6.11** some of the strain gages were not functional. The available data shows that all the geocells located under the wheel path experienced tensile strain except for Section 3-4. The geocells adjacent to the central geocell experienced tensile strain in general with one exception in case of Section 3-4. Similarly, in general, the strain gauges located on the outer geocells (42 cm to 50 cm outside the center of the wheel path) experienced a small compressive strain.

Table 6.6.3 Recorded maximum tensile strains in different reinforced sections

Base course sections above the subgrade		Maximum recorded tensile strain
Section	**Section detail**	**(%)**
1-4	17 cm thick reinforced AB-3-II with one layer of 15 cm high geocell	0.39
2-2	17 cm thick reinforced AB-3-II with one layer of 10 cm high geocell	0.72
3-4	25 cm thick reinforced AB-3-II with one layer of 10 cm high geocell	0.27

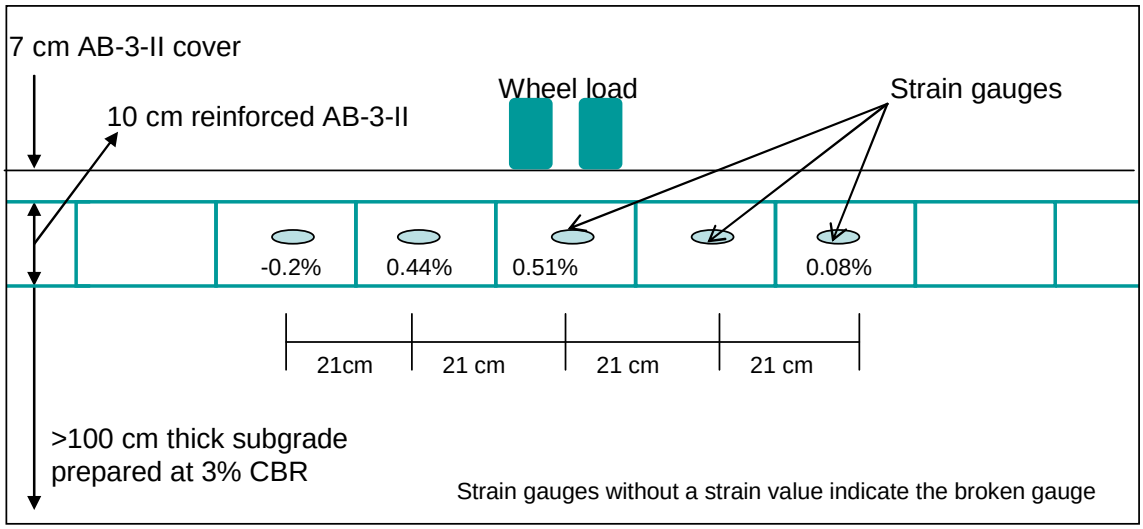

Figure 6.6.10 Measured maximum strains at shown locations in Section 2-2

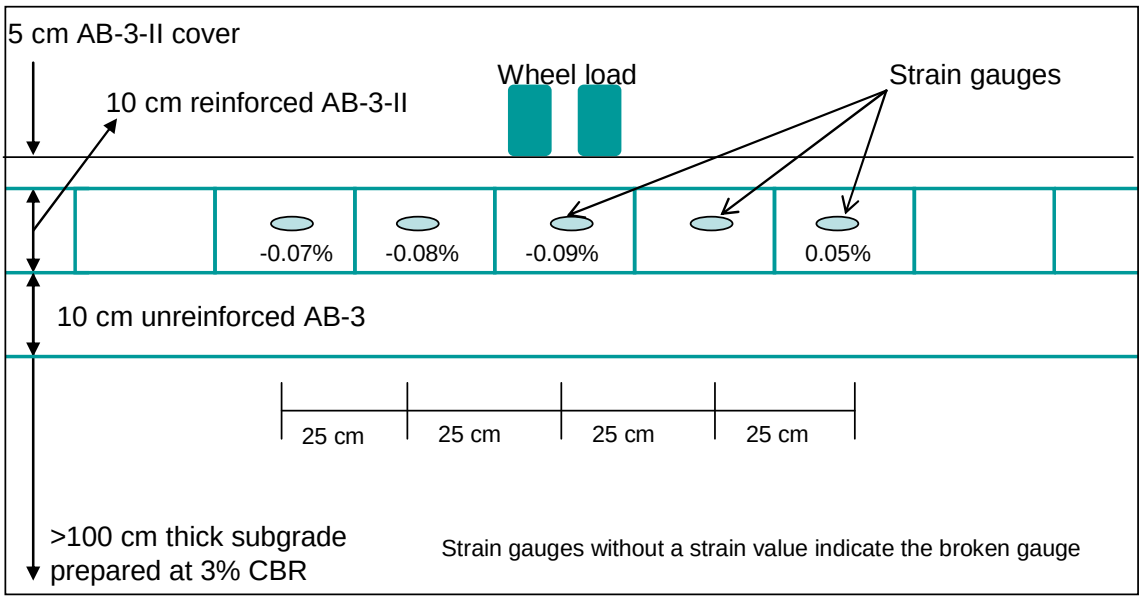

Figure 6.6.11 Measured maximum strains at shown locations in Section 3-4

6.6.6 Summary

The test results of AB-3-II sections show that NPA geocell reinforcement improved the performance of AB-3-II base course sections. At a rut depth of 75 mm, both 17 cm thick reinforced sections with 10 cm and 15 cm high NPA geocell performed better than the 30 cm thick unreinforced section. The following findings can be summarized from this comparison of four AB-3-II test sections:

1. Although the 17 cm thick reinforced bases (Sections 1-4 and 2-4) had only half the CBR value of the 30 cm unreinforced base (Section 1-1) and were 13 cm thinner than the unreinforced base, both reinforced sections performed better than the unreinforced section.
2. The weld connecting the geocell honeycomb failed in case of Section 2-2. As already discussed before in the previous sections, this failure minimized benefit of the

geocells at a large rut depth. Therefore, with a better weld connection, even better performance of NPA geocell reinforced unpaved section can be expected.

3. A better performance was observed when the reinforced section was better compacted (for example, Section 3-4). Therefore, it can be concluded that in addition to geocell reinforcement, compaction plays a vital role in overall performance of the geocell-reinforced unpaved road sections.

4. NPA geocell reinforcement increased the stress distribution angle by 7^{o} to 14^{o} for the reinforced AB-3-II sections when compared with the unreinforced section.

5. The better performance of Sections 2-2 and 3-4 over the Section 1-4 suggests that a thicker fill cover (5 to 7.5 cm) is necessary to minimize the damage to the geocell.

CHAPTER SEVEN

DEVELOPMENT OF DESIGN METHOD

7.1 Existing Design Method

The design equation (**Equation 7.1.1**) developed by Giroud and Han (2004a and b) can be used to estimate the required base course thickness (h) of unreinforced and planar geosynthetic (geotextile and geogrid)-reinforced unpaved roads:

$$h = \frac{\left\{0.868 + (0.661 - 1.006\mathrm{J}^2)\left(\frac{r}{h}\right)^{1.5}\right\}\log N}{\eta\left\{1 + 0.204\left[R_E - 1\right]\right\}} \times \left(\sqrt{\frac{P}{\pi r^2\left(\frac{s}{f_s}\right)\left\{1 - \xi\exp\left[-\omega\left(\frac{r}{h}\right)^n\right]\right\}N_c c_u}} - 1\right) r$$

(**Equation 7.1.1**)

where η = the conversion factor between field and laboratory performance (0.689 for a laboratory condition under cyclic plate loading and 1.0 for a field condition under moving wheel loading); J = the aperture stability modulus, which is only suitable for geogrid and assumed to be 0 for unreinforced and geotextile-reinforced roads); r = radius of tire contact area (m); N = number passes; P = wheel load (kN); R_E = the modulus ratio of base to subgrade (limited to 5.0 for unreinforced and planar geosynthetic-reinforced roads); c_u = undrained cohesion of the subgrade soil (kPa); ξ, ω, and n = parameters determined as 0.9, 1.0, and 2.0, respectively; s = allowable rut depth (mm); f_s = factor equal to 75 mm; and N_c is the bearing capacity factor (3.14 for unreinforced roads, 5.71 for geogrid-reinforced roads, and 5.14 for geotextile-reinforced roads).

7.2 Development of Design Method for NPA Geocell-reinforced Unpaved Roads over Weak Subgrade

As **Equation 7.1.1** was developed for planar reinforcement, it needs to be modified for the design of three-dimensional geocell-reinforced unpaved roads. The reduction in the stress distribution angle with the number of passes caused by the deterioration of the base course material under the repeated loading in the laboratory was observed by Gabr (2001) and the test results from the present study (**Chapters 5** and **6**) strongly supported this observation. **Chapters 5** and **6** also show that NPA geocell reinforcement significantly slowed down the rate of deterioration in the base quality. This phenomenon is attributed to the geocell confinement of the base course to increase and maintain the modulus of the base course. A modulus improvement factor was proposed by Han et al. (2007) to account for this benefit:

$$I_f = \left(\frac{E_{bc(reinforced)}}{E_{bc(unreinforced)}} \right) \qquad \textbf{(Equation 7.2.1)}$$

where $E_{bc\ (reinforced)}$ = the modulus of the reinforced base and $E_{bc\ (unreinforced)}$ = the modulus of the unreinforced base.

The modulus ratio (R_E) given in **Equations 2.4.5** and **7.1.1** was limited to a maximum limit of 5 for unreinforced and planar geosynthetic-reinforced unpaved roads. Giroud and Han (2004b) recommended this limit considering that base courses cannot be well compacted over soft subgrade. However, the three-dimensional confinement by geocells can overcome this problem and help the base course reach and maintain its higher modulus. Han et al. (2007) reported the geocell-reinforced bases had the modulus ratios ranging from 4.8 to 10. The calculated modulus ratios from cyclic plate loading tests and accelerated moving wheel

tests in this study ranged from 3.4 to 7.6 and will presented later in this chapter. Therefore, it is reasonable to set the maximum limit of the modulus ratio to 7.6 for NPA geocell-reinforced unpaved roads until more test data are available to justify a higher limit to be used. Considering the modulus improvement factor, the modulus ratio can be expressed as follows:

$$R_E = I_f \frac{E_{bc}}{E_{sg}} = Max\left\{7.6,\ I_f\left(\frac{3.48CBR_{bc}^{0.3}}{CBR_{sg}}\right)\right\} \qquad \textbf{(Equation 7.2.2)}$$

where E_{bc} = resilient modulus of base course (MPa); E_{sg} = resilient modulus of subgrade soil (MPa); CBR_{bc} = California Bearing Ratio (CBR) of base course; and CBR_{sg} = CBR of subgrade.

The bearing capacity mobilization coefficient (m) is given by Giroud and Han (2004b) as follows:

$$m = \left(\frac{s}{f_s}\right)\left\{1 - 0.9\exp\left[-\left(\frac{r}{h}\right)^2\right]\right\} = \left(\frac{s}{75mm}\right)\left\{1 - 0.9\exp\left[-\left(\frac{r}{h}\right)^2\right]\right\} \quad \textbf{(Equation 7.2.3)}$$

Since a nonwoven geotextile sheet is commonly used below geosynthetic-reinforced bases, the bearing capacity factor (N_c) for geocell-reinforced unpaved roads can be reasonably assumed to be equal to 5.14 (Giroud and Han, 2004a).

Giroud and Han (2004b) proposed a factor (k) that controls the rate of reduction in the stress distribution angle which depends on the (r/h) ratio and the aperture stability modulus of geogrid. Obviously, the aperture stability modulus is not suitable for geocells. A factor (k') is proposed here to replace the term $(0.661 - 1.006J^2)\left(\frac{r}{h}\right)^{1.5}$ in **Equation 7.1.1** for the design of geocell-reinforced bases over weak subgrade as follows:

$$h = \frac{(0.868 + k' \log N)}{\eta\{1 + 0.204(R_E - 1)\}} \times \left(\sqrt{\frac{P}{\pi r^2 m 5.14 c_u}} - 1 \right) r \qquad \textbf{(Equation 7.2.4)}$$

The k' factor will be calibrated in the next section using the data from the cyclic plate loading tests and the accelerated moving wheel tests in this study.

The undrained shear strength (c_u) is the property of subgrade soil and can be estimated by the following correlation:

$$c_u = f_c CBR_{sg} \qquad \textbf{(Equation 7.2.5)}$$

where f_c= factor equal to 20.5 kPa for the subgrade used in the cyclic plate loading tests and 19.7 kPa in the moving wheel tests. The f_c factors were obtained from the CBR tests and unconfined compression tests carried out on the subgrade materials, which were discussed in **Chapter 3**.

7.3 Calibration of k' Factor

To calibrate the factor k' in **Equation 7.2.4**, the data from the NPA geocell-reinforced base tests, seven in the big geotechnical box (**Chapter 5**), and eight in the moving wheel test (**Chapter 6**) were used. Two separate moving wheel tests with the same loading equipment for NPA geocell-reinforced KR-I sand on relatively strong subgrade (CBR = 5%) were conducted and reported by Yang (2010). The failure mode in case of the relatively stronger subgrade was the lateral spreading of the base course material which is different from the subgrade failure mode of other 15 tests considered in this study. Therefore, the test data based on relatively strong subgrade are not considered for the present calibration. The seven tests in the big box included four tests with AB-3-I and three tests with KR-I sand base

course materials while the eight moving wheel tests included three tests with AB-3-II and five tests with RAP-I and RAP-II base course materials.

The conversion factor (η) for the cyclic plate loading tests in the big box was taken as 0.689. Since the moving wheel tests are considered as field tests, a factor of 1.0 was assigned in the calculation.

The modulus improvement factor (I_f) was calculated based on the plate loading tests carried out on the medium-size geotechnical box with the procedures and equipments discussed in **Chapter 4**. The static plate loading tests with multiple NPA geocell reinforcement were carried out with AB-3-I, RAP-I and KR-II sand materials separately and compared with the test with the same material under an unreinforced condition. The respective stiffness values of unreinforced and NPA geocell-reinforced (Type II NPA geocell from **Chapter 3.1**) base courses were calculated to find the modulus improvement factor (I_f). The pressure-displacement curves from the static plate loading tests for KR-II sand are shown in **Figures 7.3.1**. Similarly **Figures 7.3.2** and **7.3.3** show the pressure-displacement curves for RAP-I and AB-3-I bases, respectively. The ratio of the slope of the linear portion on the pressure-displacement curve of the reinforced section to that of the unreinforced section was defined as the modulus improvement factor 'I_f'. The 'I_f' values calculated from **Figures 7.3.1** through **7.3.3** were 2.0 for KR-II sand base courses and 1.7 for AB-3-I and RAP base courses. These values are considered representative for all the KR sand, AB-3, and RAP base courses and used in the calculation to calibrate k'. As these static tests were carried out with 2 cm cover, the modulus of the unreinforced material was multiplied by 'I_f' for the thickness equal to the height of geocell plus 2 cm cover. The remaining thickness of the base course was considered as unreinforced and no modulus improvement factor was applied. The final modulus was then calculated by taking the weighted average of the two values. For example,

for a 23 cm thick 15 cm high NPA geocell-reinforced RAP base section, the modulus improvement factor can be calculated as follows:

$$I_f = \left[\frac{(15+2)\times 1.7 + (23-15-2)\times 1.0}{23} \right] = 1.52$$

The number of loading cycles (or passes in case of moving wheel tests) 'N' was directly obtained from the tests. The applied pressure 'P' was 40 kN in all the tests and the radius of tire contact area (r) was 0.15 m. The CBR values of base and subgrade, CBR_{bc} and CBR_{sg}, were obtained from the DCP tests carried out on the test sections. The 'I_f' factors and these CBR values were used to calculate the modulus ratios 'R_E' in **Equation 7.2.2,** which are reported in Table 7.2.1. It is shown that R_E ranged from 3.4 to 7.6. It should be noted here that all the sections had 5 to 8 cm thick well-graded aggregate material cover on top of the NPA geocell. In case of KR-I sand, the cover was AB-3 aggregate.

The bearing capacity mobilization coefficient (m) was calculated using **Equation 7.2.3**. The allowable permanent deformation (s) was taken as 75 mm, but in cases where the tests were stopped before reaching this limit the rut value at the final number of loading cycles (N) was taken as the final value of 's'. 'c_u' was calculated using **Equation 7.2.5**.

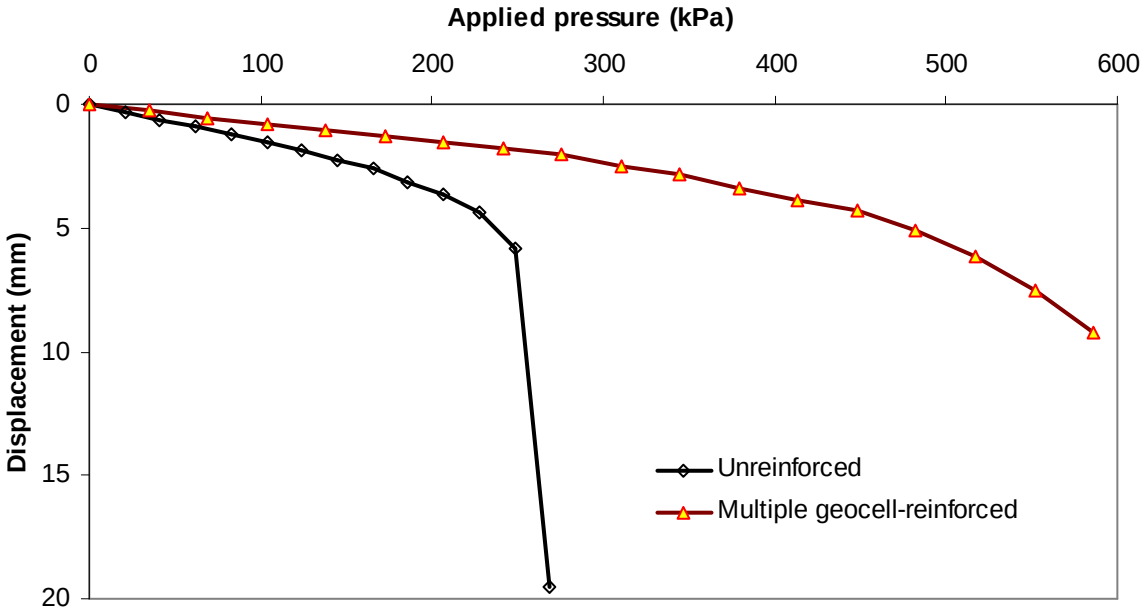

Figure 7.3.1 Pressure-displacement curves of KR-II sand under static loading

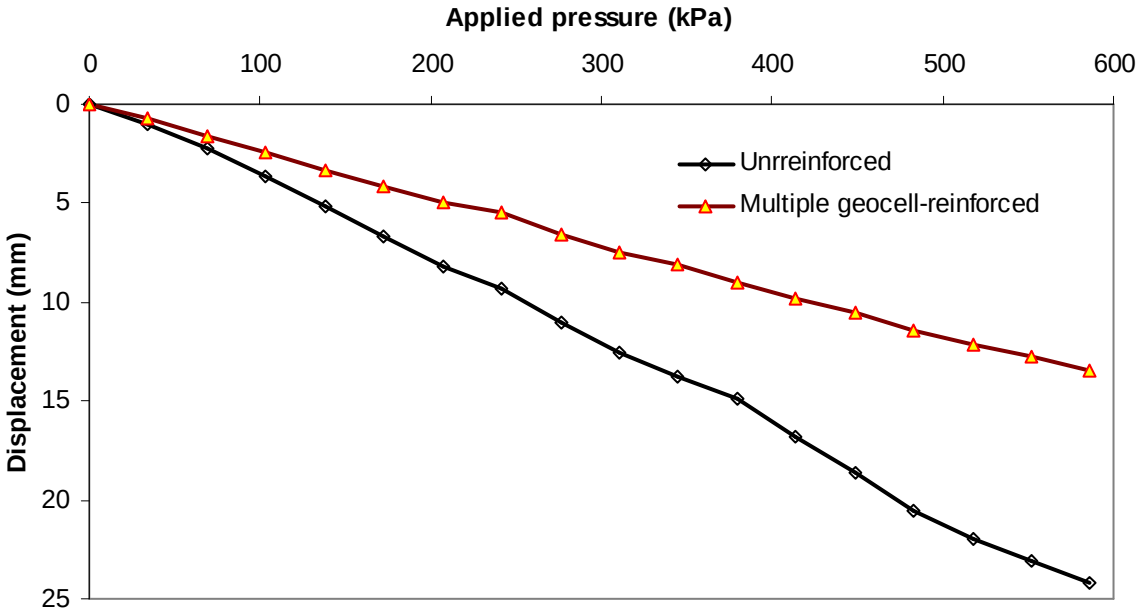

Figure 7.3.2 Pressure-displacement curves of RAP under static loading

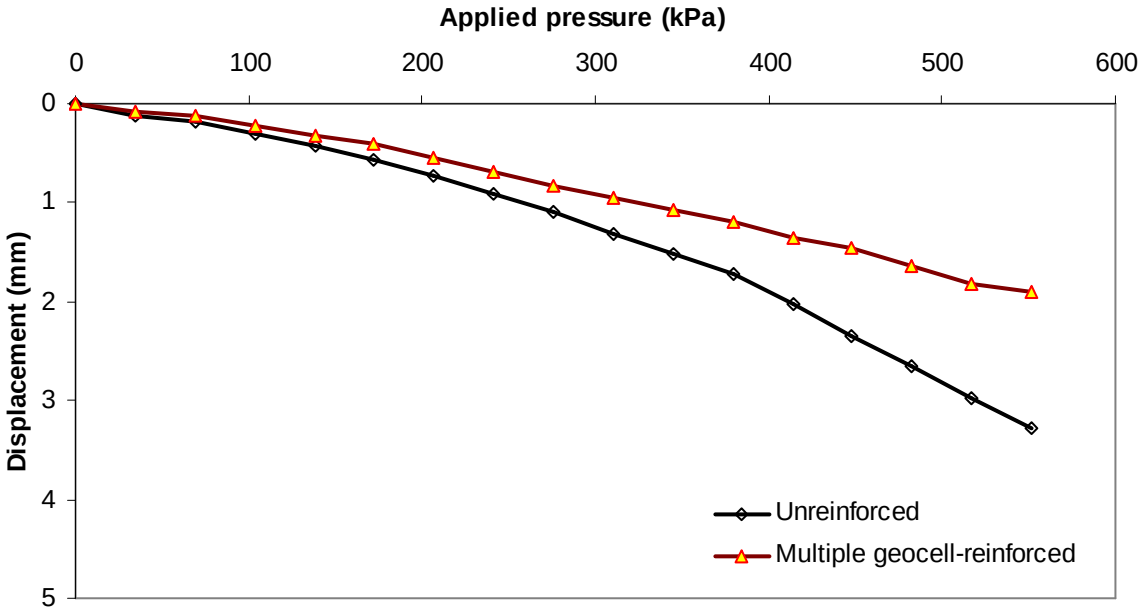

Figure 7.3.3 Pressure-displacement curves of AB-3-I under static loading

Table 7.3.1 Calculated k' values based on test data

Base material	h (cm)	h_c (cm)	N	s (cm)	CBR_{sg} (%)	CBR_{bc} (%)	I_f	R_E	k'
Cyclic plate loading test									
AB-3-I	16.0	10.0	59	7.5	2.6	13.0	1.53	4.3	0.41
AB-3-I	17.0	10.0	111	7.5	2.7	20.4	1.49	4.8	0.40
AB-3-I	22.8	15.0	136	7.5	1.9	18.3	1.52	6.7	0.27
AB-3-I	30.5	2 x 10.0	1228	7.5	1.7	20.6	1.50	7.6	0.19
KR-I sand	15.9	10.0	24	7.5	2.3	10.0	1.75	5.3	0.47
KR-I sand	22.5	15.0	17	7.5	1.6	6.7	1.76	6.8	0.32
KR-I sand	30.0	2 x 10.0	161	7.5	1.9	6.7	1.73	5.6	0.20
Moving wheel test									
AB-3-II	16.3	15.0	130	7.5	2.1	8.8	1.70	5.4	0.51
AB-3-II	15.5	10.0	300	6.4	3.2	13.8	1.54	3.7	0.50
AB-3-II	24.8	10.0	10000	7.5	2.7	20.9	1.34	4.3	0.31
RAP-I	17.0	15.0	294	7.5	2.2	7.5	1.70	4.9	0.43
RAP-I	17.0	10.0	250	7.5	2.5	7.2	1.49	3.8	0.44
RAP-I	30.0	2 x 10.0	10000	5.0	3.3	14.7	1.51	3.6	0.19
RAP-I	25.0	10.0	2000	7.5	3.1	15.4	1.34	3.4	0.38
RAP-I	23.7	7.5	1500	7.5	2.9	15.0	1.28	3.5	0.36

Note: h = base thickness, h_c = geocell height, N = number of load cycles, s = rut depth, CBR_{sg} = subgrade CBR, CBR_{bc} = base CBR, R_E = modulus ratio, I_f = modulus improvement factor, and k' = calibrated factor.

For all the fifteen NPA geocell-reinforced tests with AB-3, RAP and KR-I sand, the values of k' were calculated and provided in **Table 7.3.1**. The relationships between the calibrated value of k' and $(r/h)^{1.5}$ specifically for KR sand, RAP, and AB-3 base courses are given in **Figures 7.3.4**, **7.3.5, and 7.3.6.** A general relationship between the calibrated value of k' and $(r/h)^{1.5}$ for all types of granular base courses is given in **Figure 7.3.7**.

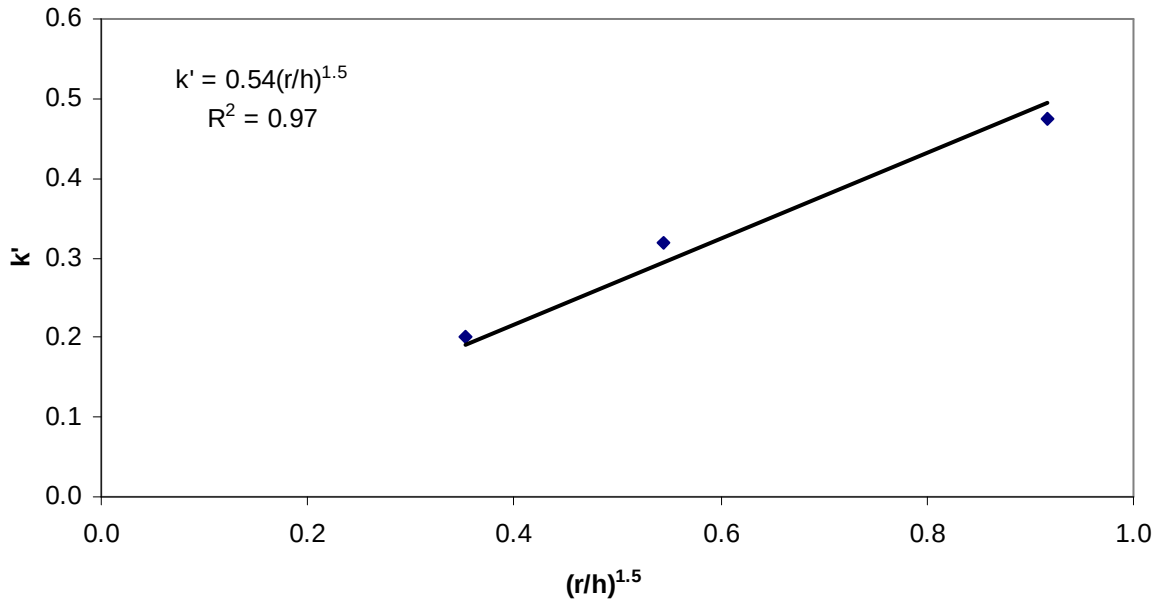

Figure 7.3.4 Relationship between k' and $(r/h)^{1.5}$ for KR-I sand base courses

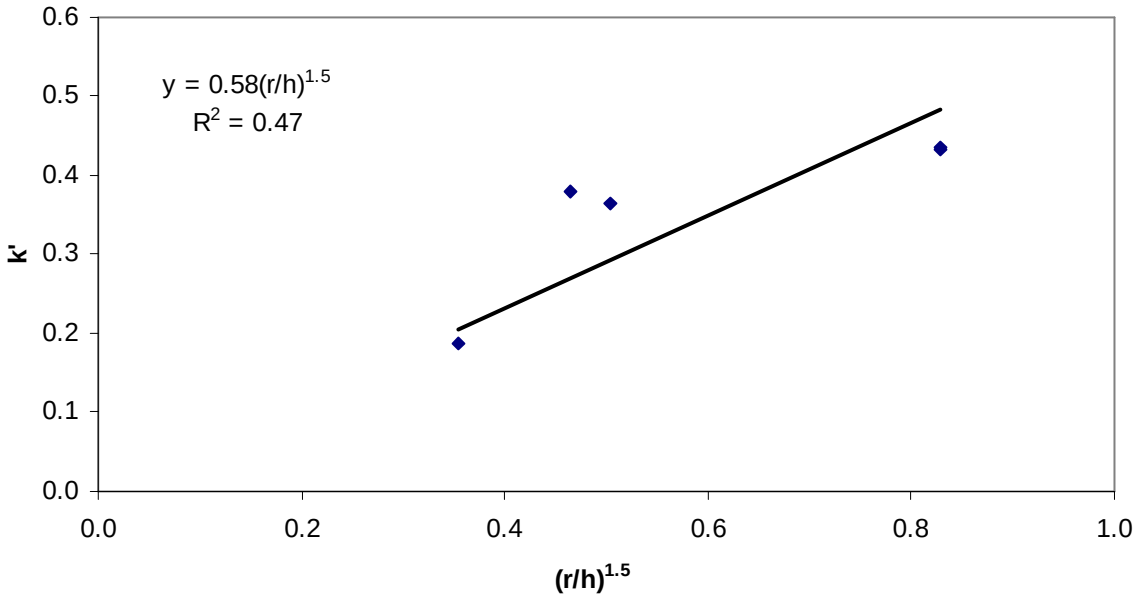

Figure 7.3.5 Relationship between k' and $(r/h)^{1.5}$ for RAP base courses

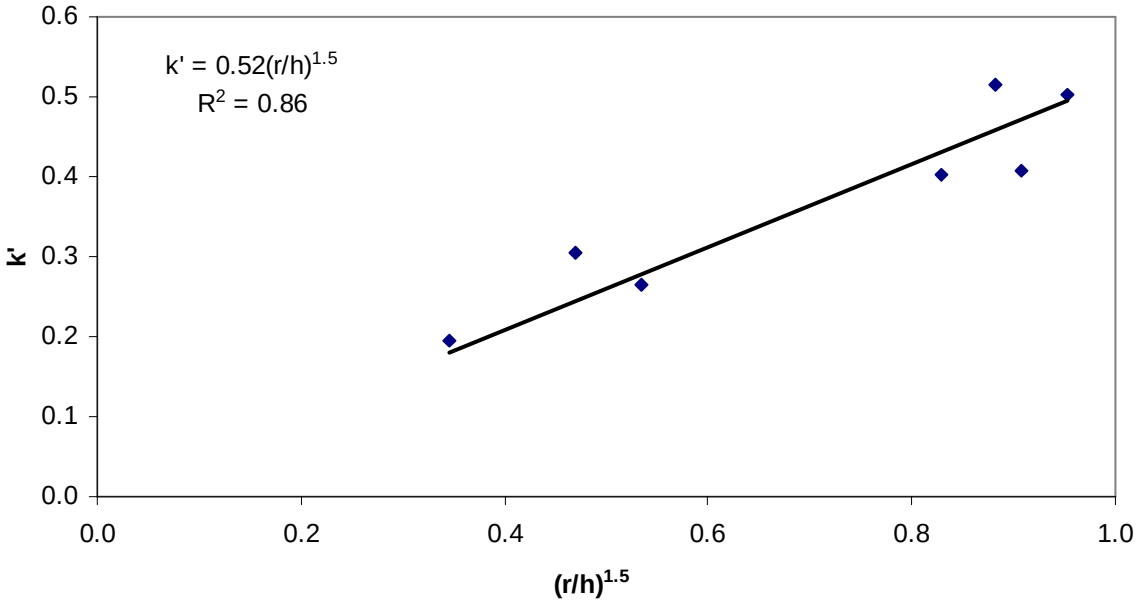

Figure 7.3.6 Relationship between k' and $(r/h)^{1.5}$ for AB-3 base courses

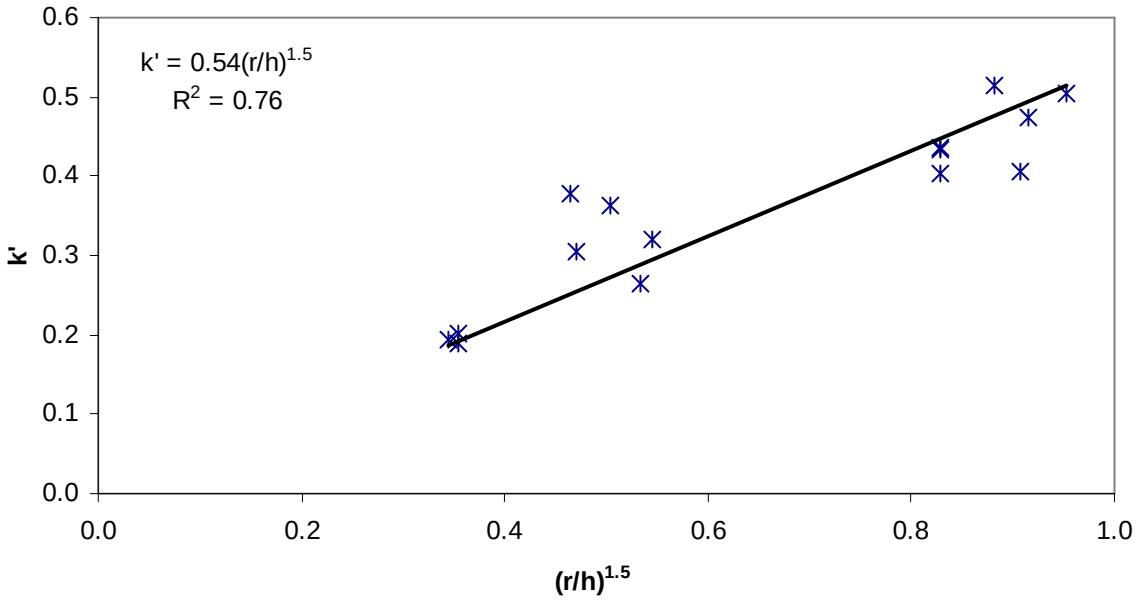

Figure 7.3.7 Relationship between k' and $(r/h)^{1.5}$ for all granular base courses

The relationship developed in **Figure 7.3.7** also includes two moving wheel test data using RAP-II and one using AB-3-II that had different cross-sectional configurations from all the other tests. These three sections had geocells placed above 10 cm thick base material (refers to Sections 3-2, 3-3, and 3-4 in **Chapter 6**). In other sections, however, geocells were placed above subgrade. The data from these three sections over-predicted the values of k' as compared with all the other test sections. Therefore, further investigation to study the effect of geocell placement at different depths within the base courses is needed before including these three test data After excluding these three sections, a generic relationship between k' and $(r/h)^{1.5}$ for NPA geocell reinforced granular base courses with geocells placed above subgrade is plotted in **Figure 7.3.8**. A better correlation ($R^2 = 0.94$) is obtained.

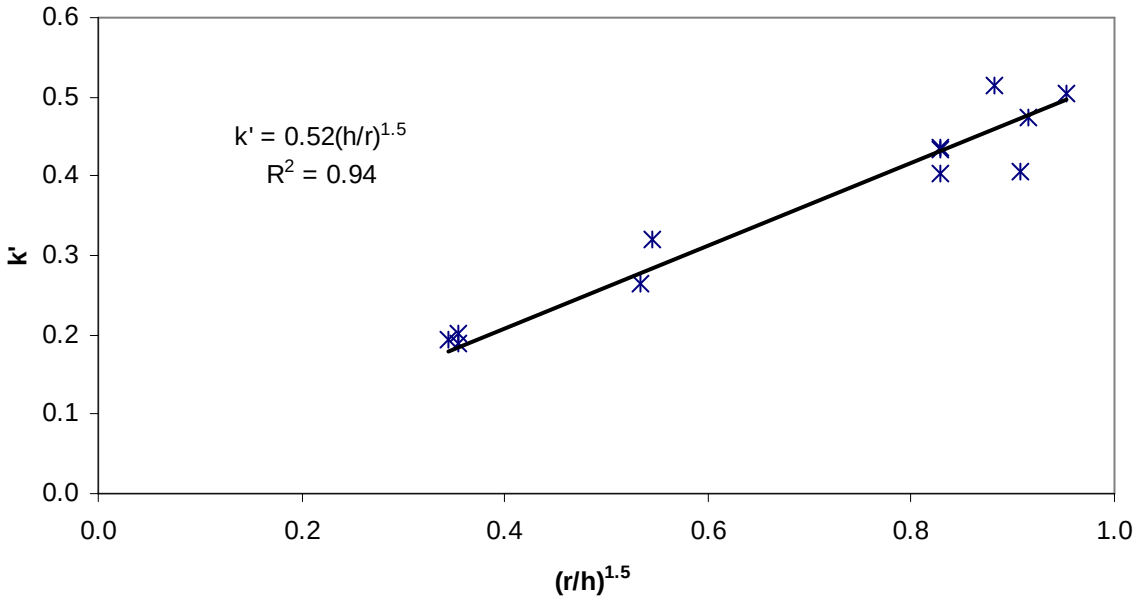

Figure 7.3.8 Generic relationship between k' and $(r/h)^{1.5}$ for granular base courses reinforced with NPA geocells above subgrade

Therefore, the following generic formula is proposed to estimate k' for NPA geocell-reinforced granular bases over weak subgrade:

$$k' = 0.52\left[\frac{r}{h}\right]^{1.5} \qquad \textbf{Equation 7.3.1}$$

The formula to estimate the thickness of a NPA geocell-reinforced base in field is as follows:

$$h = \frac{\left(0.868 + 0.52\left[\frac{r}{h}\right]^{1.5} \log N\right)}{\left\{1 + 0.204\left(R_E - 1\right)\right\}} \times \left(\sqrt{\frac{P}{\pi r^2 m\, 5.14\, c_u}} - 1\right) r \qquad \textbf{Equation 7.3.2}$$

It is important to point out that **Equation 7.3.2** is only applicable to NPA geocell because the k' value was obtained using NPA geocell. This k' value may be different for other geocell products and should be calibrated using cyclic plate loading tests and/or moving wheel tests.

7.4 Comparison of Calculated and Measured Base Thicknesses

To verify the design formula presented in **Equation 7.3.2**, the actual base thicknesses (also referred as measured herein) are compared with the calculated ones in **Figure 7.4.1**. A good agreement (R^2 = 0.86) is obtained between the calculated and measured base thicknesses. For a demonstration purpose, **Figure 7.4.2** shows the comparison of the calculated and measured base thicknesses with the three sections in which geocells were placed above 10 cm granular bases. This comparison clearly shows that a poorer correlation is obtained when the data of these three test sections are included. This demonstration shows that more research is needed to design geocell-reinforced bases over weak subgrade with geocell placed above granular materials.

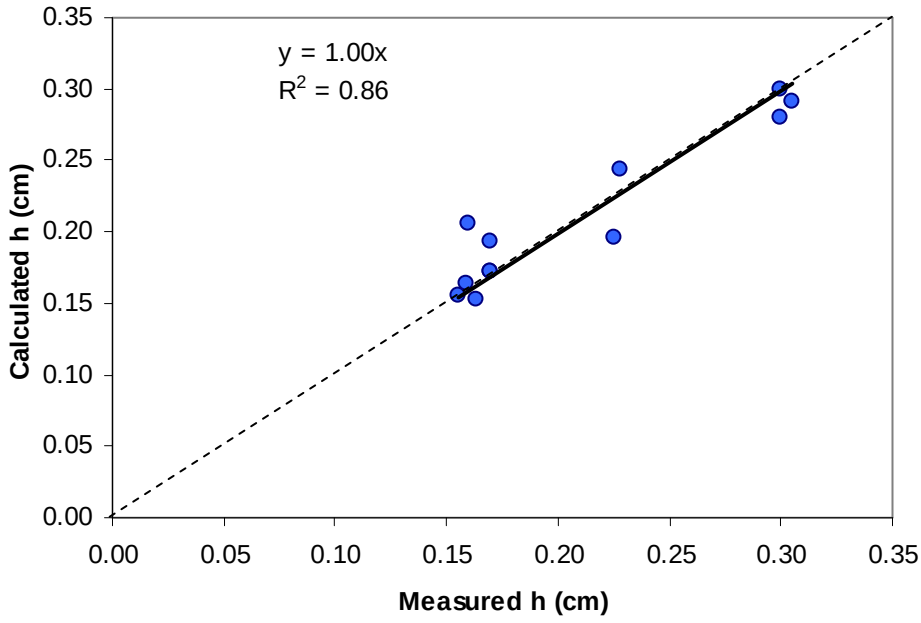

Figure 7.4.1 Comparison of the measured and calculated thicknesses of the base courses reinforced with NPA geocells above subgrade

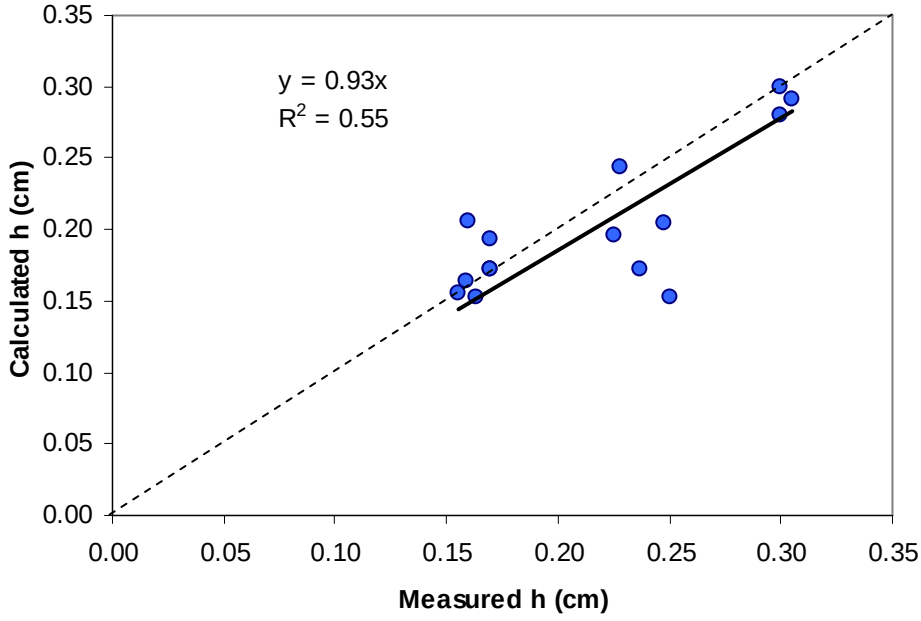

Figure 7.4.2 Comparison of the measured and calculated thicknesses of the base courses (all test sections included)

A separate check for the validity of **Equation 7.1.1** for the design of unreinforced sections was also made. The calculated and measured base thicknesses for the unreinforced sections are plotted in **Figure 7.4.3**. Except for one test section the plot shows a fair comparison between the measured and calculated base course thicknesses for the unreinforced sections. The outlier point in the figure corresponds to the RAP-I control section of the moving wheel test. This test was stopped when the rut was only 41 mm at 40,000 passes of the moving wheel test.

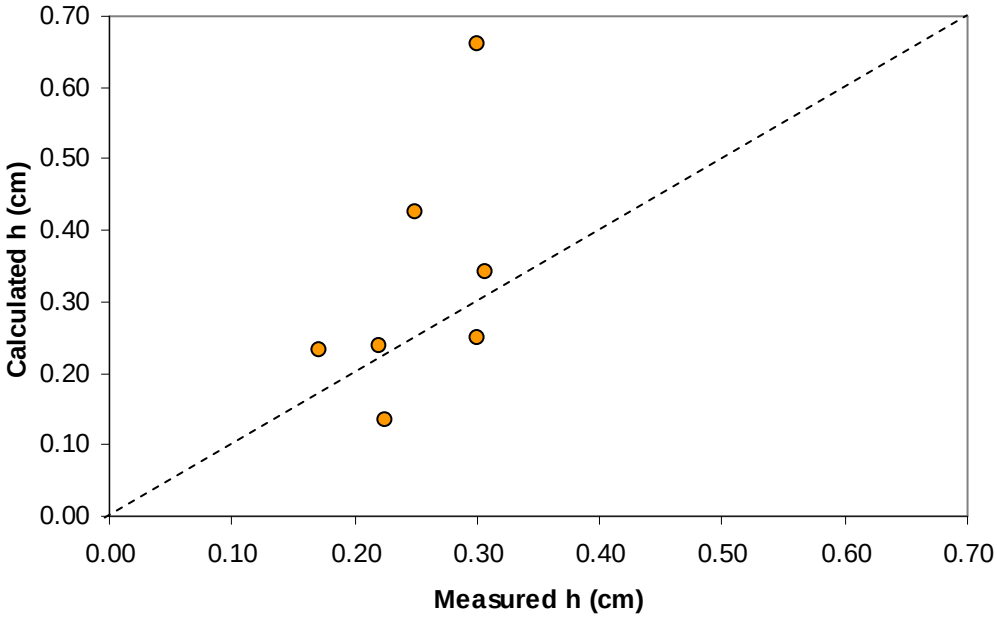

Figure 7.4.3 Comparison of the measured and calculated thicknesses of unreinforced base courses

7.5 Design Example

7.5.1 Design of an NPA geocell-reinforced section

Based on the relationship given in **Equation 7.3.2** a design example is worked out here to find the number of wheel passes for a 20 cm thick unpaved AB-3 base course section reinforced with 15 cm high NPA geocell above a weak subgrade. The CBR values of the subgrade and the base course are 2% and 20%, respectively. The allowable rut is 75 mm. The design wheel load is 40kN and the tire pressure is 552 kPa.

The radius of equivalent tire contact area is:

$$r = \left(\frac{P}{\pi p}\right)^{0.5} = \left(\frac{40}{3.14 \times 552}\right)^{0.5} = 0.15\,m$$

The modulus improvement factor (I_f) for AB-3 is 1.7 within the geocell and 2 cm cover and 1.0 for remaining unreinforced portion. The weighted average modulus improvement factor (explained in **Section 7.3**):

$$I_f = \left[\frac{(15+2)\times 1.7 + (20-15-2)\times 1.0}{20}\right] = 1.59$$

The conversion f_c = 20.0 kPa is used here to estimate the undrained cohesion of the subgrade soil (**Equation 7.2.5**):

$$c_u = f_c CBR_{sg} = 20 \times 2.0 = 40\,kPa$$

The modulus ratio (**Equation 7.2.2**) is:

$$R_E = Max\left\{7.6,\ I_f\left(\frac{3.48CBR_{bc}^{0.3}}{CBR_{sg}}\right)\right\} = Max\left\{7.6,\ 1.59\times\left(\frac{3.48\times 20^{0.3}}{2.0}\right)\right\} = 6.81$$

The bearing capacity mobilization coefficient (**Equation 7.2.3**) is:

$$m = \frac{s}{75mm}\left\{1 - 0.9\exp\left[-\left(\frac{r}{h}\right)^2\right]\right\}$$
$$= \frac{75}{75}\left\{1 - 0.9\exp\left[-\left(\frac{0.15}{0.20}\right)^2\right]\right\} = 0.49$$

The factor k' from **Equation 7.3.1** is:

$$k' = 0.52\left[\frac{0.15}{0.20}\right]^{1.5} = 0.34$$

Equation 7.3.2 is used to calculate the number of passes:

$$h = \frac{\left(0.868 + k'\log N\right)}{\eta\left\{1 + 0.204\left(R_E - 1\right)\right\}}\times\left(\sqrt{\frac{P}{\pi r^2 m\, 5.14\, c_u}} - 1\right)r$$

$$0.20 = \frac{\left(0.868 + 0.34\times\log N\right)}{1\times\left\{1 + 0.204\left(6.81 - 1\right)\right\}}\times\left(\sqrt{\frac{40000}{\pi 0.15^2\times 0.49\times 5.14\times 40000}} - 1\right)\times 0.15$$

$$0.20 = \frac{\left(0.868 + 0.34\times\log N\right)}{2.187}\times 0.205$$

$$2.14 = 0.868 + 0.34\times\log N$$

$$\log N = \frac{2.14 - 0.868}{0.34} = 3.74$$

$$N = 5500 \text{ cycles.}$$

7.5.2 Design of an unreinforced section

The required thickness of an unreinforced section corresponding to for N = 5500 passes for the NPA geocell-reinforced section designed can be determined using **Equation 7.1.1** developed by Giroud and Han (2004a, b). For the unreinforced section,

$$I_f = 1$$

$$R_E = 1 \times \left(\frac{3.48 \times CBR^{0.3}{}_{bc}}{CBR_{sg}} \right) = \frac{3.48 \times 20^{0.3}}{2.0} = 4.27$$

$$m = \frac{s}{75mm} \left\{ 1 - 0.9 \exp\left[-\left(\frac{r}{h} \right)^2 \right] \right\} = 1 - 0.9 \exp\left[-\left(\frac{0.15}{h} \right)^2 \right]$$

The equation for the unreinforced case is:

$$h = \frac{\left(0.868 + 0.661 \left(\frac{r}{h} \right)^{1.5} \log N \right)}{\eta \left\{ 1 + 0.204 \left(R_E - 1 \right) \right\}} \times \left(\sqrt{\frac{P}{\pi r^2 m \, 3.14 \, c_u}} - 1 \right) r$$

$$h = \frac{\left(0.868 + 0.661\left(\frac{0.15}{h}\right)^{1.5} \log 5500\right)}{1\times\{1+0.204(4.27-1)\}} \times \left(\sqrt{\frac{40000}{\pi 0.15^2 \times \left[1-0.9\,e^{-\left(\frac{0.15}{h}\right)^2}\right] \times 3.14 \times 40000}} - 1\right) \times 0.15$$

$$h = \frac{\left(0.868 + 2.47\left(\frac{0.15}{h}\right)^{1.5}\right)}{1.67} \times \left[\sqrt{\frac{4.57}{1-0.9\,e^{-\left(\frac{0.15}{h}\right)^2}}} - 1\right] \times 0.15$$

Assume h = 0.4 m,

$$h = \frac{0.868 + 2.47\left(\frac{0.15}{0.40}\right)^{1.5}}{1.67} \times \left[\sqrt{\frac{4.57}{1-0.9\,e^{\left[-\left(\frac{0.15}{0.40}\right)^2\right]}}} - 1\right] \times 0.15$$

$$h = 0.86 \times [3.58] \times 0.15 = 0.46\,m$$

Assume h = 0.46 m,

$$h = \frac{\left(0.868 + 2.47\left(\frac{0.15}{0.46}\right)^{1.5}\right)}{1.67} \times \left[\sqrt{\frac{4.57}{\left[1-0.9\,e^{\left[-\left(\frac{0.15}{0.46}\right)^2\right]}\right]}} - 1\right] \times 0.15$$

$$h = 0.80 \times [3.83] \times 0.15 = 0.46\,m$$

Therefore, the required thickness of the unreinforced section is 46 cm. There is a saving of 26 cm AB-3 base course when 15 cm NPA geocell is provided.

A chart developed by the Hammitt (1970) to estimate the CBR required for operation of an aircraft on unsurfaced soil is shown **Figure 7.5.1**. An estimation of the coverages (i.e., passes) based on this design chart for the unreinforced unpaved road section with a 20% CBR base shows more than 10,000 wheel passes of 9 kip (40 kN) equivalent single-wheel load and 80 psi (552 kPa) tire pressure. The number of passes is much higher than that used in the design example; therefore, the base course is strong enough to sustain the traffic loading.

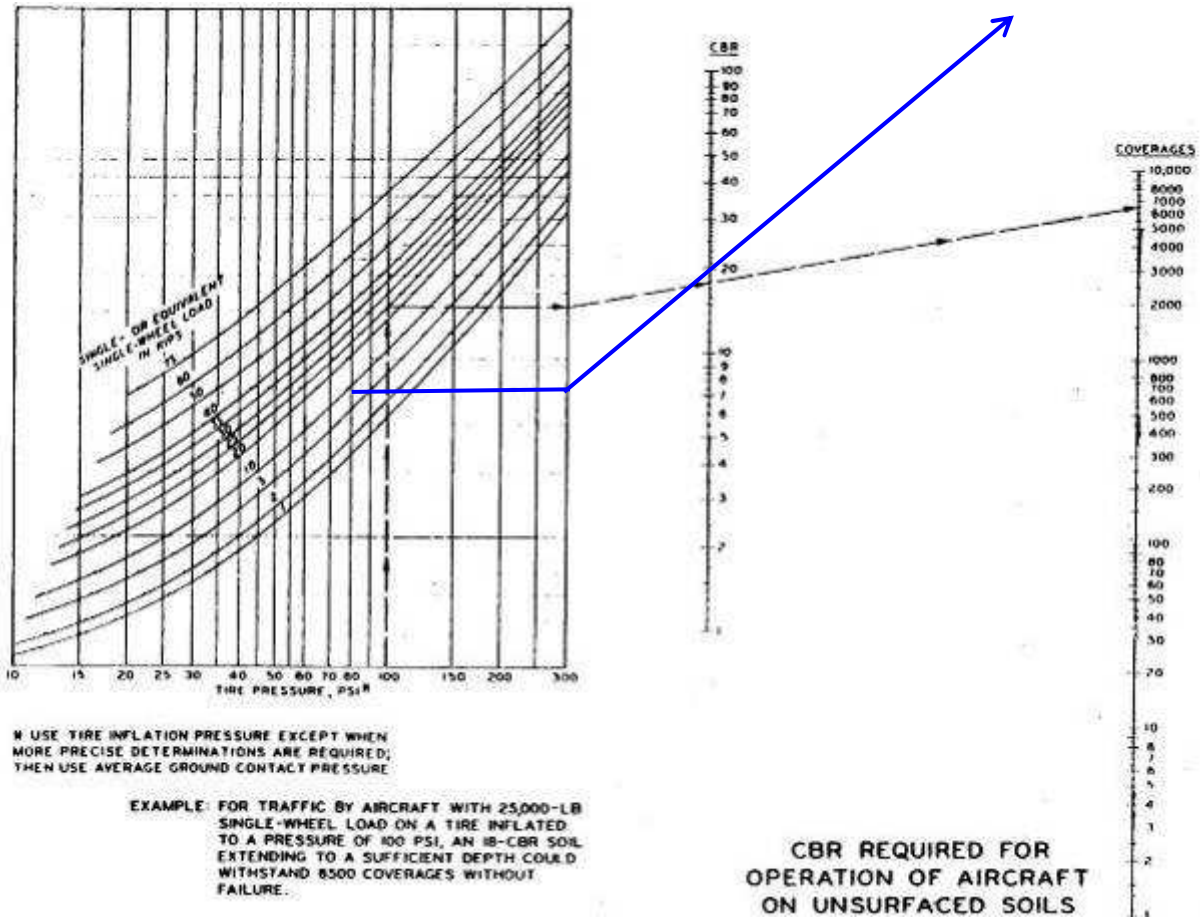

Figure 7.5.1 Design chart for the number of passes of unsurfaced soils (reproduced from Hammitt, 1970)

7.6 Limitations of the Design Method Developed in this Study

The design method developed here can be used for NPA geocell-reinforced base courses of unpaved roads on weak subgrade. It has some limitations due to the limited test conditions:

1. This design method is generic, but the k' value in **Equation 7.3.1** was calibrated against NPA geocell-reinforced base courses over weak subgrade. Therefore, it is only applicable to NPA geocells. The calibration was based on unpaved road sections reinforced with a single layer of 7.5 cm, 10 cm, or 15 cm high NPA geocell or double layers of two 10 cm high NPA geocells. All the geocells were laid out in a near circular shape with the seam side of 25 cm long and the transverse side of 21 cm wide.
2. **Equation 7.3.2** was developed based on the condition in which geocells were placed directly above subgrade. Future research is needed for geocells placed at other locations.
3. All the tests in the large geotechnical box and the accelerated moving wheel facility were conducted with the standard highway traffic wheel load of 40 kN and tire pressure of 552 kPa.
4. The test data used for the calibration of the design method were based on the subgrade CBR values ranging from 1.7% to 3.3% and the base CBR values ranging from 7% to 21%. The subgrade used in this study had the conversion factor f_c = 20 kPa between the undrained shear strength and the CBR value. Different conversion factors may exist for different subgrade.
5. This design method was calibrated with base course thicknesses ranging from 15 cm to 30 cm.

6. Based on the present study, there should be a 5 cm to 7.5 cm thick well-graded aggregate cover to minimize the damage of the geocell by moving wheels.
7. The value k' was calibrated for rut depths between 47 mm to 75 mm.
8. The number of loading cycles or passes used in the calibration ranged from 19 to 50,000. In addition, the maximum number of passes should be limited by the number in **Figure 7.5.1.**

This design method should be verified separately for conditions beyond the limits at which this study was carried out.

7.7 Summary

The design method developed in this chapter derives its theoretical basis from Giroud and Han (2004a). The factor (k') depending on the geocell reinforcement was calibrated based on large-scale laboratory cyclic plate loading tests and full-scale moving wheel tests on NPA geocell-reinforced granular bases over weak subgrdae. The design formula was verified by the test data. The design methodology is generic; however, the factors I_f and k' obtained in this study were based on NPA geocells. Calibrations are necessary if other geocell products are used.

An example was presented to demonstrate how to use the design method to design NPA geocell-reinforced bases over weak subgrade. The design example demonstrated the benefit of geocell reinforcement in the reduction in base course thickness.

The limitations of the design method were discussed, which require further verifications of this design method if field conditions deviate from the test sections.

CHAPTER EIGHT

CONCLUSIONS AND RECOMMENDATIONS

8.1 Conclusions

The results from the three stages of experimental studies in this research have demonstrated clear benefits of geocell reinforcement in terms of increased stiffness and bearing capacity, wider stress distribution, and reduced permanent deformation. This study has proposed and verified a design method for novel polymeric alloy (NPA) geocell-reinforced granular base courses for unpaved roads based on the experimental data from the plate loading tests and moving wheel tests. The following conclusions can be drawn from the present study:

a) Medium-scale plate loading tests

1. The base course reinforced with geocell placed in a circular shape had higher stiffness and bearing capacity than that with geocell placed in an elliptical shape.
2. NPA geocell reinforcement improved the stiffness of granular base courses by up to 2 times and the bearing capacity by up to 2.5 times compared with the unreinforced base course. The geocell with a higher elastic modulus produced greater improvement.
3. Under cyclic loading, NPA geocell reinforcement significantly reduced the permanent deformation of the granular base. The percentage of elastic deformation was higher in case of stronger infill materials as compared with the weaker fill material.

b) Large-scale cyclic plate loading tests

1. The NPA geocell reinforcement improved the strength and life of the unpaved road sections over weak subgrade. The reinforced sections had much higher percentage of elastic deformation (more than 90%) as compared with the unreinforced sections.
2. The NPA geocell reinforcement increased the stress distribution angle, reduced the stress transferred to the subgrade, and slowed down the rate of base course deterioration.
3. The cracks lines on the surface of NPA geocell-reinforced sections at failure had a diameter about 3 times that of the loading plate. The crack lines together with strain measurements on the geocell confirmed the beam effect of the geocell-reinforced base.

c) Full-scale moving wheel tests

1. The NPA geocell-reinforced recycled asphalt pavement (RAP) and well-graded AB-3 sections performed better than the quarry waste (QW) section. The QW compacted at wet of the optimum moisture was too weak to sustain the traffic loading.
2. NPA geocell reinforcement improved the life of the unpaved road sections, increased the stress distribution angle, and reduced the vertical stress transferred to the subgrade as compared with the unreinforced control section.
3. A thicker fill cover (5 to 7.5 cm) is necessary to minimize the damage to the geocell.
4. The compaction of the base course plays a vital role in overall performance of the geocell-reinforced unpaved road sections.

d) Design method

The design method developed in this study can be used to design NPA geocell-reinforced unpaved roads on weak subgrade. The calculated base thicknesses from the proposed design formula were compared well with the measured values from the experiments. A design example was provided to illustrate how the required thickness of NPA geocell-reinforced bases can be determined.

These conclusions were obtained based on the tests using NPA geocells. Geocells made of other materials may have different behavior and should be evaluated by separate testing.

8.2 Recommendations for Future Study

The experimental work in this study was comprehensive as compared with other contemporary research on geocell reinforcement. However, there is still space for future research to further improve the design method. Some of the topics that will be needed to improve the design method are as follows:

1. This study has considered only one type of the geocell (NPA geocell) for the design method. A study with other types of geocell with different stiffness is needed to verify the design equation for the modulus improvement factor.
2. All the cyclic plate loading tests and the moving wheel tests were carried out under a wheel load of 40 kN and a tire pressure of 552 kPa. The proposed design equation should be verified further for other wheel loads and tire pressures.

3. Another study of interest would be to check the relationship between the modulus improvement factor and the degree of compaction of the base course material.
4. In the present study most of the tests were conducted on the sections where the bottom of the NPA geocell reinforcement was placed at the interface between the subgrade and the base course. There were only three experiments where the reinforcement was placed some distance above the interface. The results from these three tests were found different from other test results. Therefore, further tests by placing geocells at different depths within the base course are recommended.

REFERENCES

American Association of State Highway and Transportation Officials (AASHTO) (1993). *Guide for Design of Pavement Structures*, Washington, D.C.

Bathurst, R.J., and P.M. Jarrett (1988). "Large-scale model tests of geocomposite mattresses over peat subgrades." *Transportation Research Record 1188*, 28-36.

Bathurst, R.J. and Karpurapu, R. (1993). "Large-scale triaxial compression testing of geocell-reinforced granular soils." *Geotechnical Testing Journal*, GTJODJ, 16 (32), 296-303.

Bhandari, A. and Han, J. (2009). "DEM study of a shallow foundation under vertical loading." In: Iskander, M., Laefer, D.F., and Hussein, M.H. (eds.), *Contemporary Topics in Ground Modification, Problem Soils, and Geo-support, Proceedings of the 2009 International Foundation Congress & Equipment Expo*, March 15-19, Orlando, Florida. ASCE Geotechnical Special Publication 187, 465-472.

Carter, G. R., and Dixon, J. H. (1995). "Oriented polymer grid reinforcement." *Construction and Building Materials*, 9 (6), 389-401.

Chang, D. T., Chang, C. H. and Pai, S.W. (2007). "Investigation of bearing capacity and dynamic-elastic behavior of mechanical stabilization of sandy subgrade using geocells." *Transportation Research Board 86th Annual Meeting, CD ROM*, 07-1445, January 21 to 25, 2007.

Chang, D. T.; Chang, C. H.; Kou, C. H.; and Chien T. W. (2008). "Bearing capacity and resilient property studies for sandy soil with confinement of geocells." *Transportation Research Board 87th annual meeting, CD ROM*, January 13–17, 2008 Washington, D.C.

Cowland, J.W. and Wong S.C.K. (1993). "Performance of road embankment on soft clay supported on a geocell mattress foundation." *Geotextiles and Geomembranes*, 12 (8), 687-705.

Dash, S. K., Krishnaswamy, N. R., and Rajagopal K. (2001a). "Bearing capacity of strip footings supported on geocell-reinforced sand." *Geotextiles and Geomembranes*, 19 (4), 235-256.

Dash, S. K., Rajagopal K., and Krishnaswamy, N. R. (2001b). "Strip footing on geocell reinforced sand beds with additional planar reinforcement." *Geotextiles and Geomembranes*, 19 (8), 529-538.

Dash, S. K., Sireesh S., and Sitharam, T. G. (2003). "Model studies on circular footing supported on geocell reinforced sand underlain by soft clay." *Geotextiles and Geomembranes*, 21 (4), 197-219.

Dash, S.K., Rajagopal, K., and Krishnaswamy, N.R. (2004). "Performance of different geosynthetic reinforcement materials in sand foundations." *Geosynthetics International*, 11 (1), 35-42.

de Garidel, R. and Morel, G. (1986). "New soil strengthening techniques by textile elements for low-volume roads." *Road and Railway Applications, Third International Conference on Geotextiles*, Vienna, Austria.

Douglas, R.A. (1997). "Repeated-load behavior of geosynthetic-built unbound roads." *Canadian Geotechnical Journal*, 34 (2), 197-203.

Edil, T.B., Benson, C.H., Shafique, M.S.J., Tanyu, B.F., Kim, W.H., and Senol, A. (2002). "Field evaluation of construction alternatives for roadway over soft subgrade." *Transportation Research Board, 81st Annual Meeting*, January 13-17, 2002.

Gabr, M. (2001). *Cyclic Plate Loading Tests on Geogrid Reinforced Roads*. Research report to Tensar Earth Technologies, Inc., NC State University, 43 p.

Giroud, J.P. and Han, J. (2004a). "Design method for geogrid-reinforced unpaved roads. I. Development of design method." *Journal of Geotechnical and Geoenvironmental Engineering*, 130 (8), 775-786.

Giroud, J.P. and Han, J. (2004b). "Design method for geogrid-reinforced unpaved roads. II. Calibration of applications." *Journal of Geotechnical and Geoenvironmental Engineering*, 130 (8), 787-797.

Giroud, J.P. and Noiray, L. (1981). "Geotextile- reinforced unpaved road design." *Journal of the Geotechnical Engineering Division*, 107 (GT9), 1233-1254.

Gourves, R, Reiffsteck, P., and Vignon, J.F. (1996). "Study of confinement effect in geocells." *Geosynthetics: Applications, Design and Construction*, 1 (1996), 455 – 458.

Hammitt, G.M. (1970). *Thickness Requirements for Unsurfaced Roads and Airfields: Bare Base Support*, Project 3782-65, Technical Report S-70-5, U.S. Army Engineer Waterways Experiment Station, CE, Vicksburg, Miss.

Han, J., Yang, X., Parsons, R.L., Leshchinsky, D. (2007). Design of Geocell-reinforced Bases. Internal Report to PRS, the University of Kansas.

Han, J., Yang, X.M., Leshchinsky, D., and Parsons, R.L. (2008a). "Behavior of geocell-reinforced sand under a vertical load." *Journal of Transportation Research Board*, No. 2045, 95-101.

Han, J., Yang, X.M., Leshchinsky, D., Parsons, R.L., and Rosen, A. (2008b). "Numerical analysis for mechanism of a geocell-reinforced base under a vertical load." *Proceeding of 4th Asian Regional Conference on Geosynthetics*, June 17-20, 2008 Shanghai, China, 741-746.

Han, J., Pokharel, S.K., Leshchinsky, D., Parsons, R.L., and Halahmi, I. (2010). "Effect of infill material on the performance of geocell-reinforced bases." *9th International Conference on Geosynthetics, ICG 2010*, May 23-27, 2010, Brazil.

Harr M.E. (1966). "Foundations of theoretical soil mechanics." New York: McGraw-Hill.

Jamnejad, G., Kazerani, B., Harvey, R.C., and Clarke, J.D. (1986). "Polymer grid cell reinforcement in pavement construction." *Proceedings of 2nd International Conference on Bearing Capacity of Roads and Airfields*, September 16-18, 1986, Plymouth, England, 1, 537-546.

Kazerani, B. and Jamnejad, G. (1987). "Polymer grid cell reinforcement in construction of pavement structures. Section 1A, unpaved and paved roads." *Geosynthetic '87 Conference*, New Orleans, USA.

Madhavi Latha, G.M., Rajagopal, K., and Krishnaswamy, N.R. (2006). "Experimental and theoretical investigations on geocell-supported embankments." *International Journal of Geomechanics*, 6 (1), 30-35.

Madhavi Latha, G. and Murthy, V.S. (2007). "Effects of reinforcement form on the behavior of geosynthetic reinforced sand." *Geotextiles and Geomembranes*, 25 (1), 23-32.

Mandal, N.J. and Gupta, P. (1994). "Stability of geocell-reinforced soil." *Construction and Building Materials*, 8 (1), 55-62.

Mandel and Salençon (1972) Mandel, J. and Salençon, J., 1972. "Force portante d'un sol une assise rigide." *Géotechnique*, 22 (1), 79-93.

Mengelt, M.J., Edil, T.B., and Benson, C.H. (2000). *Reinforcement of Flexible Pavements Using Geocells*. Geo Engineering Report no. 00-04, Geotechnical Engineering Program, Department of Civil & Environmental Engineering, University of Wisconsin-Madison.

Mengelt, M.J., Edil, T.B., and Benson, C.H. (2006). "Resilient modulus and plastic deformation of soil confined in a geocell." *Geosynthetic International*, 13 (5), 195-205.

Meyer, N. (2007). *Determination of Bearing Capacity of Geocell Reinforced Soil over Soft Subgrade with Static and Dynamic Plate Load Tests: Results Analysis*. TU Clausthal, Institute of Geotechnical Engineering and Mine Surveying.

Mhaiskar, S.Y. and Mandal, J.N. (1992a). "Comparison of geocell and horizontal inclusion for paved road structure." *Earth Reinforcement Practice*, Ochiai, Hayashi and Otani. Balkema, Rotterdam.

Mhaiskar, S.Y. and Mandal, J.N. (1992b). "Subgrade stabilization using geocells." *ASCE Geotechnical Special Publication*, 2 (30), 1092-1103.

Mhaiskar, S.Y. and Mandal, J.N. (1994). "Three dimensional geocell structure - performance under repetitive loads." *Proceedings of 5th International Conference on Geotextiles, Geomembranes and Related Products*, Singapore, 5-9 September 1994.

Mhaiskar, S.Y. and Mandal, J.N. (1996). "Investigation on soft clay subgrade strengthening using geocells." *Construction and Building Materials*, 10 (4), 281-286.

Mitchell, J. K., Kao, T. C., and Kavazanjian, E. (1979). *Analysis of Grid Cell Reinforced Pavement Bases.* Report GL-79-8, Geotechnical Laboratory, U.S. Army Engineer Waterways Experiment Station, Vicksburg, MS.

Pokharel, S.K., Han, J., Leshchinsky, D., Parsons, R.L., and Halahmi, I. (2009a). "Experimental evaluation of influence factors for single geocell-reinforced sand". *Transportation Research Board 88th annual meeting*, January 11-15, 2009, Washington, DC.

Pokharel, S.K., Han, J., Leshchinsky, D., Parsons, R.L., and Halahmi, I. (2009b). "Behavior of geocell-reinforced granular bases under static and repeated loads". *Contemporary topics in Ground Modification, Problem Soils, and Geo-Support*, (Eds. Iskander, M., Laefer, D.F., and Hussein, M.H.), 2009 International Foundation Congress & Equipment Expo, March 15-19, 2009, Orlando, Florida. ASCE Geotechnical Special Publication 187, 409-416.

Pokharel, S.K., Han, J., Parsons, R.L., Qian, Y., Leshchinsky, D., and Halahmi, I. (2009c). "Experimental study on bearing capacity of geocell-reinforced bases." *8th International Conference on Bearing Capacity of Roads, Railways and Airfields*, June 29 - July 2, 2009, Champaign, Illinois.

Pokharel, S.K., Han, J., Leshchinsky, D., Parsons, R.L., and Halahmi, I. (2010). "Investigation of factors influencing behavior of single geocell-reinforced bases under static loading." *Geotextiles and Geomembranes*, 28, 570-578.

Rajagopal, K., Krishnaswamy, N.R., and Madhavi Latha, G. (1999). "Behaviour of sand confined with single and multiple geocells." *Geotextiles and Geomembranes*, 17 (3), 171 -184.

Rea, M and Mitchell, J.K. (1978). "Sand reinforcement using paper grid cells." *Regular meeting- Rocky Mountain Coal Mining Institute*, 644-663.

Shimizu, M and Inui, T. (1990). "Increase in the bearing capacity of ground with geotextile wall frame." *Geotextiles, Geomembranes and Related Products*, Den Hoedt (ed.), Balkema, Rotterdam, 254.

Steward, J., Williamson, R., and Mahoney, J. (1977). *Guidelines for Use of Fabrics in Construction and Maintenance of Low-Volume Roads*. Rep. PB-276 972, Forest Service, USDA, Portland, Oregon.

Tingle, J.S. and Jersey, S.R. (2007). "Empirical design methods for geosynthetic-reinforced low-volume roads." *Journal of the Transportation Research Board*, No. 1989 (2), 91-101.

Ullidtz, P. (1987). *Pavement Analysis*. Elsevier Science Publisher, New York.

Wayne, M.H., Han, J., and Akins, K. (1998). "The design of geosynthetic reinforced foundations." *Proceedings of ASCE's 1998 annual convention and Exposition*, Boston, Massachusetts, October 18-21, ASCE Geotechnical Special Publication, No. 76, 1-18.

Webster, S. L. and Watkins, J. E. (1977). *Investigation of Construction Techniques for Tactical Approach Roads Across Soft Ground.* Report S-77-1, Soils and Pavements Laboratory, U.S. Army Engineer Waterways Experiment Station, Vicksburg.

Webster, S. L. and Alford, S. J. (1978). *Investigation of Construction Concepts for Pavements Across Soft Ground*. Report S-78-6, Geotechnical Laboratory, U.S. Army Engineer Waterways Experiment Station, Vicksburg, MS.

Webster, S. L. (1979a). *Investigation of Beach sand Trafficability Enhancement Using Sand-grid Confinement and Membrane Reinforcement Concepts*. Report GL-79-20 (1), U.S. Army Engineer Waterways Experiment Station, Vicksburg, MS.

Webster, S. L. (1979b). *Investigation of Beach Sand Trafficability Enhancement Using Sand-grid Confinement and Membrane Reinforcement Concepts*. Report GL-79-20 (2), U.S. Army Engineer Waterways Experiment Station, Vicksburg.

Webster, S. L., R. H. Grau, and T. P Williams (1992). *Description and Application of Dual Mass Dynamic Cone Penetrometer*. Instruction Report GL-92-3, Department of the Army, US Army Corp of Engineers, Washington, DC.

Yang, X.M. (2010). *Numerical Analyses of Geocell-Reinforced Granular Soils under Static and Repeated Loads*. Ph.D. dissertation, CEAE Department, the University of Kansas.

Yoder, E.J. and Witczak, M.W. (1975). *Principles of Pavement Design*. Second edition, John Wiley & Sons, Inc.

Yuu, J., Han, J., Rosen, A., Parsons, R.L., and Leshchinsky, D. (2008). "Technical review of geocell-reinforced base courses over weak subgrade." *Proceedings of the First Pan*

American Geosynthetics Conference & Exhibition, 2-5 March 2008, Cancún, Mexico, 1022-1030.

Zhou, H. and Wen, X. (2008). "Model studies on geogrid - or geocell-reinforced sand cushion on soft soil." *Geotextiles and Geomembranes*, 26(3), 231-238.